Concepts & Engineering Aspects of a Neutron Resonance Spin-Echo Spectrometer for the National Institute of Standards and Technology Center for Neutron Research

Jeremy C. Cook

Center for Neutron Research, National Institute of Standards and Technology, Gaithersburg, Maryland, USA.

Abstract

After a brief introduction, the Neutron Resonance Spin Echo (NRSE) principle is discussed classically in Sec. 2. In Sec. 3, two idealized 4-coil NRSE spectrometers are discussed (one using single π coil units and one using paired "bootstrap" coils), some ideal-case expressions are given for the spin-echo signal from these spectrometers and some theoretical limitations are discussed. A more quantum mechanical discussion of NRSE is presented in Sec. 4 and some theory about the spin echo signal is given is Sec. 5. Factors affecting the spectrometer's instrumental resolution are discussed in Sec. 6. In Sec. 7, a variety of engineering issues are assessed in the context of stated performance goals for a NIST Center for Neutron Research (NCNR) NRSE spectrometer. In Sec. 8 some Monte Carlo simulations of the NRSE signal examining the combined influences of some of the spectrometer imperfections are presented and compared with the analytical predictions developed in previous sections. In Sec. 9 possible alternatives for a NCNR NRSE spectrometer configuration are assessed and a preliminary discussion of the spectrometer neutron guide requirements is presented. A summary of some of the useful formulas can be found in Appendix A.

Key words: Quasi-elastic neutron scattering, Neutron resonance spin-echo spectrometers, Neutron Instrumentation Simulations.

1 Introduction

Neutron Resonance Spin Echo (NRSE) [1, 2] is variant of the conventional Neutron Spin Echo (NSE) [3] technique, whereby the long solenoids used in the latter are replaced by r.f. spin-flippers separated by gaps in which there is nominally zero magnetic field. For this reason the former is sometimes also referred to as "Zero Field Spin

Echo". Neutron Spin Echo spectrometers distinguish themselves from all other types of neutron spectrometer by their ability to resolve energy changes in a neutron scattering event that are much smaller than the energy width of the incident beam. This is because the degree of "fan-out" of the neutron spin orientation caused by the incident neutron velocity spread in a constant magnetic field is correlated with the neutron speed and can be canceled, to first order, over the scattered neutron beam path by reversing the magnetic field direction over an equivalent[1] flight path. The very small neutron velocity changes that occur in the scattering are revealed by measurement and comparison of the final beam polarization with a reference in which no energy change is known to occur. By contrast, in conventional time-of-flight spectrometers where the measured quantity is the neutron arrival time, a minimum arrival time uncertainty is imposed by the incident pulse duration and the velocity spread of the incident beam that it causes. These can only be reduced by restricting the neutron energy bandwidth with the associated loss of intensity. Some of the more important issues for NRSE spectrometers are explored in the following sections.

2 Classical description of resonance spin echo

2.1 Classical principle of operation

One of the advantages of neutron resonance spin echo (NRSE) spectrometers over classical precession path (NSE) machines is geometrical. The long solenoids that impose significant restrictions on the incident and scattered beam paths in NSE spectrometers is eliminated in NRSE.

In NSE and NRSE instruments the mechanism of the neutron velocity determination is quite different. In the most common NRSE configuration, four short resonant r.f. flipper coils replace the static field boundaries of the classical NSE spectrometer and the intervening space between the flippers has zero magnetic field. The r.f. fields in the first and second coils must be phased-locked and also in the third and fourth coils. This is because the phase of the r.f. field at the time of neutron passage through the coil effectively acts as the neutron clock as opposed to the number of Larmor precessions in the solenoids of a conventional NSE instrument.

Descriptions of the r.f. π flipper coil as used in NRSE machines can be found in Refs. [1] and [2]. Henceforth, we use the coordinate system used by Gähler and Golub in Ref. [2]. Note that this coordinate system differs from the one used in Ref. [1].

[1] Such that the product of the magnetic field and the flight path length is equal in magnitude for quasi-elastic neutron scattering.

With reference to Figure 1(a), consider an incident monochromatic beam of neutrons of velocity v_n, traveling along the *y* axis, initially polarized parallel to the *x* axis. In the coil, a static magnetic field of magnitude B_0 is applied in the *z* direction and an oscillating r.f. field is applied in a plane perpendicular to B_0 (i.e., in the *xy* plane). We will use the notation l_π to define the length (in the beam direction) of the region of intersection of the static field region (length l_{B0}) with the r.f. field region (length l_{rf}), i.e.,

$$l_\pi = l_{B_0} \cap l_{rf} \qquad (1),$$

since l_{B0} and l_{rf} can never be exactly the same. Therefore, if the static field region completely encloses the r.f. region, $l_\pi = l_{rf}$ and if the r.f. region completely encloses the static field region $l_\pi = l_{B0}$. Note that l_π is distinct from the *length of the coil*, which is a useful parameter in some instances and is defined by

$$l_{coil} = l_{B_0} \cup l_{rf} \qquad (2).$$

If one field region completely encloses the other (as it usually does), Eq. (2) simplifies to

$$l_{coil} = \max\left(l_{B_0}, l_{rf}\right) \qquad (3).$$

It is usual in r.f. flipper coils for the static field to completely enclose the r.f. field region. Therefore, when discussing flipper coils we will always assume $l_\pi = l_{rf}$ and $l_{coil} = l_{B0}$ (which is slightly larger than l_{rf}) as indicated in Figure 1. *Thereby, it is always assumed that the r.f. field is combined with a perpendicular static field in the coils whereas there is the possibility for (usually short) static-only field regions either side of the r.f. coil.*

The following classical argument is not rigorously true but provides the most "pictorial" illustration of the NRSE principle. The classical result agrees well with the quantum mechanical result provided that the following approximations can be made:

1. The magnitude of B_0 is very much greater than the magnitude of B_{rf} (see [4, 5]).
2. The oscillatory field can be approximated by a pure rotating field for the most important magnetic field interactions.
3. The Zeeman splitting due to B_0 ($\mu_n B_0$) « the kinetic energy of the neutron, $m_n v^2/2$.

Thus, it is convenient to consider the oscillating field as consisting of two counter-rotating components as shown in Figure 2, where the *resonant* component is the one that rotates in the *same direction* as the Larmor precession due to the static field B_0 and can be described by

$$\vec{B}_{rf} = B_{rf}\left(\hat{i}\cos\omega_{rf}t + \hat{j}\sin\omega_{rf}t\right) \tag{4}$$

where the sign of ω_{rf} is chosen appropriately. The current classical approximation ignores the much weaker influence of the counter-rotating (non-resonant) component of the r.f. field.

Consider first the neutron spin with respect to the static field B_0. If $B_0 \gg B_{rf}$, the neutron spin may be assumed to precess in the *xy* plane with a Larmor angular frequency ω_0

$$\omega_0 = \gamma_n B_0 \tag{5}$$

where γ_n is the gyromagnetic ratio for the neutron, defined as the ratio of the magnitude of the neutron magnetic moment to the magnitude of its angular momentum, where

$$\gamma_n = \frac{2|\mu_n|}{\hbar} = 1.832472\times10^8 \text{ rad s}^{-1}\text{T}^{-1} \tag{6}$$

and μ_n is traditionally defined as the maximum component of the neutron magnetic moment measurable along a single axis.

If B_0 is measured in Tesla, we have

$$\omega_0\left[\text{rads s}^{-1}\right] = 1.832472\times10^8\, B_0\left[\text{T}\right] \tag{7}$$

or

$$\nu_0\left[\text{MHz}\right] = 29.1647\, B_0\left[\text{T}\right] \tag{8}$$

If the r.f. angular *frequency*, ω_{rf}, is tuned exactly to the value ω_0, one component of the r.f. field rotates synchronously with the precessing neutron spin about the *z* axis (i.e., is "on resonance"-Figure 1(b)), so we can also write

$$\omega_{rf}\left[\text{rad s}^{-1}\right] = 1.832472\times10^8\, B_0\left[\text{T}\right] \qquad \textbf{\textit{on-resonance}} \tag{9}$$

and

$$\nu_{rf}\left[\text{MHz}\right] = 29.1647\, B_0\left[\text{T}\right] \qquad \textbf{\textit{on-resonance}} \tag{10}.$$

Because we are ignoring the effects of the counter-rotating (non-resonant) r.f. component, Figure 1(b) shows only the resonant component of the r.f. field.

In the rest frame of the resonant component of B_{rf} (i.e. the frame rotating in the *xy* plane at angular speed $\omega_{rf}=\omega_0$), the neutron spin precesses around the axis defined by the direction of B_{rf} in this frame (Figure 1(c)) at an angular frequency ω_p, where

$$\omega_p = \gamma_n B_{rf} \tag{11}$$

and gains a precession angle β around this axis that depends on the time spent in the r.f. (combined) field region, i.e.,

$$\beta = \gamma_n B_{rf} t \quad \approx \quad \gamma_n B_{rf} \frac{l_{rf}}{v_n} = \frac{\gamma_n m_n}{h} B_{rf} l_{rf} \lambda_n \quad (\textit{approx valid for small beam divergence}) \tag{12}$$

where t is the time of flight of the neutron through across the region l_{rf}. Note that the approximation in Eq. (12) originates from the assumption that the beam divergence is sufficiently small that the substitution $t \approx l_\pi / v_n$ can be made. In order to create a π flip of the neutron spin around B_{rf} (such that the neutron spin returns to the *x*-*y* plane), the magnitude of B_{rf} must be tuned to satisfy

$$\left|B_{rf}\right| \quad \approx \quad \pi \frac{v_n}{\gamma_n l_{rf}} \quad = \quad \pi \frac{h}{\gamma_n m_n l_{rf} \lambda_n} \qquad \textit{for small beam divergence} \tag{13}$$

from which we have

$$B_{rf}\left[\mathrm{T}\right] \simeq \frac{6.782232\times10^{-5}}{l_{rf}\left[\mathrm{m}\right]\lambda_n\left[\mathrm{\mathring{A}}\right]} \quad = \quad \frac{6.782232\times10^{-5}}{l_\pi\left[\mathrm{m}\right]\lambda_n\left[\mathrm{\mathring{A}}\right]} \tag{14}.$$

Note that the peak amplitude of the r.f. field has *twice* the magnitude of the resonant component (i.e., $B_{rf}^{pk} = 2B_{rf}$). In other words,

$$B_{rf}^{pk}\left[\mathrm{T}\right] \quad = 2B_{rf}\left[\mathrm{T}\right] \quad \simeq \frac{1.35645\times10^{-4}}{l_{rf}\left[\mathrm{m}\right]\lambda_n\left[\mathrm{\mathring{A}}\right]} \quad = \frac{1.35645\times10^{-4}}{l_\pi\left[\mathrm{m}\right]\lambda_n\left[\mathrm{\mathring{A}}\right]} \tag{15}.$$

Typically, the time of flight through such coils (of several cm in length) is around 50μs (within a factor of a few, depending on the neutron wavelength), therefore B_{rf} is typically only a few tenths of a mT. This contrasts with B_0 that ranges up to about 25 mT or beyond. Certainly for the higher values of B_0, our assumption that $B_0 \gg B_{rf}$ is still valid.

If the initial phase angle of the neutron spin *lags* the resonant component of B_{rf} at the point of entry into the r.f. field by ψ (see Figure 1 (c)), and if Eq. (13) is satisfied, on exiting the field region the neutron spin *leads* B_{rf} by ψ in

the rotating frame. Transforming back into the lab frame at the coil exit, we must add on the phase change of the r.f. field during the neutron flight time through the coil (= $\omega_0 l_\pi / v_n$) plus the (usually small) additional Larmor precession angle in the *xy* plane due to the B_0 field-only regions either side of the r.f. coil ($\omega_0(l_{B0}-l_\pi)/v_n$). Consequently we find that the neutron spin has changed its phase angle by an amount $2\psi + \omega_0 l_\pi / v_n = 2\psi + \omega_0 l_{coil}/v_n$. In fact, for an *ideal* π-flipper, the neutron spin phase change in the coil is governed by the operator

$$\varphi' = \psi' + \psi - \varphi \qquad (16),$$

where "unprimed" and "primed" refer to the "entrance" and "exit" of the coil respectively. It is important that a consistent sign convention is adopted (see Sec. 3.2) to account for changes in the directions of the static fields (and consequently the direction of the resonant r.f. field components)[2].

Noting also that when the coil is tuned for resonance

$$\psi' \approx \psi + \omega_0 \frac{l_{B_0}}{v_n} \qquad (17),$$

the operator in Eq. (16) can be rewritten as

$$\varphi' \approx 2\psi + \omega_0 \frac{l_{B_0}}{v_n} - \varphi \qquad (18).$$

Again we have assumed small beam divergence by replacing the time of flight through the coil by l_{B0}/v_n. If an intervening zero field region of length L_{AB} between the first coil (*A*) and second coil (*B*) truly has zero field, the outgoing phase angle of the neutron spin from coil *A* is preserved until its entry into coil *B* (a time L_{AB}/v_n later), whilst the r.f. field in coil *B* (which is phase locked to the field in coil *A*) has advanced by an amount $\omega_0 L_{AB}/v_n$. Thus we have

$$\varphi_B \quad = \quad \varphi'_A \quad \approx \quad 2\psi_A + \omega_0 \frac{l_{B_0}}{v_n} - \varphi_A \qquad (19)$$

We have chosen the initial polarization direction (along the *x*-axis) to define φ_A=0, therefore Eq. (19) becomes

$$\varphi_B \approx 2\psi_A + \omega_0 \frac{l_{B_0}}{v_n} \qquad (20)$$

and

[2] Note that the π flipper device that is used in conventional NSE between the first and second solenoids is not necessary in NRSE because the fields *really* are reversed. In conventional NSE the two solenoids have the same field direction (to avoid strong repulsion of the solenoids) and the effective reversal of the field is achieved with the additional π flipper.

$$\psi_B \approx \psi'_A + \omega_0 \frac{L_{AB}}{v_n} \approx \psi_A + \omega_0 \frac{\left(L_{AB} + l_{B_0}\right)}{v_n} \quad (21).$$

Applying Eq. (18) again at the exit of the second (identical) coil (*B*) with the *same field directions*, we obtain

$$\varphi'_B - \varphi_A = \varphi'_B \approx 2\omega_0 \frac{\left(L_{AB} + l_{B_0}\right)}{v_n} \quad (22).$$

We notice that after exiting coil *B* the initial phase angle, ψ_A, between the r.f. field in coil *A* and the neutron spin at the entrance to coil *A* (which is random for a continuous neutron beam) disappears from the equation. Similar arguments hold for the third and fourth coils (*C* and *D*), other than the signs of the spin phase changes are reversed by applying the static fields in the opposite direction to those in coils *A* and *B*, i.e.,

$$\varphi'_D - \varphi_C \approx -2\omega_0 \frac{\left(L_{CD} + l_{B_0}\right)}{v_n} \quad (23)$$

In principle, this means that phase locking of the r.f. fields between coils *A* and *B* can be performed independently of that in coils *C* and *D*, provided that the frequencies, ω_0, are the same.

We conclude that the net spin turn in each arm of the spectrometer is proportional to the time of flight of the neutron in each arm, independently of *when* the neutron enters each arm. The net spin phase change in the whole spectrometer is therefore

$$\varphi = \varphi'_D - \varphi_A \approx 2\omega_0 \left[\frac{\left(L_{AB} + l_{B_0}\right)}{v_i} - \frac{\left(L_{CD} + l_{B_0}\right)}{v_f}\right] = 2\gamma_n B_0 \left[\frac{\left(L_{AB} + l_{B_0}\right)}{v_i} - \frac{\left(L_{CD} + l_{B_0}\right)}{v_f}\right] \quad (24),$$

where we have substituted v_i for v_n in Eq. (22) (incident beam) and v_f for v_n in Eq. (23) (scattered beam) to account for the fact that the neutron speed can change in a scattering event.

Note that this expression is identical to the expression for a conventional NSE spectrometer with precession solenoids of length $L = L_{AB}+l_{B0} = L_{CD}+l_{B0}$ with axial fields of magnitude B_0, apart from the factor 2. Note that $L_{AB}+l_{B0}$ and $L_{CD}+l_{B0}$ correspond to the separation of the mid points of the two coils in each arm of the spectrometer and where typically L_{AB}, $L_{CD} \gg l_{B0}$. The factor 2 corresponds to a factor 2 increase in resolution at equivalent B_0L in both techniques. However, achieving higher values of B_0 in the long solenoids of a NSE machine is usually more easily achieved than in the compact coils traditionally employed in the r.f. π flipper (see for example Sec. 7.3.3.1) consequently, the factor 2 does not automatically signify “twice as good”. A slightly more general case of the 4

single π-coil arrangement is treated in Sec. 3.3 where the possibility of different coil lengths is accounted for and specific phase angles are tabulated for each field boundary of the spectrometer. In Sec. 3.4 and following sections the "bootstrap coil" technique [2] is introduced where it is shown how the factor 2 can become $2N$, where N is most commonly a small even integer ($N \geq 2$).

In contrast with conventional NSE, classically no precessions occur along the zero-field beam paths in NRSE. However, the similarity of the equations describing the net spin phase change (Eq. (24)) means that the echo signals may be analyzed in identical ways for both techniques. Henceforth, we will concentrate on elastic/quasielastic applications of the NRSE technique.

2.2 Dispersion of the flipper coils

2.2.1 Single flipper

For *polychromatic* beams, the coil is tuned for π spin flips for the mean incident neutron velocity, $\langle v_i \rangle$ or mean incident wavelength, $\langle \lambda_i \rangle$ so that according to Eq. (12)

$$\left| B_{rf} \right| = \frac{\pi \left\langle v_i \right\rangle}{\gamma_n l_{rf}} = \pi \frac{h}{\gamma_n m_n l_{rf} \left\langle \lambda_i \right\rangle} \qquad \text{coil } \pi\text{-flip tuning condition} \qquad (25)$$

We see immediately that exact π flips around B_{rf} occur only for a *single* velocity or wavelength if $|B_{rf}|$ is kept constant[3]. We refer to the wavelength-dependence of the precession angle around B_{rf} as *dispersion*. For a general wavelength, λ_i, corresponding to a deviation from the mean $\Delta\lambda_i = \lambda_i - \langle \lambda_i \rangle$, we have:

$$\beta(\lambda_i) \simeq \pi \left(1 + \frac{\Delta\lambda_i}{\left\langle \lambda_i \right\rangle} \right) = \pi \frac{\lambda_i}{\left\langle \lambda_i \right\rangle} \qquad (26).$$

Eq. (26) ignores differences in neutron flight times through the coil due to beam divergence, which are usually small compared to those caused by $\Delta\lambda_i/\lambda_i$.

A less than π rotation of the neutron magnetic moment around B_{rf} in the rotating frame is illustrated in Figure 3 for the particular case of $\lambda_i < \langle \lambda_i \rangle$. From Figure 3 we see that some depolarization occurs due to the velocity spread. For moderate $\Delta\lambda$, this is largely determined by the component of the magnetic moment out of the *xy* plane, (i.e., the angle ε), however, a (usually) smaller uncertainty in the spin direction within the *xy* plane also occurs (i.e., the angle

[3] It has been proposed to ramp $|B_{rf}|$ for situations where the neutron energy is strongly correlated with its time of emission, for example at spallation sources. However for continuous sources this is not feasible.

χ). For symmetric distributions of λ about the mean, the angle ε is uniformly distributed above and below the *xy* plane and its magnitude depends on the angle ψ. It is zero for $\psi = 0$ and maximum for $\psi = \pi/2$. In fact,

$$\cos\varepsilon = \sqrt{\cos^2\psi + \sin^2\psi\cos^2\beta} \tag{27}$$

and

$$\cos\chi = \frac{\cos^2\psi - \sin^2\psi\cos\beta}{\cos\varepsilon} \tag{28}.$$

We see from Figure 3 that for $\Delta\lambda \to 0$, $\beta \to \pi$, $\varepsilon \to 0$, and therefore $\chi \to 0$, as expected.

The ratio of the polarization with dispersion to the polarization ignoring dispersion (= 1) after passing through the device for a spectrum of (continuous beam) incoming neutrons is therefore

$$\left\langle \frac{P_{disp}}{P_{ideal}} \right\rangle_{I(\lambda_i),\psi} = \langle \cos\varepsilon\cos\chi \rangle = \langle \cos^2\psi - \sin^2\psi\cos\beta \rangle = \left\langle 1 - \sin^2\psi\left[1 + \cos\left(\pi\frac{\lambda_i}{\langle\lambda_i\rangle}\right)\right]\right\rangle_{I(\lambda_i),\psi} \tag{29}.$$

(Qualitatively this is the component of the actual spin unit vectors projected onto the "perfect" spin direction, averaged over all ψ and over the neutron spectrum, I(λ_i)). We note that for a continuous beam ψ is random over 2π radians and when performing the average over ψ in Eq. (29) for many random values of ψ, we can set $\langle\sin^2\psi\rangle = 1/2$, therefore

$$\frac{P_{disp}}{P_{ideal}} = \langle \cos\varepsilon\cos\chi \rangle = \frac{1}{2}\left[1 - \cos\left(\pi\frac{\lambda_i}{\langle\lambda_i\rangle}\right)\right] \quad \text{after average over } \psi\text{, continuous beam} \tag{30}.$$

Using the identity $\cos\beta = 1 - 2\sin^2(\beta/2)$, we end up with

$$\frac{P_{disp}}{P_{ideal}} = \sin^2\left(\frac{\pi}{2}\frac{\lambda_i}{\langle\lambda_i\rangle}\right) \quad \text{averaged over } \psi\text{, continuous beam} \tag{31}.$$

This is exactly the quantum-mechanically derived result for the spin flip probability for the π flipper (see Eq. (122) *in Sec. 4.2.1.1) when the flipper is tuned for resonance and for exact π flips for the mean neutron wavelength $\langle\lambda_i\rangle$.*

Finally, Eq. (31) must be averaged over $I(\lambda_i)$, the normalized incident wavelength spectrum so that

$$\left\langle \frac{P_{disp}}{P_{ideal}} \right\rangle_{I(\lambda_i),\psi} = \int I(\lambda_i)\sin^2\left(\frac{\pi}{2}\frac{\lambda_i}{\langle\lambda_i\rangle}\right)d\lambda_i \tag{32}.$$

For *rectangular intensity distributions* with $\langle\lambda_i\rangle$-$\Delta\lambda_{FW}/2 \le \lambda_i \le \langle\lambda_i\rangle$+$\Delta\lambda_{FW}/2$ and $I(\lambda_i)$ within this range given by $I_{pk} = 1/\Delta\lambda_{FW}$, we have

$$\left\langle \frac{P_{disp}}{P_{ideal}} \right\rangle_{1\,coil} (\text{rectangular}) = \frac{1}{\Delta\lambda_{FW}} \int_{\frac{2\langle\lambda_i\rangle-\Delta\lambda_{FW}}{2}}^{\frac{2\langle\lambda_i\rangle+\Delta\lambda_{FW}}{2}} \sin^2\left(\frac{\pi}{2}\frac{\lambda_i}{\langle\lambda_i\rangle}\right) d\lambda_i$$

$$= \frac{2}{\Delta\lambda_{FW}} \int_{\langle\lambda_i\rangle}^{\frac{2\langle\lambda_i\rangle+\Delta\lambda_{FW}}{2}} \sin^2\left(\frac{\pi}{2}\frac{\lambda_i}{\langle\lambda_i\rangle}\right) d\lambda_i \qquad (33).$$

$$= \left[\frac{1}{2} + \frac{\langle\lambda_i\rangle}{\Delta\lambda_{FW}\pi}\sin\left(\frac{\pi}{2}\frac{\Delta\lambda_{FW}}{\langle\lambda_i\rangle}\right)\right]$$

For neatness, we define the fractional full width of the spectrum by *a*, i.e.,

$$\alpha_{FW} = \frac{\Delta\lambda_{FW}}{\langle\lambda_i\rangle} \qquad (34),$$

then Eq. (33) is expressed more neatly as

$$\left\langle \frac{P_{disp}}{P_{ideal}} \right\rangle_{1\,coil} (\text{rectangular}) = \left[\frac{1}{2} + \frac{1}{\alpha_{FW}\pi}\sin\left(\frac{\pi}{2}\alpha_{FW}\right)\right] \qquad (35).$$

For *triangular intensity distributions* with FWHM = $\Delta\lambda_{FWHM}$, we can use the symmetry of the integral for the two halves of the triangle, where we can use the normalized function

$$I(\lambda_i) = \frac{1}{\Delta\lambda_{FWHM}}\left[1 + \frac{(\lambda_i - \langle\lambda_i\rangle)}{\Delta\lambda_{FWHM}}\right] \qquad (36)$$

in the interval $\langle\lambda_i\rangle$ - $\Delta\lambda_{FWHM} \le \lambda_i \le \langle\lambda_i\rangle$, therefore

$$\left\langle \frac{P_{disp}}{P_{ideal}} \right\rangle_{1\,coil} (\text{triangular}) = \frac{2}{\Delta\lambda_{FWHM}} \int_{\langle\lambda_i\rangle-\Delta\lambda_{FWHM}}^{\langle\lambda_i\rangle} \left(1 + \frac{\lambda_i - \langle\lambda_i\rangle}{\Delta\lambda_{FWHM}}\right)\sin^2\left(\frac{\pi}{2}\frac{\lambda_i}{\langle\lambda_i\rangle}\right) d\lambda_i \qquad (37).$$

In analogy with Eq. (34) we set

$$\alpha_{FWHM} = \frac{\Delta\lambda_{FWHM}}{\langle\lambda_i\rangle} \qquad (38),$$

then this integral becomes

$$\left\langle \frac{P_{disp}}{P_{ideal}} \right\rangle_{1\,coil} (\text{triangular}) = \frac{1}{2} + \frac{1}{\pi^2 \alpha_{FWHM}^2}\left(1 - \cos\left(\pi \alpha_{FWHM}\right)\right) \tag{39}.$$

For *Gaussian intensity distributions* with FWHM = $\Delta\lambda_{FWHM}$, we can also use the symmetry of the integral for the two halves of the Gaussian with the normalized function

$$I\left(\lambda_i\right) = \sqrt{\frac{4\ln 2}{\pi \Delta\lambda_{FWHM}^2}} \exp\left[-\frac{4\ln 2}{\Delta\lambda_{FWHM}^2}\left(\lambda_i - \left\langle \lambda_i \right\rangle\right)^2 \right] \tag{40},$$

therefore,

$$\left\langle \frac{P_{disp}}{P_{ideal}} \right\rangle_{1\,coil} (\text{Gaussian}) = 4\sqrt{\frac{\ln 2}{\pi \Delta\lambda_{FWHM}^2}} \int_0^\infty \exp\left[-\frac{4\ln 2}{\Delta\lambda_{FWHM}^2}\left(\lambda_i - \left\langle \lambda_i \right\rangle\right)^2 \right] \sin^2\left(\frac{\pi}{2} \frac{\lambda_i}{\left\langle \lambda_i \right\rangle} \right) d\lambda_i \tag{41}$$

Using the definition of α_{FWHM} from Eq. (38) for the Gaussian distribution this integral becomes

$$\left\langle \frac{P_{disp}}{P_{ideal}} \right\rangle_{1\,coil} (\text{Gaussian}) = \frac{1}{2}\left(1 + \exp\left[-\left(\frac{\pi}{4} \right)^2 \frac{\alpha_{FWHM}^2}{\ln 2} \right] \right) \tag{42}.$$

2.2.2 Approximation for M flippers

The above equations apply to a single flipper coil. When there are *M* flippers (e.g. *M* = 8 for a 4-coil *N* = 2 bootstrap machine), and we assume that the neutron spectrum remains unchanged as the neutrons traverse the spectrometer (elastic, no absorption/scattering approximation) with identical coils, we can make the following approximation as long as the cumulative spin rotation out of the *xy* plane stays relatively small: We write Eq. (31) approximately as the product of the flipper efficiencies for the *M* coils, prior to averaging over the spectrum $I(\lambda_i)$, i.e.,

$$\frac{P_{disp}}{P_{ideal}}(M) \approx \sin^{2M}\left(\frac{\pi}{2} \frac{\lambda_i}{\left\langle \lambda_i \right\rangle} \right) \tag{43}.$$

The overall average flipping efficiency for the spectrometer is therefore described for the rectangular, triangular, and Gaussian incident spectra by expressions similar to Eqs. (33), (37), and (41), but with the $\sin^2$ replaced by $\sin^{2M}$, i.e.,

$$\left\langle \frac{P_{disp}}{P_{ideal}} \right\rangle_{M\ coils} \left(\text{rectangular}\right) \approx \frac{2}{\Delta\lambda_{FW}} \int_{\langle\lambda_i\rangle}^{\frac{2\langle\lambda_i\rangle+\Delta\lambda_{FW}}{2}} \sin^{2M}\left(\frac{\pi}{2}\frac{\lambda_i}{\langle\lambda_i\rangle}\right) d\lambda_i$$

$$= \frac{2}{\Delta\lambda_{FW}} \left[\frac{1}{2^{2M}}\binom{2M}{M}\lambda_i + \frac{(-1)^M}{2^{2(M-1)}}\frac{\langle\lambda_i\rangle}{\pi}\sum_{k=0}^{M-1}(-1)^k\binom{2M}{k}\frac{\sin\left((M-k)\pi\frac{\lambda_i}{\langle\lambda_i\rangle}\right)}{2(M-k)} \right]_{\langle\lambda_i\rangle}^{\frac{2\langle\lambda_i\rangle+\Delta\lambda_{FW}}{2}} \quad (44)$$

where $\binom{n}{k}$ implies the binomial coefficient

$$\binom{n}{k} = \frac{n(n-1)(n-2)\ldots(n-k+1)}{k!} \quad (45).$$

From Eq. (44) we have

$$\left\langle \frac{P_{disp}}{P_{ideal}} \right\rangle_{M\ coils} \left(\text{rectangular}\right) \approx \frac{1}{2^{2M}} \left[\binom{2M}{M} + \frac{4}{\pi\alpha_{FW}} \sum_{k=0}^{M-1} \binom{2M}{k} \frac{\sin\left((M-k)\frac{\pi}{2}\alpha_{FW}\right)}{(M-k)} \right] \quad (46).$$

For triangular $I(\lambda_i)$:

$$\left\langle \frac{P_{disp}}{P_{ideal}} \right\rangle_{M\ coils} \left(\text{triangular}\right) \approx \frac{2}{\Delta\lambda_{FWHM}} \int_{\langle\lambda_i\rangle-\Delta\lambda_{FWHM}}^{\langle\lambda_i\rangle} \left(1+\frac{\lambda_i-\langle\lambda_i\rangle}{\Delta\lambda_{FWHM}}\right) \sin^{2M}\left(\frac{\pi}{2}\frac{\lambda_i}{\langle\lambda_i\rangle}\right) d\lambda_i \quad (47),$$

from which we obtain

$$\left\langle \frac{P_{disp}}{P_{ideal}} \right\rangle_{M\ coils} \left(\text{triangular}\right) \approx \frac{1}{2^{2M}} \left[\binom{2M}{M} + \frac{4}{\pi^2\alpha_{FWHM}^2} \sum_{k=0}^{M-1} \binom{2M}{k} \left[\frac{1-\cos\left[(M-k)\pi\alpha_{FWHM}\right]}{(M-k)^2} \right] \right] \quad (48).$$

Finally, for Gaussian $I(\lambda_i)$

$$\left\langle \frac{P_{disp}}{P_{ideal}} \right\rangle_{M\ coils} \left(\text{Gaussian}\right) \approx 4\sqrt{\frac{\ln 2}{\pi\Delta\lambda_{FWHM}^2}} \int_{\langle\lambda_i\rangle}^{\infty} \exp\left[-\frac{4\ln 2}{\Delta\lambda_{FWHM}^2}\left(\lambda_i-\langle\lambda_i\rangle\right)^2\right] \sin^{2M}\left(\frac{\pi}{2}\frac{\lambda_i}{\langle\lambda_i\rangle}\right) d\lambda_i \quad (49).$$

Note that this expression does not account for the obvious truncation required by $\lambda \geq 0$. This integral is complicated and a good approximation is provided by numerical evaluation of the integral to an upper limit of two to three times the FWHM.

The accuracy of the approximation for $M > 1$ is demonstrated by some special case Monte Carlo calculations in Sec. 8.2.1.

Table 1 and Table 2 show some predicted values of $\left\langle \frac{P_{disp}}{P_{ideal}} \right\rangle_{M\ coils}$ for uniform, triangular, and Gaussian wavelength distributions about the mean and for $M = 8$ (i.e., a typical 4-coil, $N = 2$ bootstrap configuration) and $M = 6$ (i.e., a MIEZE-II type, $N = 2$ bootstrap configuration) respectively. The Gaussian results were obtained by numerical integration of Eq. (49) between the limits $\langle\lambda_i\rangle \rightarrow \langle\lambda_i\rangle + 2\Delta\lambda_{FWHM}$. Using higher upper limits of integration showed no change in the fifth significant figure and no spectral truncation problems are encountered for α up to 0.5 in this case, so the values in the tables should be reliable. Note that they are quite similar to the triangular case.

These figures, which are independent of the Fourier time to a very good approximation, represent the theoretically maximum attainable signal for a non-zero wavelength band in the limit of an otherwise perfectly constructed spectrometer with perfect polarizers. When imperfections are present, typically this is an upper limit on the spin-echo signal in the short Fourier time limit.

Table 1. Flipping efficiency versus full width (FW) (rectangular distribution) or full width at half maximum (FWHM) (triangular, Gaussian distributions) for $M = 8$ π coils.

$\alpha_{FW/FWHM}$	P_{disp}/P_{ideal} ($M=8$)		
	Rectangular	Triangular	Gaussian
0.1	0.98378	0.96831	0.96613
0.2	0.93778	0.88600	0.88155
0.3	0.86916	0.78127	0.77880
0.4	0.78750	0.67898	0.68064
0.5	0.70237	0.59115	0.59587

Table 2. Flipping efficiency versus full width (FW) (rectangular distribution) or full width at half maximum (FWHM) (triangular, Gaussian distributions) for $M = 6\ \pi$ coils.

$\alpha_{\mathrm{FW/FWHM}}$	P_{disp}/P_{ideal} (M=6)		
	Rectangular	Triangular	Gaussian
0.1	0.98779	0.97600	0.97427
0.2	0.95266	0.91138	0.90715
0.3	0.89874	0.82378	0.81999
0.4	0.83194	0.73158	0.73102
0.5	0.75870	0.64689	0.64987

Special Note

Gähler and Golub [2] ignore the (usually small) angle χ and give an expression for $\langle \cos\varepsilon \rangle$ in terms of the root mean square (r.m.s.) value of ε, ε_{rms}, which works for small values of ε. However, for these reasons, their expression does not predict exactly the quantum mechanical flipping efficiency and also the reader should beware of substituting, for example, FWHM values for δv into their expression (their Eq. (33)). The latter equation is valid for discrete $\pm\delta v$ about the mean, therefore their expression must be averaged over the appropriate velocity distribution, $F(v_n)$.

For sufficiently small ε, we have $\cos\varepsilon \approx 1-\varepsilon^2/2$ and

$$P \approx \langle \cos\varepsilon \rangle \simeq \left\langle 1-\frac{\varepsilon^2}{2} \right\rangle = 1-\frac{\langle \varepsilon^2 \rangle}{2} \approx \cos\varepsilon_{rms} \qquad (50).$$

This is convenient for assessing the combined effect for a neutron beam passing through M similar π coils, where the ε's add in quadrature [ii], whence

$$\varepsilon(M) \approx \sqrt{M}\,\varepsilon \qquad (51)$$

and ε is the value for a *single* π-flipper. Therefore,

$$P(M) \approx \left\langle \cos\sqrt{M}\,\varepsilon \right\rangle \approx \cos\sqrt{M}\,\varepsilon_{rms} \qquad (52)$$

where the approximation is valid provided that $\sqrt{M}\,\varepsilon$ is sufficiently small.

2.3 Coil resonance width

The coil flipping efficiencies given in the previous section are for optimally-tuned coils (exact resonance $\omega_{rf} = \omega_0$ and exact π-flips for the mean wavelength $\langle \lambda_i \rangle$). They account only for dispersion. For moderate $\Delta\lambda/\lambda$, dispersion leads mainly to rotation of the spin vector out of the intended x-y plane accompanied by a usually small rotation of the spin component within the x-y plane. An interesting additional question concerns non-optimal tuning of the coils arising either from (i) systematic differences between the Larmor frequency (ω_0) and r.f. frequency (ω_{rf}) or (ii) that caused by static field inhomogeneity when $\omega_{rf} = \omega_0$; i.e., to what tolerance must ω_{rf} match ω_0? Or alternatively, what is the resonance width? Alvarez and Bloch [6] provided a quantum mechanical result for the flipping efficiency (valid for static field magnitudes that are much larger than the oscillating field magnitude) that includes the effects of these frequency differences, which (almost) in their original notation is

$$P = \frac{\sin^2\left[\left(\frac{\mu H_1 t}{2\hbar}\right)\sqrt{\left(1+\left\{\frac{2\Delta H}{H_1}\right\}^2\right)}\right]}{\left[1+\left\{\frac{2\Delta H}{H_1}\right\}^2\right]} \tag{53}$$

where t is the time spent in the oscillating field, $\mu H_1 t$ equates to our $\beta/2$ in Eq. (12) (thus containing the *dispersive* part of the depolarization), H_1 is the amplitude of the oscillating field $\equiv 2B_{rf} = B_{rf}^{pk}$, and

$$\Delta H = H_0 - H_0^* \tag{54}$$

is the difference between the actual value of the static field and the value required for exact resonance (i.e., when $\omega_0 = \omega_{rf}$). Thus, we can re-express Eq. (54) as

$$\Delta H = \frac{1}{\gamma_n}\left(\omega_0 - \omega_{rf}\right) = \frac{2\pi}{\gamma_n}\left(\nu_0 - \nu_{rf}\right) \tag{55}.$$

In our notation Eq. (53) becomes

$$P = \frac{\sin^2\left[\left(\frac{\gamma_n B_{rf} l_\pi m_n \lambda_n}{2h}\right)\sqrt{\left(1+\left\{\frac{2\left(\omega_0-\omega_{rf}\right)}{\gamma_n B_{rf}^{pk}}\right\}^2\right)}\right]}{\left[1+\left\{\frac{2\left(\omega_0-\omega_{rf}\right)}{\gamma_n B_{rf}^{pk}}\right\}^2\right]}$$

$$= \frac{\sin^2\left[\left(\frac{\gamma_n B_{rf} l_\pi m_n \lambda_n}{2h}\right)\sqrt{\left(1+\left\{\frac{\omega_0-\omega_{rf}}{\gamma_n B_{rf}}\right\}^2\right)}\right]}{\left[1+\left\{\frac{\omega_0-\omega_{rf}}{\gamma_n B_{rf}}\right\}^2\right]} \tag{56},$$

where it is understood that $l_\pi = l_{rf}$ for the typical flipper coil. For the special case that B_{rf} is tuned to produce exact π flips for the mean wavelength $\langle\lambda_i\rangle$, Eq. (56) becomes (see also Eq. (11))

$$P = \frac{\sin^2\left[\left(\frac{\pi\lambda_n}{2\langle\lambda_n\rangle}\right)\sqrt{\left(1+\left\{\frac{\omega_0-\omega_{rf}}{\gamma_n B_{rf}}\right\}^2\right)}\right]}{\left[1+\left\{\frac{\omega_0-\omega_{rf}}{\gamma_n B_{rf}}\right\}^2\right]}$$

$$= \frac{\sin^2\left[\left(\frac{\pi\lambda_n}{2\langle\lambda_n\rangle}\right)\sqrt{\left(1+\left\{\frac{\omega_0-\omega_{rf}}{\omega_p}\right\}^2\right)}\right]}{\left[1+\left\{\frac{\omega_0-\omega_{rf}}{\omega_p}\right\}^2\right]}$$

B_{rf} tuned for exact π flips for $\lambda_n=\langle\lambda_n\rangle$ (57).

For B_{rf} tuned for exact π flips for $\lambda_n = \langle\lambda_n\rangle$, we can also write Eq. (57) (using Eq. (13)) as

$$P = \frac{\sin^2\left[\left(\frac{\pi\lambda_n}{2\langle\lambda_n\rangle}\right)\sqrt{\left(1+\left\{\frac{m_n\left(\omega_0-\omega_{rf}\right)l_\pi\langle\lambda_n\rangle}{\pi h}\right\}^2\right)}\right]}{\left[1+\left\{\frac{m_n\left(\omega_0-\omega_{rf}\right)l_\pi\langle\lambda_n\rangle}{\pi h}\right\}^2\right]}$$

B_{rf} tuned for exact π flips for $\lambda_n = \langle\lambda_n\rangle$ (58),

which, for exact resonance ($\omega_{rf} = \omega_0$) reduces to Eq.(31).

These equations can be used either to examine the flipping efficiency as the r.f. frequency is detuned from a precise nominal Larmor precession frequency (perfect static field homogeneity, fixed ω_0) or to calculate the effects of static field inhomogeneities (giving rise to a spread of ω_0 values), when ω_{rf} is tuned to the mean value of ω_0. The first of these cases is of interest when operating the spectrometer and the latter is of concern at the spectrometer design stage. We plot the function in Eq. (58) versus the frequency difference (in kHz) in Figure 4 for l_π= 3 cm and for the special case of the *single* wavelength $\lambda_n = \langle\lambda_n\rangle$ (zero dispersion approximation). This isolates the effects due to ω_0-ω_{rf} (which, in contrast to dispersion, lead mainly to depolarizing rotations of the spin *within* the *x*-*y* plane) from the effects of dispersion itself, as described in the Sec. 2.2. Of course both effects co-exist in general.

Note that the Alvarez and Bloch formalism does *not* account for the case where the static field magnitude can no longer be considered large compared to the oscillating field magnitude. In this case, the Bloch-Siegert shift (see

Sec. 7.3.6.1) must be taken into account and eventually the r.f. flipper cannot function as intended when B_0/B_{rf} falls too low.

The full width at half maximum of these resonance curves for a general value of l_π is very well fitted by

$$\Delta\nu_{FWHM}\left[\mathrm{Hz}\right]=\frac{3.16\times10^{3}}{l_\pi\left[\mathrm{m}\right]\lambda_n\left[\overset{\circ}{\mathrm{A}}\right]} \tag{59}$$

Perhaps a more useful quantity is the frequency shift for a 1% drop in the flipping efficiency. This is well fitted by the following similar expression

$$\Delta\nu_{99\%}\left[\mathrm{Hz}\right]=\frac{198}{l_\pi\left[\mathrm{m}\right]\lambda_n\left[\overset{\circ}{\mathrm{A}}\right]} \tag{60}$$

Thus for longer wavelengths and longer coils the resonance sharpens, requiring a greater coil tuning accuracy with respect to ω_0-ω_{rf}. Consequently, the tolerable field inhomogeneity decreases as l_π and λ_n increase.

2.4 Influence of π-flipper efficiency on polarization

The term "flipper efficiency" conventionally excludes spin-independent inefficiencies such as scattering or absorption in the device. Thus for a π-flipper of flipper efficiency f = 1, a fraction f of the spin-down component of a beam is converted to spin up and vice-versa. Conversely, fractions (1-f) of the spin down and spin up components are transmitted with no change of their spin directions. Thus for an incoming beam containing intensities of spin up and spin down neutrons given by I_0^+ and I_0^- respectively, the corresponding intensities in the outgoing beam are

$$I_1^+ = fI_0^- + (1-f)\,I_0^+ \tag{61}$$

and

$$I_1^- = fI_0^+ + (1-f)\,I_0^- \tag{62}$$

The incident beam polarization is, by definition,

$$P_0=\frac{I_0^+-I_0^-}{I_0^++I_0^-} \tag{63}$$

so by the same definition, the outgoing beam has polarization

$$P_1 = \frac{I_1^+ - I_1^-}{I_1^+ + I_1^-} = \frac{(1-2f)\left(I_0^+ - I_0^-\right)}{I_0^+ + I_0^-} = (1-2f)\,P_0 \qquad (64)$$

Thus the outgoing beam polarization is just the incoming beam polarization multiplied by the factor (1-2*f*). Note that for a perfect π-flipper (f = 1), $P_1 = -P_0$, as expected.

3 Illustrations of idealized 4-coil NRSE instruments

In the following examples, we illustrate the performance of a 4-coil unit NRSE spectrometer by assuming "perfect" π-flipper coils (Sec. 3.1). In Secs. 6 and 7, we discuss departures from the idealized performance due to the non-ideal nature of the components.

3.1 The perfect π-flipper coil

We define the "perfect" π-flipper coil as having the following properties:

1. "Dispersionless" – the exact π flip operation is assumed to be independent of wavelength (i.e., all neutron spins start and finish in the *xy* plane - see Sec. 2.2).
2. Perfectly uniform and stable applied static field B_0 within the beam area.
3. Perfectly stable (frequency and magnitude) and sinusoidal r.f. field B_{rf}.
4. Perfect perpendicularity of the static, r.f. fields, and beam direction ($\Rightarrow$ zero divergence beam).
5. Perfectly-defined field boundaries along the beam direction.
6. Zero stray fields or leakage fields in the "zero-field" regions.
7. Perfectly transmitting for neutrons.

Consider the coordinate system in Figure 5 where the origin of the *y*-axis is chosen to coincide with the entrance to the first π flipper (*A*) as shown. We will assume that the static field magnitude, B_0, in coils *A* and *B* is the same and that the static field magnitude, B_1, in coils *C* and *D* is the same. i.e.,

$$B_0^A = B_0^B = B_0 \qquad (65)$$

and

$$B_0^C = B_0^D = B_1 \qquad (66).$$

When the π-flipper r.f. frequency is on-resonance, we can write

$$\omega_{rf}^{A} = \omega_{rf}^{B} = \omega_0 = \gamma_n B_0 \qquad (67)$$

$$\omega_{rf}^{C} = \omega_{rf}^{D} = \omega_1 = \gamma_n B_1 \qquad (68).$$

For elastic and small energy transfer quasielastic scattering (where the detailed balance factor is essentially 1 and the scattering function is symmetrical around zero energy transfer), we have $\langle v_i \rangle = \langle v_f \rangle$. Therefore, the magnitude of the r.f. field is tuned to create π-flips for the mean incident velocity $\langle v_i \rangle$ for all coils. This implies

$$\left| B_{rf}^{k} \right| = \frac{\pi \langle v_i \rangle}{\gamma_n l_k} = \pi \frac{h}{\gamma_n m_n l_k \langle \lambda_i \rangle} \qquad \text{for } k = A, B, C, D \qquad (69).$$

3.2 An important note about signs

In Sec. 3.3 and especially in Sec. 3.5 we must account for reversals of the directions of the static fields B_0 from one coil to the next. This is important because the reversed direction of B_0 reverses the direction of the Larmor precession and consequently switches the resonant r.f. field component to the counter-rotating component (that has a different absolute phase angle). This latter situation is simplified mathematically (with no loss of generality) if we assume that the r.f. field oscillates along the x-axis, since the shift of r.f. phase angle that accompanies the change of sign amounts only to a flip of the sign of ψ. In the following sections, expressions for the phase changes throughout the spectrometer are written in tabular form, initially with signs that account for general static field directions in the coils. This helps when justifying specific sequences of static field directions required for the spectrometer to work, especially in the discussion of bootstrap coil pairs.

3.3 A 4 "perfect" dispersionless single π-coil NRSE with zero stray fields and well-collimated beams

The 4-single π flipper arrangement is illustrated in Figure 5. We use the operator (Eq. (16)) for the neutron spin phase in the coil regions and assume truly zero field in the gaps between the coils (allowing Eq. (19) to be used). Phase locking of the r.f. frequency between coils A and B and between C and D is assumed (allowing expressions of the type (21) to be used), but no phase locking of the r.f. between the two arms of the spectrometer is required (hence ψ_C is unrelated to ψ_A). By assuming well-collimated beams ($\cos\theta \approx 1$), we have replaced neutron flight times with expressions of the type l/v_n or L/v_n where l or L is a dimension along the beam (y) axis.

We now construct a table of phases through the spectrometer, applying the above assumptions and signs to account for general static field directions. For example, sgn(B_0) = "+" if the static field lies along +z and sgn(B_0) = "-" if the static field lies along –z. The result is shown in Table 3.

Table 3. Phases for single π coils with zero stray fields between coils showing how the field direction signs for the resonant component of the r.f. field apply (B_{rf} is chosen to oscillate along the x axis).

Location	y	Neutron spin phase angle φ	r.f. field phase ψ
Entrance A	0	0	ψ_A
Exit coil A	l_A	$2\psi_A+\mathrm{sgn}(B_0^A)(1/v_i)\gamma_n\lvert B_0\rvert l_A$	$\psi_A+\mathrm{sgn}(B_0^A)(1/v_i)\gamma_n\lvert B_0\rvert l_A$
Entrance B	l_A+L_{AB}	$2\psi_A+\mathrm{sgn}(B_0^A)(1/v_i)\gamma_n\lvert B_0\rvert l_A$	$\mathrm{sgn}(B_0^A)\mathrm{sgn}(B_0^B)[\psi_A+\mathrm{sgn}(B_0^A)(1/v_i)\gamma_n\lvert B_0\rvert(l_A+L_{AB})]$
Exit coil B	$l_A+L_{AB}+l_B$	$2\mathrm{sgn}(B_0^A)\mathrm{sgn}(B_0^B)[\psi_A+\mathrm{sgn}(B_0^A)(1/v_i)\gamma_n\lvert B_0\rvert(L_{AB}+l_A)]+\mathrm{sgn}(B_0^B)(1/v_i)\gamma_n\lvert B_0\rvert l_B-2\psi_A-\mathrm{sgn}(B_0^A)(1/v_i)\gamma_n\lvert B_0\rvert l_A$	$\mathrm{sgn}(B_0^A)\mathrm{sgn}(B_0^B)[\psi_A+\mathrm{sgn}(B_0^A)(1/v_i)\gamma_n\lvert B_0\rvert(l_A+L_{AB})]+\mathrm{sgn}(B_0^B)(1/v_i)\gamma_n\lvert B_0\rvert l_B$
Sample (non-spin flip or coherent scatterer)	$l_A+L_{AB}+l_B+L_{BS}$	$2\mathrm{sgn}(B_0^A)\mathrm{sgn}(B_0^B)[\psi_A+\mathrm{sgn}(B_0^A)(1/v_i)\gamma_n\lvert B_0\rvert(L_{AB}+l_A)]+\mathrm{sgn}(B_0^B)(1/v_i)\gamma_n\lvert B_0\rvert l_B-2\psi_A-\mathrm{sgn}(B_0^A)(1/v_i)\gamma_n\lvert B_0\rvert l_A$	$\mathrm{sgn}(B_0^A)\mathrm{sgn}(B_0^B)[\psi_A+\mathrm{sgn}(B_0^A)(1/v_i)\gamma_n\lvert B_0\rvert(L_{AB}+l_A)]+\mathrm{sgn}(B_0^B)(1/v_i)\gamma_n\lvert B_0\rvert(l_B+L_{BS})$
Entrance C	$l_A+L_{AB}+l_B+L_{BS}+L_{SC}$	$2\mathrm{sgn}(B_0^A)\mathrm{sgn}(B_0^B)[\psi_A+\mathrm{sgn}(B_0^A)(1/v_i)\gamma_n\lvert B_0\rvert(L_{AB}+l_A)]+\mathrm{sgn}(B_0^B)(1/v_i)\gamma_n\lvert B_0\rvert l_B-2\psi_A-\mathrm{sgn}(B_0^A)(1/v_i)\gamma_n\lvert B_0\rvert l_A$	ψ_C
Exit coil C	$l_A+L_{AB}+l_B+L_{BS}+L_{SC}+l_C$	$2\psi_C+\mathrm{sgn}(B_0^C)(1/v_f)\gamma_n\lvert B_1\rvert l_C-(2\mathrm{sgn}(B_0^A)\mathrm{sgn}(B_0^B)[\psi_A+\mathrm{sgn}(B_0^A)(1/v_i)\gamma_n\lvert B_0\rvert(L_{AB}+l_A)]+\mathrm{sgn}(B_0^B)(1/v_i)\gamma_n\lvert B_0\rvert l_B-2\psi_A-\mathrm{sgn}(B_0^A)(1/v_i)\gamma_n\lvert B_0\rvert l_A)$	$\psi_C+\mathrm{sgn}(B_0^C)(1/v_f)\gamma_n\lvert B_1\rvert l_C$
Entrance D	$l_A+L_{AB}+l_B+L_{BS}+L_{SC}+l_C+L_{CD}$	$2\psi_C+\mathrm{sgn}(B_0^C)(1/v_f)\gamma_n\lvert B_1\rvert l_C-(2\mathrm{sgn}(B_0^A)\mathrm{sgn}(B_0^B)[\psi_A+\mathrm{sgn}(B_0^A)(1/v_i)\gamma_n\lvert B_0\rvert(L_{AB}+l_A)]+\mathrm{sgn}(B_0^B)(1/v_i)\gamma_n\lvert B_0\rvert l_B-2\psi_A-\mathrm{sgn}(B_0^A)(1/v_i)\gamma_n\lvert B_0\rvert l_A)$	$\mathrm{sgn}(B_0^C)\mathrm{sgn}(B_0^D)[\psi_C+\mathrm{sgn}(B_0^C)(1/v_f)\gamma_n\lvert B_1\rvert(l_C+L_{CD})]$
Exit coil D	$l_A+L_{AB}+l_B+L_{BS}+L_{SC}+l_C+L_{CD}+l_D$	$2(\mathrm{sgn}(B_0^C)\mathrm{sgn}(B_0^D)[\psi_C+\mathrm{sgn}(B_0^C)(1/v_f)\gamma_n\lvert B_1$	$\mathrm{sgn}(B_0^C)\mathrm{sgn}(B_0^D)[\psi_C+\mathrm{sgn}(B_0^C)(1/v_f)\gamma_n\lvert$

	$\|(l_C+L_{CD})\])+\mathrm{sgn}(B_0^D)(1/v_f)\gamma_n\|B_1\|l_D-$	$B_1\|(l_C+L_{CD})]+\mathrm{sgn}(B_0^D)(1/v_f)\gamma_n\|B_1\|l_D$
	$\{2\psi_C+\mathrm{sgn}(B_0^C)(1/v_f)\gamma_n\|B_1\|l_C-$	
	$(2\mathrm{sgn}(B_0^A)\mathrm{sgn}(B_0^B)[\psi_A+\mathrm{sgn}(B_0^A)(1/v_i)\gamma_n\|B_0\|$	
	$(L_{AB}+l_A)]+\mathrm{sgn}(B_0^B)(1/v_i)\gamma_n\|B_0\|l_B-2\psi_A-$	
	$\mathrm{sgn}(B_0^A)(1/v_i)\gamma_n\|B_0\|l_A)\}$	

Applying the signs shown in Figure 5 (i.e., sgn(B_0^A) = sgn(B_0^B) = "+" and sgn(B_0^C) = sgn(B_0^D) = "-"), we reconstruct Table 3 as shown in Table 4.

Table 4. Phases for single π coils with zero stray fields between coils applying the field direction signs indicated in Figure 5.

Location	y	Neutron spin phase angle φ	r.f. field phase ψ
Entrance *A*	0	0	ψ_A
Exit coil *A*	l_A	$2\psi_A+(1/v_i)\gamma_n\lvert B_0\rvert l_A$	$\psi_A+(1/v_i)\gamma_n\lvert B_0\rvert l_A$
Entrance *B*	l_A+L_{AB}	$2\psi_A+(1/v_i)\gamma_n\lvert B_0\rvert l_A$	$\psi_A+(1/v_i)\gamma_n\lvert B_0\rvert(L_{AB}+l_A)$
Exit coil *B*	$l_A+L_{AB}+l_B$	$(1/v_i)\gamma_n\lvert B_0\rvert(2L_{AB}+l_A+l_B)$	$\psi_A+(1/v_i)\gamma_n\lvert B_0\rvert(L_{AB}+l_A+l_B)$
Sample (non-spin flip or coherent scatterer)	$l_A+L_{AB}+l_B+L_{BS}$	$(1/v_i)\gamma_n\lvert B_0\rvert(2L_{AB}+l_A+l_B)$	$\psi_A+(1/v_i)\gamma_n\lvert B_0\rvert(L_{AB}+l_A+l_B+L_{BS})$
Entrance *C*	$l_A+L_{AB}+l_B+L_{BS}+L_{SC}$	$(1/v_i)\gamma_n\lvert B_0\rvert(2L_{AB}+l_A+l_B)$	ψ_C
Exit coil *C*	$l_A+L_{AB}+l_B+L_{BS}+L_{SC}+l_C$	$2\psi_C-(1/v_f)\gamma_n\lvert B_1\rvert l_C-(1/v_i)\gamma_n\lvert B_0\rvert(2L_{AB}+l_A+l_B)$	$\psi_C-(1/v_f)\gamma_n\lvert B_1\rvert l_C$
Entrance *D*	$l_A+L_{AB}+l_B+L_{BS}+L_{SC}+l_C+L_{CD}$	$2\psi_C-(1/v_f)\gamma_n\lvert B_1\rvert l_C-(1/v_i)\gamma_n\lvert B_0\rvert(2L_{AB}+l_A+l_B)$	$\psi_C-(1/v_f)\gamma_n\lvert B_1\rvert(l_C+L_{CD})$
Exit coil *D*	$l_A+L_{AB}+l_B+L_{BS}+L_{SC}+l_C+L_{CD}+l_D$	$(1/v_i)\gamma_n\lvert B_0\rvert(2L_{AB}+l_A+l_B)-$ $(1/v_f)\gamma_n\lvert B_1\rvert(2L_{CD}+l_C+l_D)$	$\psi_C-(1/v_f)\gamma_n\lvert B_1\rvert(l_C+L_{CD}+l_D)$

Observations

1. From Table 4, it can be seen that unrelated phases of the r.f. in each arm of the spectrometer is immaterial. This is because the random r.f. phase angles ψ_A and ψ_C on entry to coils *A* and *C* are canceled on leaving coils *C* and *D* respectively.
2. The final spin phase angle of the neutron exiting coil *D* does not depend on the distance between the second coil *B* and the sample (L_{BS}) and the sample and the third coil *C* (L_{SC}).
3. The final neutron spin phase from Table 4 is:

$$\begin{aligned}\varphi_D^{'} &= \left[\frac{\omega_0\left(2L_{AB}+l_A+l_B\right)}{v_i}-\frac{\omega_1\left(2L_{CD}+l_C+l_D\right)}{v_f}\right] \\ &= \gamma_n\left[\frac{B_0\left(2L_{AB}+l_A+l_B\right)}{v_i}-\frac{B_1\left(2L_{CD}+l_C+l_D\right)}{v_f}\right]\end{aligned} \quad (70).$$

If each of the coils are identical in length (i.e., $l_A = l_B = l_C = l_D = l_{B0} = l_{coil} = l$), then the phase angle of the neutron spin at the exit of coil *D* reduces to

$$\varphi_D^{'} = 2\left[\frac{\omega_0\left(L_{AB}+l\right)}{v_i}-\frac{\omega_1\left(L_{CD}+l\right)}{v_f}\right] = 2\gamma_n\left[\frac{B_0\left(L_{AB}+l\right)}{v_i}-\frac{B_1\left(L_{CD}+l\right)}{v_f}\right] \quad (71).$$

Finally, Eq. (71) can be rewritten more neatly by introducing L_0 and L_1, the distances between the *mid-points* of the coils in the first arm and second arm respectively, where

$$L_0 = L_{AB} + l \quad (72)$$

and

$$L_1 = L_{CD} + l \quad (73)$$

so that Eq. (71) becomes

$$\varphi_D^{'} = 2\left[\frac{\omega_0 L_0}{v_i}-\frac{\omega_1 L_1}{v_f}\right] = 2\gamma_n\left[\frac{B_0 L_0}{v_i}-\frac{B_1 L_1}{v_f}\right] \quad (74).$$

3.4 The “bootstrap” coil technique

3.4.1 Bootstrap configurations

Gähler and Golub [2] appreciated that spin echo configurations of resonant π-flippers are not limited to single π-flipper unit arrangements, such as the one just described. Multiple flippers placed back-to-back with alternating static field directions can replace the single π-flippers at the zero field region boundaries. Several 4-coil unit spin-echo arrangements are shown in Figure 6. When more than one π-flipper ($N > 1$) comprises one unit, the combination is referred to as a “bootstrap coil”. The technique was first demonstrated experimentally in Ref. [7]. Note that the static field directions in the second arm always mirror-image those in the first arm. Because closed magnetic field loops are produced within the coil unit for even-*N*, leakage fields outside the coil regions are strongly reduced with respect to odd-*N* combinations and it has been demonstrated [8] that the field homogeneity within the beam area is improved for $N = 2$ with respect to $N = 1$. Furthermore, the (small) leakage fields each side of the even-*N* bootstrap coil cancel to first order because the Larmor precession that they induce is approximately equal in magnitude but opposite in sign.

3.4.2 Practical limits to the value of N

Bootstrap coils with *N* flippers effectively multiply the spin turn by a factor of *N*, thereby increasing the resolution of the spectrometer by the same factor *N*. This will be illustrated for $N=2$ in Sec. 3.5. However, instrumental non-ideality can limit the maximum value of *N* that can be used.

1. The most obvious practical limitation is imposed by the fact that the beam must traverse *N* times the number of coil windings, multiplying the thickness of absorbing and scattering material in the beam by the same factor.
2. The total power dissipation is proportional to *N* and the difficulty of heat removal from the coils units is increased.
3. The dispersion of the π-flippers means that increasing non-zero *z*-components of the spin vectors result as the neutron traverses more coils. Gähler and Golub show [2] that the expectation values of $\langle\sigma_x\rangle$ and $\langle\sigma_z\rangle$ each contain 2^N terms in $\sin^m(\mu B_{rf} l/\hbar v_n)$ and/or $\cos^m(\mu B_{rf} l/\hbar v_n)$ where *m* runs up to *N* and v_n is the neutron velocity.

   Because these rapidly-varying functions of velocity lead to depolarization of the beam, Gähler and Golub also show that $\Delta v_n/v_n$ must become increasingly small as *N* increases to compensate their negative effect.

In view of the compromises imposed by 1, 2, and 3, and the advantages of even-N for stray field suppression, $N = 2$ is almost universally used in existing NRSE spectrometers.

3.5 A 4 “perfect” dispersionless N=2 bootstrap coil NRSE with zero stray fields and well-collimated beams

In the bootstrap pair the main consequence of the field direction reversal mid-way across the coil unit is that the resonant component of the r.f. field switches to the counter-rotating component in the second π-flipper. This has the effect of reversing the sign of ψ and of ω_0. In order to illustrate features that are likely present in a real bootstrap coil, it is assumed that the transition from one π-flipper of the pair to the other takes place across a small gap l_g, which is the same for all coils. This gap is also assumed to be "zero field" (or a region where the stray fields of the adjacent coils exactly cancel resulting in zero net field). By adopting the procedure outlined in Sec. 3.3 and applying the specific field direction signs indicated in Figure 6 for $N = 2$, we obtain the values given in Table 5.

Table 5. Phase angles for a 4-N = 2 bootstrap coil NRSE applying the static field signs as indicated in Figure 6 for N = 2.

Location	y	Neutron spin phase angle φ	r.f. field phase ψ
Entrance A_1	0	0	ψ_{A1}
Exit A_1	l_{A1}	$2\psi_{A1}+(1/v_i)\gamma_n\lvert B_0\rvert l_{A1}$	$\psi_{A1}+(1/v_i)\gamma_n\lvert B_0\rvert l_{A1}$
Entrance A_2	$l_{A1}+l_g$	$2\psi_{A1}+(1/v_i)\gamma_n\lvert B_0\rvert l_{A1}$	$-\psi_{A1}-(1/v_i)\gamma_n\lvert B_0\rvert(l_{A1}+l_g)$
Exit A_2	$l_{A1}+l_g+l_{A2}$	$-4\psi_{A1}-(1/v_i)\gamma_n\lvert B_0\rvert(3l_{A1}+2l_g+l_{A2})$	$-\psi_{A1}-(1/v_i)\gamma_n\lvert B_0\rvert(l_{A1}+l_g+l_{A2})$
Entrance B_1	$l_{A1}+l_g+l_{A2}+L_{AB}$	$-4\psi_{A1}-(1/v_i)\gamma_n\lvert B_0\rvert(3l_{A1}+2l_g+l_{A2})$	$-\psi_{A1}-(1/v_i)\gamma_n\lvert B_0\rvert(l_{A1}+l_g+l_{A2}+L_{AB})$
Exit B_1	$l_{A1}+l_g+l_{A2}+L_{AB}+l_{B1}$	$2\psi_{A1}+(1/v_i)\gamma_n\lvert B_0\rvert(l_{A1}-l_{A2}-2L_{AB}-l_{B1})$	$-\psi_{A1}-(1/v_i)\gamma_n\lvert B_0\rvert(l_{A1}+l_g+l_{A2}+L_{AB}+l_{B1})$
Entrance B_2	$l_{A1}+2l_g+l_{A2}+L_{AB}+l_{B1}$	$2\psi_{A1}+(1/v_i)\gamma_n\lvert B_0\rvert(l_{A1}-l_{A2}-2L_{AB}-l_{B1})$	$\psi_{A1}+(1/v_i)\gamma_n\lvert B_0\rvert(l_{A1}+2l_g+l_{A2}+L_{AB}+l_{B1})$
Exit B_2	$l_{A1}+2l_g+l_{A2}+L_{AB}+l_{B1}+l_{B2}$	$(1/v_i)\gamma_n\lvert B_0\rvert(l_{A1}+4l_g+3l_{A2}+4L_{AB}+3l_{B1}+l_{B2})$ = φ_{B2}'	$\psi_{A1}+(1/v_i)\gamma_n\lvert B_0\rvert(l_{A1}+2l_g+l_{A2}+L_{AB}+l_{B1}+l_{B2})$
Sample (non-spin flip or coherent scatterer)	$l_{A1}+2l_g+l_{A2}+L_{AB}+l_{B1}+l_{B2}+L_{BS}$	φ_{B2}'	$\psi_{A1}+(1/v_i)\gamma_n\lvert B_0\rvert(l_{A1}+2l_g+l_{A2}+L_{AB}+l_{B1}+l_{B2}+L_{BS})$
Entrance C_1	$l_{A1}+2l_g+l_{A2}+L_{AB}+l_{B1}+l_{B2}+L_{BS}+L_{SC}$	φ_{B2}'	ψ_{C1}
Exit C_1	$l_{A1}+2l_g+l_{A2}+L_{AB}+l_{B1}+l_{B2}+L_{BS}+L_{SC}+l_{C1}$	$2\psi_{C1}-(1/v_f)\gamma_n\lvert B_1\rvert l_{C1}-\varphi_{B2}'$	$\psi_{C1}-(1/v_f)\gamma_n\lvert B_1\rvert l_{C1}$
Entrance C_2	$l_{A1}+3l_g+l_{A2}+L_{AB}+l_{B1}+l_{B2}+L_{BS}+L_{SC}+l_{C1}$	$2\psi_{C1}-(1/v_f)\gamma_n\lvert B_1\rvert l_{C1}-\varphi_{B2}'$	$-\psi_{C1}+(1/v_f)\gamma_n\lvert B_1\rvert(l_{C1}+l_g)$
Exit C_2	$l_{A1}+3l_g+l_{A2}+L_{AB}+l_{B1}+l_{B2}+L_{BS}+L_{SC}+l_{C1}+l_{C2}$	$-4\psi_{C1}+(1/v_f)\gamma_n\lvert B_1\rvert(3l_{C1}+2l_g+l_{C2})+\varphi_{B2}'$	$-\psi_{C1}+(1/v_f)\gamma_n\lvert B_1\rvert(l_{C1}+l_g+l_{C2})$

Entrance D_1	$l_{A1}+3l_g+l_{A2}+L_{AB}+l_{B1}+l_{B2}+L_{BS}+L_{SC}+l_{C1}+l_{C2}+L_{CD}$	$-4\psi_{C1}+(1/v_f)\gamma_n\lvert B_1\rvert(3l_{C1}+2l_g+l_{C2})+\varphi_{B2}'$	$-\psi_{C1}+(1/v_f)\gamma_n\lvert B_1\rvert(l_{C1}+l_g+l_{C2}+L_{CD})$
Exit D_1	$l_{A1}+3l_g+l_{A2}+L_{AB}+l_{B1}+l_{B2}+L_{BS}+L_{SC}+l_{C1}+l_{C2}+L_{CD}+l_{D1}$	$2\psi_{C1}+(1/v_f)\gamma_n\lvert B_1\rvert(-l_{C1}+l_{C2}+2L_{CD}+l_{D1})-\varphi_{B2}'$	$-\psi_{C1}+(1/v_f)\gamma_n\lvert B_1\rvert(l_{C1}+l_g+l_{C2}+L_{CD}+l_{D1})$
Entrance D_2	$l_{A1}+4l_g+l_{A2}+L_{AB}+l_{B1}+l_{B2}+L_{BS}+L_{SC}+l_{C1}+l_{C2}+L_{CD}+l_{D1}$	$2\psi_{C1}+(1/v_f)\gamma_n\lvert B_1\rvert(-l_{C1}+l_{C2}+2L_{CD}+l_{D1})-\varphi_{B2}'$	$\psi_{C1}-(1/v_f)\gamma_n\lvert B_1\rvert(l_{C1}+2l_g+l_{C2}+L_{CD}+l_{D1})$
Exit D_2	$l_{A1}+4l_g+l_{A2}+L_{AB}+l_{B1}+l_{B2}+L_{BS}+L_{SC}+l_{C1}+l_{C2}+L_{CD}+l_{D1}+l_{D2}$	$\varphi_{B2}'-(1/v_f)\gamma_n\lvert B_1\rvert(l_{C1}+4l_g+3l_{C2}+4L_{CD}+3l_{D1}+l_{D2})=(1/v_i)\gamma_n\lvert B_0\rvert(l_{A1}+4l_g+3l_{A2}+4L_{AB}+3l_{B1}+l_{B2})-(1/v_f)\gamma_n\lvert B_1\rvert(l_{C1}+4l_g+3l_{C2}+4L_{CD}+3l_{D1}+l_{D2})$	$\psi_{C1}-(1/v_f)\gamma_n\lvert B_1\rvert(l_{C1}+2l_g+l_{C2}+L_{CD}+l_{D1}+l_{D2})$

Observations

1. From Table 5, it can be seen that unrelated phases of the r.f. in each arm of the spectrometer is immaterial.
2. The final spin phase angle of the neutron exiting coil D_2 does not depend on the distance between the coil B_2 and the sample (L_{BS}) and between the sample and the coil C_1 (L_{SC}).
3. The final neutron spin phase from Table 5 is:

$$\varphi_{D2}^{'} = \gamma_n \left[\begin{array}{l} \dfrac{B_0\left[l_{A1} + l_{B2} + 3\left(l_{A2} + l_{B1}\right) + 4\left(L_{AB} + l_g\right)\right]}{v_i} \\ -\dfrac{B_1\left[l_{C1} + l_{D2} + 3\left(l_{C2} + l_{D1}\right) + 4\left(L_{CD} + l_g\right)\right]}{v_f} \end{array} \right] \quad (75)$$

If the individual π-flippers are identical in length (i.e., $l_{A1} = l_{A2} = l_{B1} = l_{B2} = l_{C1} = l_{C2} = l_{D1} = l_{D2} = l_{B0}$), and we consistently use the symbol l to define the total length of the entire bootstrap pair unit, i.e., $l = 2l_{B0} + l_g$ (i.e., including the gap in the middle), then the phase angle of the neutron spin at the exit of coil D_2 (Eq. (75)) reduces to

$$\varphi_{D2}^{'} \quad = \quad \varphi_{NRSE} \quad = \quad 4\gamma_n \left[\frac{B_0\left[L_{AB} + l\right]}{v_i} - \frac{B_1\left[L_{CD} + l\right]}{v_f} \right] \quad (76)$$

By comparing Eq. (76), with the equivalent Eq. for the single ($N = 1$) π-flipper case (Eq. (71)), we see that there is an additional *doubling* of the spin phase angle change by using bootstrap pairs. In fact it can be shown [ii] that this additional factor of 2 actually corresponds to N, the number of coils in the bootstrap coil unit, therefore we can rewrite Eq. (76) quite generally as

$$\varphi_{NRSE} = 2N\gamma_n \left[\frac{B_0\left[L_{AB} + l\right]}{v_i} - \frac{B_1\left[L_{CD} + l\right]}{v_f} \right] \quad (77).$$

Finally, Eq. (77) can be rewritten more neatly by introducing L_0 and L_1, the distances between the *mid-points* of the bootstrap coil units (i.e., with equivalent physical interpretation as Eqs. (72) and (73) in the $N = 1$ case) for the first arm and second arm respectively, where

$$L_0 = L_{AB} + l \quad (78)$$

and

$$L_1 = L_{CD} + l \quad (79)$$

so that Eq. (77) becomes

$$\varphi_{NRSE} = 2N\gamma_n\left[\frac{B_0L_0}{v_i}-\frac{B_1L_1}{v_f}\right] = \frac{2Nm_n\gamma_n}{h}\left[B_0L_0\lambda_i - B_1L_1\lambda_f\right]$$
$$= 92641.8N\left[B_0[\mathrm{T}]L_0[\mathrm{m}]\lambda_i\left[\overset{\circ}{\mathrm{A}}\right]-B_1[\mathrm{T}]L_1[\mathrm{m}]\lambda_f\left[\overset{\circ}{\mathrm{A}}\right]\right] \quad (80)$$

With regard to differences that may exist in the flippers of a real spectrometer it is interesting to note from Table 5 that the inner π-flippers in each arm contribute three times the spin turn of the outer coils whereas the zero-field gaps between the coils of a pair (designated by l_g) contribute at the same rate per unit length as the inter-coil zero-field gaps (see also Eq. (75)).

3.6 Coils with dimensional uncertainties

In order to analyze the effect of dimensional uncertainties, we use the following model. The model assumes that the center lines of each π coil are fixed and that (Gaussian) fluctuations in the coil length, Δl_{B0}, are created by equal width but independent Gaussian distributions (of width $\Delta f^{FWHM} = \Delta l_{B0}{}^{FWHM}/\sqrt{2}$) of the winding flatness on each side of the coil. For now, the zero-field flight paths between the coils are assumed to be truly zero field so that the neutron spin direction does not change in them.

We define the coil length deviation on the left and right hand sides of the coil as Δf_L and Δf_R respectively, where Δf is negative if the coil surface is on the $-y$ side of the nominal coil surface position (neutron arrives earlier) and positive if on the $+y$ side of the nominal position (neutron arrives later). We see that the r.f. phase at the entrance to the first coil can vary about the nominal value due to fluctuations in the coil length where

$$\psi_A = \psi_{in} + \mathrm{sgn}\left(B_0^A\right)\frac{\omega_{rf}}{v_n}\Delta f_L(A) \quad (81),$$

where ψ_{in} is the instantaneous phase of the resonant component of the r.f. field with respect to the neutron spin at the entrance to the coil in the *perfect* situation. At the coil exit the r.f. phase is

$$\psi'_A = \psi_A + \mathrm{sgn}\left(B_0^A\right)\frac{\omega_{rf}}{v_n}\left(l_{B_0} - \Delta f_L(A) + \Delta f_R(A)\right)$$
$$= \psi_{in} + \mathrm{sgn}\left(B_0^A\right)\frac{\omega_{rf}}{v_n}\left(l_{B_0} + \Delta f_R(A)\right) \quad (82)$$

so from Eq. (16), the neutron phase at the exit of π coil *A* is

$$\varphi'_A = 2\psi_{in} + \mathrm{sgn}\left(B_0^A\right)\frac{\omega_{rf}}{v_n}\left(l_{B_0} + \Delta f_L(A) + \Delta f_R(A)\right) - \varphi_{in} \tag{83}.$$

On entry to the second coil *B*, we have

$$\varphi_B = \varphi'_A \tag{84}$$

and

$$\begin{aligned}\psi_B &= \mathrm{sgn}\left(B_0^B\right)\mathrm{sgn}\left(B_0^A\right)\left[\psi'_A + \mathrm{sgn}\left(B_0^A\right)\frac{\omega_{rf}}{v_n}\left(L_{AB} - \Delta f_R(A) + \Delta f_L(B)\right)\right] \\ &= \mathrm{sgn}\left(B_0^B\right)\mathrm{sgn}\left(B_0^A\right)\left[\psi_{in} + \mathrm{sgn}\left(B_0^A\right)\frac{\omega_{rf}}{v_n}\left(L_{AB} + l_{B_0} + \Delta f_L(B)\right)\right]\end{aligned} \tag{85}.$$

At the exit of coil *B*, we have

$$\begin{aligned}\psi'_B &= \psi_B + \mathrm{sgn}\left(B_0^B\right)\frac{\omega_{rf}}{v_n}\left(l_{B_0} - \Delta f_L(B) + \Delta f_R(B)\right) \\ &= \mathrm{sgn}\left(B_0^B\right)\mathrm{sgn}\left(B_0^A\right)\left[\psi_{in} + \mathrm{sgn}\left(B_0^A\right)\frac{\omega_{rf}}{v_n}\left(L_{AB} + l_{B_0} + \Delta f_L(B)\right)\right] \\ &+ \mathrm{sgn}\left(B_0^B\right)\frac{\omega_{rf}}{v_n}\left(l_{B_0} - \Delta f_L(B) + \Delta f_R(B)\right)\end{aligned} \tag{86}.$$

Therefore the neutron phase at the exit of π coil *B* is

$$\begin{aligned}\varphi'_B &= 2\,\mathrm{sgn}\left(B_0^B\right)\mathrm{sgn}\left(B_0^A\right)\left[\psi_{in} + \mathrm{sgn}\left(B_0^A\right)\frac{\omega_{rf}}{v_n}\left(L_{AB} + l_{B_0} + \Delta f_L(B)\right)\right] \\ &+ \mathrm{sgn}\left(B_0^B\right)\frac{\omega_{rf}}{v_n}\left(l_{B_0} - \Delta f_L(B) + \Delta f_R(B)\right) - \mathrm{sgn}\left(B_0^A\right)\frac{\omega_{rf}}{v_n}\left(l_{B_0} + \Delta f_L(A) + \Delta f_R(A)\right) \\ &- 2\psi_{in} + \varphi_{in}\end{aligned} \tag{87}.$$

At the entrance to a third coil *C*, we have

$$\varphi_C = \varphi'_B \tag{88}.$$

Assuming that the r.f. in coil *C* is phase locked to coil *B* (we do this so that this 4 π-flipper coil argument can be extended to an N = 2, 4 π-flipper *per spectrometer arm* arrangement in Sec. 3.6.2)

$$\psi_C = \mathrm{sgn}\left(B_0^C\right)\mathrm{sgn}\left(B_0^B\right)\left[\psi'_B + \mathrm{sgn}\left(B_0^B\right)\frac{\omega_{rf}}{v_n}\left(L_{BC} - \Delta f_R\left(B\right) + \Delta f_L\left(C\right)\right)\right]$$

$$= \mathrm{sgn}\left(B_0^C\right)\mathrm{sgn}\left(B_0^B\right)\left[\begin{array}{l}\mathrm{sgn}\left(B_0^B\right)\mathrm{sgn}\left(B_0^A\right)\left[\psi_{in} + \mathrm{sgn}\left(B_0^A\right)\frac{\omega_{rf}}{v_n}\left(L_{AB} + l_{B_0} + \Delta f_L\left(B\right)\right)\right] \\ + \mathrm{sgn}\left(B_0^B\right)\frac{\omega_{rf}}{v_n}\left(L_{BC} + l_{B_0} + \Delta f_L\left(C\right) - \Delta f_L\left(B\right)\right)\end{array}\right] \quad (89).$$

At the exit of coil *C*, we have

$$\psi'_C = \psi_C + \mathrm{sgn}\left(B_0^C\right)\frac{\omega_{rf}}{v_n}\left(l_{B_0} - \Delta f_L\left(C\right) + \Delta f_R\left(C\right)\right)$$

$$= \mathrm{sgn}\left(B_0^C\right)\mathrm{sgn}\left(B_0^B\right)\left[\begin{array}{l}\mathrm{sgn}\left(B_0^B\right)\mathrm{sgn}\left(B_0^A\right)\left[\psi_{in} + \mathrm{sgn}\left(B_0^A\right)\frac{\omega_{rf}}{v_n}\left(L_{AB} + l_{B_0} + \Delta f_L\left(B\right)\right)\right] \\ + \mathrm{sgn}\left(B_0^B\right)\frac{\omega_{rf}}{v_n}\left(L_{BC} + l_{B_0} + \Delta f_L\left(C\right) - \Delta f_L\left(B\right)\right)\end{array}\right] \quad (90)$$

$$+ \mathrm{sgn}\left(B_0^C\right)\frac{\omega_{rf}}{v_n}\left(l_{B_0} - \Delta f_L\left(C\right) + \Delta f_R\left(C\right)\right)$$

so that

$$\varphi'_C = 2\,\mathrm{sgn}\left(B_0^C\right)\mathrm{sgn}\left(B_0^B\right)\left[\begin{array}{l}\mathrm{sgn}\left(B_0^B\right)\mathrm{sgn}\left(B_0^A\right)\left[\psi_{in} + \mathrm{sgn}\left(B_0^A\right)\frac{\omega_{rf}}{v_n}\left(L_{AB} + l_{B_0} + \Delta f_L\left(B\right)\right)\right] \\ + \mathrm{sgn}\left(B_0^B\right)\frac{\omega_{rf}}{v_n}\left(L_{BC} + l_{B_0} + \Delta f_L\left(C\right) - \Delta f_L\left(B\right)\right)\end{array}\right]$$

$$-2\,\mathrm{sgn}\left(B_0^B\right)\mathrm{sgn}\left(B_0^A\right)\left[\psi_{in} + \mathrm{sgn}\left(B_0^A\right)\frac{\omega_{rf}}{v_n}\left(L_{AB} + l_{B_0} + \Delta f_L\left(B\right)\right)\right] \quad (91).$$

$$+ \mathrm{sgn}\left(B_0^C\right)\frac{\omega_{rf}}{v_n}\left(l_{B_0} - \Delta f_L\left(C\right) + \Delta f_R\left(C\right)\right) - \mathrm{sgn}\left(B_0^B\right)\frac{\omega_{rf}}{v_n}\left(l_{B_0} - \Delta f_L\left(B\right) + \Delta f_R\left(B\right)\right)$$

$$+ \mathrm{sgn}\left(B_0^A\right)\frac{\omega_{rf}}{v_n}\left(l_{B_0} + \Delta f_L\left(A\right) + \Delta f_R\left(A\right)\right) + 2\psi_{in} - \varphi_{in}$$

At the entrance to the 4th coil *D*

$$\varphi_D = \varphi'_C \quad (92)$$

and

$$\psi_D = \mathrm{sgn}\left(B_0^D\right)\mathrm{sgn}\left(B_0^C\right)\left[\psi_C' + \mathrm{sgn}\left(B_0^C\right)\frac{\omega_{rf}}{v_n}\left(L_{CD} - \Delta f_R(C) + \Delta f_L(D)\right)\right]$$

$$= \mathrm{sgn}\left(B_0^D\right)\mathrm{sgn}\left(B_0^C\right)\times \tag{93}$$

$$\left[\begin{array}{l} \mathrm{sgn}\left(B_0^C\right)\mathrm{sgn}\left(B_0^B\right)\left[\begin{array}{l} \mathrm{sgn}\left(B_0^B\right)\mathrm{sgn}\left(B_0^A\right)\left[\psi_{in} + \mathrm{sgn}\left(B_0^A\right)\frac{\omega_{rf}}{v_n}\left(L_{AB} + l_{B_0} + \Delta f_L(B)\right)\right] \\ + \mathrm{sgn}\left(B_0^B\right)\frac{\omega_{rf}}{v_n}\left(L_{BC} + l_{B_0} + \Delta f_L(C) - \Delta f_L(B)\right) \end{array}\right] \\ + \mathrm{sgn}\left(B_0^C\right)\frac{\omega_{rf}}{v_n}\left(L_{CD} + l_{B_0} + \Delta f_L(D) - \Delta f_L(C)\right) \end{array}\right]$$

At the exit of coil *D*, we have

$$\psi_D' = \psi_D + \mathrm{sgn}\left(B_0^D\right)\frac{\omega_{rf}}{v_n}\left(l_{B_0} - \Delta f_L(D) + \Delta f_R(D)\right)$$

$$= \mathrm{sgn}\left(B_0^D\right)\mathrm{sgn}\left(B_0^C\right)\times$$

$$\left[\begin{array}{l} \mathrm{sgn}\left(B_0^C\right)\mathrm{sgn}\left(B_0^B\right)\left[\begin{array}{l} \mathrm{sgn}\left(B_0^B\right)\mathrm{sgn}\left(B_0^A\right)\left[\psi_{in} + \mathrm{sgn}\left(B_0^A\right)\frac{\omega_{rf}}{v_n}\left(L_{AB} + l_{B_0} + \Delta f_L(B)\right)\right] \\ + \mathrm{sgn}\left(B_0^B\right)\frac{\omega_{rf}}{v_n}\left(L_{BC} + l_{B_0} + \Delta f_L(C) - \Delta f_L(B)\right) \end{array}\right] \\ + \mathrm{sgn}\left(B_0^C\right)\frac{\omega_{rf}}{v_n}\left(L_{CD} + l_{B_0} + \Delta f_L(D) - \Delta f_L(C)\right) \end{array}\right] \tag{94}$$

$$+ \mathrm{sgn}\left(B_0^D\right)\frac{\omega_{rf}}{v_n}\left(l_{B_0} - \Delta f_L(D) + \Delta f_R(D)\right)$$

so that the neutron phase at the exit of the 4th coil is

$$
\begin{aligned}
\varphi_D' = {} & 2\,\mathrm{sgn}\left(B_0^D\right)\mathrm{sgn}\left(B_0^C\right)\left[\begin{array}{l}
\mathrm{sgn}\left(B_0^C\right)\mathrm{sgn}\left(B_0^B\right)\times \\
\left[\begin{array}{l}
\mathrm{sgn}\left(B_0^B\right)\mathrm{sgn}\left(B_0^A\right)\left[\psi_{in}+\mathrm{sgn}\left(B_0^A\right)\dfrac{\omega_{rf}}{\nu_n}\left(L_{AB}+l_{B_0}+\Delta f_L(B)\right)\right] \\
+\mathrm{sgn}\left(B_0^B\right)\dfrac{\omega_{rf}}{\nu_n}\left(L_{BC}+l_{B_0}+\Delta f_L(C)-\Delta f_L(B)\right)
\end{array}\right] \\
+\mathrm{sgn}\left(B_0^C\right)\dfrac{\omega_{rf}}{\nu_n}\left(L_{CD}+l_{B_0}+\Delta f_L(D)-\Delta f_L(C)\right)
\end{array}\right] \\
& -2\,\mathrm{sgn}\left(B_0^C\right)\mathrm{sgn}\left(B_0^B\right)\left[\begin{array}{l}
\mathrm{sgn}\left(B_0^B\right)\mathrm{sgn}\left(B_0^A\right)\left[\psi_{in}+\mathrm{sgn}\left(B_0^A\right)\dfrac{\omega_{rf}}{\nu_n}\left(L_{AB}+l_{B_0}+\Delta f_L(B)\right)\right] \\
+\mathrm{sgn}\left(B_0^B\right)\dfrac{\omega_{rf}}{\nu_n}\left(L_{BC}+l_{B_0}+\Delta f_L(C)-\Delta f_L(B)\right)
\end{array}\right] \\
& +2\,\mathrm{sgn}\left(B_0^B\right)\mathrm{sgn}\left(B_0^A\right)\left[\psi_{in}+\mathrm{sgn}\left(B_0^A\right)\frac{\omega_{rf}}{\nu_n}\left(L_{AB}+l_{B_0}+\Delta f_L(B)\right)\right] \\
& +\mathrm{sgn}\left(B_0^D\right)\frac{\omega_{rf}}{\nu_n}\left(l_{B_0}-\Delta f_L(D)+\Delta f_R(D)\right)-\mathrm{sgn}\left(B_0^C\right)\frac{\omega_{rf}}{\nu_n}\left(l_{B_0}-\Delta f_L(C)+\Delta f_R(C)\right) \\
& +\mathrm{sgn}\left(B_0^B\right)\frac{\omega_{rf}}{\nu_n}\left(l_{B_0}-\Delta f_L(B)+\Delta f_R(B)\right)-\mathrm{sgn}\left(B_0^A\right)\frac{\omega_{rf}}{\nu_n}\left(l_{B_0}+\Delta f_L(A)+\Delta f_R(A)\right)-2\psi_{in}+\varphi_{in}
\end{aligned}
\tag{95}
$$

We now consider two cases.

3.6.1 First arm of a 4-N=1 π-coil NRSE

In this case, the net spin turn in the first arm of the spectrometer in the absence of stray fields is given by Eq. (87) with $\mathrm{sgn}(B_0^A) = \mathrm{sgn}(B_0^B)$ = "+" so that

$$
\begin{aligned}
\varphi_B' &= 2\frac{\omega_{rf}}{\nu_n}\left(L_{AB}+l_{B_0}\right)+\frac{\omega_{rf}}{\nu_n}\left[\Delta f_L(B)+\Delta f_R(B)-\Delta f_L(A)-\Delta f_R(A)\right]+\varphi_{in} \\
&= \frac{\omega_{rf}}{\nu_n}\left[2L_0+\Delta f_L(B)+\Delta f_R(B)-\Delta f_L(A)-\Delta f_R(A)\right]+\varphi_{in}
\end{aligned}
\tag{96}
$$

3.6.2 First arm of a 4-N=2 π-coil NRSE

In this case, the net spin turn in the first arm of the spectrometer in the absence of stray fields is given by Eq. (95) where, for consistency with previous notation used in Sec. 3.5, we interpret "L_{AB}" as the nominal gap l_g between the bootstrap coil pair, "L_{BC}" as "L_{AB}" and "L_{CD}" as l_g of the second coil pair. We also change the notation $A \rightarrow A_1$,

$B \rightarrow A_2$ etc. for consistency with notation in the previous discussion of bootstrap coils (Sec. 3.5). In this case we have $\mathrm{sgn}(B_0^{A1}) = \mathrm{sgn}(B_0^{B2})$ = "+" and $\mathrm{sgn}(B_0^{A2}) = \mathrm{sgn}(B_0^{B1})$ = "-" and Eq. (95) becomes

$$\begin{aligned}\varphi'_{B_2} &= \frac{\omega_{rf}}{v_n}\begin{pmatrix}4L_{AB}+4l_g+8l_{B_0}-\Delta f_L(A_1)-\Delta f_R(A_1)-\Delta f_L(A_2)-\Delta f_R(A_2)\\+\Delta f_L(B_1)+\Delta f_R(B_1)+\Delta f_L(B_2)+\Delta f_R(B_2)\end{pmatrix}+\varphi_{in}\\&=\frac{\omega_{rf}}{v_n}\begin{pmatrix}4L_0-\Delta f_L(A_1)-\Delta f_R(A_1)-\Delta f_L(A_2)-\Delta f_R(A_2)\\+\Delta f_L(B_1)+\Delta f_R(B_1)+\Delta f_L(B_2)+\Delta f_R(B_2)\end{pmatrix}+\varphi_{in}\end{aligned} \quad (97).$$

4 Quantum mechanical description of NRSE

Gähler, Golub, and Keller [8] have discussed particle beam magnetic resonance in quantum mechanical terms and derived formulas for spin ½ particles passing along the *y* axis. They show that for neutron magnetic interaction energies very much smaller than the neutron kinetic energy entering the field region ($\mu B_0 \ll \frac{1}{2} m_n v_i^2$) (where reflected matter waves at the field boundary can be neglected), quantum mechanics predicts the same physical results as the classical treatment, although the interpretation of the mechanism involved appears different.

Quantum mechanically, a spin s = ½ particle such as the neutron has spin angular momentum of magnitude $\sqrt{s(s+1)}\hbar = \sqrt{3}\hbar/2$ but its component along any given axis may only have a magnitude $m_s\hbar$ where $m_s = \pm\frac{1}{2}$.

4.1 Polarized beam traversing a static field

Consider a beam initially polarized along the *x* direction traveling along *y* whose wavefunction can be written as a plane wave (which can be considered as the superposition of equally probable spin up and spin down states with respect to the *z* axis)

$$\psi_i = \frac{1}{\sqrt{2}}\begin{bmatrix}1\\1\end{bmatrix} e^{i(k_i y-\omega_i t)} \quad (98)$$

When the neutron enters a static magnetic field applied along the *z*-direction, the *z*-component of spin angular momentum is either +½$\hbar$ or -½$\hbar$. The associated parallel spin state is reduced in potential energy by $\mu_n B_0$ and the antiparallel spin state is increased in potential energy by $\mu_n B_0$. At the field boundary, the potential gradient causes the kinetic energy of the of the parallel spin state to increase by $\mu_n B_0$ and the kinetic energy of the antiparallel spin

state to decrease by $\mu_n B_0$ so that the total energy is conserved. Thus the kinetic energies of the two spin states differ inside the field and the wavefunction inside the static field region is

$$\psi_{B_0} = \frac{1}{\sqrt{2}}\begin{bmatrix} e^{-i\mu_n B_0 y/\hbar v_i} \\ e^{i\mu_n B_0 y/\hbar v_i} \end{bmatrix} e^{i(k_i y-\omega_i t)} = \frac{1}{\sqrt{2}}\begin{bmatrix} e^{-i\omega_0 y/2v_i} \\ e^{i\omega_0 y/2v_i} \end{bmatrix} e^{i(k_i y-\omega_i t)} \quad (99),$$

where the total splitting of the spin up and spin down states is

$$\Delta E_{B_0} = 2\mu_n B_0 = \hbar\omega_0 \quad (100),$$

where ω_0 can be interpreted as the classical Larmor precession frequency. The expectation value of the polarization along *x* inside the field region is

$$\begin{aligned} \langle \sigma_x \rangle &= \psi^*_{B_0}[\sigma_x]\psi_{B_0} = \frac{1}{\sqrt{2}}\begin{bmatrix} e^{i\omega_0 y/2v_i} \\ e^{-i\omega_0 y/2v_i} \end{bmatrix} e^{-i(k_i y-\omega_i t)} \begin{bmatrix} 0 & 1 \\ 1 & 0 \end{bmatrix} \frac{1}{\sqrt{2}}\begin{bmatrix} e^{-i\omega_0 y/2v_i} \\ e^{i\omega_0 y/2v_i} \end{bmatrix} e^{i(k_i y-\omega_i t)} \\ &= \frac{1}{2}\begin{bmatrix} e^{i\omega_0 y/v_i} \\ e^{-i\omega_0 y/v_i} \end{bmatrix} = \cos(\omega_0 y/v_i) \end{aligned} \quad (101).$$

Here, the relative phase of the spin up and down waves is a cosine function of the distance traveled through the field. This is exactly equivalent to Larmor precession in the classical case.

On exiting the field, the two spin states become degenerate and the neutron spin states retain the accumulated relative phase angle $\omega_0 l_{B0}/v_i$ with which they exited the field region. This phase angle does not change in the subsequent zero-field region and is classically equivalent to the termination of the Larmor precession in the zero field region. This situation is illustrated in Figure 7. Further accounts of these energy changes can be found in Refs. [9], [10], [11], [12], and [13].

Sometimes Eq. (100) is expressed in terms of a splitting in wavevector magnitude of the two states. For NRSE applications it is always true that $\Delta E_{B0} \ll \hbar\omega_i$, the incident neutron energy, therefore we can write

$$\Delta k \simeq \frac{2m_n\mu_n}{\hbar^2}\frac{B_0}{k_i} \quad (102)$$

and the accumulated phase difference can be written equivalently as $l_{B0}\Delta k$.

Note that the initial eigenvector (Eq. (98)) of the neutron is not an eigenvector of $[\sigma_z]$, but can be expressed as a linear combination of the spin-up and spin-down spinors for the *z* component, i.e.,

$$\frac{1}{\sqrt{2}}\begin{bmatrix}1\\1\end{bmatrix}=\frac{1}{\sqrt{2}}\left(\begin{bmatrix}1\\0\end{bmatrix}+\begin{bmatrix}0\\1\end{bmatrix}\right) \qquad (103).$$

Eq. (103) implies that if the expectation value of the *z*-component of the spin at the exit of the field region was measured, the spins would be equally distributed spin up and spin down with respect to *z*.

4.2 Passage through a static field with superimposed perpendicular oscillatory field

With a superimposed perpendicular oscillating field (see Krüger [14]), tuned such that $\omega_0 = \omega_{rf}$, transitions between the spin up and spin down states (separated by $\Delta E = \hbar\omega_0$) can be induced via exchange of quanta with the r.f. field. Golub, Gähler, and Keller [13] treat a general case consisting of three regions; two static field regions (I and III) sandwiching an intermediate region (II) were the static field coexists with a perpendicular oscillating field of length *d* along the beam direction. These authors use the properties of Eq. (103) to simplify the problem by treating the +*z* and –*z* components of the eigenvector separately. Further, they assume $\omega_{rf} \ll \omega_i$ (equivalent to the ($\mu B_0 \ll$ $\frac{1}{2}m_n v_i^2$) assumption above) where $\frac{1}{2}m_n v_i^2 = \hbar\omega_i$ (whereby reflected matter waves at the potential boundary can be ignored and various simplifying approximations e.g. $\delta k_{B0} \approx \omega_0/v_i$ etc. can be made outside of the exponentials). Using the symbols *T* for the transmission amplitude with subscript "0" for elastic (no exchange of quanta – i.e., no spin flip) and "1" for inelastic (exchange of quanta with spin flip) and "+" and "–" for spin up and down respectively with respect to *z*, these authors produce the following expressions:

For the spin up state $\begin{bmatrix}1\\0\end{bmatrix}$

$$T_0^- = T_1^+ = 0 \qquad (104),$$

$$T_1^- = -i\frac{\omega_r}{2\omega_A}e^{i\varepsilon\frac{d}{v_i}}\sin\left(\omega_A\frac{d}{v_i}\right) \qquad (105),$$

$$T_0^+ = e^{-i\varepsilon\frac{d}{v_i}}\left(\cos\left(\omega_A\frac{d}{v_i}\right)+i\frac{\varepsilon}{\omega_A}\sin\left(\omega_A\frac{d}{v_i}\right)\right) \qquad (106)$$

and for the wavefunction of the neutron in the third region (i.e., after exiting the combined field region)

$$\psi_{III}(1)=\begin{bmatrix} T_0^+ e^{-i\omega_0 y/2v} \\ T_1^- e^{-i\left[\left(\omega_{rf}-\frac{\omega_0}{2}\right)y/v-\omega_{rf}t\right]} \end{bmatrix} e^{i(k_i y-\omega_i t)}$$

$$=\begin{bmatrix} e^{-i\varepsilon\frac{d}{v}}\left(\cos\left(\omega_A\frac{d}{v}\right)+i\frac{\varepsilon}{\omega_A}\sin\left(\omega_A\frac{d}{v}\right)\right)e^{-i\omega_0 y/2v} \\ -i\frac{\omega_r}{2\omega_A}e^{i\varepsilon\frac{d}{v}}\sin\left(\omega_A\frac{d}{v}\right)e^{-i\left[\left(\omega_{rf}-\frac{\omega_0}{2}\right)y/v-\omega_{rf}t\right]} \end{bmatrix} e^{i(k_i y-\omega_i t)} \quad (107),$$

where

$$\omega_A=\sqrt{\frac{\omega_r^2}{4}+\varepsilon^2} \quad (108)$$

with

$$\varepsilon=\frac{1}{2}\left(\omega_{rf}-\omega_0\right) \quad (109)$$

where ω_r (in their notation) is the classical Larmor precession frequency of the neutron spin around B_{rf} (equivalent to ω_p (Eq.(11))), i.e.,

$$\omega_r=\gamma_n B_{rf} \quad (110)$$

Likewise, for the spin down state $\begin{bmatrix}0\\1\end{bmatrix}$

$$T_1^-=T_0^+=0 \quad (111)$$

$$T_0^-=e^{i\varepsilon\frac{d}{v_i}}\left(\cos\left(\omega_A\frac{d}{v_i}\right)-i\frac{\varepsilon}{\omega_A}\sin\left(\omega_A\frac{d}{v_i}\right)\right) \quad (112)$$

$$T_1^+=-i\frac{\omega_r}{2\omega_A}e^{-i\varepsilon\frac{d}{v_i}}\sin\left(\omega_A\frac{d}{v_i}\right) \quad (113)$$

and

$$\psi_{III}(2)=\begin{bmatrix} -i\frac{\omega_r}{2\omega_A}e^{-i\varepsilon\frac{d}{v_i}}\sin\left(\omega_A\frac{d}{v_i}\right)e^{i\left[\left(\omega_{rf}-\frac{\omega_0}{2}\right)y/v_i-\omega_{rf}t\right]} \\ e^{i\varepsilon\frac{d}{v_i}}\left(\cos\left(\omega_A\frac{d}{v_i}\right)-i\frac{\varepsilon}{\omega_A}\sin\left(\omega_A\frac{d}{v_i}\right)\right)e^{i\omega_0 y/2v_i} \end{bmatrix} e^{i(k_i y-\omega_i t)} \quad (114)$$

so that the wavefunction in region III given an incoming beam polarized along *x*, $\psi_i = \frac{1}{\sqrt{2}}\begin{bmatrix}1\\1\end{bmatrix}$ is

$$\psi_{III} = \frac{1}{\sqrt{2}}\begin{bmatrix} e^{-i\varepsilon\frac{d}{v_i}}\left(\cos\left(\omega_A\frac{d}{v_i}\right)+i\frac{\varepsilon}{\omega_A}\sin\left(\omega_A\frac{d}{v_i}\right)\right)e^{-i\omega_0 y/2v_i} - i\frac{\omega_r}{2\omega_A}e^{-i\varepsilon\frac{d}{v_i}}\sin\left(\omega_A\frac{d}{v_i}\right)e^{i\left[\left(\omega_{rf}-\frac{\omega_0}{2}\right)y/v_i-\omega_{rf}t\right]} \\ -i\frac{\omega_r}{2\omega_A}e^{i\varepsilon\frac{d}{v_i}}\sin\left(\omega_A\frac{d}{v_i}\right)e^{-i\left[\left(\omega_{rf}-\frac{\omega_0}{2}\right)y/v_i-\omega_{rf}t\right]} + e^{i\varepsilon\frac{d}{v_i}}\left(\cos\left(\omega_A\frac{d}{v_i}\right)-i\frac{\varepsilon}{\omega_A}\sin\left(\omega_A\frac{d}{v_i}\right)\right)e^{i\omega_0 y/2v_i} \end{bmatrix} e^{i(k_i y-\omega_i t)}$$

(115).

The probability of a spin-flip involving a photon exchange with the r.f. field is

$$\left|T_1^-\right|^2(1) = \left|T_1^+\right|^2(2) = \left|-i\frac{\omega_r}{2\omega_A}e^{i\varepsilon\frac{d}{v_i}}\sin\left(\omega_A\frac{d}{v_i}\right)\right|^2 \tag{116}$$

and the non-spin flip probability (where the energy does not change) is

$$\left|T_0^+\right|^2(1) = \left|T_0^-\right|^2(2) = \left|e^{-i\varepsilon\frac{d}{v_i}}\left(\cos\left(\omega_A\frac{d}{v_i}\right)+i\frac{\varepsilon}{\omega_A}\sin\left(\omega_A\frac{d}{v_i}\right)\right)\right|^2 \tag{117}.$$

4.2.1 Special cases

4.2.1.1 Exact resonance

This is the condition for which $\omega_{rf} = \omega_0$, therefore $\varepsilon = 0$, $\omega_A = \omega_r/2$, consequently

$$\psi_{III} = \frac{1}{\sqrt{2}}\begin{bmatrix} \cos\left(\frac{\omega_r d}{2v_i}\right)e^{-i\omega_0\frac{y}{2v_i}} - i\sin\left(\frac{\omega_r d}{2v_i}\right)e^{i\omega_0\left(\frac{y}{2v_i}-t\right)} \\ -i\sin\left(\frac{\omega_r d}{2v_i}\right)e^{-i\omega_0\left(\frac{y}{2v_i}-t\right)} + \cos\left(\frac{\omega_r d}{2v_i}\right)e^{i\omega_0\frac{y}{2v_i}} \end{bmatrix} e^{i(k_i y-\omega_i t)} \tag{118}$$

and the probability of a spin-flip involving a photon exchange with the r.f. field is

$$\left|T_1^-\right|^2(1) = \left|T_1^+\right|^2(2) = \sin^2\left(\frac{\omega_r d}{2v_i}\right) \tag{119}$$

and the non-spin flip probability is

$$\left|T_0^+\right|^2(1)=\left|T_0^-\right|^2(2)=\cos^2\left(\frac{\omega_r d}{2v_i}\right) \qquad (120)$$

We see that unless $\omega_r d/v_i = (2N+1)\pi$, where N is an integer, an incomplete spin inversion occurs (corresponding to a flipper efficiency < 1); i.e., r.f. π-flippers only produce exact π-flips for a unique velocity (as was shown classically in Sec. 2.2).

4.2.1.2 On-resonance, with dispersion, flipper tuned optimally for $v_i=\langle v_i\rangle$

If, additionally, the flipper is tuned optimally for the average velocity $\langle v_i\rangle$, we have

$$\omega_r\frac{d}{\langle v_i\rangle}=\pi \qquad (121).$$

Thus, Eqs. (119) and (120) can be re-expressed as

$$\left|T_1^-\right|^2(1)=\left|T_1^+\right|^2(2)=\sin^2\left(\frac{\pi}{2}\frac{\langle v_i\rangle}{v_i}\right)=\sin^2\left(\frac{\pi}{2}\frac{\lambda_i}{\langle\lambda_i\rangle}\right) \quad P(\text{sf}) \text{ tuned for exact } \pi\text{-flips for } \lambda_i=\langle\lambda_i\rangle \quad (122)$$

and

$$\left|T_0^+\right|^2(1)=\left|T_0^-\right|^2(2)=\cos^2\left(\frac{\pi}{2}\frac{\langle v_i\rangle}{v_i}\right)=\cos^2\left(\frac{\pi}{2}\frac{\lambda_i}{\langle\lambda_i\rangle}\right) \quad P(\text{nsf}) \text{ tuned for exact } \pi\text{-flips for } \lambda_i=\langle\lambda_i\rangle \quad (123)$$

respectively.

Note that the quantum mechanical spin-flip probability for a neutron of wavelength λ_i (Eq.(122)*) is exactly equivalent to the quantity* $\frac{P_{disp}}{P_{ideal}}=\langle\cos\varepsilon\cos\chi\rangle$ *derived from the classical treatment* (*see Sec. 2.2 and Eq.*(31)).

4.2.1.3 On-resonance, exact π-flips for all velocities (i.e., no dispersion or monochromatic)

"No-dispersion" implies that the classical condition for exact π-flips around B_{rf} is satisfied for *all* velocities, i.e., $\omega_r d/v_i = \pi$, therefore Eq. (118) becomes

$$\psi_{III}=\frac{-i}{\sqrt{2}}\begin{bmatrix} e^{i\omega_0\left(\frac{y}{2v_i}-t\right)} \\ e^{-i\omega_0\left(\frac{y}{2v_i}-t\right)}\end{bmatrix}e^{i(k_i y-\omega_r t)} \qquad (124)$$

and the probability of a spin-flip involving a photon exchange with the r.f. field is

$$\left|T_1^-\right|^2(1)=\left|T_1^+\right|^2(2)=1 \tag{125}$$

and the non-spin flip probability (where the energy stays the same) is

$$\left|T_0^+\right|^2(1)=\left|T_0^-\right|^2(2)=0 \tag{126}.$$

Note that under these conditions exact spin inversion occurred in region II.

Region II is defined from $0 \le y \le d$ so that shifting the coordinate system to the exit of region II, we have

$$\psi_{III}=\frac{-i}{\sqrt{2}}\begin{bmatrix} e^{i\omega_0\left(\frac{y-d}{2v_i}-t\right)} \\ e^{-i\omega_0\left(\frac{y-d}{2v_i}-t\right)} \end{bmatrix} e^{i(k_i y-\omega_i t)} \tag{127}$$

The expectation value of σ_x at the exit of the coil is

$$\begin{aligned} \langle\sigma_x\rangle &= \psi_{III}^{*}\begin{bmatrix}0 & 1\\ 1 & 0\end{bmatrix}\psi_{III}=\frac{1}{2}\begin{bmatrix} e^{-i2\omega_0\left(\frac{y-d}{2v_i}-t\right)} \\ e^{i2\omega_0\left(\frac{y-d}{2v_i}-t\right)} \end{bmatrix} \\ &= \cos\left(2\omega_0\left(\frac{y-d}{2v_i}-t\right)\right)=\cos\left(2\omega_{rf}\left(\frac{y-d}{2v_i}-t\right)\right) \end{aligned} \tag{128}$$

Thus, at a fixed position y, the spin precesses at angular frequency $2\omega_0$. This precession is sometimes called "anomalous" because it is not predicted in the classical case where the neutron spin stops precessing after exiting the coil. This quantum-mechanical result is used to explain why MIEZE spectrometers work.

We should be able to equate the argument of Eq. (128) with the spin phase angle of a neutron at the exit of coil *A*, given in Table 4, where it was assumed that the neutron spin was initially polarized along *x*, and the same assumptions of exact resonance ($\omega_0 = \omega_{rf}$) and zero dispersion were made, i.e.,

$$\varphi_{\mathrm{A}}^{'}=2\psi_{\mathrm{A}}+\frac{1}{v_i}\gamma_n\left|B_0\right|l_A \quad =2\psi_{\mathrm{A}}+\frac{1}{v_i}\omega_0 l_A \quad =2\psi_{\mathrm{A}}+\frac{1}{v_i}\omega_{rf} l_A \quad \text{from Table 4} \tag{129}$$

with the argument in Eq. (128) evaluated at y=0 (the coil exit)

$$\varphi_{\mathrm{A}}^{'}=2\omega_{rf}\left(\frac{d}{2v_i}-t\right) \tag{130}.$$

By identifying ψ_A with $\omega_{rf}t$ and d with l_A, we see that the two equations are equivalent.

Qualitatively, a kinetic energy splitting of the two spin states occurs on entry to the coil ($\Delta E_k = \hbar\omega_0$) due to the static field gradient, whilst the total energy (= kinetic + potential) remains constant initially. The total spin inversion that occurs in the flipper involving exchange of photons with the r.f. field (see Eq. (125)) causes the *total* energy of the two states to become split by $2\hbar\omega_0$, but leaves their kinetic energy unchanged (still split by $\Delta E_k = \hbar\omega_0$). At the coil exit, when crossing the static field boundary, the kinetic energy splitting does not disappear (as it did in the static-only field case (Sec. 4.1)). If the spin inversion due to the r.f. field is 100%, an *additional* splitting in kinetic energy (by $\hbar\omega_0$) due to the static field gradient at the exit boundary occurs (i.e., the kinetic energy splitting doubles at the exit of the first coil ($\Delta E_k = 2\hbar\omega_0$)). This explains the $2\omega_0$ precession frequency in region III (see Eq. (128)). This situation is shown (for perfect spin state inversion) in Figure 8. Further accounts of these energy changes can be found in Refs. [9], [10], [11], [12], and [13].

4.2.1.4 Off-resonance, exact π-flips for all velocities (i.e., no dispersion or monochromatic)

"No-dispersion" implies that the classical condition for exact π-flips around B_{rf} is satisfied for *all* velocities, i.e., $\omega_1 d/v_i = \pi$, therefore from Eq. (108)

$$\omega_A = \sqrt{\frac{\pi^2 v_i^2}{4d^2} + \varepsilon^2} \tag{131}$$

so there is no simplification of the wavefunction for $\varepsilon \neq 0$.

4.2.1.5 Passage through a second similar coil a distance L downstream (on-resonance, no dispersion or monochromatic)

Golub, Gähler, and Keller [13] extrapolate the wavefunction exiting the first coil through a zero field path length L to the entrance of a second similar coil downstream (equivalent to the first arm of a $N = 1$ NRSE) and show that the wavefunction exiting the second coil is given by

$$\psi_{exit\,B} = \frac{1}{\sqrt{2}} \begin{bmatrix} e^{-i\omega_0\left(\frac{L+d}{v_i}\right)} \\ e^{i\omega_0\left(\frac{L+d}{v_i}\right)} \end{bmatrix} e^{i(k_i y - \omega_t t)} \tag{132}$$

so that the expectation value of the polarization with respect to x at the exit of the second coil is

$$\langle \sigma_x \rangle = \psi^*_{exit\,B} \begin{bmatrix} 0 & 1 \\ 1 & 0 \end{bmatrix} \psi_{exit\,B} = \frac{1}{2} \begin{bmatrix} e^{i2\omega_0\left(\frac{L+d}{v_i}\right)} \\ e^{-i2\omega_0\left(\frac{L+d}{v_i}\right)} \end{bmatrix} \tag{133}$$

$$= \cos\left(2\omega_0\left(\frac{L+d}{v_i}\right)\right)$$

The presence of the second similar flipper coil with the same static field orientation as the first "mirror images" the neutron energy history shown in Figure 8 and the kinetic and total energies of the two spin states revert to their starting value E_i. Therefore, in contrast with the precession seen at the exit of the first coil, the polarization at the exit of the second coil and thereafter remains constant. The phase angle, $2\omega_0(L+d)/v_i$, agrees exactly with the classical result for the phase change in the first arm of the $N = 1$ spectrometer, as expected (see e.g. Eq. (71)).

4.3 What is the effect of $l_{rf} \neq l_{B0}$? - Coil tuning

For *any* spin inversion to take place, the r.f. field must be applied in a region where the static field is also present (i.e., there is a Zeeman splitting to induce transitions between states). Secondly, the r.f. photons must have a frequency close to that of the splitting (resonance) so that transitions occur with high probability (see Sec. 2.3). Finally, for optimum flipping probability, Eq. (13) must be satisfied in the overlap region between the static and r.f. fields, of length l_π, applying the definition in Eq. (1).

4.3.1 Monochromatic beam with static field region enclosing the r.f. region ($l_{coil}=l_{B0}$, $l_\pi=l_{rf}$)

The monochromatic beam case eliminates the complication of dispersion and for a coil tuned as described above, therefore the spins always remain in the *xy* plane after passage through the coil. This is exactly the situation depicted in Figure 8. The static-field-only regions each side of the r.f. region behave only as Larmor precession regions as described in Sec. 4.1 where the spins precess at rate ω_0 around the *z* axis with the corresponding spin phase angle shift in the *x*-*y* plane. However, because the effect of the spin inversion in the "r.f. + B_0" region (length $l_\pi = l_{rf}$) is not manifested until the neutron reaches the exit of the static field region, the effective Larmor precession continues at a rate ω_0 over the entire coil length ($l_{coil} = l_{B0}$) and at a rate $2\omega_0$ in the zero field region after the coil.

Thus for an initial spin direction along *x*, the phase of the spin a distance *L* downstream of the static field region is given by

$$\sigma_x(L) = \omega_0\left(l_{B_0} + 2L\right) \qquad l_{B0} \text{ encloses } l_{rf} \qquad (134).$$

Using the definition of coil length in Eq. (3), we have $l_{coil} = l_{B_0}$, therefore we can equally write for this case

$$\sigma_x(L) = \omega_0\left(l_{coil} + 2L\right) \qquad l_{B0} \text{ encloses } l_{rf} \qquad (135)$$

with $l_\pi = l_{rf}$ so that the specific π-flip condition is

$$B_{rf} = \pi\frac{h}{\gamma_n m_n l_{rf}\lambda_n} \qquad l_{B0} \text{ encloses } l_{rf} \qquad (136).$$

4.3.2 Monochromatic beam with r.f. region enclosing the static field region ($l_{coil}=l_{rf}$, $l_\pi=l_{B0}$)

This case averaged over time is depicted in Figure 9. Note that in the "r.f.-field-only" regions each side of the static field, the time-averaged field direction is random with respect to the neutron spin and so the average kinetic energy and total energy of the neutron spin states remain unchanged. Spin inversion and photon exchange occur only in the region where the static and r.f. fields are coincident, where all the change in total energy takes place. As before, the effect of the spin inversion on the kinetic energy is only felt at the static field boundary after which the time-averaged r.f. field does not change the total or kinetic energy. Thus for an initial spin direction along *x*, the phase of the spin a distance *L* downstream of the *static field region* is given by

$$\sigma_x(L) = \omega_0\left(l_{B_0} + 2L\right) \qquad l_{rf} \text{ encloses } l_{B0} \qquad (137).$$

However, using the definition of coil length in Eq. (3), $l_{coil} = l_{rf}$, no longer allows us to write an expression for σ_x in terms of the coil length l_{coil} as in Eq. (135). Therefore, if we always define *L* as the distance downstream of the *static field region* Eq. (134) can be used for both geometrical cases.

For this case, we have $l_\pi = l_{B0}$ so that the specific π-flip condition is

$$B_{rf} = \pi\frac{h}{\gamma_n m_n l_{B0}\lambda_n} \qquad l_{rf} \text{ encloses } l_{B0} \qquad (138).$$

4.3.3 With dispersion or when detuned from resonance (B_0 region encloses B_{rf})

With dispersion or when the coil is not exactly on-resonance for all neutrons (e.g., due to static field inhomogeneities), a fraction of the neutrons do not flip in the superimposed "static field + r.f. field" region. Thus the unflipped neutrons behave similarly to neutrons in a pure static field (see Sec. 4.1 above), whilst the flipped component is subject to the behavior described in Sec. 4.2 and subsequent sections. This situation is illustrated (for the case where the B_0 field region encloses the r.f. field region) in Figure 10.

5 Analysis of the spin echo signal

In the following, the emphasis is on quasielastic applications of the NRSE. Equation (77) is appropriate for a well-collimated beam. If we now account for the vector nature and a more general direction of the beam, we can write the neutron spin phase gain in the first arm of the spectrometer as

$$\varphi_1 = 2N\gamma_n \frac{B_0 L_0}{\mathbf{v_i}.\hat{\mathbf{L}}_\mathbf{0}} \qquad (139).$$

Similarly, the spin phase change (loss) in the second arm is

$$\varphi_2 = -2N\gamma_n \frac{B_1 L_1}{\mathbf{v_f}.\hat{\mathbf{L}}_\mathbf{1}} \qquad (140)$$

where γ_n is the neutron gyromagnetic ratio, $\mathbf{v_{i,f}}$ is the initial/final neutron velocity vector and $\hat{\mathbf{L}}_{0,1}$ is a unit vector parallel to the axes of the first and second arms of the spectrometer (and perpendicular to the coil axis), and it is understood by the "-" sign in Eq. (140) that the field directions in the second arm are such that they reverse the spin phase angle change with respect to the first arm.

5.1 Small divergence approximation

For *small beam divergences* with coil axes that are perpendicular to $\mathbf{v_i}$ and $\mathbf{v_f}$, we can approximate Eqs. (139) and (140) by

$$\varphi_0 = 2N\gamma_n \frac{B_0 L_0}{v_i} \qquad (141)$$

and

$$\varphi_1 = -2N\gamma_n \frac{B_1 L_1}{v_f} \tag{142}$$

respectively, where v_i and v_f are scalars, so that the net spin turn at the analyzer is given by Eq. (80).

For *quasielastic* non-spin flip scattering that is sufficiently narrow ($\delta v \ll v_i$), we can write

$$v_f \approx v_i + \delta v \tag{143}$$

so that Eq. (80) is approximately

$$\varphi_{NRSE} \approx 2N\gamma_n \left[\frac{(B_0 L_0 - B_1 L_1) v_i + B_0 L_0 \delta v}{v_i (v_i + \delta v)} \right] \approx 2N\gamma_n \left[\frac{\delta(BL) v_i + B_0 L_0 \delta v}{v_i^2} \right] \tag{144}$$

where

$$\delta(BL) = B_0 L_0 - B_1 L_1 \tag{145}$$

is often called the spectrometer *asymmetry*.

The measured quantity in neutron spin echo is related to the polarization of the scattered beam. If the polarization is analyzed in the same direction as the polarization direction of the incident beam (assumed here to be the *x* axis), the polarization of the scattered beam is related (classically) to the cosine of φ_{NRSE}, averaged over all the scattered neutron trajectories i.e.,

$$P_x = \langle \cos \varphi_{NRSE} \rangle \tag{146},$$

where $\langle\rangle$ implies a statistical average over a *large* sample of scattered neutrons, where from Eq. (144) we have

$$P_x = \langle \cos \varphi_{NRSE} \rangle = \left\langle \cos\left(2N\gamma_n \left[\frac{\delta(BL) v_i + B_0 L_0 \delta v}{v_i^2} \right] \right) \right\rangle$$

$$= \left\langle \cos\left(2N\gamma_n \left[\frac{\delta(BL)}{v_i} \right] \right) \cos\left(2N\gamma_n \left[\frac{B_0 L_0 \delta v}{v_i^2} \right] \right) - \sin\left(2N\gamma_n \left[\frac{\delta(BL)}{v_i} \right] \right) \sin\left(2N\gamma_n \left[\frac{B_0 L_0 \delta v}{v_i^2} \right] \right) \right\rangle$$

(147)

This expression must be averaged over all possible values of v_i (the incident spectrum) and all possible values of δv (= v_i - v_f) determined by the scattering. Noting that Q is approximately independent of ω, i.e.,

$$Q \approx \frac{2m_n v_i}{\hbar} \sin\theta \tag{148},$$

where 2θ is the scattering angle, we can write

$$P(v_i, \delta v)\, d(\delta v) \simeq S(Q,\omega)\, d\omega \tag{149}$$

and for *small* energy transfers (small ω and $v_i \approx v_f$) we have from the definition of kinetic energy

$$\delta v \quad = \left(v_f - v_i\right) = \frac{2\hbar\omega}{m_n\left(v_f + v_i\right)} \quad \approx \frac{\hbar\omega}{m_n v_i} \quad \approx \frac{\hbar\omega}{m_n v_f} \tag{150}.$$

If $S(Q,\omega)$ is *symmetric* in ω (usually a good approximation for quasielastic scattering) and substituting $\delta v \approx \hbar\omega/m_n v_i$ from Eq. (150), the average over the δv distribution characteristic of the scattering sample for a given v_i becomes

$$P_x(v_i) = \cos\left(2N\gamma_n\left[\frac{\delta(BL)}{v_i}\right]\right)\int_{-\infty}^{\infty} S(Q,\omega)\cos\left(\frac{2N\hbar\gamma_n B_0 L_0}{m_n v_i^3}\omega\right)d\omega \tag{151},$$

where the "sine" part of the expansion in Eq. (147) disappears in the integral for symmetric $S(Q,\omega)$ and the denominator $\int_{-\infty}^{\infty} S(Q,\omega)\, d\omega = 1$ for a normalized scattering function is implicit.

Note that the quantity preceding ω in the second cosine argument in Eq. (151) when $\delta(BL) = 0$ (i.e., $B_0L_0 = B_1L_1$) is often referred to as the spin-echo time τ_{NRSE}, i.e.,

$$\tau_{NRSE} \quad = \quad \frac{2N\hbar\gamma_n B_0 L_0}{m_n v_i^3} \quad = \quad \frac{N\gamma_n}{\pi}\left(\frac{m_n}{h}\right)^2 B_0 L_0 \lambda_i^3 \tag{152}$$

where

$$\begin{aligned}\tau_{NRSE}\left[\text{ns}\right] &= 0.37271\, N\, B_0\left[\text{T}\right] L_0\left[\text{m}\right]\left(\lambda_i\left[\mathring{\text{A}}\right]\right)^3 \\ &= 1.27794\times10^{-2}\, N\, \nu_0\left[\text{MHz}\right] L_0\left[\text{m}\right]\left(\lambda_i\left[\mathring{\text{A}}\right]\right)^3\end{aligned} \tag{153}$$

so that (6.13) may be rewritten as

$$P_x(v_i) = \cos\left(2N\gamma_n\left[\frac{\delta(BL)}{v_i}\right]\right)\int_{-\infty}^{\infty} S(Q,\omega)\cos\left(\omega\tau_{NRSE}\right)d\omega \tag{154}.$$

Averaging over the normalized incident velocity distribution, $F(v_i)$, the final polarization is

$$P_x = \int_0^\infty F(v_i)\cos\left(2N\gamma_n\left[\frac{\delta(BL)}{v_i}\right]\right)dv_i \int_{-\infty}^{\infty} S(Q,\omega)\cos(\omega\tau_{NRSE})\,d\omega \quad \text{symmetric } S(Q,\omega) \quad (155)$$

where the denominator $\int_0^\infty F(v_i)\,dv_i = 1$ is implied. It is convenient to express the left hand integral in terms of the normalized incident *wavelength* distribution, $I(\lambda_i)$, so that Eq. (155) becomes

$$P_x = \int_0^\infty I(\lambda_i)\cos\left(\frac{2N\gamma_n m_n \delta(BL)}{h}\lambda_i\right)d\lambda_i \int_{-\infty}^{\infty} S(Q,\omega)\cos(\omega\tau_{NRSE})\,d\omega \quad \text{symmetric } S(Q,\omega) \quad (156)$$

where the first integral

$$\int_0^\infty I(\lambda_i)\cos(K\lambda_i)\,d\lambda_i = F(K) \qquad \text{with } K = \frac{2N\gamma_n m_n \delta(BL)}{h} \qquad (157)$$

is the Fourier cosine transform of the incident wavelength distribution with respect to *K*. This Fourier transform gives the oscillatory echo signal in asymmetric scans (scans of $\delta(BL)$ around 0 at fixed τ_{NRSE}) whose precise form is characteristic of the form of the incident spectrum, $I(\lambda_i)$.

5.2 The echo point

For *elastic* scattering (or no sample), we have $v_i = v_f$ and $\delta v = 0$ for all neutrons. For *quasielastic* scattering, (ignoring the very small influence of detailed balance at these small energy transfers), we have $\langle v_i\rangle = \langle v_f\rangle$, $\langle\delta v\rangle = 0$ and $v_i \neq v_f$ in general. In both cases, if the incident beam is initially polarized, the maximum polarization at the analyzer is found when the first term in Eq. (144) is zero (i.e., two arms of the spectrometer are symmetrized [tuned such that $\delta(BL)=0$]). This is called the "echo point". At the echo point Eq. (144) becomes

$$\varphi_{NRSE} \approx 2N\gamma_n \frac{B_0 L_0 \delta v}{v_i^2} \qquad \text{at the echo point } (\delta(BL)=0) \qquad (158).$$

We note that:

1. For *elastic* non-spin flip scattering ($\delta v = 0$), the initial polarization state of the beam is theoretically reproduced at the analyzer when tuned to the echo point.

2. For narrow *quasielastic* non-spin flip scattering where we can make the approximation

$$\hbar\omega = \frac{m_n}{2}\left(v_i^2 - v_f^2\right) \quad = \quad \frac{m_n}{2}\left(v_i + v_f\right)\left(v_i - v_f\right) \quad \approx \quad m_n v_i \delta v \qquad (159),$$

therefore we can write Eq. (158) as

$$\varphi_{NRSE} \approx \frac{2N\gamma_n B_0 L_0}{m_n v_i^3}\hbar\omega \quad = \quad \omega\tau_{NRSE} \qquad \text{at the echo point} \qquad (160).$$

where τ_{NRSE} was defined in Eq. (152).

To find the echo point (i.e., tuning $\delta(BL) = 0$) usually either B or L is fixed. In conventional NSE spectrometers L (for the two precession paths) is fixed and δB is varied. In 4-coil NRSE spectrometers, usually B is fixed for all coils and δL (L of one arm) is varied.

5.3 Some special cases

From Eq. (156), we have

$$P_x = \int_0^\infty I(\lambda_i)\cos\left(\frac{2N\gamma_n m_n \delta(BL)}{h}\lambda_i\right)d\lambda_i \int_{-\infty}^{\infty} S(Q,\omega)\cos(\omega\tau_{NRSE})\,d\omega$$

We note the following:

(i). At the echo point ($\delta(BL) = 0$), P_x is the cosine Fourier transform of the scattering function $S(Q,\omega)$ with respect to ω, i.e.,

$$P_x = \int_{-\infty}^{\infty} S(Q,\omega)\cos(\omega\tau_{NRSE})\,d\omega \quad \text{quasielastic non-spin flip scattering at echo point } (\delta(BL) = 0) \quad (161).$$

(ii). For elastic non-spin flip scattering or no sample ($S(Q,\omega) = \delta(\omega)$, $\cos(\omega\tau_{NRSE}) = 1$), then

$$P_x = \int_0^\infty I(\lambda_i)\cos\left(\frac{2N\gamma_n m_n \delta(BL)}{h}\lambda_i\right)d\lambda_i \quad \text{elastic non-sin flip scattering or no sample} \quad (162).$$

(iii). For elastic, non-spin flip scattering or no sample ($S(Q,\omega) = \delta(\omega)$) with a quasi-monochromatic incident wavelength spectrum (i.e., $I(\lambda_i) \rightarrow \delta(\lambda_i)$), then

$$P_x \rightarrow \cos\left(\frac{2N\gamma_n m_n \delta(BL)}{h}\lambda_i\right) \qquad \text{elastic non-sin flip scattering or no sample and } I(\lambda_i) \rightarrow \delta(\lambda_i) \quad (163).$$

This means that:

(a) At the echo point ($\delta(BL) = 0$), $P_x = 1$ at *all* values of B_0.

(b) The signal varies consinusoidally as a function of asymmetry $\delta(BL)$ with a periodicity given by

$$\delta(BL)_{2\pi} = \frac{h}{m_n}\frac{\pi}{\gamma_n N}\frac{1}{\lambda_i} = \frac{\pi v_i}{\gamma_n N} \quad (164).$$

5.4 Detected Signal

5.4.1 Perfect polarizer, analyzer and non-spin flip scattering

In an NRSE instrument, for a perfect polarizer and analyzer, the non-spin flip quasielastic signal in the detector is

$$\begin{aligned} I_+ &= \frac{1}{2}\left(1+\left\langle\cos\varphi_{NRSE}\right\rangle\right) = \frac{1}{2}\left(1+\left\langle\cos\omega\tau_{NRSE}\right\rangle\right) = \frac{1}{2}\left(1+P_x\right) \\ &= \frac{1}{2}\left(1+\int_0^\infty F\left(v_i\right)\cos\left(2N\gamma_n\left[\frac{\delta(BL)}{v_i}\right]\right)dv_i\int_{-\infty}^{\infty} S\left(Q,\omega\right)\cos\left(\omega\tau_{NRSE}\right)d\omega\right) \end{aligned} \quad (165).$$

For quasielastic scattering whose scattering function can be represented by

$$S\left(Q,\omega\right) = \frac{1}{\pi}\frac{\Gamma}{\Gamma^2+\hbar^2\omega^2} \quad (166)$$

where Γ is the energy half width at half maximum, the detected signal at the echo point ($\delta(BL) = 0$) is

$$I_+ = \frac{1}{2}\left(1+\exp\left(-\frac{\Gamma}{\hbar}\tau_{NRSE}\right)\right) \quad (167)$$

where the second term is proportional to the intermediate scattering function. The advantages of measuring the scattering function in the time domain instead of the energy domain are especially of significance because the measured data, which is the convolution of the scattering function with the instrumental resolution function in the energy domain, becomes the product in the time domain. Thus, the scattering function is extracted from the measured data simply by division by the resolution function. This feature allows for very sensitive lineshape analysis.

Monte Carlo simulations of spin-echo signals that illustrate the behavior of Eq. (165) are shown in figure 11 for a variety of incoming and scattered beam characteristics (non-spin flip elastic and quasi-elastic scattering). Columns 1 to 3 are for elastic non spin-flip scattering (or no neutron energy change through the spectrometer).

Column 4 is for quasielastic non spin-flip scattering. For each of these simulations there are no sample size effects, coil dispersion is switched off, and $\Delta B_0 = \Delta l_{B0}$ (zero field inhomogeneity and perfect dimensions of the flipper coils). Additionally for columns 1 and 4 zero beam divergence is assumed. The effects of coil dispersion on the spin echo signal are studied in Sec. 8.2. These particular simulations were performed for a 4 N=2 bootstrap coil NRSE with L_1 = 2.0 m, l_π= 3.0 cm, l_g = 0.0 cm, and λ_i = 8Å, for $10^{-3} \leq B_0(\mathrm{T}) \leq 0.025$. The asymmetric scan is performed with B_0 = B_1, with (L_0 - L_1) varied ten minimum periods each side of the symmetric position (i.e., between $\pm 10 \dfrac{\pi v_i}{\gamma_n N B_0^{\max}}$, where B_0^{max} is the maximum applied static field (0.025 T), corresponding to τ_{NRSE} = 19.1 ns. $\delta(BL)$ was varied by changing L_1 with respect to L_0. (i.e., $\delta(BL) = B\delta L$). The beam divergence, if any, is symmetrical about the nominal axes of the spectrometer arms. Under these conditions, the echo is found at $L_0 = L_1$. The left hand column of Figure 11 illustrates the effect of broadening $\Delta\lambda_i$ for elastic, non-spin flip scattering (or no sample). In the extreme, purely monochromatic case of $\Delta\lambda_i$ = 0, the signal is cosinusoidal with respect to δL (as predicted in Sec. 5.3 case (iii)) with $\delta(BL) = B\delta L$ for one signal period given by Eq. (164). For $\Delta\lambda_i > 0$ the maximum signal is achieved at a unique spectrometer setting and as $\Delta\lambda_i$ increases the primary envelope of the echo signal tightens around the echo point. Note that the period also decreases inversely proportional to B_0 (= B_1) (and hence τ_{NRSE}), as predicted by Eq. (164).

The second and third columns show the effect of increasing the neutron flight path differences through the spectrometer for (i) a purely monochromatic incident beam and (ii) a triangular wavelength distribution with $\Delta\lambda_i/\langle\lambda_i\rangle$ = 10% respectively. The divergence figures indicate the maximum angle per unit wavelength with respect to the beam axis.

The fourth column demonstrates the increasingly rapid decay of the echo point signal with respect to τ_{NRSE} as the quasielastic width is increased (as predicted by Eq. (167)). This example was calculated using a purely monochromatic incident beam ($\Delta\lambda_i$ = 0). The Lorentzian scattering function was generated by selecting random Lorentzian deviates according to

$$\hbar\omega = -\Gamma \tan\left[\pi\left(ran\{-0.5, 0.5\}\right)\right] \qquad (168),$$

subject to the maximum sample energy gain restriction $\hbar\omega \leq E_i$, where E_i is the incident neutron energy.

5.4.2 Imperfect polarizers with non-spin flip scattering or no sample

Real polarizing devices transmit a fraction of the wrong spin state which results in a reduction of the NRSE signal. It is important therefore to correct data in such a way as to isolate depolarization due to the sample dynamics from instrumental depolarization as far as it is possible.

Considering the quantum mechanical description of the polarization in terms of spin up and spin down neutrons, the polarizing efficiency of a "+" polarizer is numerically equal to the polarization of an initially unpolarized beam obtained after action of the polarizer. Using the definition in Eq. (63), the polarization after the action of the initial polarizer is

$$P_P = \frac{I_P^+ - I_P^-}{I_P^+ + I_P^-} \tag{169}$$

where I_P^+ and I_P^- are the intensities of + and – neutrons in the beam after the polarizer *P*. Note that P_P can vary between +1 and -1. The incoming unpolarized beam of total intensity I_0 can be described by equal + and - components, i.e.,

$$I_0^+ = I_0^- = \frac{I_0}{2} \tag{170}$$

The total intensity after the polarizer

$$I_P^{tot} = I_P^+ + I_P^- = T_P \frac{I_0}{2} = T_P I_0^+ \tag{171}$$

where we have used the boundary condition that for perfect + polarization efficiency (P_P=1), only the + state neutrons of the originally unpolarized beam are transmitted (i.e., one half of the neutrons of the incoming beam) and we assume that this total number is conserved for inefficient polarizers. T_P is the spin-independent transmission factor of the device with $0 < T_P < 1$ due to effects such as absorption or scattering. From Eqs. (169) and (171) it is easy to show that after the polarizer:

$$I_P^+ = T_P \frac{I_0}{4}\left(1 + P_P\right) = T_P \frac{I_0^+}{2}\left(1 + P_P\right) \tag{172}$$

and

$$I_P^- = T_P \frac{I_0}{4}\left(1 - P_P\right) = T_P \frac{I_0^-}{2}\left(1 - P_P\right) \tag{173}$$

Therefore, the combined action of the polarizer (*P*) with the analyzer (*A*), both oriented to transmit + spin neutrons, for non-spin flip scattering is expected to give transmitted intensities

$$I_{PA}^{+} = T_A \frac{I_P^{+}}{2}\left(1+P_A\right) = T_P T_A \frac{I_0^{+}}{4}\left(1+P_P\right)\left(1+P_A\right) = T_P T_A \frac{I_0}{8}\left(1+P_P\right)\left(1+P_A\right) \qquad (174).$$

Likewise

$$I_{PA}^{-} = T_A \frac{I_P^{-}}{2}\left(1-P_A\right) = T_P T_A \frac{I_0^{-}}{4}\left(1-P_P\right)\left(1-P_A\right) = T_P T_A \frac{I_0}{8}\left(1-P_P\right)\left(1-P_A\right) \qquad (175)$$

with the total beam intensity after the analyzer

$$I_{PA}^{tot} = I_{PA}^{+} + I_{PA}^{-} = T_P T_A \frac{I_0}{4}\left(1+P_P P_A\right) \qquad (176).$$

Therefore, the final polarization for non-spin flip scattering is

$$P_{PA} = \frac{I_{PA}^{+} - I_{PA}^{-}}{I_{PA}^{+} + I_{PA}^{-}} = \frac{P_P + P_A}{1+P_P P_A} \qquad (177).$$

If two π-flippers of efficiency f_1 and f_2 (see Sec. 2.4) and spin-independent transmission T_{f1} and T_{f2} and are placed between the polarizer and the analyzer, and remembering that the effect of a π-flipper of efficiency f is to multiply the incoming polarization by the factor (1-2f) (see also Sec. 2.4), we infer by analogy with Eqs. (174) and (175) that the + and - intensities downstream of the analyzer (i.e., at the detector) are

$$\left.\begin{aligned} I_{PA}^{+} &= T_{f_1} T_{f_2} T_P T_A \frac{I_0}{8}\left(1+P_P\right)\left(1+P_A\right) \\ I_{PA}^{-} &= T_{f_1} T_{f_2} T_P T_A \frac{I_0}{8}\left(1-P_P\right)\left(1-P_A\right) \\ I_{PA}^{tot} &= T_{f_1} T_{f_2} T_P T_A \frac{I_0}{4}\left(1+P_P P_A\right) \end{aligned}\right\} \quad \text{both flippers off} \qquad (178)$$

$$\left.\begin{aligned} I_{PA}^{+} &= T_{f_1} T_{f_2} T_P T_A \frac{I_0}{8}\left(1+\left[1-2f_1\right]P_P\right)\left(1+P_A\right) \\ I_{PA}^{-} &= T_{f_1} T_{f_2} T_P T_A \frac{I_0}{8}\left(1-\left[1-2f_1\right]P_P\right)\left(1-P_A\right) \\ I_{PA}^{tot} &= T_{f_1} T_{f_2} T_P T_A \frac{I_0}{4}\left(1+\left[1-2f_1\right]P_P P_A\right) \end{aligned}\right\} \quad \text{only flipper 1 on} \qquad (179)$$

$$\left.\begin{aligned} I_{PA}^{+} &= T_{f_1} T_{f_2} T_P T_A \frac{I_0}{8}\left(1+\left[1-2f_2\right]P_P\right)\left(1+P_A\right) \\ I_{PA}^{-} &= T_{f_1} T_{f_2} T_P T_A \frac{I_0}{8}\left(1-\left[1-2f_2\right]P_P\right)\left(1-P_A\right) \\ I_{PA}^{tot} &= T_{f_1} T_{f_2} T_P T_A \frac{I_0}{4}\left(1+\left[1-2f_2\right]P_P P_A\right) \end{aligned}\right\} \quad \text{only flipper 2 on} \qquad (180)$$

$$\left.\begin{aligned} I_{PA}^{+} &= T_{f_1} T_{f_2} T_P T_A \frac{I_0}{8}\left(1+\left[1-2f_1\right]\left[1-2f_2\right]P_P\right)\left(1+P_A\right) \\ I_{PA}^{-} &= T_{f_1} T_{f_2} T_P T_A \frac{I_0}{8}\left(1-\left[1-2f_1\right]\left[1-2f_2\right]P_P\right)\left(1-P_A\right) \\ I_{PA}^{tot} &= T_{f_1} T_{f_2} T_P T_A \frac{I_0}{4}\left(1+\left[1-2f_1\right]\left[1-2f_2\right]P_P P_A\right) \end{aligned}\right\} \quad \text{both flippers 1 and 2 on} \qquad (181)$$

As pointed out by Hayter [15], the ratio of the detector count rates, I_{PA}^{tot}, measured with both π-flippers switched off to the count rates with the two flippers switched "on-off", "off-on" and "on-on" provides three "flipping ratios" R_1, R_2, and R_{12} respectively which no longer have the spin-independent pre-factors common to each measurement. We thus have three equations for the three unknowns f_1, f_2, and the product of the polarizer and analyzer efficiencies $P_P P_A$, which can be solved to obtain

$$P_P P_A = \frac{R_{12}\left(R_1-1\right)\left(R_2-1\right)}{\left(R_1 R_2 - R_{12}\right)} \qquad (182)$$

$$f_i = \frac{\left(R_i-1\right)}{2R_i}\frac{\left(1+P_P P_A\right)}{P_P P_A} \qquad (183)$$

The flipping ratios can be determined for multi-angle instruments by using a diffuse, non-spin flip scattering sample such as quartz.

In an *M*-coil NRSE instrument with non-spin flipping samples (e.g. pure nuclear coherently scattering samples), the polarization (NRSE signal) is reduced from the ideal value by the product of these instrumental inefficiencies. Therefore, the corrected signal, P_{corr}, is related to the measured signal, P_{meas}, by

$$P_{corr} = \frac{P_{meas}}{P_P P_A \prod_{i=1}^{M} (1 - 2 f_i)} \tag{184}$$

5.4.3 Imperfect polarizers with spin flip scattering

When there is a sample that modifies the spin state of the incoming neutrons, the spin transfer function of the sample has to be taken into account just like the function (1 - 2*f*) for the flippers. Table 6 shows relative spin-flip probabilities for various types of nuclear scattering for non-magnetic samples.

Table 6. Spin flip probabilities for non-magnetic samples.

Scatter	Coherent	Incoherent	
		Spin	Isotope
Non-spin flip	1	1/3	1
Spin flip	0	2/3	0

Consider a non-magnetic sample that flips a fraction q of the neutron spins, so that in exact analogy with the π-flipper (Sec. 2.4) and Eq. (64), the polarization after the sample, P_S, is related to the polarization before the sample, P_i, by

$$P_S = (1-2q)P_i \tag{185}$$

Consider the simplest example of a single isotope, pure incoherent scatterer. We see that 1/3 of the neutrons have their spins unchanged by the sample whilst 2/3 of the neutrons have their spins flipped by π. Thus we have a sample flipping efficiency given by $q = 2/3$ and consequently

$$\frac{P_S}{P_i} = -\frac{1}{3} \qquad \text{non-magnetic, pure isotope incoherent scatterer} \tag{186}.$$

This means that the spin-echo signal amplitude is reduced to 1/3 and the minus sign means that the echo signal is inverted (i.e., minima instead of maxima). For this case, Eq. (184) would become

$$P_{corr} = -\frac{3P_{meas}}{P_P P_A \prod_{i=1}^{M}(1-2f_i)} \tag{187}$$

For a more general non-magnetic case where both spin-incoherent and coherent scattering are present, we might have

$$q \approx \frac{2S_{inc}(Q)}{3\left(S_{coh}(Q)+S_{inc}(Q)\right)} \tag{188}$$

where we have assumed that the relative probabilities of coherent and spin-incoherent scattering are given by $S_{coh}(Q)$ and $S_{inc}(Q)$ respectively, therefore

$$\frac{P_S}{P_i} = \frac{3S_{coh}(Q)-S_{inc}(Q)}{3\left(S_{coh}(Q)+S_{inc}(Q)\right)} \tag{189}.$$

This represents an upper limit on the size of the spin echo signal. For this case, Eq. (184) would become

$$P_{corr} = \frac{3P_{meas}\left(S_{coh}(Q)+S_{inc}(Q)\right)}{P_P P_A \prod_{i=1}^{M}(1-2f_i)\left[3S_{coh}(Q)-S_{inc}(Q)\right]} \tag{190}.$$

Other scattering cases including paramagnetic, ferromagnetic, and antiferromagnetic samples have been discussed by Mezei [3].

In order to determine the exact spin-flip / non-spin flip behavior of the sample, it can be measured with just the polarizer and analyzer with just one flipper on or off in a conventional polarization analysis arrangement.

6 Elastic instrumental resolution function

The spin echo phase is given by Eq. (80), i.e.,

$$\varphi_{NRSE} = \varphi_0 - \varphi_1 = \frac{2Nm_n\gamma_n}{h}\left[B_0L_0\lambda_i - B_1L_1\lambda_f \right]$$

At the echo point $\langle\varphi_{NRSE}\rangle = 0$, however, even for elastic scattering or no sample ($\lambda_i = \lambda_f$), φ_{NRSE} has a spread of values, $\Delta\varphi_{NRSE}$ around its mean value because the terms B_0L_0 and B_1L_1 have some spread $\Delta(B_0L_0)$ and $\Delta(B_1L_1)$ [4] due to instrumental imperfections. Consequently, $\Delta\varphi_0$ and $\Delta\varphi_1$ are non-zero and this "blurs" the real information that we wish to obtain which is the change in polarization *due to the energy transfer distribution of the scattering process*.

The instrumental blurring, $\Delta(BL)$, which can never be completely eliminated, determines the *elastic instrumental resolution function*. Ideally, for the widest dynamic range we desire that $\Delta\varphi_{NRSE}$ be dominated by the spread in $\lambda_i - \lambda_f$, not by uncertainties in the terms BL to as high fields as possible. As τ_{NRSE} increases, the spectrometer signal becomes increasingly destroyed by $\Delta(BL)$ as the spin fan-out that it creates increases. Eventually, when the fan-out increases beyond about 2π, the polarization (NRSE signal) may become too small for the spectrometer to be usefully operated. Therefore, pushing to higher Fourier times usually involves keeping $\Delta(BL)$ within increasingly tight tolerances.

Assuming Gaussian uncertainties on the values of B and L and if B and L are assumed to be independent variables, we expect φ_{NRSE} also to have a Gaussian distribution, $g(\varphi_{NRSE})$. At the echo point ($\langle B_0L_0\rangle = (\langle B_1L_1\rangle)$, $g(\varphi_{NRSE})$ is symmetrically distributed about zero (polarization aligned along the x-axis). For the Gaussian distribution $g(\varphi_{NRSE})$, the elastic scattering polarization along x, P_x^0, is

[4] PLEASE NOTE we use the symbol "Δ" to imply a *statistical spread,* not to be confused with the "δ" used to imply a *difference* when talking about the asymmetry B_0L_0 - B_1L_1.

$$P_x^0\left(\Delta\varphi_{NRSE}^{FWHM}\right)=\frac{\int_0^\infty \cos\left(\varphi_{NRSE}\right) g\left(\varphi_{NRSE}\right) d\varphi_{NRSE}}{\int_0^\infty g\left(\varphi_{NRSE}\right) d\varphi_{NRSE}} \qquad (191)$$

$$=\exp\left[-\frac{\left(\Delta\varphi_{NRSE}^{FWHM}\right)^2}{16\ln 2}\right] \approx \exp\left[-0.09\left(\Delta\varphi_{NRSE}^{FWHM}\right)^2\right]$$

or the inverse relation

$$\Delta\varphi_{NRSE}^{FWHM}=4\sqrt{\ln 2\ \ln\left[\frac{1}{P_x^0}\right]} \approx \sqrt{11.1\ln\left[\frac{1}{P_x^0}\right]} \qquad (192).$$

We use this convenient relation when estimating spectrometer tolerances in Sec. 6.1.

For a *linear* fan-out of the spins centered about zero, characterized by limiting values $\pm \Delta\varphi_{NRSE}^{max}$, we have

$$P_x^0\left(\Delta\varphi_{NRSE}^{\max}\right)=\frac{\sin\Delta\varphi_{NRSE}^{\max}}{\Delta\varphi_{NRSE}^{\max}} \qquad (193).$$

$P_x^0(\tau_{NRSE})$ must remain comfortably greater than zero (typically $P_x^0 > 0.2$ defines an absolute minimum for quasi-elastic measurements to be feasible at most neutron sources). This is because the elastic and quasi-elastic signal strength cannot exceed a maximum proportional to P_x^0 (for pure coherent scatterers) and sometimes considerably less for incoherent scatterers (see Sec. 5.4.3). Therefore, excessive counting times or poor signal to noise ratio are likely to result from increasing τ_{NRSE} into a regime where the P_x^0 becomes too small. Consequently the magnitude of $\Delta(BL)$ may ultimately limit the spectrometer measuring range.

Purely coherent, elastic scatterers such as Grafoil, Carbopack, and carbon black have all been used for measuring the resolution function in spin-echo spectrometers.

6.1 Analysis of contributions to resolution function: Allowable flight path differences and static field inhomogeneity

The spin echo phase for a perfectly tuned spectrometer ($\omega_{rf}^0=\gamma_n\left|B_0\right|$, $\omega_{rf}^1=\gamma_n\left|B_1\right|$) is given by Eq. (80), i.e.,

$$\varphi_{NRSE} \quad = \quad 2N\gamma_n\left[\frac{B_0L_0}{v_i}-\frac{B_1L_1}{v_f}\right] \quad = \quad \frac{2Nm_n\gamma_n}{h}\left[B_0L_0\lambda_i-B_1L_1\lambda_f\right]$$

$$=92641.8N\left[B_0[\mathrm{T}]L_0[\mathrm{m}]\lambda_i\left[\mathrm{\mathring{A}}\right]-B_1[\mathrm{T}]L_1[\mathrm{m}]\lambda_f\left[\mathrm{\mathring{A}}\right]\right]$$

The above equation provides the mean value of φ_{NRSE} brought about by the mean values of B_0L_0 and B_1L_1. In order to estimate the spread of φ_{NRSE} about the mean, $\Delta\varphi_{NRSE}$, due to static field, dimensional uncertainties, and beam divergence, we assume equal spreads on φ_0 and φ_1, i.e., $\Delta\varphi_0 = \Delta\varphi_1$ and that the spectrometer is operated at the echo point (i.e., $\langle\varphi_0\rangle = \langle\varphi_1\rangle$), so that for Gaussian uncertainties we have

$$\Delta\varphi_{NRSE} \quad = \quad \sqrt{\Delta\varphi_0^2+\Delta\varphi_1^2} \quad \approx \quad \sqrt{2}\,\Delta\varphi_0 \qquad (194).$$

We also use Eq. (192) to conveniently relate the Gaussian FWHM phase fan-out $\Delta\varphi_{NRSE}$ to the elastic (resolution) polarization, $P_x^{\,0}$, i.e.,

$$\Delta\varphi_{NRSE}^{FWHM} = 4\sqrt{\ln 2\,\ln\left(\frac{1}{P_x^0}\right)}$$

We analyze first the effect of field inhomogeneities by assuming zero flight path uncertainties, and secondly, the flight path uncertainties by assuming zero field inhomogeneities. We also separate the flight path uncertainties caused by spectrometer dimensional fluctuations from those due to beam divergence. For the effect of divergence, we cannot assume Gaussian uncertainties as explained in Sec. 6.1.4.

6.1.1 Field inhomogeneities

We remember that the effect of fluctuations in the static field B_0 can be considered classically as providing an additional advance or lag of the spin direction with respect to the rotating frame of the resonant r.f. component. For a single π-flipper we have

$$\Delta\varphi_\pi = \left(\omega_0-\langle\omega_0\rangle\right)t_{B_0} \approx \frac{m_n}{h}\gamma_n\left(B_0-\langle B_0\rangle\right)l_{B_0}\lambda_i = \frac{m_n}{h}\gamma_n\Delta B_0 l_{B_0}\lambda_i \qquad (195).$$

For $2N$ π-flippers in each arm with similar Gaussian fluctuations in the field values about the mean, $\Delta B_0^{\,FWHM}$, the contribution to $\Delta\varphi_0$ is given by

$$\Delta\varphi_0^{FWHM} = \Delta\varphi_1^{FWHM} = \sqrt{2N}\,\frac{m_n}{h}\gamma_n l_{B_0}\lambda_i\,\Delta B_0^{FWHM} \qquad (196)$$

so that (using Eq. (194))

$$\Delta B_0^{FWHM} = \frac{h}{m_n \gamma_n} \frac{1}{\sqrt{M}\, l_{B_0} \lambda_i} \Delta\varphi_{NRSE}^{FWHM} \tag{197}$$

where M is the total number of π-flippers in the spectrometer. Therefore

$$\Delta B_0^{FWHM}\Big|_{\Delta l_\pi = 0, \Delta\theta = 0} = \frac{h}{m_n \gamma_n} \frac{4\sqrt{\ln 2 \ln\left(\frac{1}{P_x^0}\right)}}{\sqrt{M}\, l_{B_0} \lambda_i} \approx \frac{7.2\times 10^{-5} \sqrt{\ln\left(\frac{1}{P_x^0}\right)}}{\sqrt{M}\, l_{B_0}\,[\mathrm{m}]\, \lambda_i \left[\mathrm{\AA}\right]} \text{ Tesla} \tag{198}.$$

Specifically for a 4-coil unit spectrometer where $M = 4N$

$$\Delta B_0^{FWHM}\Big|_{\Delta l_\pi = 0, \Delta\theta = 0} = \frac{h}{m_n \gamma_n} \frac{2\sqrt{\ln 2 \ln\left(\frac{1}{P_x^0}\right)}}{\sqrt{N}\, l_{B_0} \lambda_i} \approx \frac{3.6\times 10^{-5} \sqrt{\ln\left(\frac{1}{P_x^0}\right)}}{\sqrt{N}\, l_{B_0}\,[\mathrm{m}]\, \lambda_i \left[\mathrm{\AA}\right]} \text{ Tesla} \tag{199}.$$

The success of Eq. (198) is demonstrated in Figure 12 and Figure 13 for $N = 1$ and $N = 2$ respectively.

6.1.2 Coil flatness

In order to estimate tolerances on the flight path lengths, we return to the expanded equations representing φ_0 (and φ_1) which contain the individual contributions (the flatness model used is that described in Sec. 3.6), and now we assume $\Delta_{B0} = 0$.

(a) For a 4 (N=1)-coil NRSE, we have from Eq. (96) for a given neutron trajectory,

$$\varphi_0 = \frac{\omega_{rf}}{v_n}\left[2L_0 + \Delta f_R(B) + \Delta f_L(B) - \Delta f_L(A) - \Delta f_R(A)\right]$$

where we have set φ_{in}=0 (perfectly polarized incoming beam) and the terms Δf_L and Δf_R are the deviations of the coil surface from perfect flatness on the left and right hand sides of the coil respectively. Assuming, for similar coils, Δf_L and Δf_R have Gaussian distributions of equal FWHM $=\Delta f^{FWHM}$, we can write

$$\frac{\Delta\varphi_0}{\varphi_0} = \frac{\sqrt{4N}\,\Delta f^{FWHM}}{2NL_0} = \frac{\Delta f^{FWHM}}{L_0} \qquad N = 1 \tag{200}$$

whence

$$\Delta f_{FWHM} = \frac{L_0}{\sqrt{2}} \frac{\Delta\varphi_{NRSE}^{FWHM}}{\varphi_0} = \frac{h}{m_n \gamma_n} \frac{\sqrt{2\ln 2\ \ln\left(\frac{1}{P_x^0}\right)}}{B_0 \lambda_i} \approx \frac{2.54\times10^{-5}\sqrt{\ln\left(\frac{1}{P_x^0}\right)}}{B_0[\mathrm{T}]\lambda_i\left[\mathrm{\AA}\right]} \text{ meters} \quad (201).$$

We can also write the FWHM fluctuation in the coil length, Δl_π, in terms of Δf^{FWHM}, where

$$\Delta l_\pi^{FWHM}\Big|_{\Delta B_0=0,\Delta\theta=0} = \sqrt{2}\Delta f_{FWHM} = L_0 \frac{\Delta\varphi_{NRSE}^{FWHM}}{\varphi_0} = \frac{2h}{m_n\gamma_n} \frac{\sqrt{\ln 2\ \ln\left(\frac{1}{P_x^0}\right)}}{B_0\lambda_i}$$

$$\approx \frac{3.6\times10^{-5}\sqrt{\ln\left(\frac{1}{P_x^0}\right)}}{B_0[\mathrm{T}]\lambda_i\left[\mathrm{\AA}\right]} \text{ meters} \quad (202).$$

(b) For N=2 bootstrap coils, for a given neutron trajectory, we have from Eq. (97):

$$\varphi'_{B_2} = \frac{\omega_{rf}}{v_n}\begin{pmatrix} 4L_{AB} + 4l_g + 8l_{B_0} - \Delta f_L(A_1) - \Delta f_R(A_1) - \Delta f_L(A_2) - \Delta f_R(A_2) \\ +\Delta f_L(B_1) + \Delta f_R(B_1) + \Delta f_L(B_2) + \Delta f_R(B_2) \end{pmatrix}$$

$$= \frac{\omega_{rf}}{v_n}\left(4L_0 - \Delta f_L(A_1) - \Delta f_R(A_1) - \Delta f_L(A_2) - \Delta f_R(A_2) + \Delta f_L(B_1) + \Delta f_R(B_1) + \Delta f_L(B_2) + \Delta f_R(B_2)\right)$$

where we have set φ_{in}=0 (perfectly polarized incoming beam) and the terms Δf_L and Δf_R are the deviations of the coil surface from perfect flatness on the left and right hand sides of the coil respectively. Assuming, for similar coils, that Δf_L and Δf_R have Gaussian distributions of equal FWHM = Δf^{FWHM}, we can write

$$\frac{\Delta\varphi_0}{\varphi_0} = \frac{\sqrt{4N}\Delta f_{FWHM}}{2NL_0} = \frac{\Delta f_{FWHM}}{\sqrt{N}L_0} \qquad , N = 2 \quad (203)$$

whence

$$\Delta f_{FWHM} = L_0 \frac{\Delta\varphi_{NRSE}^{FWHM}}{\varphi_0} = \frac{h}{m_n\gamma_n} \frac{\sqrt{2\ln 2\ \ln\left(\frac{1}{P_x^0}\right)}}{\sqrt{N}B_0\lambda_i} \approx \frac{2.54\times10^{-5}\sqrt{\ln\left(\frac{1}{P_x^0}\right)}}{\sqrt{N}B_0[\mathrm{T}]\lambda_i\left[\mathrm{\AA}\right]} \quad (204)$$

We can also write the FWHM fluctuation in the coil length (length of the B_0 field) in terms of Δf^{FWHM}, where

$$\Delta l_{\pi}^{FWHM}\Big|_{\Delta B_0=0,\Delta\theta=0} = \sqrt{2}\Delta f_{FWHM} \quad = \frac{2h}{m_n\gamma_n}\frac{\sqrt{\ln 2\,\ln\left(\frac{1}{P_x^0}\right)}}{\sqrt{N}B_0\lambda_i} \quad \approx \frac{3.6\times10^{-5}\sqrt{\ln\left(\frac{1}{P_x^0}\right)}}{\sqrt{N}B_0[\mathrm{T}]\lambda_i\left[\mathrm{\mathring{A}}\right]}\ \text{meters} \quad (205).$$

Eq. (205) seems to be generally valid, the "$\sqrt{N}$" not being apparent in the N=1 case (Eq. (202)). The success of Eq. (205) is demonstrated in Figure 14 and Figure 15 for N = 1 and N = 2 respectively.

6.1.3 Coil parallelism

Related to the coil flatness is the question of parallelism which may actually impose the major engineering limitation. The tolerances on the coil length are the same as indicated in Sec. 6.1.2, however, a lack of parallelism leads to a predictable and continuous change of field paths over the beam area. If we assume that Eq. (205) defines approximately the maximum tolerance in the static field length, then we can introduce an approximate coil parallelism tolerance where

$$\vartheta_{\max}^{surf} = \frac{1}{\max(a,l_{axial})}\frac{2h}{m_n\gamma_n}\frac{\sqrt{\ln 2\,\ln\left(\frac{1}{P_x^0}\right)}}{\sqrt{N}B_0\lambda_i} \quad \approx \frac{1}{\max(a,l_{axial})[\mathrm{m}]}\frac{3.6\times10^{-5}\sqrt{\ln\left(\frac{1}{P_x^0}\right)}}{\sqrt{N}B_0[\mathrm{T}]\lambda_i\left[\mathrm{\mathring{A}}\right]}\ \text{rad} \quad (206),$$

where $\vartheta_{\max}^{surf}$ is the maximum tolerance angle between the entrance and exit surfaces of the static coil windings and a and l_{axial} are the coil dimensions defined in Figure 15.

6.1.4 Beam divergence (simplified model)

We use a simplified model in order to estimate analytically the effects of beam divergence on the elastic resolution (polarization). More realistic beam divergence models have to be treated numerically and are described later (see Sec. 8.3). The simplified model assumes that the spectrometer components (coil boundaries, samples etc.) can be described by thin planes perpendicular to a nominal beam direction which is assumed to apply equally for the incident and scattered beams. A divergent incident or scattered beam is represented by randomly selecting trajectory polar angles $\Delta\theta_i$ or $\Delta\theta_f$ up to specified maxima $\Delta\theta_i^{max}$ and $\Delta\theta_f^{max}$ respectively where all $\Delta\theta$ are defined with respect to any axis parallel to the nominal beam axis.

$\Delta\theta_i$ is assumed to affect all path lengths before the sample and $\Delta\theta_f$ all path lengths downstream of the sample plane. This situation is illustrated in Figure 16. In such a model, the effect of beam divergence is to increase *all* distances between planes normal to the nominal beam axis by the same factor $1/\cos(\Delta\theta_{i,f})$.

In order to isolate the effect of the beam divergence on the elastic resolution one can consider a symmetrical spectrometer at the echo point with no field inhomogeneities such that $B_1L_1=B_0L_0$, $\langle\varphi_0\rangle=\langle\varphi_1\rangle$ etc. The elastic resolution is still given by Eq. (146), i.e.,

$$P_x^0 = \left\langle \cos\varphi_{NRSE} \right\rangle \quad = \left\langle \cos\left(\varphi_0 - \varphi_1\right) \right\rangle$$

We also assume small divergence which allows one to write $\varphi_0 = \dfrac{2Nm_n\gamma_n B_0 L_0 \lambda_i}{h}$ etc. (see Sec. 5.1). With these assumptions the expression for P_x^0 simplifies to

$$P_x^0 = \left\langle \cos\left(\varphi_0 - \varphi_1\right) \right\rangle = \left\langle \cos\left(\left\langle\varphi_0\right\rangle + \Delta\varphi_0 - \left[\left\langle\varphi_1\right\rangle + \Delta\varphi_1\right]\right) \right\rangle = \left\langle \cos\left(\Delta\varphi_0 - \Delta\varphi_1\right) \right\rangle \qquad (207)$$

For a trajectory in the incident arm of the spectrometer, we have

$$\frac{\Delta\varphi_0}{\left\langle\varphi_0\right\rangle} \approx \frac{\Delta L_0}{L_0} = \left[\frac{1}{\cos\Delta\theta_i} - 1\right] \qquad (208).$$

The distribution of $\Delta\varphi_0$ for random $\Delta\theta$ is *by no means* close to Gaussian or uniform. Because we are assuming small divergences (i.e. $\Delta\theta_i^{max}$ and $\Delta\theta_f^{max}$ are small - certainly within the range of angles encountered in the NRSE), we can write for all incident arm trajectories:

$$\Delta\varphi_0 \approx \left\langle\varphi_0\right\rangle\left(1-\cos\Delta\theta_i\right) \approx \left\langle\varphi_0\right\rangle\frac{\Delta\theta_i^2}{2} \qquad (209)$$

and likewise at the echo point

$$\Delta\varphi_1 \approx \left\langle\varphi_1\right\rangle\left(1-\cos\Delta\theta_f\right) \approx \left\langle\varphi_1\right\rangle\frac{\Delta\theta_f^2}{2} \quad = \left\langle\varphi_0\right\rangle\frac{\Delta\theta_f^2}{2} \qquad (210).$$

(Note $\Delta\varphi_0$ and $\Delta\varphi_1$ are not necessarily small numbers because $\langle\varphi_0\rangle$ can be very large). Therefore, finally

$$P_x^0\Big|_{\Delta B_0=0,\Delta l_\pi=0} \approx \left\langle \cos\left(\frac{\left\langle\varphi_0\right\rangle}{2}\left[\Delta\theta_i^2 - \Delta\theta_f^2\right] \right) \right\rangle \quad \text{(small divergence, at echo point, only angular uncertainties)}$$

(211).

The average in Eq. (211) can be expressed in terms of the double integral over the range of $\Delta\theta_i$ and $\Delta\theta_f$ which are both assumed to be uniform in probability in the range $(0,\Delta\theta_i^{max})$, $(0,\Delta\theta_f^{max})$ permitting the average to be written simply as

$$P_x^0 \approx \frac{\int_0^{\Delta\theta_f^{\max}} \int_0^{\Delta\theta_i^{\max}} \cos\left(\frac{\langle\varphi_0\rangle}{2}\left[\Delta\theta_i^2 - \Delta\theta_f^2\right]\right) d\Delta\theta_i \, d\Delta\theta_f}{\Delta\theta_i^{\max}\Delta\theta_f^{\max}} \qquad (212).$$

It can be shown that Eq. (212) reduces to

$$P_x^0\Big|_{\Delta B_0=0,\Delta l_\pi=0} \approx \frac{\pi}{\langle\varphi_0\rangle} \frac{\left\{C_1\left(\sqrt{\frac{\langle\varphi_0\rangle}{\pi}}\Delta\theta_i^{\max}\right)C_1\left(\sqrt{\frac{\langle\varphi_0\rangle}{\pi}}\Delta\theta_f^{\max}\right) + S_1\left(\sqrt{\frac{\langle\varphi_0\rangle}{\pi}}\Delta\theta_i^{\max}\right)S_1\left(\sqrt{\frac{\langle\varphi_0\rangle}{\pi}}\Delta\theta_f^{\max}\right)\right\}}{\Delta\theta_i^{\max}\Delta\theta_f^{\max}} \qquad (213)$$

where C_1 and S_1 are the Fresnel cosine and sine integrals respectively defined by

$$C_1(x) = \int_0^x \cos\left(\frac{\pi}{2}t^2\right)dt$$
$$S_1(x) = \int_0^x \sin\left(\frac{\pi}{2}t^2\right)dt \qquad (214)$$

and

$$\langle\varphi_0\rangle \approx \varphi_0 = \frac{2Nm_n\gamma_n B_0 L_0 \lambda_i}{h} = 9.26418\times10^4 NB_0[\mathrm{T}]L_0[\mathrm{m}]\lambda_i\left[\mathrm{\AA}\right] \qquad (215).$$

Certain approximations to C_1 and S_1 for simplified programmability have been discussed by Mielenz [16] (note that the $\pi/6$ term in his Eq. 3b should be multiplied by x^3) and Heald [17] or the integrals can be evaluated numerically.

For the particular case of $|\Delta\theta_i^{max}| = |\Delta\theta_f^{max}| = |\Delta\theta_{max}|$, Eq. (213) becomes

$$P_x^0\Big|_{\Delta B_0=0,\Delta l_\pi=0} \approx \frac{\pi}{\langle\varphi_0\rangle} \frac{\left\{C_1^2\left(\sqrt{\frac{\langle\varphi_0\rangle}{\pi}}\Delta\theta_{\max}\right) + S_1^2\left(\sqrt{\frac{\langle\varphi_0\rangle}{\pi}}\Delta\theta_{\max}\right)\right\}}{\Delta\theta_{\max}^2} \qquad (216)$$

or in terms of the instrument parameters:

$$P_x^0\Big|_{\Delta B_0=0,\Delta l_\pi=0} \approx \frac{\pi h\Delta\theta_{\max}^2}{2Nm_n\gamma_n B_0 L_0\lambda_i}\left\{C_1^2\left(\sqrt{\frac{2Nm_n\gamma_n B_0 L_0\lambda_i}{\pi h}}\Delta\theta_{\max}\right)+S_1^2\left(\sqrt{\frac{2Nm_n\gamma_n B_0 L_0\lambda_i}{\pi h}}\Delta\theta_{\max}\right)\right\}$$

(case of $|\Delta\theta_i^{max}| = |\Delta\theta_f^{max}| = |\Delta\theta_{max}|$) (217).

The success of Eq. (213) in describing the relationship between $\Delta\theta_{max}$ and P_x^0 is demonstrated in Figure 21 and Figure 22 for realistic examples with quite large values of $\langle\varphi_0\rangle$ (τ_{NRSE}=15 ns, N=1 and τ_{NRSE}=30ns N=2 respectively) such that the arguments of C_1 and S_1 exceed unity in the plotted range (as evidenced by the values shown on the right hand side y-axes) and with $|\Delta\theta_i^{max}| = |\Delta\theta_f^{max}| = |\Delta\theta_{max}|$ (Eq. (216)) for simplicity.

In the present context it is useful to have P_x^0 as the dependent variable and ask "what is the maximum permissible value of $|\Delta\theta_{max}|$ to achieve a given value of P_x^0?" Unfortunately, because of the complex $\Delta\theta_{max}$ dependence of the right hand side of Eq. (216), inversion of the equation is not tractable. Furthermore, the traditional approximations for C_1 and S_1 discussed in Refs. [16, 17] and others do not lend themselves to neat closed forms either, even for small arguments, since the numerator of Eq. (216) involves large powers of the argument for sufficient accuracy. However, we note that the expansion of $C_1^2(x)+S_1^2(x)$ involves terms in x^{4n+2}, n = 0, 1, 2,…, ∞ with alternating signs for the first few terms. Another function that has the same powers and signs as these first terms would be $x^2\exp(-ax^4)$:

$$x^2\exp\left(-ax^4\right)=\sum_{n=0}^{\infty}\frac{a^n x^{4n+2}}{n!}=x^2-\frac{ax^6}{1!}+\frac{a^2x^{10}}{2!}-\frac{a^3x^{14}}{3!}+\ldots \qquad (218).$$

The expansion of $C_1^2(x)+S_1^2(x)$ for the first few terms is

$$C_1^2\left(x\right)+S_1^2\left(x\right)=x^2-0.21932x^6+0.020616x^{10}-0.0010163x^{14}-7.7553\times10^{-5}x^{18}+ \\ +1.9623\times10^{-5}x^{22}-1.9468\times10^{-6}x^{26}+9.7417\times10^{-8}x^{30}+\ldots \qquad (219),$$

therefore it seems logical to try setting the parameter a in Eq. (218) to the value of the magnitude of second term coefficient in Eq. (219) = $\pi^2/45 \approx 0.21932$ which would make the two leading terms identical in Eqs. (218) and (219). This should certainly work well for $x < 1$ since the higher order terms rapidly become negligible. The resulting terms of Eq. (218) are then

$$x^2 \exp\left(-\frac{\pi^2 x^4}{45}\right) = x^2 - 0.21932x^6 + 0.024051x^{10} - 0.0017583x^{14} + 9.6405\times10^{-5}x^{18} + \\ -4.2287\times10^{-6}x^{22} + 1.5457\times10^{-7}x^{26} - 4.843\times10^{-9}x^{30} + \ldots \quad (220)$$

for which the first four terms are quite similar to those in Eq. (219). It turns out that this approximation can be applied with about 1% accuracy up to $x \sim x_{1\%} \sim 1.15$, where the fan-out of the spins due to the divergence (= $\Delta\varphi_0$ (see Eq. (209)) $\approx \pi x_{1\%}^2/2 \sim 0.7\pi$) is still less than 2π radians, i.e.,

$$C_1^2(x) + S_1^2(x) \approx x^2 \exp\left(-\frac{\pi^2 x^4}{45}\right) \quad , x <\sim 1.15 \qquad (221).$$

In fact the approximation does not deviate above 15% for x up to about 1.8, at which point $\Delta\varphi_0 \approx 1.6\pi$ (as is seen from Figure 21 and Figure 22.

Now identifying x with $\sqrt{\frac{2Nm_n\gamma_n B_0 L_0 \lambda_i}{\pi h}}\Delta\theta_{\max}$, Eq. (217) can be inverted using the approximation in Eq. (221) yielding

$$\Delta\theta_{\max}\big|_{\Delta B_0=0,\Delta l_\pi=0} \approx \sqrt{\frac{h\sqrt{45\ln\left(\frac{1}{P_x^0}\right)}}{2Nm_n\gamma_n B_0 L_0 \lambda_i}} \simeq 8.51\times10^{-3}\sqrt{\frac{\sqrt{\ln\left(\frac{1}{P_x^0}\right)}}{NB_0[\mathrm{T}]L_0[\mathrm{m}]\lambda_i\left[\overset{\circ}{\mathrm{A}}\right]}}[\mathrm{rad}] \qquad (222).$$

$$, |\Delta\theta_{\max}| <\sim 1.15\sqrt{\frac{\pi h}{2Nm_n\gamma_n B_0 L_0 \lambda_i}} = \frac{6.7\times10^{-3}}{\sqrt{NB_0[\mathrm{T}]L_0[\mathrm{m}]\lambda_i\left[\overset{\circ}{\mathrm{A}}\right]}}[\mathrm{rad}]$$

The results of this latter approximation are plotted as the blue curves in Figure 17 and Figure 18.

Although the suggested limits of applicability implied by Eq. (222) (for 1% accuracy of Eq. (221)) are 8.4 mrad and 6.0 mrad for the $N = 1$ and $N = 2$ cases respectively shown in the figures, the approximation works quite well also for larger angles.

In the preceding sections, the relations between the uncertain quantities and the elastic polarization P_x^0 are valid assuming that ΔB_0, Δl_{B0}, or $\Delta\theta$ in isolation is the only uncertain quantity contributing to the resolution function. Because all three parameters will have some uncertainty, their individual tolerances have to be tighter than predicted above to compensate for the depolarization created by the other two. It is difficult to assess which parameter

tolerance is easiest to achieve but some idea of the spectrometer requirements is obtained by setting the ΔB_0, Δl_{B0}, and $\Delta\theta$ contributions to the depolarization approximately equal. For *equal contributions*, we assume that the tolerances will be approximately $1/\sqrt{3}$ times the values given by Eqs. (199), (205), and (222) respectively, i.e.,

$$\Delta B_0^{FWHM} = \frac{h}{m_n \gamma_n} \frac{2\sqrt{\ln 2 \ln\left(\frac{1}{P_x^0}\right)}}{\sqrt{3N} l_{B_0} \lambda_i} \approx \frac{2.08\times10^{-5}\sqrt{\ln\left(\frac{1}{P_x^0}\right)}}{\sqrt{N} l_{B_0}[\mathrm{m}]\lambda_i\left[\mathrm{\AA}\right]} \text{ Tesla} \quad \text{(equal contribs to } P_x^{\,0}\text{)} \qquad (223).$$

Note that ΔB_0 is defined by N, l_{B0}, and λ_i only and is independent of B_0 or zero field region parameters.

$$\Delta l_\pi^{FWHM} = \frac{2h}{m_n \gamma_n} \frac{\sqrt{\ln 2 \ln\left(\frac{1}{P_x^0}\right)}}{\sqrt{3N} B_0 \lambda_i} \approx \frac{2.08\times10^{-5}\sqrt{\ln\left(\frac{1}{P_x^0}\right)}}{\sqrt{N} B_0[\mathrm{T}]\lambda_i\left[\mathrm{\AA}\right]} \text{ meters} \quad \text{(equal contribs to } P_x^{\,0}\text{)} \qquad (224).$$

Note that Δl_π is defined by N, B_0 and λ only and is independent of l_{B0} or zero field region parameters. Finally,

$$\Delta\theta_{\max} \approx \sqrt{\frac{h\sqrt{45\ln\left(\frac{1}{P_x^0}\right)}}{6Nm_n\gamma_n B_0 L_0 \lambda_i}} \simeq 4.91\times10^{-3}\sqrt{\frac{\sqrt{\ln\left(\frac{1}{P_x^0}\right)}}{NB_0[\mathrm{T}]L_0[\mathrm{m}]\lambda_i\left[\mathrm{\AA}\right]}}[\mathrm{rad}] \quad \text{(equal contribs to } P_x^{\,0}\text{)} \qquad (225).$$

$$\text{, for} \quad |\Delta\theta_{\max}| <\sim \frac{6.7\times10^{-3}}{\sqrt{NB_0[\mathrm{T}]L_0[\mathrm{m}]\lambda_i\left[\mathrm{\AA}\right]}}[\mathrm{rad}]$$

Note that $\Delta\theta_{max}$ depends on λ and on both the flipper coil and zero-field parameters (N, B_0, L_0 (i.e., L_{AB}, l_{B0}, and l_g)). Even though these parameters also appear in the expression for τ_{NRSE}, the λ^3-dependence of the latter means that $\Delta\theta_{max}$ is not uniquely defined by the quantity τ_{NRSE} (i.e., the same value of τ_{NRSE} may require different values of $\Delta\theta_{max}$ depending on the values of N, B_0, L_0 and λ).

6.1.5 Some examples (equal contributions to depolarization)

Consider requiring the elastic (resolution) polarization $P_x^{\,0}$ to be greater than some specified minimum value at a reference point with equal contributions coming from ΔB_0, Δl_{B0}, and $\Delta\theta_{max}$. We consider the point $\tau_{NRSE} \approx 30$ ns at

8 Å with $N = 2$, for $M = 8\ \pi$ coils, with $B_0 = 0.0393$ T, $L_0 = 2$ m. Using Eqs. (223), (224), and (225), several results are shown in Table 7.

Table 7. Parameter tolerances required to achieve a specified minimum elastic (resolution) polarization P_x^0 for τ_{NRSE} = 30 ns at 8 Å with the above spectrometer dimensions (B_0=0.0393 T) with approximately equal contributions to the depolarization coming from ΔB_0, Δl_{B0}, and $\Delta\theta_{max}$. The final column puts $\Delta\theta_{max}$ in the context of the critical angle of natural Ni at the same wavelength.

For P_x^0 >	ΔB_0 (FWHM)[μT] <	Δl_{B0} (FWHM)[μm] <	$\Delta\theta_{max}$ [mrad] <	$\Delta\theta_{max}/\theta_c$(8Å, nat. Ni) %
0.1	93	71	5.4	39.0
0.2	78	59	4.9	35.6
0.3	67	51	4.6	33.1
0.4	59	45	4.3	31.0
0.5	51	39	4.0	28.9
0.6	44	33	3.7	26.7
0.7	37	28	3.4	24.4
0.8	29	22	3.0	21.7
0.9	20	15	2.5	18.0
0.95	14	11	2.1	15.1
0.99	6	5	1.4	10.0

The results in Table 7 are summarized in Figure 19. Note the particular sensitivity of the instrumental resolution on the beam divergence once a certain threshold angle is reached.

7 NIST NRSE PROJECT GOALS

7.1 Desired function

The most desirable criteria for a NIST NRSE instrument are summarized as follows:

1. Emphasis on quasi-elastic scattering – coil tilting is not necessary.
2. Large solid angle coverage and multi-angle measurement capability.
3. If possible, the spectrometer should be able to access Fourier times of τ_{NRSE} = 30 ns at λ = 8Å and be fabricated with sufficient precision to allow useful measurements to be performed at this measurement point.
4. Offer usable incident wavelengths at least down to 3 Å for high-*Q* capability.
5. Must have a short Fourier time measurement capability.

7.2 Spectrometer dimensions and field magnitudes required to access τ_{NRSE} = 30 ns at λ = 8 Å

From Eq. (153) we have

$$\tau_{NRSE}\left[\mathrm{ns}\right] = 0.37271\, N\, B_0\left[\mathrm{T}\right] L_0\left[\mathrm{m}\right] \lambda_i \left[\mathring{\mathrm{A}}\right]^3,$$

where we assume that $B_0 = B_1$ so that $L_0 = L_1$ at the QENS echo point. In order to access τ_{NRSE} = 30 ns at λ = 8 Å, we must satisfy the condition

$$N\left(B_0\left[\mathrm{T}\right] L_0\left[\mathrm{m}\right]\right)_{max} \geq 0.157 \qquad \text{criterion for accessing } \tau_{NRSE} = 30 \text{ ns at } \lambda = 8 \text{ Å} \qquad (226)$$

where $(B_0L_0)_{max}$ implies the maximum attainable value of the product B_0L_0. If we chose N=2 as the most likely bootstrap factor, noting the advantages of even N and the disadvantages of N being too large as outlined in Sec. 3.4, this condition amounts to fulfilling:

$$\left(B_0\left[\mathrm{T}\right] L_0\left[\mathrm{m}\right]\right)_{\max} \geq 0.079\ \mathrm{Tm} \qquad \text{criterion for accessing } \tau_{NRSE} = 30 \text{ ns at } \lambda = 8\text{Å with } N = 2 \qquad (227).$$

Obvious limitations on the maximum value of B_0 are imposed by the maximum current × winding density of the static field coils. This depends on the length, cross-section, material, temperature of the windings, and the ability to

remove heat. Increasing the zero-field drift path lengths linearly increases the maximum achievable value of τ_{NRSE}, however the major disadvantages are the consequent rapid reduction in solid angle ($\propto 1/L^2$) and possibly limitations imposed by available space. Owing to these constraints and the linear dependence of τ_{NRSE} on B_0, it seems reasonable to attempt to maximize the static field B_0 as far as possible. Evaluating B_0 and L_0 for τ_{NRSE} =30 ns at $\lambda_i = \langle\lambda_i\rangle$ = 8Å, we have, for example,

$B_0 \approx 0.08$ T, $L_0 = 1$ m, $N = 2$

$B_0 \approx 0.04$ T, $L_0 = 2$ m, $N = 2$.

The largest static fields produced to date in water-cooled NRSE coils using pure aluminum windings are about $B_0 \approx$ 0.025 T. In this case we would need $L_0 = 3.14$ m for $N = 2$ (which appears too long for our available floor space) or else $L_0 = 1.57$ m for N=4. Apart from the increased restrictions on the maximum incoming bandwidth $\Delta\lambda/\lambda$ when using $N = 4$, doubling the number of π-flipper coils has the obvious disadvantage of greatly increasing the complexity and setup of the spectrometer and this option is very unattractive for a multi-angle instrument.

Confining ourselves to $N = 2$ and a maximum L_0 of 2 m, pursuing the goal of increasing B_0 towards 0.04 T presents itself as one of the more attractive options. The consequences of attempting to reach this field magnitude are explored in the following sections.

7.3 Bootstrap NRSE coil components and specifications

7.3.1 General description

The N=2 bootstrap NRSE coil, a most recent example of which is shown in Figure 20, is composed of back-to-back static field coils with equal but oppositely-opposed field directions. Each static field coil encloses an r.f. coil (whose coil axis is perpendicular to that of the static coil). The r.f. coil must be placed inside the static field coil in order to avoid significant r.f. attenuation in the metallic structures of an enclosed static field coil. μ-metal plates capping each end of the static field coils conduct magnetic flux between the two coils. An outer μ-metal shield enclosing the entire assembly apart from the beam windows helps reduce the magnitude of stray fields entering the zero field regions. For quasi-elastic applications, both the static and the r.f. coil axes are perpendicular to the beam direction. To profit from the advantages of the NRSE technique over conventional NSE, the NRSE coils must be moderately compact in the beam direction. Because the beam traverses both the static and the r.f. coil windings,

there are particular restrictions on the winding materials that may be used in the beam area (see Sec. 7.3.2). High resolution requirements also impose restrictions on the shape of the windings themselves. These and other factors will be discussed in the following sections.

7.3.2 Aluminum windings: transmission and small angle scattering

Because the beam must traverse both the static field coil and the r.f. coil windings, the neutronic properties of copper exclude it as a winding material for the beam region. For non-superconducting windings, the most obvious choice is aluminum. However, even pure aluminum has nearly 60 % greater resistivity at room temperature than pure copper.

For a 4-N = 2 coil NRSE instrument, the beam must traverse a total of 16N = 32 layers of static and r.f. coil windings. Assuming that each winding layer has the same thickness, t, we can estimate the anticipated maximum transmission of all the coils from the total scattering cross-section of pure aluminum at room temperature. Some results for different winding thicknesses t are shown in Figure 21. Note that the values in Figure 21 are optimistic because (i) impurities (e.g. from anodization of the actual winding material) are not accounted for and (ii) the transmission especially above 4.7 Å will be reduced if the operational winding temperature exceeds 300 K (which it is likely to do significantly).

Very crudely, ignoring Bragg peak structure at wavelengths below about 4.7 Å, we can assume the macroscopic neutron cross-section of Al at all temperatures of interest is about 0.11 cm^{-1} for $\lambda < 4.7$Å. Therefore, we have

$$T_{Al} \sim \exp\left(-0.11\, t\left[\mathrm{cm}\right]\right) \qquad , \lambda < 4.7\,\mathrm{\mathring{A}} \tag{228}$$

Calculating the equilibrium temperature and temperature gradients of the windings is complicated and depends on the detailed coil design. In order to partially compensate for elevated winding temperatures at high-field operation of the coils (and perhaps to some extent the decreased transmission due to the anodization), we approximate the macroscopic cross-section for $\lambda > 4.7$Å using the average of available data for pure aluminum [18] at T = 300 K and at T = 800 K in the hope that this provides a conservative estimate. For the 300 K data we have approximately

$$\Sigma_{Al}\left(300\mathrm{K}\right)\left[\mathrm{cm}^{-1}\right] \approx \left(6.4 + 8.94\lambda\left[\mathrm{\mathring{A}}\right]\right)\times 10^{-3} \qquad , \lambda \geq 4.7\,\mathrm{\mathring{A}} \tag{229}$$

and for the 800 K data we have approximately

$$\Sigma_{Al}\left(800\mathrm{K}\right)\left[\mathrm{cm}^{-1}\right]\approx\left(1.91+1.175\lambda\left[\mathring{\mathrm{A}}\right]\right)\times10^{-2}\qquad,\lambda\geq4.7\,\mathring{\mathrm{A}}\qquad(230).$$

Therefore, we use an effective aluminum macroscopic cross-section of

$$\Sigma_{Al}^{eff}\left[\mathrm{cm}^{-1}\right]\approx\left(1.28+1.03\lambda\left[\mathring{\mathrm{A}}\right]\right)\times10^{-2}\qquad,\lambda\geq4.7\,\mathring{\mathrm{A}}\qquad(231)$$

for the purposes of estimating the coil transmission.

In order to estimate maximum tolerable thicknesses for the coil windings in the beam direction from the neutron transmission perspective, we assume that the static field coil windings (which usually have to carry higher maximum currents than the r.f. windings) have thickness t and the r.f. windings have thickness $t/2$, such that the total thickness of windings traversed by the beam in the spectrometer is $12Nt = 24t$ for $N = 2$. If we choose a transmission criterion such that $T_{Al}(\lambda = 8\ \text{Å}) >\sim 80\%$, then, using Σ_{Al}^{eff} in Eq.(231), we require that t must not exceed a maximum value, t_{max}, of about 1.0 mm (i.e., the static field coil windings have thickness of about 1 mm, the r.f. windings have thickness of about 0.5 mm). For the *r.f. coils* the skin effect at ~1 MHz frequencies may restrict the r.f. winding thickness to smaller values (see Sec. 7.3.4.7).

In coils constructed by the Institut Laue-Langevin (ILL), Grenoble, France, Laboratoire Léon Brillouin (LLB), Saclay, France, and the Forschungs-Reaktor München-II (FRM-II), Munich, Germany, 0.4 mm thick anodized aluminum band has been used for the windings with an anodization depth of about 3μm for insulation. However the anodization layer has incorporated water which gives rise to strong small angle scattering that may be anisotropic. This small angle scattering can be greatly reduced by boiling the wire in D_2O under pressure at about 200 °C [11].

7.3.3 Static field coils

An early static field coil using circular section Al wire developed for the Zeta spectrometer at the ILL, Grenoble, is shown in Figure 22.

7.3.3.1 Current in the static field coil

Sufficient static field homogeneity over the beam area may be achieved by passing the beam through a restricted area near the axial center of a long solenoid. The field at the center of a long solenoid is

$$B=\mu_0 nI\qquad(232)$$

where μ_0 is the permeability of free space with $\mu_0 = 4\pi\times10^{-7}$ NA^{-2}. In SI units we have

$$B_0\left[\mathrm{T}\right] \approx 4\pi\times10^{-7}\, n\left[\mathrm{m}^{-1}\right] I\left[\mathrm{A}\right] \simeq 1.26\times10^{-6}\, n\left[\mathrm{m}^{-1}\right] I\left[\mathrm{A}\right] \quad \text{long solenoid approximation (233),}$$

where B_0 is the static field in Tesla, n is the winding density in m^{-1}, I is the current in Amps. Equivalently, the current in the coil at field B_0 is

$$I\left[\mathrm{A}\right] = \frac{2.5\times10^{6}}{\pi}\frac{B_0\left[\mathrm{T}\right]}{n\left[\mathrm{m}^{-1}\right]} \approx 8\times10^{5}\frac{B_0\left[\mathrm{T}\right]}{n\left[\mathrm{m}^{-1}\right]} \qquad (234).$$

Thus the required current is inversely proportional to the winding density and is directly proportional to the required field B_0.

7.3.3.2 Resistance of the static field coil windings

The resistance of the static field coil winding is

$$R = \frac{\rho(T) l_w}{A_w} \qquad (235)$$

where l_w is the total length of the coil winding, A_w is the cross-sectional area of the winding wire and $\rho(T)$ is the resistivity of the winding at its operating temperature T. The winding length per turn (see Figure 23) for the rectangular cross-section coil is approximately $2(a+ l_{B0})$ assuming the winding thickness is negligible compared with a and l_{B0}. For the particular case of single layer windings, the total number of turns, N_{B0}, is

$$N_{B_0} = l_{axial}\, n \qquad \text{any single layer winding} \qquad (236)$$

so that the total length of any single layer winding around the rectangular coil form shown in Figure 15 is

$$l_w \approx 2N_{B_0}\left(a + l_{B_0}\right) = 2l_{axial} n\left(a + l_{B_0}\right) \qquad (237).$$

The outer surface area of the rectangular coil form is

$$A_{surf} = 2l_{axial}\left(a + l_{B_0}\right) \qquad (238),$$

so Eq. (237) can be rewritten as

$$l_w = A_{surf}\, n \qquad \text{any thin single layer winding around rectangular coil form} \qquad (239).$$

7.3.3.2.1 Resistance of single layer rectangular cross-section windings

For *rectangular* cross-section section windings (Figure 23) the cross-sectional area A_w is given by

$$A_w = th \qquad \text{rectangular cross-section windings width } h\text{, thickness } t \qquad (240)$$

so that, using Eqs. (239) and (240), and noting that for a single winding $h \le 1/n$ with the equality representing the tightly wound limit Eq. (235) becomes

$$R = \frac{\rho(T)\, n A_{surf}}{th} \quad \ge \frac{\rho(T)\, n^2 A_{surf}}{t} \quad \text{any rectangular cross-section, single layer winding} \quad (241)$$

with

$$R = \frac{\rho(T)\, n^2 A_{surf}}{t} \qquad \textit{tightly-wound} \text{ rectangular windings thickness } t \qquad (242),$$

representing the tightly-wound limit of $h=1/n$. Thus, for a given A_{surf}, the resistance of the *tightly-wound* coil increases as the *square* of the winding density and is inversely proportional to the winding thickness t. Logically the resistance is always *minimized* for a given n, A_{surf}, t, by ensuring that the windings are tightly wound since this maximizes A_w for a given l_w.

7.3.3.2.2 Resistance of single layer circular cross-section windings

For *circular* cross-section section windings, the cross-sectional area of the winding, A_w, is

$$A_w = \pi r_w^2 \qquad \text{circular cross-section windings of radius } r_w \qquad (243)$$

so that using Eq. (239) again and noting that for a single-layer circular winding we have the constraint $n \le 2r_w$ with the equality representing the tightly-wound case, Eq. (235) becomes

$$R = \frac{\rho(T)\, n A_{surf}}{\pi r_w^2} \quad \ge \frac{4\rho(T)\, n^3 A_{surf}}{\pi} \quad \text{any circular cross-section winding, radius } r_w \quad (244)$$

with

$$R = \frac{4\rho(T)\, n^3 A_{surf}}{\pi} \quad \textit{tightly-wound} \text{ circular windings, radius } r_w \quad (245)$$

representing the tightly-wound limit. Thus, for a given A_{surf}, the *tight-winding* resistance increases as the *cube* of n (as opposed to n^2 in the tightly-would *rectangular* winding case where it is assumed that t is kept fixed).

7.3.3.3 Voltage for static field coil

7.3.3.3.1 Voltage for single layer rectangular cross-section windings

The D.C. voltage required to maintain the static field B_0 in the general rectangular winding case is (from Eqs. (234) and (241)), and noting that for a single winding $h \le 1/n$ with the equality representing the tightly wound limit

$$V = IR \quad = \frac{2.5\times10^{6}}{\pi}\frac{\rho(T)[\Omega\mathrm{m}]A_{surf}\left[\mathrm{m}^{2}\right]}{t[\mathrm{m}]h[\mathrm{m}]}B_0[\mathrm{T}]$$
$$\ge \frac{2.5\times10^{6}}{\pi}\frac{\rho(T)[\Omega\mathrm{m}]n\left[\mathrm{m}^{-1}\right]A_{surf}\left[\mathrm{m}^{2}\right]}{t[\mathrm{m}]}B_0[\mathrm{T}] \quad \text{single rectangular winding, width } h\text{, thickness } t \qquad (246)$$

with

$$V[\mathrm{V}] = \frac{2.5\times10^{6}}{\pi}\frac{\rho(T)[\Omega\mathrm{m}]n\left[\mathrm{m}^{-1}\right]A_{surf}\left[\mathrm{m}^{2}\right]}{t[\mathrm{m}]}B_0[\mathrm{T}] \quad \text{tightly-wound rectang windings, thickness } t \quad (247)$$

representing the tightly-wound limit. Thus, the voltage required to maintain a field B_0 for the tightly-wound case increases proportional to $B_{0,}$ proportional to the winding density, and inversely proportional to the winding thickness in the beam direction for a given coil surface area. We see that the voltage is *minimized* for a given B_0 by tightly winding the coil within the available surface area.

7.3.3.3.2 Voltage for single layer circular cross-section windings

The D.C. voltage required to maintain the static field B_0 in the general circular winding case is (from Eqs. (234) and (244))

$$V[\mathrm{V}] = 2.5\times10^{-6}\frac{\rho(T)[\Omega\mathrm{m}]A_{surf}\left[\mathrm{m}^{2}\right]}{\left(\pi r_w[\mathrm{m}]\right)^{2}}B_0[\mathrm{T}] \quad \text{any single circular winding, radius } r_w \quad (248).$$

The D.C. voltage required to maintain the static field B_0 in the *tightly-wound* circular winding case is (from Eqs. (234) and (245))

$$V[\mathrm{V}] = \frac{10^{7}}{\pi^{2}}\rho(T)[\Omega\mathrm{m}]\left(n\left[\mathrm{m}^{-1}\right]\right)^{2}A_{surf}\left[\mathrm{m}^{2}\right]B_0[\mathrm{T}]$$
$$= 2.5\times10^{-6}\frac{\rho(T)[\Omega\mathrm{m}]A_{surf}\left[\mathrm{m}^{2}\right]}{\left(\pi r_w[\mathrm{m}]\right)^{2}}B_0[\mathrm{T}] \quad \text{tightly-wound, circular windings} \quad (249).$$

Thus the voltage required to achieve a given B_0 in the circular wire case is independent of the winding density other than n cannot exceed a value of $1/(2r_w)$ for a single layer. Qualitatively, this is because decreasing n decreases R at the same rate that I (see Eq. (234)) must increase to maintain B_0.

7.3.3.4 Power dissipated in the static field coil

7.3.3.4.1 Power dissipated in single layer rectangular cross-section windings

The power dissipated in the coil with single layer, rectangular windings in the general case is (from Eqs. (234) and (241) or (246))

$$P[\mathrm{W}] = \left(I[\mathrm{A}]\right)^2 R[\Omega]$$

$$\approx \frac{6.25\times10^{12}}{\pi^2}\frac{\rho(T)[\Omega\mathrm{m}]A_{surf}\left[\mathrm{m}^2\right]}{n\left[\mathrm{m}^{-1}\right]t[\mathrm{m}]h[\mathrm{m}]}\left(B_0[\mathrm{T}]\right)^2$$ any single rectangular winding, width h, thickness t (250).

The power dissipated in the coil in the tightly-wound, rectangular winding case is (from Eqs. (234) and (242), or (247)) is

$$P[\mathrm{W}] \approx \frac{6.25\times10^{12}}{\pi^2}\frac{\rho(T)[\Omega\mathrm{m}]A_{surf}\left[\mathrm{m}^2\right]}{t[\mathrm{m}]}\left(B_0[\mathrm{T}]\right)^2$$ *tightly-wound* rectangular windings thickness t (251).

Thus, for a given A_{surf}, the power dissipated in the tightly-wound coil increases inversely proportionally to the winding thickness t and is independent of n or h (essentially a current sheet). We also note that the power increases as the square of the required field B_0. As was the case for the voltage, we note that for a single winding $h \leq 1/n$ with the equality representing the tight-winding limit; therefore by comparing the general case (Eq. (250)) with the tight winding case (Eq. (251)), we see that the power dissipated is *minimized* for a given B_0 by tightly winding the coil within the available surface area of the coil form.

7.3.3.4.2 Power dissipated in single layer circular cross-section windings

The power dissipated in the coil with single layer, circular windings in the general case is (from Eqs. (234) and (244) or (248))

$$P[\mathrm{W}] \approx \frac{6.25\times10^{12}}{\pi^3}\frac{\rho(T)[\Omega\mathrm{m}]A_{surf}\left[\mathrm{m}^2\right]}{n\left[\mathrm{m}^{-1}\right]\left(r_w[\mathrm{m}]\right)^2}\left(B_0[\mathrm{T}]\right)^2$$

$$\geq \frac{1.25\times10^{13}}{\pi^3}\frac{\rho(T)[\Omega\mathrm{m}]A_{surf}\left[\mathrm{m}^2\right]}{r_w[\mathrm{m}]}\left(B_0[\mathrm{T}]\right)^2 \quad \text{any single circular winding, radius } r_w \text{ (252).}$$

where the equality represents the tightly-wound case with $n=1/(2r_w)$ (from Eqs. (234) and (245), or (249)):

$$P[\mathrm{W}] \approx \frac{1.25\times10^{13}}{\pi^3}\frac{\rho(T)[\Omega\mathrm{m}]A_{surf}\left[\mathrm{m}^2\right]}{r_w[\mathrm{m}]}\left(B_0[\mathrm{T}]\right)^2 \quad \textit{tightly-wound} \text{ circular windings of radius } r_w \qquad (253)$$

.

Therefore, the tightly-wound coil represents the *minimum* power condition for circular wire. Furthermore, the circular wire should be as thick as is tolerable to minimize the power.

7.3.3.5 Summary and static field coil power concerns

As we saw in Sec. 6.1.2, we are likely to be dealing with *rectangular* cross-section wires for the static field coils. Two primary concerns arise if: (i) excessive current must be supplied to the coil and/or (ii) there is excessive heat dissipation in the coil. Item (i) can be addressed by choosing a value of n that is sufficiently high that reaching the current for the required maximum value of B_0 is not an issue. The first step to addressing item (ii) is to tightly wind the coil because this minimizes the power dissipation as heat for rectangular windings, as shown in Sec. 7.3.3.4.1. After that, the problem becomes quite constrained. Equation (251) identifies these constraints: Firstly, A_{surf} cannot be too small because the coil has to be sufficiently large to ensure adequate field homogeneity within the beam area. At high τ_{NRSE}, the field homogeneity requirement is quite strict (see e.g. Sec. 6.1.1 and Sec. 6.1.6). Secondly, the winding thickness in the beam direction, t, must remain sufficiently small to ensure good neutron transmission (see Sec. 7.3.2), and thirdly the resistivity is constrained by the limited choices of winding material that can be used in the beam area and the temperature at which the windings can be maintained. Although the required maximum fields of a few 10s of mT do not appear dauntingly high, heat production from the coil is potentially quite large. This is illustrated in the following examples:

The coils produced for the neutron centers LLB, ILL, FRM-II, and Hahn-Meitner Institut (HMI), Berlin use tightly-wound 4 mm wide × 0.4 mm thick anodized aluminum band supplied by Wesselmann Umwelttechnik[5], with $n \approx 250$ m^{-1}, $l_{axial} \approx 0.2$ m, $a + l_{B0} \approx 0.25$ m for a beam size of about 2.5 cm × 2.5 cm, so that A_{surf} (see Eq. (238)) ≈ 0.1 m^2. For these coils at maximum field ($B_0 \approx 0.025$ T), we have (from Eq. (234)) $I \approx 80$ A. For pure Al down to about liquid nitrogen temperature, we have

$$\rho_{Al}(T)[\Omega\mathrm{m}] \approx 1.14\times10^{-10} T(\mathrm{K}) - 6.9\times10^{-9} \qquad (254).$$

Therefore, specifically for aluminum, we have (from Eq. (251))

$$P_{Al}[\mathrm{W}] \approx \left(B_0[\mathrm{T}]\right)^2 \frac{A_{surf}\left[\mathrm{m}^2\right]}{t[\mathrm{m}]}\left(72.2T(\mathrm{K}) - 4.37\times10^3\right) \text{ tightly-wound rectangular windings} \quad (255).$$

For $T \approx 300$ K we have $P_{Al}(0.025\ \mathrm{T}) \approx 2.7$ kW. For $T \approx 350$ K, we have $P_{Al}(0.025\ \mathrm{T}) \approx 3.3$ kW. Note that if the coils could be cooled to liquid nitrogen temperature ≈ 80 K, P_{Al} is more than an order of magnitude smaller (≈ 220 W).

If the same coils were used to achieve 0.04 Tesla, we would have $I \approx 128$A (which is likely excessive), with a room-temperature power dissipation of approximately $(0.04^2/0.025^2) \times 2.7$ kW ≈ 6.9 kW. This is challenging because we cannot allow neutron-absorbing coolants to traverse the beam area. Furthermore, the equilibrium winding temperatures are likely to significantly exceed room temperature with associated temperature gradients.

7.3.3.6 Required static field coil current stability

The values in Table 7 imply that $\Delta B_0/B_0$ must be around 0.1% in order to achieve P_x^0(8 Å, 30 ns) ≥ 0.5 for typical spectrometer dimensions. Even if the static field coil were to produce perfect field homogeneity ($\Delta B_0 = 0$), we would nonetheless have to impose a coil current stability of the order of 0.1 % (i.e., $\Delta I/I <\sim 10^{-3}$). However, we certainly do not wish to have the current stability come close to being the limiting factor on ΔB_0. Preferably the current stability should be at least an order of magnitude better (i.e., $\Delta I/I < 10^{-4}$). Furthermore, long term current drift (e.g. in response to temperature changes) should also be in this range. Current supplies offering stabilities in the 10^{-5} range are commercially-available, so we do not anticipate this being a major problem.

[5] Certain commercial equipment, instruments, or materials are identified in this paper to foster understanding. Such identification does not imply recommendation or endorsement by the National Institute of Standards and Technology, nor does it imply that the materials or equipment identified are necessarily the best available for the purpose.

7.3.3.7 Effect of coil dimensions on field homogeneity and field magnitude

From geometrical, field homogeneity, field strength, and winding resistance points of view, it is preferable that the static field coils be short in the beam direction, given that the coil width must to be somewhat wider than the beam width. Reducing the coil thickness in the beam direction tends to allow the perpendicular axial length of the coil to be reduced without loss in field homogeneity within the beam area. This principle is illustrated by considering the axial field of a *cylindrical open-ended* solenoid (see Figure 24), where instead of the coil thickness in the beam direction we refer to the coil radius. The field at axial position x is

$$B = \frac{\mu_0 nI}{2}\left(\cos\alpha - \cos\beta\right) = \frac{\mu_0 nI}{2}\left[\frac{l_{axial}/2 - x}{\sqrt{\left(r^2 + \left(l_{axial}/2 - x\right)^2\right)}} + \frac{l_{axial}/2 + x}{\sqrt{\left(r^2 + \left(l_{axial}/2 + x\right)^2\right)}}\right] \quad (256).$$

This can be re-expressed in terms of the dimensionless quantities

$$\mu = \frac{2x}{l_{axial}} \quad (257)$$

which is the axial distance from the solenoid center expressed as a fraction of the half-length of the solenoid and

$$\eta = \frac{2r}{l_{axial}} \quad (258)$$

which is the ratio of the diameter, d, of the coil to its axial length, so that

$$\frac{B}{\mu_0 nI} = \frac{1}{2}\left[\frac{1-\mu}{\sqrt{\left(\eta^2 + \left(1-\mu\right)^2\right)}} + \frac{1+\mu}{\sqrt{\left(\eta^2 + \left(1+\mu\right)^2\right)}}\right] \quad (259).$$

In the "long" solenoid limit ($l_{axial} \gg r$), the field at the coil center is maximized ($=\mu_0 nI$), whereas at its ends it is half this value ($=\mu_0 nI/2$ – limit of Eq. (259) with $\mu = 1$ and $\eta^2 \ll (1+\mu)^2$). This fact alone shows that the axial length of the coil must be substantially greater than the height of the neutron beam. Figure 24 shows the variation of the axial field normalized to the maximum attainable field ($=\mu_0 nI$) for solenoids with various ratios $\eta = d/l_{axial}$, calculated using Eq. (256). Figure 25 reveals that as η increases:

(i) The axial range over which the field can be held close to $B(x = 0)$ decreases.

(ii) The maximum achievable field (at the center) decreases. This reduction becomes quite significant once η increases above about 0.4.

This latter consideration is particularly important in the present application where the goal of achieving the highest fields is already hampered by high current magnitudes and where field reduction due to oversized coils should be avoided wherever possible. Usually, detailed field calculations are required to optimize details of the coil windings and coil dimensions.

Using the crude example of the cylindrical solenoid above, suppose we wish the maximum axial length of the static field coil to be 0.3 m, the beam height is 0.03 m, and the required $\Delta B_0/B_0$ is about 0.1%. With reference to Figure 25, this means that $B_0(\mu = 0.1) \geq 0.999 B_0(\mu = 0)$. This occurs for η <~ 0.045, i.e., for coil diameters of 0.0135 m or less. Although this example just considers the axial field variation for a cylindrical solenoid, it suggests that careful control of the coil dimensions perpendicular to the coil axis may be required to achieve sufficient field homogeneity over the beam area in the NRSE coils. Of course, detailed field calculations are required for the approximately rectangular cross-section NRSE coils to establish what is acceptable.

7.3.3.8 Coil flatness issues

As demonstrated in Sec. 6.1, the dimensional tolerances on the coils to achieve high resolution are demanding. This means that the winding support must be accurately machined and the windings themselves must be very flat. The use of anodized pure aluminum band not only helps to create a geometrically well-defined field region but also eliminates the curved field lines that can be generated in the vicinity of circular cross-section wires. This has been discussed by Dubbers *et al.* [19]. The existence of a magnetic pressure (see Sec. 7.3.3.10) is also of concern for maintaining the shape of the windings. Usually this requires some kind of clamping of the windings at high fields outside of the areas that are traversed by the beam.

7.3.3.9 Winding methods

Coil winding machines exist commercially, however, good experience has been obtained using machinist's lathes. These machines offer the desirable combination of precise translational and rotational speeds, and adjustable torque settings.

7.3.3.10 Magnetic pressure on the coil windings and their mechanical constraint

Magnetic pressure in a coil refers to the radial force exerted on the coil windings due to the difference in magnetic flux density inside the coil compared with that outside the coil. The magnetic pressure, P_{mag}, exerted on the windings at the center of a long circular solenoid is

$$P_{mag} = \frac{B^2}{2\mu_0} \tag{260}$$

from which we have

$$P_{mag}\left[\mathrm{Nm^{-2}}\right] = \frac{\left(B[\mathrm{T}]\right)^2}{8\pi\times10^{-7}} \approx 4\times10^5\left(B[\mathrm{T}]\right)^2 \tag{261}.$$

For B = 0.04 T, $P_{mag} \approx 637\ \mathrm{Nm^{-2}}$ (≈ 0.0063 Atm).

For the approximately rectangular section coils used in NRSE, Ampere's law predicts that the magnitude of the field inside the coil is similar to that of a cylindrical coil carrying the same current, assuming that the field outside the coil is negligible with respect to the field inside the coil. Therefore, we assume that the magnetic pressure is also given by Eq. (261) near the center of a long rectangular section coil.

For a coil wound on a rectangular former with slight pre-tension, we can approximate the action of the magnetic pressure on the band-like windings by the mechanical problem of an evenly-loaded beam whose ends are constrained. According to Ref. [20], the maximum deflection of the winding at the center is

$$y_{\max} = \frac{w l_u^4}{384 E I} \tag{262},$$

where w is the load per unit length of the beam, l_u is the unconstrained length of the beam, E is Young's modulus for the winding material, and I is the moment of inertia. For the band-like (rectangular) windings of width h and (small) thickness t, the moment of inertia is

$$I = \frac{ht^3}{12} \tag{263}$$

The load per unit length is

$$w = P_{mag} h \tag{264}$$

so that Eq. (262) can be re-expressed as

$$y_{\max} = \frac{P_{mag} l_u^4}{32 E t^3} \tag{265}$$

i.e.,

$$y_{\max}\left[\mathrm{m}\right] \approx 1.25\times10^{4} \frac{\left(B\left[\mathrm{T}\right]\right)^2 l_u\left[\mathrm{m}\right]^4}{E\left[\mathrm{Nm^{-2}}\right] t\left[\mathrm{m}\right]^3} \tag{266}.$$

For pure Al windings ($E = 7.1\times10^{10}$ Nm^{-2}) with $t = 0.4$ mm (as used in existing coils), $B = 0.04$ T, and a typical l_u for the coil face traversed by the beam of about 0.25 m, we have $y_{max} \approx 17$ mm. This is clearly unacceptably large, therefore in order to maintain the coil dimensions within required tolerances, the windings must be clamped for high fields.

Note that Eq. (265) contains the unconstrained length of the winding to the 4th power, therefore it is often feasible for the clamping plates to incorporate an open window that allows passage of the beam (see for example Figure 12). For example, if this window is 0.03 m wide, then $l_u \approx 0.03$ m and Eq. (265) yields $y_{max} \approx 3.5$ μm, which is well within the acceptable range (see for example Table 7).

7.3.4 r.f. coils

7.3.4.1 Brief description of existing r.f. coil designs

The r.f. coils, two examples of which are shown in Figure 26, are of similar general design with the beam passing through the (gray) aluminum windings at the coil center. The fields are returned through the two arch-shaped coils which greatly reduce r.f. power loss via induced currents in (and consequent heating of) surrounding metallic structures, including the static field coils. This also prevents significant perturbations to the static field. The coils outside of the beam area are wound with high-frequency (very thin stranded) copper wire to maximize electrical conductivity. The electrically-insulating return coil former material, used by our European colleagues, is similar to the fiberglass/epoxy composite used in printed circuit boards. The method used at the ILL for maintaining tension on the aluminum windings is to stretch the windings over silicon-based rubber o-rings covered with Kapton tape (rubber containing carbon has been found to burn).

7.3.4.2 r.f. circuit and impedance matching

The NRSE spectrometer operates at a single frequency for each scan point (or τ_{NRSE}). Typically, an NRSE scan might consist of 10 or 20 points and therefore 10 or 20 different r.f. frequencies. Thus, even though the drive circuit is "narrow" band for each measurement point, it must be tunable through more than a decade of r.f. frequencies.

In this application at high frequencies, it is important to match the characteristic impedances of the transmission line with that of the load to prevent reflections of r.f. power from the load toward the source. Reactive elements in a circuit (inductance and capacitance) store and return energy to the source unless the circuit appears purely resistive (i.e., the voltage and the current are in phase). This is the condition for impedance matching. Equivalently-stated, the power factor (= $\cos\theta$), where θ is the phase angle between the current and the voltage must ideally equal 1. Alternatively stated, the net capacitative reactance of the circuit cancels the net inductive reactance. Impedance matching not only maximizes the efficiency of the circuit, but also prevents distortion of the r.f. signal caused by reflected, delayed signals. A lossless coaxial cable may be considered as an inductance in parallel with a capacitance as shown in Figure 27. By lossless, we mean a perfectly insulating coaxial dielectric with negligible wire resistance. In this case, the characteristic impedance, Z_0, of an *impedance-matched* cable at *any* frequency appears purely resistive with magnitude

$$Z_0 = \sqrt{\frac{L_{cable}}{C_{cable}}} = \sqrt{\frac{L'}{C'}} \qquad (267),$$

where L' and C' are the characteristic inductance and capacitance per unit length of cable if the cable is uniform. Typically, for coaxial r.f. cables, Z_0 is 50 Ω by design. The task is then to match the impedance of the rest of the circuit (including the r.f. coil) to emulate a resistive value of magnitude Z_0. Consider the r.f. filter circuit shown in Figure 27. The power supply acts like a current source and the choke protects the source by giving it a high output impedance at high frequency. The r.f. coil can be considered as the combination of the inductance and the series resistance, *R*. The parallel tunable capacitance C_2 allows maximization of the power factor by canceling the inductive reactance of the r.f. coil (which increases proportional to the frequency). In other words, the tunable capacitance C_2 is necessary to maintain the imaginary part of the impedance of the circuit at zero, because the capacitance C_1 must also change with frequency to maintain the *real* part of the circuit impedance at the value Z_0 (the impedance would otherwise decrease with increasing frequency causing signal reflection back towards the source and most of the voltage drop would occur across the cable). C_1 also A.C.-couples the r.f. coil to the power

supply so that the undistorted r.f. voltage truly oscillates about 0 V. The reciprocal load impedance of the combined C_1, C_2, L, R part of the circuit is

$$\frac{1}{Z_{load}} = j\omega C_2 + \frac{1}{R + j\left(\omega L - \frac{1}{\omega C_1}\right)} = j\omega C_2 + \frac{R - j\left(\omega L - \frac{1}{\omega C_1}\right)}{R^2 + \left(\omega L - \frac{1}{\omega C_1}\right)^2} \qquad (268),$$

where we have used $X_C = -j/\omega C$, $X_L = j\omega L$, and the complex identity $y = y\,y^*/y^*$, etc. For exact impedance matching, we require $\mathrm{Re}(Z_{load}) = Z_0$ with a zero voltage-current phase difference which means that $\mathrm{Im}(Z_{load})$ (and consequently $\mathrm{Im}(1/Z_{load})$) is zero. From Eq. (268), therefore, we have

$$\frac{1}{Z_0} = \frac{R}{R^2 + \left(\omega L - \frac{1}{\omega C_1}\right)^2} \quad \text{(for exact impedance matching)} \qquad (269)$$

and

$$\omega C_2 - \frac{\left(\omega L - \frac{1}{\omega C_1}\right)}{R^2 + \left(\omega L - \frac{1}{\omega C_1}\right)^2} = 0 \quad \text{(for exact impedance matching)} \qquad (270).$$

Note that we consider R, L, and Z_0 as fixed (for the moment we are neglecting the possible high frequency dependence of $R(\omega)$ due to the reduction of the effective conducting cross-sectional area of the wire caused by the skin effect (see Sec. 7.3.4.7)). From the impedance matching conditions (269) and (270), we obtain

$$C_1(\omega) = \frac{1}{\omega\left(\omega L - \sqrt{R(Z_0 - R)}\right)} \quad \text{(for exact impedance matching)} \qquad (271)$$

and

$$C_2(\omega) = \frac{L - \frac{1}{\omega^2 C_1(\omega)}}{R^2 + \left(\omega L - \frac{1}{\omega C_1(\omega)}\right)^2} = \frac{1}{\omega Z_0}\sqrt{\frac{Z_0 - R}{R}} \quad \text{(for exact impedance matching)} \quad (272).$$

For these particular values of C_1 and C_2, we can construct a simplified table of voltages, currents, and impedances remembering that the cable acts like a pure resistance of Z_0 (as does the C_1, C_2, L, R part of the circuit), and these two sub-circuits reduce to a 2:1 voltage divider (Table 8).

Table 8. Circuit values at exact impedance matching (i.e., when C_1 and C_2 are given by Eqs. (271) and (272)).

	C_1	L	R	C_2	C_1LR	C_2 // C_1LR	Z_0, C_2 // C_1LR
V	$\frac{V_{in}}{2C_1}\left(C_2-\frac{j}{Z_0\omega}\right)$	$\frac{V_{in}}{2}\left(j\frac{1}{Z_0}-\omega C_2\right)\omega L$	$\frac{V_{in}}{2}\left(\frac{1}{Z_0}+j\omega C_2\right)R$	$\frac{V_{in}}{2}$	$\frac{V_{in}}{2}$	$\frac{V_{in}}{2}$	V_{in}
I	$\frac{V_{in}}{2}\left(\frac{1}{Z_0}+j\omega C_2\right)$	$\frac{V_{in}}{2}\left(\frac{1}{Z_0}+j\omega C_2\right)$	$\frac{V_{in}}{2}\left(\frac{1}{Z_0}+j\omega C_2\right)$	$\frac{jV_{in}\omega C_2}{2}$	$\frac{V_{in}}{2}\left(\frac{1}{Z_0}+j\omega C_2\right)$	$\frac{V_{in}}{2Z_0}$	$\frac{V_{in}}{2Z_0}$
Z	$-\frac{j}{\omega C_1}$	$j\omega L$	R	$-\frac{j}{\omega C_2}$	$R+j\left(\omega L-\frac{1}{\omega C_1}\right)$	Z_0	$2Z_0$

More realistically, the transmission line insulator has some conductance (represented by G_{cable}) and non-zero resistance, represented by R_{cable} (as shown in Figure 28). Distortionless cables are fabricated such that

$$\frac{G'}{C'} = \frac{R'}{L'} \tag{273}$$

where again the prime represents "per unit length". Note that if such a circuit is used to drive M coils in parallel (for example the four coils of one arm of a 4-N=2 coil NRSE), the current through C_1 will be M times greater than for the single coil. Care must be taken to ensure that the capacitors handle these currents.

7.3.4.3 r.f. coil frequency, currents, and voltages

The r.f. coil dimensions used in this and subsequent sections are shown in Figure 30. The symbols used try to preserve consistency with the static field coil parameters shown in Figure 23. From Table 8 at exact impedance matching we have (substituting the value of $C_2(\omega)$ from Eq. (272)):

$$V_L = \omega L \frac{V_{in}}{2Z_0}\left(j - \sqrt{\frac{Z_0 - R}{R}} \right) \tag{274}$$

where V_{in} is the *supply* voltage with

$$\left|V_L\right| = \omega L \frac{V_{in}}{2}\sqrt{\frac{1}{Z_0 R}} \tag{275}$$

and

$$I_L = \frac{V_{in}}{2Z_0}\left(1 + j\sqrt{\frac{Z_0 - R}{R}} \right) \tag{276}$$

with

$$\left|I_L\right| = \frac{V_{in}}{2}\sqrt{\frac{1}{Z_0 R}} \tag{277}$$

so that

$$I_L = -j\frac{V_L}{\omega L} \tag{278}.$$

We see that V_L is proportional to the frequency and L and the current lags the voltage by 90°, as expected for a pure inductance.

Obtaining the maximum frequency of operation of the r.f. coil imposes the principal technical challenge. Because the r.f. frequency must match the Larmor precession frequency in the static field coils, we have (according to Eq. (10)) $\nu_{rf} \approx 1.17$ MHz for $B_0 \approx 0.04$ T (729 KHz for $B_0 = 0.025$ T). Also, according to Eq. (15), the peak r.f. field is optimally-tuned according to the mean incident wavelength with

$$B_{rf}^{pk}\left[\mathrm{T}\right] \simeq \frac{1.35645\times10^{-4}}{l_{rf}\left[\mathrm{m}\right]\left\langle\lambda_i\right\rangle\left[\mathrm{\mathring{A}}\right]} \tag{279}$$

so that the largest r.f. field magnitude is defined by the *minimum* incident wavelength. Using the long solenoid approximation (Eq. (233)), we conclude that the peak current required in the r.f. coil is approximately

$$\begin{aligned} I_{rf}^{pk}\left[\mathrm{A}\right] &\simeq \frac{B_{rf}^{pk}\left[\mathrm{T}\right]}{\mu\left[\mathrm{NA^{-2}}\right]n_{rf}\left[\mathrm{m^{-1}}\right]} \simeq \frac{1.356\times10^{-4}}{\mu\left[\mathrm{NA^{-2}}\right]n_{rf}\left[\mathrm{m^{-1}}\right]l_{rf}\left[\mathrm{m}\right]\left\langle\lambda_i\right\rangle\left[\mathrm{\mathring{A}}\right]} \\ &\simeq \frac{108}{n_{rf}\left[\mathrm{m^{-1}}\right]l_{rf}\left[\mathrm{m}\right]\left\langle\lambda_i\right\rangle\left[\mathrm{\mathring{A}}\right]} \quad \left(\text{in air}\right) \end{aligned} \tag{280},$$

where n_{rf} is the winding density of the r.f. coil, so that the root mean square (r.m.s.) current is approximately

$$I_{rf}^{rms}\left[\mathrm{A}\right] = \frac{I_{rf}^{pk}\left[\mathrm{A}\right]}{\sqrt{2}} \simeq \frac{9.592\times10^{-5}}{\mu\left[\mathrm{NA^{-2}}\right]n_{rf}\left[\mathrm{m^{-1}}\right]l_{rf}\left[\mathrm{m}\right]\left\langle\lambda_i\right\rangle\left[\mathrm{\mathring{A}}\right]} \simeq \frac{76.3}{n_{rf}\left[\mathrm{m^{-1}}\right]l_{rf}\left[\mathrm{m}\right]\left\langle\lambda_i\right\rangle\left[\mathrm{\mathring{A}}\right]} \tag{281}.$$

According to Faraday's law applied to a coil of inductance L,

$$V = -L\frac{dI}{dt} \tag{282}$$

of which Eq. (278) is obviously a solution for sinusoidally-varying currents and voltages. For a sinusoidally-varying current $I_{rf}\left(t\right) = I_{rf}^{pk}\sin\omega_{rf}t$ the maximum rate of change of the current is

$$\left(dI/dt\right)_{\max}\left[\mathrm{As^{-1}}\right] = I_{rf}^{pk}\left[\mathrm{A}\right]\omega_{rf}\left[\mathrm{s^{-1}}\right] \approx 1.832\times10^{8}\, I_{rf}^{pk}\left[\mathrm{A}\right]B_0\left[\mathrm{T}\right] \tag{283}$$

and for a long solenoid we can use the approximation

$$L \approx \mu n_{rf}^2 l_{axial}^{rf} A_{rf} \tag{284}$$

($A_{rf} = a_{rf} \times l_{rf}$ see Figure 57), whence

$$
\begin{aligned}
L\left[\mathrm{H}\right] &\approx 4\pi\times 10^{-7}\left(n_{rf}\left[\mathrm{m}^{-1}\right]\right)^{2} l_{axial}^{rf}\left[\mathrm{m}\right] A_{rf}\left[\mathrm{m}^{2}\right] \\
&\approx 1.26\times 10^{-6}\left(n_{rf}\left[\mathrm{m}^{-1}\right]\right)^{2} l_{axial}^{rf}\left[\mathrm{m}\right] A_{rf}\left[\mathrm{m}^{2}\right]
\end{aligned}
\tag{285}
$$

so that Eq. (282) can be rewritten using Eqs. (280), (283), and (284), and replacing A_{rf} by $a_{rf}\times l_{rf}$, where a_{rf} is the r.f. coil dimension perpendicular to both the beam direction and to the r.f. field direction:

$$
V_{rf}^{pk}\left[\mathrm{V}\right] \approx 2.5\times 10^{4}\,\frac{n_{rf}\left[\mathrm{m}^{-1}\right] l_{axial}^{rf}\left[\mathrm{m}\right] a_{rf}\left[\mathrm{m}\right]}{\left\langle \lambda_{i}\right\rangle\left[\mathrm{\overset{o}{A}}\right]} B_{0}\left[\mathrm{T}\right] \tag{286}.
$$

We see from Eq. (286) that the maximum voltage occurs at maximum B_0 and minimum λ. We will assume that the minimum useful wavelength is 2 Å. From Eq. (14) for a typical r.f. coil thickness l_{rf} (in the beam direction) of 2.5 cm, we have $B_{rf}^{pk}(l_{rf} = 0.025$ m, $\langle\lambda_i\rangle = 2$ Å) ≈ 2.71 mT. The peak current in the r.f. coil with winding density $n_{rf} =$ 250 m^{-1} is approximately $I_{rf}^{pk}(n_{rf} = 250$ m^{-1}, $l_{rf} = 0.025$ m, $\langle\lambda_i\rangle = 2$ Å) ≈ 8.64 A. This is approximately one order of magnitude less that the maximum currents required in the static field coils of similar winding densities.

Typical r.f. coils such as those shown in Figure 26, may have self-inductances of the order of (40 to 50) μH. For $L = 50$ μH, $I_{pk} \approx 8.64$ A, $\omega_0 = 2\pi\nu_0(\max) \approx 7.35\times 10^6$ rad s^{-1}, we have $dI/dt \approx 6.3\times 10^7$ As^{-1} and a peak voltage across the r.f. coil of around $V_{rf}^{pk}(n_{rf} = 250$ m^{-1}, $l_{rf} = 0.025$ m, $\langle\lambda_i\rangle = 2$ Å) ≈ 3.2 kV. This high peak voltage poses various challenges for electrical insulation, switching, and other circuit issues covered in Sec. 7.3.4.2. Typically Teflon-insulated high voltage cables are limited to about 1.5 kV. The peak voltage in this example would perhaps impose a limitation on the minimum operational wavelength.

Another quantity of interest which must be maintained below breakdown voltage is the voltage between two adjacent windings in a tightly-wound coil, V_{pk}^{ww}. This is simply the total voltage difference across the coil multiplied by the fractional length of one turn with respect to the total winding length on the coil. The latter fraction for tightly-wound rectangular windings is just $h_{rf}/l_{axial} = 1/(n_{rf}\, l_{axial}) = 1/N_{rf}$, where N_{rf} is the total number of turns on the r.f. coil, i.e.,

$$
V_{pk}^{ww} = \frac{V_{pk}^{\max}}{n_{rf} l_{axial}} = \frac{V_{pk}^{\max}}{N_{rf}} \tag{287}.
$$

7.3.4.4 r.f. power supply voltage at exact impedance matching

We can equate the magnitude of the r.m.s. current in the coil at exact impedance matching (from Table 8 with V_{in} replaced by V_{rms}^{PS} with the required value of C_2 (from Eq. (272)) and with the required r.m.s. current magnitude from Eq. (281), whence

$$I_{rf}^{rms}\left[\mathrm{A}\right] \simeq \frac{9.592\times10^{-5}}{\mu\left[\mathrm{NA^{-2}}\right] n_{rf}\left[\mathrm{m^{-1}}\right] l_{rf}\left[\mathrm{m}\right]\left\langle\lambda_i\right\rangle\left[\mathrm{\mathring{A}}\right]} = \frac{V_{rms}^{PS}}{2\sqrt{Z_0 R}} \quad \text{exact impedance matching} \quad (288),$$

where V_{rms}^{PS} is the r.m.s. voltage of the *power supply*. Therefore, if we assume Z_0 is 50 Ω, we require a power supply voltage of

$$V_{rms}^{PS}\left[\mathrm{V}\right] \simeq \frac{152.7\sqrt{Z_0\left[\Omega\right]R\left[\Omega\right]}}{n_{rf}\left[\mathrm{m^{-1}}\right] l_{rf}\left[\mathrm{m}\right]\left\langle\lambda_i\right\rangle\left[\mathrm{\mathring{A}}\right]} = \frac{1079.4\sqrt{R\left[\Omega\right]}}{n_{rf}\left[\mathrm{m^{-1}}\right] l_{rf}\left[\mathrm{m}\right]\left\langle\lambda_i\right\rangle\left[\mathrm{\mathring{A}}\right]} \quad \text{exact impedance matching, } Z_0\text{=50 Ω}$$

(289).

For $R \approx 1$ Ω, $n_{rf}[\mathrm{m^{-1}}] l_{rf}[\mathrm{m}] \approx 10$, the supply voltage is approximately 100 V/λ[Å]. Note that this is typically much smaller than the high frequency voltages generated across the r.f. coil itself.

7.3.4.5 Power dissipation in the r.f. circuit and in the r.f. coil

At exact impedance matching $\mathrm{Re}(Z_{load}) = Z_0$, $\mathrm{Im}(Z_{load}) = 0$ (see Sec. 7.3.4.2), and the resistance of the entire circuit is $2Z_0$, therefore the heat dissipated in the whole circuit is

$$P_{rf\ circuit} = 2\left(I_{rms}^{PS}\right)^2 Z_0 = \frac{\left(V_{rms}^{PS}\right)^2}{2Z_0} \quad \text{exact impedance matching} \quad (290)$$

where I_{rms}^{PS} is the total current delivered to the circuit from the power supply. Using Eq. (289) for V_{rms}^{PS} with Z_0 = 50 Ω, we have

$$P_{rf\ circuit}\left[\mathrm{W}\right] = 1.165\times10^{4}\, R\left[\Omega\right]\left(\frac{1}{n_{rf}\left[\mathrm{m^{-1}}\right] l_{rf}\left[\mathrm{m}\right]\left\langle\lambda_i\right\rangle\left[\mathrm{\mathring{A}}\right]}\right)^2 \quad \text{exact impedance matching, } Z_0 = 50\ \Omega \quad (291).$$

Using the example given in the previous section (i.e., for $R \approx 1$ Ω, $n_{rf}[\mathrm{m^{-1}}] l_{rf}[\mathrm{m}] \approx 10$) we have $P_{rf\ circuit} \approx 117$ W/(λ[Å])^2, i.e., ≈ 30 W for a minimum wavelength of 2 Å.

The power dissipated as heat in the r.f. coil is only due to the coil resistance (the reactance alternately stores and releases energy back towards the source). From Table 8 at exact impedance matching the voltage across the coil (assuming essentially all the resistance R is due to the coil) is

$$V_{coil} \simeq \frac{V_{rms}^{PS}}{2}\left(\frac{1}{Z_0} + j\omega C_2\right)R \qquad \text{at exact impedance matching} \qquad (292).$$

Therefore the power dissipated as heat in the coil at exact impedance matching is

$$P_{coil} = \left|\frac{V_{rms}^{PS}}{2}\left(\frac{1}{Z_0} + j\omega C_2\right)\right|^2 R \quad = \frac{\left(V_{rms}^{PS}\right)^2}{4Z_0} \quad = \quad \left(I_{rf}^{rms}\right)^2 R \quad \text{exact impedance matching} \quad (293),$$

where we have used the value of C_2 for exact impedance matching given by Eq. (272), i.e., one half of the total power dissipated in the circuit (c.f. Eq. (290)) is dissipated in the r.f. coil at exact impedance matching.

7.3.4.6 r.f. coil cooling

Because the maximum currents required in the r.f. coils are not so large (of order 10 A), experience has shown that compressed air cooling of the r.f. coil surface is usually adequate to maintain the coils at reasonable temperatures (certainly below 100 °C) for coils working at frequencies of up to about 750 kHz.

7.3.4.7 The skin effect and the resistance of the r.f. coil windings

An unfortunate consequence of induced eddy currents and Lenz's law at high frequencies is the concentration of current towards the outer surface of the conductor. This phenomenon is commonly referred to as the "skin effect". The skin depth (or thickness for the current to fall to 1/e of its outer surface value for a thick conductor), δ, is inversely proportional to the square root of the frequency; in fact

$$\delta = \sqrt{\frac{2}{\mu\sigma\omega}} \qquad (294),$$

where σ is the conductivity and μ is the permeability of the wire.

Two undesirable consequences result. Firstly the resistance of the wire can increase rapidly when δ becomes comparable to or less than the wire diameter. For example, the skin depth for copper at the highest frequencies required (~1 MHz) is about 66 μm (0.065 mm). Secondly, the rise in resistance with increasing frequency affects the

signal velocity at different frequencies causing dispersion even in a 'distortionless' cable. However, this latter effect is mitigated in this case because bandwidth of the r.f. is extremely narrow for each spectrometer setting.

One solution for minimizing the skin effect in the r.f. coils operating at about 1 MHz is to use multiple small diameter (preferably < δ), individually-insulated copper wires in parallel rather than fewer thicker conductors. This is the method that has been used for the coils shown in Figure 26. Unfortunately, this is only possible for the return coils and not the part of the coil that is in the beam which must use aluminum windings for adequate transmission. For aluminum, the skin depth at 1 MHz is about 83 μm (0.083 mm), i.e., for aluminum we may assume that

$$\delta_{Al}\left[\text{mm}\right] \simeq \frac{83}{\sqrt{\nu\left[\text{Hz}\right]}} \qquad (295).$$

For band-type windings, where $h \gg t$, the ratio of the D.C. resistance, R_0, to the winding resistance at frequency ν, $R(\nu)$, is approximately given by

$$\frac{R(\nu)}{R_0} \approx \frac{\int_0^{t/2} dx}{\int_0^{t/2} \exp\left(-\frac{x}{\delta}\right) dx} = \frac{t}{2\delta\left[1-\exp\left(-\frac{t}{2\delta}\right)\right]} \quad \text{band-like windings with } h \gg t \quad (296).$$

Note that in the low frequency limit $\delta \gg t$, therefore

$$\frac{R(\nu)}{R_0} \approx \frac{t}{2\delta\left[1-\left(1-\frac{t}{2\delta}\right)\right]} = 1 \qquad \delta \gg t \qquad (297).$$

as expected, and in the high-frequency limit $t \gg \delta$, therefore

$$\frac{R(\nu)}{R_0} \approx \frac{t}{2\delta} \qquad t \gg \delta \qquad (298),$$

i.e., the winding of thickness t in the high frequency limit has approximately the D.C. resistance of a conductor of thickness 2δ with the central core volume behaving like a perfect insulator. Applying Eqs. (295) and (296) for the t = 0.4 mm thick aluminum band cited in Sec. 7.3.2,we see that the resistance at 1 MHz is about 5 times greater than the D.C. resistance with a current at the center of the conductor less than 9% of the value near the surface. Note that in this particular example, the conductor resistance at 1 MHz would drop by less than 10% even if the conductor was

made arbitrarily thick. Consequently, increasing the thickness of the windings beyond a few 1/10ths of a millimeter at MHz frequencies leads only to small power reductions with unnecessary losses in neutron transmission.

7.3.4.8 Allowable $\Delta B_{rf}/B_{rf}$ and $\Delta l_{rf}/l_{rf}$

In each π-flipper coil, the neutron spin ideally precesses through an angle π around B_{rf} during neutron passage through the coil. The actual angle of precession of the spin about B_{rf} is determined by the dispersion due to the spread of incident wavelengths, as discussed in Sec. 2.2. However, an additional loss of polarization/flipping efficiency by a similar mechanism results if there is a spread in the magnitude of B_{rf} or of the length of the r.f. field, l_{rf}. We wish to maximize the operational neutron bandwidth of the spectrometer in the interests of maximizing intensity. Therefore, it is reasonable to require that the effects of $\Delta(B_{rf}l_{rf})$ be small compared with the effects due to dispersion. In this way, acceptable operation of the instrument is sustained for the largest possible $\Delta\lambda/\lambda$. $\Delta(B_{rf}l_{rf})$ can be reduced by appropriate coil engineering. Because of the similarities with dispersion, we can use Eq. (48) (for triangular distributions for both $\Delta(B_{rf}l_{rf})$ and $\Delta\lambda$) with α_{FWHM} (see Eq. (38)) replaced by an effective value

$$\alpha_{FWHM}^{eff} \approx \sqrt{\left(\frac{\Delta\left(B_{rf}\,l_{rf}\right)}{B_{rf}\,l_{rf}}\right)^2 + \left(\frac{\Delta\lambda_{FWHM}}{\langle\lambda_i\rangle}\right)^2} \qquad (299)$$

or else the equivalent of Eq. (49) for Gaussian distributions with similar parameter substitutions.

We choose a reasonable criterion whereby $(\Delta(B_{rf}l_{rf})/B_{rf}l_{rf})^2$ is at most 10% of $(\Delta\lambda_{FWHM}/\langle\lambda_i\rangle)^2$, i.e.,

$$\alpha_{FWHM}^{eff} \leq 1.05\,\alpha_{FWHM} \qquad (300).$$

A comparison of the estimated flipping efficiencies for triangular distributions and for M = 8 flipper coils assuming (i) only dispersion and (ii) the above criterion (Eq. (300)) for the combined effects of dispersion and $\Delta(B_{rf}l_{rf})$ is shown in Table 9, which demonstrates that these tolerances create measurable but reasonably small reductions in the flipping efficiency.

Table 9. Flipping efficiency for triangular distributions of (i) $\Delta\lambda$ (dispersion only) and (ii) $\Delta\lambda$ combined with effects of $\Delta(B_{rf}l_{rf})$ using the criterion expressed in Eq. (300) for M=8 π coils.

α_{FWHM}	P_{disp}/P_{ideal} (M=8)	
(= $\Delta\lambda_{FWHM}/\langle\lambda_i\rangle$) (%)	α_{FWHM} (only)	with $\alpha_{FWHM}^{eff} = 1.05\alpha_{FWHM}$
10	0.96831	0.96519
20	0.88600	0.87604
30	0.78127	0.76533
40	0.67898	0.66009
50	0.59115	0.57179

If we assume typical spectrometer operation at α_{FWHM} <~ 10%, then we require

$$\frac{\Delta\left(B_{rf}l_{rf}\right)}{B_{rf}l_{rf}} <\sim 0.03 \qquad (301).$$

If we assume *equal* fractional error contributions due to ΔB_{rf} and Δl_{rf}, we have

$$\frac{\Delta\left(B_{rf}l_{rf}\right)}{B_{rf}l_{rf}} = \frac{\sqrt{2}\Delta B_{rf}}{B_{rf}} = \frac{\sqrt{2}\Delta l_{rf}}{l_{rf}} <\sim 0.03 \qquad (302).$$

For l_{rf} = 0.025 m, using Eq. (302), we have Δl_{rf} <~ 0.6 mm, which is not excessively demanding with $\Delta B_{rf}/B_{rf}$ = $\Delta B_{rf}^{pk}/B_{rf}^{pk}$ <~ 2 % (which is more than an order of magnitude more relaxed than the required static field homogeneities that are of the order of tenths of one percent (see for example Table 7)). Using Eq. (279) the above criterion can be re-expressed as

$$\Delta B_{rf}^{pk}\left[\mathrm{T}\right] \simeq \frac{2.9\times10^{-6}}{l_{rf}\left[\mathrm{m}\right]\left\langle\lambda_i\right\rangle\left[\overset{\circ}{\mathrm{A}}\right]} \qquad (303).$$

For the same l_{rf} (= 0.025 m) and a wavelength range from 2 Å to 12 Å, (B_{rf}^{pk} varies from about 2.7 mT to about 0.45 mT respectively), we require ΔB_{rf}^{pk} <~ 60 μT at 2 Å and ΔB_{rf}^{pk} <~ 10 μT at 12 Å.

7.3.5 Stray fields in the “zero field” regions

There are inevitably stray fields within the "zero-field" gaps that give rise to unwanted Larmor precession around the local stray field direction. In the worst cases, these can severely reduce or even destroy the echo signal. Sources of stray fields are leakage fields from the coils themselves, the earth's magnetic field, and other externally-produced magnetic fields. Even-*N* bootstrap coils greatly reduce the coil contribution by providing compact, closed return paths due to the oppositely-opposed field directions. Furthermore, any leakage field also has opposite sign on each side of the bootstrap coil, resulting in a first order cancellation of the Larmor precession it causes upstream and downstream of the coil. The tight conduction of field lines between the coil pairs (and away from the zero field regions) is also greatly improved by using high permeability μ-metal caps linking the coil ends. Leakage fields into the zero-field flight paths are further reduced by practically encapsulating the coil in a μ-metal screen with the exception of the beam areas. External sources of stray field (such as the earth's field) are practically eliminated by surrounding the sensitive flight paths with multi-skinned μ-metal shielding [21] (see also Sec. 7.7). For a mean net

stray field integrated along the spectrometer arm path length L of magnitude B_{stray}, the corresponding mean net additional precession angle is

$$\left\langle \Delta\varphi_{stray} \right\rangle [\mathrm{rad}] \approx \frac{\gamma_n m_n}{h} B_{stray} L \left\langle \lambda_i \right\rangle = 4.63\times10^4 \, B_{stray}[\mathrm{T}] L[\mathrm{m}] \left\langle \lambda_i \right\rangle \left[\mathrm{\mathring{A}} \right] \qquad (304).$$

For example, if the dominant stray field component is from coil leakage, the leakage field lines tend to be aligned along the direction of the static fields. If we impose the constraint that the net precession angle in each arm of the spectrometer should not exceed about 10°, then we require

$$B_{stray}[\mathrm{T}] L[\mathrm{m}] \leq \frac{3.8\times10^{-6}}{\left\langle \lambda_i \right\rangle \left[\mathrm{\mathring{A}} \right]} \qquad (305).$$

If λ = 8Å this corresponds to a stray field integral of about 5×10^{-7} Tm (for L = 2 m and B_{stray} of about 0.2 μT integrated over L). Gähler, Golub, and Keller [8] show measured stray fields obtained outside a typical μ-metal capped N=2 bootstrap coil. The stray field magnitude for such a coil with an internal field B_0 of 1.67 mT is about 3 μT for about the first 0.05 m falling to less than 0.5 μT at about 0.2 m from the coil. The estimated stray field integral on one side of the coil from this measurement is about 8×10^{-7} Tm. At B_0 = 0.04 T internal field, we might expect the stray field integral to be about $(0.04\times8\times10^{-7}/1.67\times10^{-3}) \approx 1.9\times10^{-5}$ Tm (38 times greater than the value given for λ = 8 Å above). In his Ph.D. thesis, T. Keller [22] shows that the field integral of such coils could be reduced by an additional factor of about 30 by adding the μ-metal screen around the N = 2 coil. In this case we anticipate a typical stray field integral magnitude on *one* side of the coil unit of about $\Delta_1 \approx 6.3\times10^{-7}$ Tm at B_0 = 0.04 T with a similar stray field integral magnitude Δ_2 on the other side (but causing a precession in the opposite sense). If the 4-N=2 coils are arranged as shown in Figure 6 and the typical residual net leakage field integral due to each N = 2 coil unit ($=\langle\Delta_1-\Delta_2\rangle$) is added in quadrature for the two coil units of each arm, using Eq. (305) we have a stray field integral cancellation criterion given by

$$\left\langle \Delta_1 - \Delta_2 \right\rangle [\mathrm{Tm}] <\sim \frac{3.8\times10^{-6}}{\sqrt{2}\left\langle \lambda_i \right\rangle \left[\mathrm{\mathring{A}} \right]} \approx \frac{2.7\times10^{-6}}{\left\langle \lambda_i \right\rangle \left[\mathrm{\mathring{A}} \right]} \qquad (306)$$

For the λ = 8Å example above, we require $\langle \Delta_1 - \Delta_2 \rangle <\sim 3.4\times10^{-7}$ Tm for 10° net stray field precession in each arm. For $\Delta_1 \approx 6.3\times10^{-7}$ Tm, this means that the typical stray field cancellation need only be about 50% in this case. This appears entirely achievable.

7.3.6 Measurement of small τ_{NRSE}

7.3.6.1 The Bloch-Siegert shift

Up to now the resonant component of the r.f. field has been approximated as a pure rotating field and the counter-rotating component has been essentially ignored. However, the applied r.f. field is an *oscillating* field not a pure rotating field. Bloch and Siegert [5] treated the case that really exists in the resonance coil for a spin-1/2 particle traversing a static field with a superimposed, perpendicular oscillating field. This problem is complicated and does not have an exact solution. However, they showed that for increasing B_0/B_{rf}, the solution increasingly approximates to that of a "static + circular" field with a similar-shaped resonance curve, however, the resonance frequency *deviates* from the classical Larmor frequency, ω_0, by a fractional amount equal to

$$\frac{\Delta\omega_{BS}}{\omega_0} = \frac{\left|\omega_{rf} - \omega_0\right|}{\omega_0} = \frac{B_{rf}^2}{16B_0^2} \qquad (307).$$

Typically for high-resolution operation of the NRSE flipper coils this fraction is small. For example, according to Eq. (15), for l_π = 0.03 m and short wavelength operation (λ = 2 Å), B_{rf} = 2.26 mT. For B_0 = 0.04 T, $\Delta\omega_{BS}/\omega_0 \approx 2\times10^{-4}$ corresponding to about 233 Hz. However, at low τ_{NRSE}, $\Delta\omega_{BS}$ can be a significant fraction of the Larmor frequency.

7.3.6.2 Solution using NSE mode operation of coils

When B_0 starts to become comparable to B_{rf}, the flippers do not perform well. Köppe *et al.* [11] provide some idea of when this is likely to occur. Their coils cease to operate satisfactorily for static fields $B_0 < 2.7$ mT for $\lambda \leq 6$ Å. Assuming that these r.f. coils are no greater than about 0.025 m thick in the beam direction, we infer from Eq. (15) that the peak r.f. field at which problems occur is for $B_{rf}^{pk} >\sim 0.9$ mT or $B_{rf} >\sim 0.45$ mT. Thus we will assume that the π-flippers must be operated under the following condition

$$\frac{B_{rf}}{B_0} \leq 0.17 \quad \text{approximate condition for operating in NRSE mode} \qquad (308).$$

This condition clearly limits the dynamic range of the NRSE instrument with respect to low τ (low B_0) measurements. One possibility for measuring short Fourier times, proposed by Gähler, consists of turning off the r.f. field to all the coils and running in classic NSE mode. In a 4-*N*=1 coil configuration one or both of the static coils in each arm can be operated. The fields are oriented in the correct sense in this case so that no π-flipper is required between the two arms of the spectrometer as in a conventional (longitudinal field) NSE instrument; consequently Larmor precession occurs within the coil length in opposite directions on each side of the sample. This is illustrated in Figure 31. Several points at low τ can be measured by adjusting the field magnitude in the active coils.

The situation is more complicated in a bootstrap coil configuration (for example $N = 2$). In this case, all r.f. fields are switched off (as in the $N = 1$ case), however the static field directions by themselves are inappropriate for operation in NSE mode. Several solutions to this problem are illustrated in Figure 32. In case (a), all static fields remain on but a π flipper is placed between the two opposing coils of a bootstrap pair, essentially reversing the field direction of the second coil. Conceivably, the field direction in the second coil of the pair could be reversed by reversing the current direction in the coil, but often the two coils are constructed from a single winding and this option is not practical. In case (b), if the coils can be switched out of the circuit independently, only the fields that have the correct direction are switched on. (c) is like (b) but only one coil of the correct field direction is switched on in each arm. Note that if the static fields are provided by *permanent* magnets (see Sec. 9.2) only option (a) is feasible unless magnets of the wrong field direction are physically removed from the beam. For permanent magnets the NSE scan must be performed by rotating the magnets to change the field integrals.

7.3.6.3 An example of a combined NSE-NRSE mode scan

For NRSE operation we have τ_{NRSE} given by Eq. (153), i.e., τ_{NRSE}[ns] = 0.37271 $N\, B_0$[T] L_0[m] (λ_i[Å])^3, where (combining Eqs. (308) and (14)) for satisfactory NRSE mode operation we have

$$B_0\,[\mathrm{T}]\, l_\pi\,[\mathrm{m}]\, \lambda_n\left[\mathring{\mathrm{A}}\right] \;>\sim\; 4\times10^{-4}\,\mathrm{Tm}\,\mathring{\mathrm{A}} \qquad \text{for satisfactory NRSE mode operation} \qquad (309)$$

whence

$$\tau_{NRSE}\,[\mathrm{ns}] \;>\sim\; 1.5\times10^{-4}\,\frac{N L_0\,[\mathrm{m}]\left(\lambda_i\left[\mathring{\mathrm{A}}\right]\right)^2}{l_\pi\,[\mathrm{m}]} \qquad \text{for satisfactory NRSE mode operation} \qquad (310).$$

If we choose $N = 2$, $L_0 = 2$ m, $\lambda_n = 8$ Å, and $l_\pi \approx 0.03$ m for this scan we anticipate that it is possible to operate in NRSE mode for $\tau_{NRSE} >\sim 1.3$ ns. This corresponds to $B_0 >\sim 1.7$ mT in this case. For smaller values of τ, the spectrometer must be run in NSE mode. In NSE mode we have

$$\tau_{NSE}\left[\text{ns}\right] = 0.373 M B_0\left[\text{T}\right] l_\pi\left[\text{m}\right]\left(\lambda_i\left[\overset{\text{o}}{\text{A}}\right]\right)^3 \qquad (311),$$

where M is the total number of static field coils energized. If the maximum B_0 is 0.04 T with $M = 8$ (i.e., the configuration shown in Figure 32(a)), we can use NSE mode up to $\tau_{NSE} \sim 1.8$ ns for $\lambda = 8$ Å, i.e., there *is* a possible overlap between the upper NSE mode and the lower NRSE mode if the scheme in Figure 32(a) is adopted. Some dummy data points are plotted in Figure 33 showing the scan points that result from evenly-spaced values of B_0 in the range from about 1.7 mT (the minimum field for NRSE operation in this example) to 0.04 T for both NSE mode (red circles) and NRSE mode (blue squares); l_{B0} was chosen equal to l_π for this example.

7.4 Defining the major instrument parameters for the NRSE instrument using coils

We now investigate some of the major constraints on the instrument parameters imposed by the proposed instrumental performance goals combined with the more rigid technical constraints for an NRSE instrument using resonance coils. This is by no means an exhaustive list and additional compromises may be necessary. Probably the major factors are as follows:

1. We wish to access $\tau_{NRSE} = 30$ ns at $\lambda = 8$Å. This has implications for a minimum achievable magnitude of $B_0 L_0$ embodied in Eq. (226).
2. Once 30 ns at $\lambda = 8$ Å is accessible, we wish to achieve a resolution function signal (polarization) greater than or equal to a stated minimum value, $P_x^{\,0}$. These conditions are approximately described by Eqs. (223) to (225) for the required static field homogeneity, coil flatness, and beam divergence.
3. The anticipated neutron transmission of the windings should be >~ 80 % at $\lambda = 8$ Å. This concerns the thickness of the windings in the beam direction, *t*. The transmission for aluminum windings may be estimated using the macroscopic cross-section given in Eq. (231).
4. Maximum limitations on the static field coil current/ minimum coil winding density (see Eq. (234)).
5. Capacity to remove heat from the static field coils (see for example Eq. (255) for tightly-wound rectangular aluminum windings), given estimated constraints on the coil surface area, the winding thickness, *t*, maximum

operating static field, B_0^{max}, (as constrained by condition 1 above), and the means available for cooling without interfering with the neutron beam (see Sec. 7.3.3.5).

6. Maximum limitations on the voltage across the r.f. coil at B_0^{max} (see Eq. (286)), limited by cabling and insulation breakdown issues (practical maximum of about 1.5 kV).

We will assume for the reasons given in Sec. 3.4 that the number of coils in the bootstrap is universally given by $N = 2$ and that the windings are made of aluminum.

Condition 1 for $N = 2$ imposes the constraint already given by Eq. (227), i.e.,

$$\left(B_0 L_0\right)_{max} \geq 0.079\,\mathrm{Tm} \qquad \text{Condition 1: Criterion for accessing } \tau_{NRSE} = 30 \text{ ns at } \lambda = 8 \text{ Å with } N = 2 \qquad (312).$$

Condition 2 imposes resolution requirements for $N = 2$ which may be stated as follows assuming equal contributions from each term (see Eqs. (223) to (225)):

$$(a) \quad \Delta B_0^{FWHM}\left[\mathrm{T}\right] \leq \frac{1.47\times10^{-5}\sqrt{\ln\left(\frac{1}{P_x^0}\right)}}{l_{B_0}\left[\mathrm{m}\right]\lambda_i\left[\mathrm{\mathring{A}}\right]}$$

$$(b) \quad \Delta l_{B_0}^{FWHM}\left[\mathrm{m}\right] \leq \frac{1.47\times10^{-5}\sqrt{\ln\left(\frac{1}{P_x^0}\right)}}{B_0\left[\mathrm{T}\right]\lambda_i\left[\mathrm{\mathring{A}}\right]}$$

$$(c) \quad \Delta\theta_{max}\left[\mathrm{rad}\right] \leq 3.47\times10^{-3}\sqrt{\frac{\sqrt{\ln\left(\frac{1}{P_x^0}\right)}}{B_0\left[\mathrm{T}\right]L_0\left[\mathrm{m}\right]\lambda_i\left[\mathrm{\mathring{A}}\right]}} \quad , \left|\Delta\theta_{max}\right|\left[\mathrm{rad}\right] <\sim \frac{4.7\times10^{-3}}{\sqrt{B_0\left[\mathrm{T}\right]L_0\left[\mathrm{m}\right]\lambda_i\left[\mathrm{\mathring{A}}\right]}}.$$

We will also assume that these conditions must be satisfied at least for $\lambda = 8$ Å, thereby being automatically satisfied for $\lambda < 8$ Å but not for $\lambda > 8$ Å. Choosing $P_x^{\,0}$ at (30 ns, 8 Å) ≥ 0.5, the resolution conditions 2(a), (b), and (c) simplify to the approximate relations below, where in (c) we can use the *equality* in condition 1 as representing the *minimum* product B_0L_0 required to achieve 30 ns at 8 Å, i.e., the reference point at which condition 2 must apply:

$$(a)\quad \Delta B_0^{FWHM}\left[\mathrm{T}\right] \;\le\; \frac{1.5\times10^{-6}}{l_{B_0}\left[\mathrm{m}\right]}$$

$$(b)\quad \Delta l_{B_0}^{FWHM}\left[\mathrm{m}\right] \;\le\; \frac{1.5\times10^{-6}}{B_0\left[\mathrm{T}\right]}$$

Condition 2: To achieve $P_x{}^0 \geq 0.5$ at (30 ns, 8 Å) (313).

$$(c)\quad \Delta\theta_{max}\left[\mathrm{rad}\right] \;\le\; \frac{1.12\times10^{-3}}{\sqrt{B_0\left[\mathrm{T}\right]L_0\left[\mathrm{m}\right]}} \;\simeq 4\times10^{-3}$$

Condition 3 amounts to having a total aluminum winding thickness traversed by the neutrons of less than 24 mm. Using the 2:1 winding thickness ratio for the static: r.f. field coil windings used in the example in Sec. 7.3.2, we will treat this condition as only influencing one of the critical parameters in the above list, namely the thickness t of the static field coil windings. The condition for the present purposes is therefore stated as $t \leq 1$ mm on the understanding that the r.f. coil can work satisfactorily with winding thickness ≤ 0.5 mm.

Condition 4 can be stated as

$$8\times10^5\,\frac{B_0\left[\mathrm{T}\right]}{n\left[\mathrm{m^{-1}}\right]} \;\le\; I_{max}\,,$$

where I_{max} is a stated upper limit. If we choose a static field coil upper current limitation of I_{max} = 100 A, condition 4 can be restated as

$$\frac{B_0\left[\mathrm{T}\right]}{n\left[\mathrm{m^{-1}}\right]} \;\le\; 1.25\times10^{-4}$$

Condition 4: To achieve I_{max} < 100 A in the static field coil windings (314).

Condition 5 for aluminum windings amounts to determining the maximum operational power dissipated as heat in the static field coil (i.e., at the maximum operating static field $B_0{}^{max}$) – see Eq. (255), $P(B_0{}^{max})$ and assessing whether it is reasonable:

$$P_{Al}\left(B_0^{max}\right)\left[\mathrm{W}\right] \;=\; \left(B_0^{max}\left[\mathrm{T}\right]\right)^2 \frac{A_{surf}\left[\mathrm{m^2}\right]}{t\left[\mathrm{m}\right]}\left(72.2T\left(\mathrm{K}\right)-4.37\times10^3\right)$$

We will assume an equilibrium winding temperature of $T \approx 400$ K. Minimizing $P(B_0{}^{max})$ in condition 5 is aided by choosing the *maximum* allowable value of t (i.e., 1 mm from condition 3), so that condition 5 becomes:

$$P_{Al}\left(B_0^{max}\right)\left[\mathrm{W}\right] \;=\; 2.45\times10^7\left(B_0^{max}\left[\mathrm{T}\right]\right)^2 A_{surf}\left[\mathrm{m^2}\right],\ T = 400\ \mathrm{K},\ t = t_{max} = 10^{-3}\ \mathrm{m}.$$

We substitute the value of A_{surf} for a rectangular form coil (Eq. (238)) so we have

$$P_{Al}\left(B_0^{max}\right)[\mathrm{W}] \;=\; 4.9\times10^{7}\left(B_0^{max}[\mathrm{T}]\right)^2 l_{axial}[\mathrm{m}]\left(a[\mathrm{m}]+l_{B_0}[\mathrm{m}]\right),\ T = 400\ \mathrm{K},\ t = t_{max} = 10^{-3}\ \mathrm{m}.$$

We will assume from previously-developed coils that l_{axial} and a must be at least about 7 times larger than the beam dimensions to achieve sufficient static field homogeneity over the beam area. For a 3cm × 3cm beam, this translates into $a \approx l_{axial} \approx 0.2$ m. Also $l_{B0} \approx 0.03$ m, therefore, substituting these values for a typical situation we have:

$$P_{Al}\left(B_0^{max}\right)[\mathrm{W}]_{typ} \approx 2.25\times10^{6}\left(B_0^{max}[\mathrm{T}]\right)^2$$ Condition 5: Max power in typical static coil with T = 400 K, t = $t_{max} = 10^{-3}$ m (1 mm), $a \approx l_{axial} = 0.2$ m, $l_{B0} = 0.03$ m(315).

Finally, condition 6 can be stated as (see Eq. (286)):

$$2.5\times10^{4}\,\frac{n_{rf}\left[\mathrm{m}^{-1}\right] l_{axial}^{rf}[\mathrm{m}]\, a_{rf}[\mathrm{m}]}{\langle\lambda_i\rangle\left[\mathrm{\mathring{A}}\right]} B_0^{max}[\mathrm{T}] \;\le\; V_{rf}^{max}$$

where for V_{rf}^{max} = 1500 V, we have

$$\frac{n_{rf}\left[\mathrm{m}^{-1}\right] l_{axial}^{rf}[\mathrm{m}]\, a_{rf}[\mathrm{m}]}{\langle\lambda_i\rangle\left[\mathrm{\mathring{A}}\right]} B_0^{max}[\mathrm{T}] \;\le\; 0.06 \quad \text{for } V_{rf}^{max} \le 1500\ \mathrm{V}.$$

This condition must be true for *all* operating conditions and consequently also for the minimum operating wavelength, which we choose as λ = 2 Å, where the voltage is maximized. Because the r.f. field homogeneity requirements are typically an order of magnitude more relaxed (see Sec. 7.3.4.8) than the required static field homogeneities (see for example Table 7) at high resolution, we will assume that l^{rf}_{axial} and a_{rf} need be only three times the beam size (i.e., we will make $l^{rf}_{axial} = a_{rf} = 0.09$ m). Then condition 6 becomes:

$$n_{rf}\left[\mathrm{m}^{-1}\right] B_0^{max}[\mathrm{T}] \;\le\; 15$$ Condition 6: For $V_{rf}^{max} \le 1500$ V for $l^{rf}_{axial} = a_{rf}$ =0.09 m and $\lambda = \lambda_{min}$ = 2 Å (316).

We make one further simplification to express condition 1 in terms of the maximum B_0 (B_0^{max}) only. The technical conditions 2(b), 4, 5, and 6 are all worst-case at the maximum field (B_0^{max}) that can be obtained in the instrument. We might reduce the maximum necessary field B_0 by reasonably maximizing the inter-coil separation L_0 in condition 1. A value of $L0$ = 2 m is about the longest value that one may envisage in terms of available floor space for the instrument. However the disadvantage of increasing L_0 further is that the instrumental solid angle of acceptance

reduces proportional to $1/L_0^2$. Choosing $L_0 = 2$ m, therefore and also the minimum B_0 of this range which helps alleviate other tolerances, the maximum necessary field (condition 1 - Eq. (312)) becomes:

$B_0^{\max} = 0.0395\,\mathrm{T}$ for L_0=2 m.

Therefore conditions 2(b), 4, 5, and 6 become respectively:

$\Delta l_{B_0}^{FWHM}\left[\mathrm{m}\right] \le 3.8\times10^{-5}$ (i.e., about 38μm or less – see Eq. (313)(b)).

$n\left[\mathrm{m}^{-1}\right] \ge 316$ (Minimum static field coil winding density for I < 100 A – see Eq. (314)).

The minimum achievable power dissipated as heat at the maximum operating field, B_0^{max}, is (from Eq. (315)):

$P_{Al}\left(B_0^{max}\right)\left[\mathrm{W}\right]_{typ} \ge 3510\,\mathrm{W}$ T = 400 K, $t = 10^{-3}$ m, l_{axial} = 0.2 m, l_{B0} = 0.03 m (317).

From Eq. (316) we have:

$n_{rf}\left[\mathrm{m}^{-1}\right] \le 380$ (limiting r.f. coil inductance).

The parameter values 2(c), and 3 have already been determined in this example as $\Delta\theta_{max} \le 4\times10^{-3}$ rad and $t = 10^{-3}$ m respectively.

The remaining parameter range to be determined is 2(a). This is somewhat driven by what is achievable in the coil design, but we have seen (Sec. 7.3.3.7) that small values of l_{B0} aid in achieving the required static field homogeneity. Given that the static field coil must enclose both the r.f. coil and necessary structures for heat removal, we anticipate $l_{B0} \approx 0.03$ m as imposing an approximate practical lower limit on the static field coil length (as has been assumed in many of the examples given above). Using this value, condition 2(a) amounts to designing a coil that can achieve

$\Delta B_0^{FWHM}\left[\mathrm{T}\right] \le 5\times10^{-5}$

For B_0^{max} = 0.0395 T, this corresponds to a static field homogeneity to about 0.13 % or better.

7.5 Coupling coils

The author is grateful to Roland Gähler of the ILL, Grenoble, for providing information about these coils:
The μ-metal shield surrounding the coils cannot be closed because a polarized neutron beam cannot be passed through μ-metal without significant depolarization. Thus the μ-metal tube must be open-ended. The open-ended tube by itself has field lines penetrating partially into the openings, thus in order to maintain control of the

polarization direction at the entrance and exit of the μ-metal shield, coupling coils (CCs) are used. Gähler *et al.* use a μ-metal tube of about 0.1 m diameter into which is introduced a (0.15 to 0.2) m long (in the beam direction), rectangular cross-section CC. Another example of a CC penetration into a μ-metal shield on the NRSE-TAS spectrometer at the FRM-II is shown in Figure 34. The magnetic field axis of the CC is perpendicular to the beam. The residual field of the polarizer (and analyzer) at the entrance (exit) of these coils is usually a few hundred μT. The field magnitude in the CCs is also typically a few hundred μT. The windings on the polarizer side are bent outwards (this is visible in Figure 34) in order to ensure an adiabatic transition from the polarizer field to the CC guide field whilst minimizing neutron scattering and absorption in the CC windings. If the adiabatic condition is met, the neutron spins follow the direction of the CC guide field. On the inner (sample) side of the CCs, the neutrons pass abruptly through the windings and a non-adiabatic transition results, whereby the polarization direction immediately prior to passing through the windings is preserved. In order to ensure this, the CC return fields are conducted sharply into an additional μ-metal shield that surrounds the inner ends of the coil, thus avoiding a gradual stray field gradient downstream that could affect the polarization direction. Finally, the CCs (and hence the polarization direction) can be rotated through 90° without loss of polarization. For the ILL "Zeta" instrument, both the polarizer field and the initial polarization direction is vertical (along *z*). The CCs are used to rotate the polarization to lie along *x* for normal instrument operation, or along *z* for individual tests of the flipper coils.

7.5.1 Conditions for adiabatic and non-adiabatic field transitions

"Adiabatic" and "non-adiabatic" spin transitions in spatially and/or temporally-varying magnetic fields refer to two extremes:

(i) Adiabatic: the spin direction can perfectly follow the field direction at all times.

(ii) Non-adiabatic: the neutron passage is sufficiently fast that the spin cannot follow the change of field direction at all and remains in its original direction.

For the CC it is convenient to consider a rotation of a magnetic field, of constant magnitude B_{guide}, initially parallel to the spin direction, that rotates uniformly through an angle ψ over a flight path length d. The neutron of constant velocity v_n sees in its rest frame a magnetic field rotating at frequency Ω, where

$$\Omega = \psi \frac{v_n}{d} \qquad (318).$$

This situation has been represented graphically in terms of an effective field in a coordinate frame fixed to the rotating field by Ramsey [23] and other authors (see Figure 35). In the *adiabatic* case, $\boldsymbol{B}_{\boldsymbol{eff}} \approx \boldsymbol{B}_{\boldsymbol{guide}}$ (i.e., $\theta \rightarrow 0$), therefore $\boldsymbol{s}$ remains approximately parallel to $\boldsymbol{B}_{\boldsymbol{guide}}$ in the rotating frame and consequently the spin follows the change of direction of the guide field in the lab frame. In the *non-adiabatic* case, $\boldsymbol{B}_{\boldsymbol{eff}} \approx \boldsymbol{\Omega}/\gamma_n$ (approximately independent of B_{guide}, $\theta \rightarrow \pi/2$), and the spins precess at a rate $\gamma \boldsymbol{B}_{\boldsymbol{eff}} \approx \boldsymbol{\Omega}$. In the lab frame, therefore, where B_{guide} rotates with $\boldsymbol{\Omega}$, the spins stand still, i.e., they do not follow the change of direction of B_{guide}. We note that the angle θ is given by

$$\theta = \tan^{-1}\left(\frac{\boldsymbol{\Omega}}{\gamma_n B_{guide}}\right) = \tan^{-1}\left(\frac{\psi v_n}{\gamma_n B_{guide} d}\right) \qquad (319).$$

An order of magnitude for the required guide fields is obtained by considering several examples of an increasing approach to pure adiabatic rotation of spins (decreasing θ) through an angle $\psi = \pi/2$ brought about by a uniform rotation of a guide field (of constant magnitude $|B_{guide}|$) over a flight path of 0.5 m (for example, a typical spacing between the polarizer and the coupling coil). The results are shown in Table 10.

Table 10. Estimated minimum (fixed) guide field magnitudes, $|B_{guide}|$, required to produce a $\pi/2$ rotation of a neutron spin that follows a guide field rotation of $\pi/2$ radians over a distance of 0.5 m. The results show that the guide field magnitude must both increase in order to approach a pure adiabatic transition and also generally increase proportional to neutron velocity, as expected. Insufficient guide field magnitude leads to loss of polarization in the required direction. The actual conditions for adiabatic rotation are usually determined experimentally.

			$\|B_{guide}\|$ for $\theta =$		
v_n(ms^{-1})	λ (Å)	$\Omega(\psi=\pi/2, d=0.5\text{m})=\pi v_n$	$\pi/18$ (10°)	$\pi/180$ (1°)	$\pi/1800$ (0.1°)
1000	≈ 4	1000π	≈ 100 μT	≈ 1 mT	≈ 10 mT
500	≈ 8	500π	≈ 50 μT	≈ 0.5 mT	≈ 5 mT

7.6 Alignment of the B_0 fields using coupling coils

The coupling coils (Sec. 7.5) provide a convenient means of aligning the static fields of the coils in the spectrometer. This may be performed by rotating the field axis of the coupling coil such that the neutron spins are aligned along the required B_0 field axis. The B_0 field of each coil is switched on one at a time and the static field coil is adjusted until the maximum signal is measured in a detector placed downstream of the analyzer.

7.7 Magnetic Shielding

It is essential to reduce net stray field integrals in the "zero-field" flight paths to the order of a few $\times 10^{-7}$ Tm (see Sec. 7.3.5). At high static fields B_0, this partially involves magnetic screening of the individual coils units outside of the beam area. Significant sources of external magnetic fields must also be excluded. For example, the action of the unshielded earth's magnetic field may give rise to a precession of several turns over a typical 2 m drift path, which additionally can vary depending on the orientation of the spectrometer arm. Furthermore, uncompensated neighboring magnetic environments may cause worse complications, especially if the field magnitude changes. Therefore, the neutron drift paths between the coils must also be magnetically shielded.

One of the best magnetic shielding materials is so-called "μ-metal". μ-metal is an alloy with typical composition 75 % Ni, 2 % Cr, 5 % Cu, 18 % Fe, with a density of about 8.75 gcm^{-3}. It has the property of being very soft magnetically, having a very small coercive field and an extremely high permeability at low field strengths. The high permeability is associated with the materials high ability to attract and conduct magnetic flux lines. With a single-skinned, 1 mm thick μ-metal tube, Dubbers *et al* [19] were able to obtain a shielding factor for the earth's magnetic field of about 20, from about 40μT to about 2μT, although the resulting several μTm field integral over 2 m drift paths is still insufficient by nearly a order of magnitude for achieving the goals outlined in Sec. 7.3.5. It has long been known that the magnetic shielding factor is significantly improved by using multiple-skinned shields with intervening air gaps [24, 25]. The specific case for triple-skinned concentric cylindrical and spherical shields was first treated in a simplified mathematical way by Wills [21]. Dubbers [26] further simplified the cylindrical geometry, multi-skinned case for μ-metal in the thin-shell approximation that agrees with the rigorous calculations

to about 1 percent in most cases. Dubbers reiterates that the shielding is most effective when the shell diameters, D_i, grow in geometric progression, i.e.,

$$\frac{D_{i+1}}{D_i} = \kappa \tag{320}$$

where κ is a constant. Using this approximation, the total shielding factor, S, for n concentric shells with constant diameter ratio κ is given approximately by

$$S \approx \left(\frac{\mu_1 t_1}{D_1 \kappa^{\frac{n+1}{2}}} \left(\kappa^2 - 1 \right) + \frac{\left(n\kappa^2 + n - 2 \right)}{n\kappa^2} \right)^n \frac{\kappa^2}{\kappa^2 - 1} \quad \text{valid for } \kappa < \frac{n+1}{n} \tag{321}$$

where $\mu_1 t_1/D_1$ is the shielding factor of the innermost shell of diameter D_1, thickness t_1, and permeability μ_1. Equation (321) demonstrates the value of using high permeability with $n > 1$, given that t_1 cannot be large for practical purposes and D_1 cannot be smaller than allowed by the enclosed instrumentation. However, minimizing D not only increases shielding performance but also reduces the cost and weight of the shield. Magnetic shields should also be closed wherever possible since magnetic field lines can penetrate into openings by up to about five times the opening diameter. Closure better maintains the reluctance path continuity, increasing shielding performance. Shield closures should also be rounded where possible because flux lines negotiate gentle radii better than sharp angles. One disadvantage with the high permeability of μ-metal is its low saturation field (the saturation field is inversely proportional to the permeability). If this proves to be a problem, for example, in the vicinity of a superconducting magnet, the magnetic shielding layer closest to the high field can be fabricated from a lower permeability material to avoid saturation. Successive shielding layers may be fabricated from increasingly high permeability material, as the field magnitude at each layer reduces.

After fabrication of the μ-metal shielding structure, the whole assembly must be annealed in a dry hydrogen atmosphere at about 1200 °C for several hours. The hydrogen atmosphere helps remove carbon and other trace impurities. The high temperature relieves stress, built-up during fabrication, and allows the nickel crystallite grain boundaries to expand. Such an annealing can increase the permeability of the alloy significantly, typically by a factor of 40. However, careful handling of the μ-metal after annealing is required. Mechanical shocks readily disrupt the nickel grain structure and negate gains brought about by the annealing process.

7.8 Beam optics for high-resolution operation

Special corrective beam optics are likely required to achieve the high-resolution goals of the machine. Some evidence for this is presented in Sec. 8.3. A detailed study of the beam optics will be presented in a separately.

8 Monte Carlo simulations of NRSE instrument performance

Some Monte Carlo simulations are presented here that validate some of the analytical models of the NRSE presented in the previous sections. Numerical techniques are invaluable for modeling complex cases where many coupled variables play a role simultaneously, whilst the analytical models are useful for making first estimates of the required instrument parameters.

8.1 Effects of field inhomogeneity, coil length uncertainty, and beam divergence (simplified divergence model) in the absence of flipper dispersion

For *all* calculations in Sec. 8.1 the simplified beam divergence model described in Sec. 6.1.4 is adopted, the incident and scattered beams are assumed to have the *same* uniform divergence, and flipper dispersion is switched *off*. The spectrometer configuration in each case is 4-N=2 bootstrap coils, $L_0 = L_1 = 2$ m, $l_{B0} = 0.03$ m. Figure 36 to Figure 38 show instrumental resolution functions. In Figure 36 the simulation uses approximately equal contributions from field inhomogeneity, coil length uncertainty, and beam divergence, as calculated according to Eqs. (223), (224), and (225) to give an estimated P_x^0 (8 Å , τ_{NRSE} = 30 ns) = 0.7, 0.5, and 0.3 with an incident neutron wavelength of 8 Å. The specific values of ΔB_0(FWHM)/B_0, Δl_{B0}(FWHM), and half-width divergence ($\Delta\theta_{max,i}$ = $\Delta\theta_{max,f}$) calculated using these formulae are the values are shown in the legend. It can be seen that the simulated polarization values at τ_{NRSE} = 30 ns are indeed in good agreement with those predicted by the formulae.

Figure 37 uses the same instrumental uncertainties as those used for the P_x^0 (8 Å , τ_{NRSE} = 30 ns) = 0.5 case in Figure 36 (i.e., ΔB_0(FWHM)/B_0 = 0.13 %, Δl_{B0}(FWHM) = 38.9 μm, and half-width divergence $\Delta\theta_{max,i} = \Delta\theta_{max,f}$ [see Figure 16] = 5.2 mrad), but with a mean incident neutron wavelength $\langle\lambda_i\rangle$ = 12 Å instead of 8 Å. Note that P_x = 0.5 at the longer wavelength occurs at a larger value of τ_{NRSE} (≈ 67.5 ns).

Figure 38 highlights the detrimental effect of having an incident and scattered arm divergence equivalent to that of the of a natural Ni guide at λ = 8Å (i.e., $\Delta\theta_{max,i} = \Delta\theta_{max,f} = \theta_c$(Nat. Ni, λ = 8 Å) ≈ 13.8 mrad in an otherwise

perfect spectrometer ($\Delta B_0 = \Delta l_{B0} = 0$). The simulation is for $\langle \lambda_i \rangle$ = 8 Å and shows that the polarization is almost destroyed by the beam divergence for $\tau_{NRSE} > 15$ ns in this case.

Figure 39 shows a simulation that uses the same instrumental uncertainties as those used for the $P_x^{\,0}$ (8 Å , τ_{NRSE} = 30 ns) = 0.5 case in Figure 36 and in Figure 37 (i.e., ΔB_0(FWHM)/B_0 = 0.13 %, Δl_{B0}(FWHM) = 38.9 μm, and half-width divergence $\Delta\theta_{max,i} = \Delta\theta_{max,f}$ [see Figure 16] = 5.2 mrad), with a mean incident neutron wavelength $\langle \lambda_i \rangle$ = 8 Å only this time the sample is assumed to quasielastically scatter according to a Lorentzian in energy with Γ (HWHM) = 0.025 μeV. The blue curve is the simulated raw (including resolution effects) quasielastic signal (black curve) divided by the resolution function (red curve [also the blue curve in Figure 36]), which is compared with the theoretical intermediate scattering function ($\exp(-\Gamma/\hbar)\tau_{NRSE}$ - green curve) showing good agreement. The corresponding simulated *elastic* (resolution) spin echo signal (asymmetric scan) at τ_{NRSE} = 30 ns (0.0393 T for this geometry) is shown in Figure 40. The simulated *quasi-elastic* spin echo signal (asymmetric scan) at τ_{NRSE} = 30 ns (0.0393 T for this geometry) is shown in Figure 41.

Figure 42 is an identical simulation to that shown in Figure 39 apart from the quasielastic half-width of the Lorentzian is now 0.05 μeV instead of 0.025 μeV. Again very good agreement between theory and simulation is obtained if dispersion is ignored.

8.2 Simulating effects of flipper coil dispersion

All the calculations in this section use the simplified divergence model (see Sec. 6.1.4), where applicable. The π-coils only produce exact π flips for a single wavelength and a perfectly-collimated beam. These approximations are implicit in the formalism presented in Secs. 3.3 and 3.5, which is useful for illustration of the technique. The effects of coil dispersion, described in Sec. 2.2, become apparent when different wavelengths are present. They can be accounted for numerically by applying the following compound transformation on the incident spin vector:

1. Rotate the coordinate system around the z axis so that $x \rightarrow x'$ which points along the mean r.f. field direction (= $[\psi + \psi']/2 = \psi + \omega_{rf}\, t_{coil}/2$) experienced by the neutron during its passage through the coil (duration $t_{coil} = l'/v$), where $l' = l/\cos\theta$, and θ is the polar angle of the trajectory with respect to the positive y-axis.

2. Perform the Larmor rotation due to B_{rf} (angular frequency $\omega_P = \gamma_n B_{rf}$) about x' for a time t_{coil} (total angle = $\omega_p t_{coil}$).

3. Transform the resulting spin vector back into lab frame.

i.e.,

$$\begin{pmatrix} \sigma_x' \\ \sigma_y' \\ \sigma_z' \end{pmatrix} = \begin{pmatrix} \cos\left(sign\left(B_0\right)\left[\left|\psi\right| + \frac{\gamma_n B_0 l}{2v\cos\theta}\right]\right) & \sin\left(sign\left(B_0\right)\left[\left|\psi\right| + \frac{\gamma_n B_0 l}{2v\cos\theta}\right]\right) & 0 \\ -\sin\left(sign\left(B_0\right)\left[\left|\psi\right| + \frac{\gamma_n B_0 l}{2v\cos\theta}\right]\right) & \cos\left(sign\left(B_0\right)\left[\left|\psi\right| + \frac{\gamma_n B_0 l}{2v\cos\theta}\right]\right) & 0 \\ 0 & 0 & 1 \end{pmatrix}^{-1} \begin{pmatrix} 1 & 0 & 0 \\ 0 & \cos\left(\frac{\gamma_n B_{rf} l}{v\cos\theta}\right) & -\sin\left(\frac{\gamma_n B_{rf} l}{v\cos\theta}\right) \\ 0 & \sin\left(\frac{\gamma_n B_{rf} l}{v\cos\theta}\right) & \cos\left(\frac{\gamma_n B_{rf} l}{v\cos\theta}\right) \end{pmatrix} \cdot$$

$$\begin{pmatrix} \cos\left(sign\left(B_0\right)\left[\left|\psi\right| + \frac{\gamma_n B_0 l}{2v\cos\theta}\right]\right) & \sin\left(sign\left(B_0\right)\left[\left|\psi\right| + \frac{\gamma_n B_0 l}{2v\cos\theta}\right]\right) & 0 \\ -\sin\left(sign\left(B_0\right)\left[\left|\psi\right| + \frac{\gamma_n B_0 l}{2v\cos\theta}\right]\right) & \cos\left(sign\left(B_0\right)\left[\left|\psi\right| + \frac{\gamma_n B_0 l}{2v\cos\theta}\right]\right) & 0 \\ 0 & 0 & 1 \end{pmatrix} \begin{pmatrix} \sigma_x \\ \sigma_y \\ \sigma_z \end{pmatrix}$$

(322).

8.2.1 Numerical verification of analytical approximations for coil dispersion

The validity of the approximations represented by Eqs. (46), (48), and (49) (see Sec. 2.2.2) for describing the depolarizing effects of coil dispersion for *M* coils is easily demonstrated by Monte simulations in which coil dimension errors, field fluctuations, and beam divergence are all switched *off*, with "perfect" polarizers, and no sample (or perfectly-collimated elastic scattering), and with dispersion switched *on* according to Eq. (322). In this case, the simulated polarization with respect to the *x*-axis at the exit of the spectrometer should be approximately equal to the values given by the above equations for rectangular, triangular, and Gaussian-shaped incident wavelength spectra. Results for rectangular wavelength spectra with $\alpha_{FW} = \Delta\lambda_i^{FW}/\langle\lambda_i\rangle$ between 0.1 and 0.5 are shown in Figure 43. Results for triangular and Gaussian wavelength spectra with $\alpha_{FWHM} = \Delta\lambda_i^{FWHM}/\langle\lambda_i\rangle$ between 0.1 and 0.5 are shown in Figure 44 and Figure 45 respectively. The results for $\alpha_{FW(FWHM)} = 0.2$ show that the approximations made in Sec. 2.2.2 for extending the single coil case to the *M*-coil case are accurate to about 0.06 % (rectangular) and about 0.4 % (triangular or Gaussian). For $\alpha_{FW(FWHM)} = 0.5$, the approximations are accurate to about 2.2 % (rectangular) and about 6 % (triangular or Gaussian).

8.2.2 Simulations of spectrometer signal with flipper coil dispersion turned on

All the simulations in this section use the same basic spectrometer configuration as used in Sec. 8.1, namely 4-N = 2 bootstrap coils, $L_0 = L_1$ = 2 m, l_{B0} = 0.03 m, l_g=1 mm. Additionally $\langle\lambda_i\rangle$ = 8 Å and the instrumental uncertainty parameters calculated according to Eqs. (223), (224), and (225) that give a predicted combined effect (in the dispersionless case) of P_x^0 (8 Å , τ_{NRSE} = 30 ns) = 0.5 (i.e., ΔB_0(FWHM)/B_0 = 0.13 %, Δl_{B0}(FWHM) = 38.9 μm, and half-width divergence $\Delta\theta_{max,i} = \Delta\theta_{max,f}$ = 5.2 mrad). However, now with dispersion the incident wavelength monochromatization, $\Delta\lambda_i^{FWHM}/\langle\lambda_i\rangle$, comes into play.

Figure 46 shows the dispersive elastic resolution function for $\Delta\lambda_i^{FWHM}/\langle\lambda_i\rangle$ = 10 % (triangular) (black curve) with the above instrumental uncertainties. The blue curve is the equivalent resolution function in the absence of dispersion (which is also the blue curve in Figure 36 and the red curves in Figure 39 and Figure 42). The red curve is the simulated resolution function for $\Delta\lambda_i^{FWHM}/\langle\lambda_i\rangle$ = 10% in the absence of instrumental imperfections (i.e., the simulated effect of the dispersion in isolation, which is practically independent of τ_{NRSE}). The green curve is the result of dividing the dispersive resolution function by the effect of the dispersion in isolation (red curve) which essentially reproduces the dispersionless resolution function. In this case, therefore, the effect of the dispersion due to $\Delta\lambda_i^{FWHM}/\langle\lambda_i\rangle$ = 10% is to reduce the polarization to about 97% of the dispersionless resolution for all τ_{NRSE}.

Figure 47 shows the identical resolution function simulation as that in Figure 46 apart from the incident wavelength band has been increased from $\Delta\lambda_i^{FWHM}/\langle\lambda_i\rangle$ = 10% (triangular) to $\Delta\lambda_i^{FWHM}/\langle\lambda_i\rangle$ = 30% (triangular). The larger incident wavelength band has a significantly larger but still approximately τ_{NRSE}-independent effect on the resolution function. In this case the effect of the dispersion due to $\Delta\lambda_i^{FWHM}/\langle\lambda_i\rangle$ = 30% is to reduce the polarization to about 79% of the dispersionless resolution for all τ_{NRSE}.

Figure 48 is the exact analogue of the quasielastic simulation shown in Figure 39 (also with Γ(FWHM) = 0.025 μeV) except that dispersion is now turned on with the broad incident wavelength band of $\Delta\lambda_i^{FWHM}/\langle\lambda_i\rangle$ = 30% (triangular). The blue curve is the simulated raw (including resolution effects) quasielastic signal (black curve) divided by the resolution function (red curve [also the black curve in Figure 47]), which is compared with the theoretical intermediate scattering function ($\exp(-\Gamma/\hbar)\tau_{NRSE}$ - green curve). Even for the very broad $\Delta\lambda$, there is quite reasonable agreement between the blue and the green curve. The simulated elastic (resolution) spin-echo signal and

quasi-elastic spin-echo signal (asymmetric scans) at τ_{NRSE} = 30 ns (0.0393 T for this geometry, dispersive case) are shown in Figure 49 and Figure 50, respectively.

8.3 Simulations with an improved divergence model and sample/beam size effects (no corrective optics)

In the previous calculations (Sec. 8.1 and Sec. 8.2) the simplified beam divergence model (Sec. 6.1.4) was used to verify the validity of the analytical approximations given in Sec. 6.1. This model is useful for predicting orders of magnitude of resolution effects. However, the incident beam is usually provided by a neutron guide that gives rise to approximately random *x* and *z* components of the trajectory angle up to maxima of $\theta_c^x(\lambda_i)$ and $\theta_c^z(\lambda_i)$ respectively. Furthermore, the scattered beam divergence, in the absence of special optics, is usually defined by the sample and the collimation between the sample and the detector. This more realistic situation is sketched in Figure 51 and forms the basis of the model used in the following calculations. For the polar angle θ_i at the guide exit, we have

$$\tan\theta_i = \sqrt{\left(\tan\theta_x\right)^2 + \left(\tan\theta_z\right)^2} \qquad (323)$$

or in the small angle approximation

$$\theta_i = \sqrt{\theta_x^2 + \theta_z^2} \qquad (324).$$

If the spectrometer is designed to accept this angular range, the polar angle θ_i also characterizes the beam divergence in the incident arm of the spectrometer.

In the small angle approximation (Eq. (324)), we can readily calculate the probability density distribution of the polar angle θ produced by an ideal guide. This situation is illustrated in Figure 52 for a general case where $\theta_x \neq \theta_z$. Equation (324) represents an arc of a circle of radius θ with origin (θ_x, θ_z) = (0, 0), confined to the box whose upper limits are $\theta_x = \theta_c^x$ and $\theta_z = \theta_c^z$. Because the θ_x and θ_z distributions are assumed to be uniform, the probability density for a polar angle θ is just proportional to the length of the arc segment of radius θ. Therefore, we have

$$P(\theta) = \frac{\pi}{2}\frac{\theta}{\theta_c^x\theta_c^z} \qquad \text{for } \theta \le \min\left(\theta_c^x, \theta_c^z\right) \qquad (325),$$

$$P(\theta)=\left[\frac{\pi}{2}-\cos^{-1}\left(\frac{\min\left(\theta_c^x,\theta_c^z\right)}{\theta}\right)\right]\frac{\theta}{\theta_c^x\theta_c^z} \qquad \text{for } \min\left(\theta_c^x,\theta_c^z\right)<\theta\le\max\left(\theta_c^x,\theta_c^z\right) \quad (326),$$

and

$$P(\theta)=\left[\frac{\pi}{2}-\cos^{-1}\left(\frac{\theta_c^x}{\theta}\right)-\cos^{-1}\left(\frac{\theta_c^z}{\theta}\right)\right]\frac{\theta}{\theta_c^x\theta_c^z} \qquad \text{for } \max\left(\theta_c^x,\theta_c^z\right)<\theta\le\sqrt{\left(\theta_c^x\right)^2+\left(\theta_c^z\right)^2} \quad (327).$$

where the denominator $\theta_c^x \times \theta_c^z$ is the area of the rectangle which normalizes $P(\theta)$ to unit area for uniform $P(\theta_x)$ and $P(\theta_z)$. The probability density distribution, $P(\theta)$, for the case illustrated on the left of Figure 52 is shown on the right of the figure. It is immediately obvious that $P(\theta)$ is far from uniform, whence the main weakness of the simplified divergence model (Sec. 6.1.4) is identified. The simpler case of equal horizontal and vertical divergence gives $\theta_c^x = \theta_c^z = \theta_c$ and the above Eqs. for $P(\theta)$ reduce to

$$P(\theta)=\frac{\pi}{2}\frac{\theta}{\theta_c^2} \qquad \text{for } \theta\le\theta_c \qquad (328)$$

and

$$P(\theta)=\left[\frac{\pi}{2}-2\cos^{-1}\left(\frac{\theta_c}{\theta}\right)\right]\frac{\theta}{\theta_c^2} \qquad \text{for } \theta_c<\theta\le\sqrt{2}\theta_c \qquad (329).$$

The resulting $P(\theta)$ function is illustrated in Figure 53. Therefore, clearly an improved model is necessary for rigorous calculations.

In the following more realistic calculations, all coils are assumed to have equally sized beam-defining windows at their entrances and exits. The entrance of the first coil is assumed to be uniformly-illuminated with a beam that has uniform *x*-*y* and *z*-*y* plane angular distributions with θ up to $\theta_c^x(\lambda_i) = \kappa_x\lambda_i$ and $\theta_c^z(\lambda_i) = \kappa_z\lambda_i$ respectively, where κ_x and κ_z are independently-specified constants. The sample is assumed to be a thin cylindrical shell of radius *r* with its axis along the *z*-direction (about the worst typically-encountered sample geometry with respect to maximum flight-path differences). The neutron trajectories arriving at the sample are those that can be drawn between random points on the first coil entrance window to random points on the sample without obstruction, subject to the conditions that $|\theta_x| \le \theta_c^x(\lambda_i)$ and $|\theta_z| \le \theta_c^z(\lambda_i)$. The sample is assumed to be an isotropic scatterer with no self-shielding so that all possible trajectories between the scattering point to the exit window of the last coil are assumed to be equally probable and 100% detected.

Figure 54 shows examples of resolution functions using this model for $\lambda = 8$ Å with $\Delta\lambda/\lambda = 10$ % (triangular) for three coil window sizes ($W_{win} = H_{win} = 1$ cm, 2 cm, and 3 cm) assuming that a natural Ni guide (i.e., with $\kappa_x = \kappa_z = 1.73\times10^{-3}$ rad Å^{-1}) is placed very close to the entrance to the first coil. The diameter, d_s, and the height, h_s, of the sample in each case were chosen so that the projected sample cross-sectional area is equal to the window size (i.e., $d_s = W_{win}$, $h_s = H_{win}$). For ease of comparison with results in the previous section, the dimensions of the spectrometer were chosen identical ($L_0 = 2$ m, $l_\pi = 0.03$ m, $N = 2$) and $\Delta B_0/B_0$ and Δl_{B0} were chosen to have exactly the values that gave $P_x^0(\lambda = 8$ Å, $\tau_{NRSE} = 30$ ns) = 0.5 with the simplified divergence model (non-dispersive case). The differences with respect to Figure 36 are then attributable to the different incoming and outgoing beam divergences and to the cylindrical sample geometry. Note that the only curve in Figure 54 to resemble the curves in Figure 36 is for the smallest window size (1 cm × 1 cm). For each of the three cases shown in Figure 54, $W_{win}/L_0 < \theta_c$(8Å) for $W_{win}(H_{win})$ = 1 cm, 2 cm and $W_{win}/L_0 \approx \theta_c$(8Å) for $W_{win}(H_{win})$ = 3 cm, so we expect that the coil windows more-or-less determine both the incoming and outgoing beam divergence in all three cases. The Monte-Carlo-generated $P(\theta)$ for the incoming (*i*) and scattered (*f*) trajectories of *detected* neutrons, corresponding to the cases in Figure 54, are shown in Figure 55. For comparison, Monte Carlo values of $P(\theta)$ for $W_{win}(H_{win}) = 3$ cm and $\lambda_i = 1$ Å are shown in Figure 56. In this case, $W_{win}/L_0 \approx 9\theta_c$(1 Å), therefore we expect that the *incoming* beam divergence is driven by the guide characteristics rather than the coil window size. We see from Figure 56 that $P(\theta)$ for the *incident* neutrons indeed resembles that of the guide (c.f. Figure 53), whereas the scattered divergence is determined more by $W_{win}(H_{win})$ and resembles that of the maroon curve in Figure 55, as expected. It is clear from Figure 54 that the degradation of the resolution function caused by increasing W_{win} (H_{win}) limits the size of these windows unless additional corrective optics is applied to narrow the flight path distribution through the spectrometer. For example, in the context of being able to perform useful measurements at $\tau_{NRSE} = 30$ ns with $\lambda_0 = 8$ Å, the use of 3 cm × 3 cm windows without corrective optics gives an unacceptably poor signal (see Figure 54). Even 2 cm × 2 cm is on the limit of being useful in this case.

Studies of corrective optics permitting the use of larger incident beam sizes and larger scattered beam solid angles will be presented elsewhere.

9 Towards the definition of the NIST NRSE instrument

9.1 Possibilities using MIEZE-II configuration

9.1.1 General instrument features

The general features of the so-called MIEZE-II spectrometer [27] are shown in Figure 57. In the configuration shown, the MIEZE-II can be equated to a multi-arm version of a conventional anti-symmetric arrangement of flipper coils but with the fourth coil unit replaced by a "thin" detector at exactly the same position. (The second and third bootstrap coils are formed by the annular coil surrounding the sample area). In contrast to similarly-named MIEZE ("Modulation of Intensity Emerging from Zero Effort!") spectrometers, the r.f. frequency of the three coil units is identical. The discussion in Sec. 4.2.1.3 illustrates what happens when the 4th coil unit is absent: When the r.f. angular frequency is tuned to the Larmor frequency, ω_0, the spin up and spin down states of the neutron retain their kinetic energy spitting after leaving the third coil unit, corresponding of a precessional angular frequency of $2\omega_0$ (for $N = 1$ coils) or $4\omega_0$ (for $N = 2$) coils. Because the quasielastic echo point is found for $L_0 = L_1$ for the 4 (identical) coil unit arrangement, a modulation in the detected intensity at angular frequency $2\omega_0$ ($N = 1$) or $4\omega_0$ ($N = 2$) is found when the separation between the third coil center and the detector plane is equal to the separation of the first and second coil center planes (L_0). At this position, the intensity oscillates between the maximum and minimum polarization states with maximum amplitude.

9.1.2 Toroidal r.f. solenoid

An annular π-flipper that serves as the 2nd and 3rd coil units (as illustrated in Figure 57) would be a novel development for NRSE. It is conceivable that the r.f. coil could be constructed as a single rectangular cross-section toroidal solenoid as long as the voltages can be kept within reasonable limits.

9.1.2.1 Self-inductance of the toroidal r.f. solenoid

The self-inductance for a toroidal r.f. solenoid or toroid radius r_{toroid} is approximately

$$L = \frac{\mu_0 N_{rf}^2 A_{rf}}{l_{axial}^{rf}} = \frac{\mu_0 N_{rf}^2 A_{rf}}{2\pi r_{toroid}} \qquad (330)$$

where N_{rf} is the total number of turns on the r.f. solenoid, l^{rf}_{axial} is the axial length of the solenoid (in this case the mean circumference) ($l^{rf}_{axial} = 2\pi r_{toroid}$), and A_{rf} is the cross-sectional area of the solenoid (the area enclosed by a single winding). Substituting the winding density n_{rf} (= N_{rf}/l^{rf}_{axial}) into Eq. (330), we have

$$\begin{aligned} L_{toroid}\left[\mathrm{H}\right] &= 2\pi r_{toroid}\mu_0 n_{rf}^2 A_{rf} \quad = \quad 8\pi^2\times10^{-7}\left(n_{rf}\left[\mathrm{m}^{-1}\right]\right)^2 r_{toroid}\left[\mathrm{m}\right]A_{rf}\left[\mathrm{m}^2\right] \\ &= 7.9\times10^{-6}\left(n_{rf}\left[\mathrm{m}^{-1}\right]\right)^2 r_{toroid}\left[\mathrm{m}\right]A_{rf}\left[\mathrm{m}^2\right] \end{aligned} \qquad (331).$$

We now consider the probable dimensions of the toroidal coil. The uncertainty on $B_{rf}\times l_{rf}$ may be somewhat relaxed for the r.f. coils when compared with that required for the static field coils at the highest values of B_0 because only a single π rotation of the spin is required around B_{rf}. The flipping efficiency is naturally limited by coil dispersion so that relaxing the tolerance on $\Delta(B_{rf}l_{rf})$ must usually be accompanied by a restriction of the bandwidth, $\Delta\lambda$ (see Sec. 7.3.4.8). Nonetheless, it is likely that the r.f. coil does not have to be greatly oversized with respect to the beam height in order to achieve a field homogeneity that is not too costly in bandwidth. From Eq. (286), for a toroidal coil, we may substitute $2\pi r_{toroid}$ for l_{axial}. If we impose a high voltage restriction $V_{rf}^{pk} \leq 1500$ V we end up with

$$\frac{n_{rf}\left[\mathrm{m}^{-1}\right]r_{toroid}\left[\mathrm{m}\right]a_{rf}\left[\mathrm{m}\right]}{\left\langle\lambda_i\right\rangle\left[\mathrm{\mathring{A}}\right]}B_0\left[\mathrm{T}\right] \quad \leq 9.5\times10^{-3} \qquad (332).$$

We assume that a coil height (side of the rectangle perpendicular to the beam direction) $a_{rf} \approx 0.1$ m provides sufficient r.f. field homogeneity within the beam area. The toroid radius, r_{toroid}, must be sufficiently large to accommodate sample environments. A reasonable value is $r_{toroid} \approx 0.3$ m. The choice of r_{toroid} does not affect the instrumental resolution but it may affect the usable solid angle. In order to estimate the worst case we use the maximum envisioned value of B_0 and the minimum value of $\langle\lambda_i\rangle$ (about 0.04 T and 2 Å respectively), then it follows from Eq. (332) that $n_{rf}(B_0 = 0.04\ T, \langle\lambda_i\rangle = 2$ Å, $r_{toroid} = 0.3$ m, $a_{rf} = 0.1$ m) ≤ 16 m^{-1} (or 1 turn every 6.3 cm) to maintain the r.f. voltage within acceptable ranges at the spectrometer limits.

9.1.2.2 Resistance and inductive reactance of the toroidal r.f. solenoid

The resistance of the r.f. coil winding is

$$R_{toroid} = \rho(T)\frac{l_w^{rf}}{A_w^{rf}} \tag{333},$$

where l_w^{rf} is the total length of the r.f. winding and A_w^{rf} is the cross-sectional area of the r.f. winding, i.e.,

$$l_w^{rf} \approx 4\pi r_{toroid}\, n_{rf}\left(a_{rf} + l_{rf}\right) \tag{334}$$

and

$$A_w^{rf} = t_{rf} h_{rf} \tag{335}$$

so that Eq. (333) may be rewritten as

$$R_{toroid} = \rho(T)\frac{4\pi r_{toroid}\, n_{rf}\left(a_{rf} + l_{rf}\right)}{t_{rf} h_{rf}} \tag{336}.$$

Using the above example with l_{rf} = 0.025 m and r_{toroid} = 0.3 m, the perimeter of one winding is $2(a_{rf}+l_{rf})$ = 0.25 m, the total length of the r.f. winding for n_{rf} = 16 m^{-1} is approximately $l_w^{rf}(n_{rf}$ = 16 m^{-1}, a_{rf} = 0.1 m, l_{rf} = 0.025 m) ≈ $25r_{toroid}$ ≈ 7.5 m. If the windings are rectangular and the maximum width possible (tightly wound), we can set the width of the winding $h_{rf} = h_{rf}^{max} \approx 1/n_{rf}$. For n_{rf} = 16 m^{-1}, we have h_{rf} ≈ 0.063 m. Choosing a value for the winding thickness in the beam direction $t_{rf} = t_{max}$ = 400 μm given in Sec. 7.3.2, the cross-sectional area of the aluminum winding is A_w^{rf} = $4\times10^{-4}/16 = 2.5\times10^{-5}$ m^2 (0.25 cm^2). The minimum resistance of the rectangular section winding is therefore

$$R_{toroid}^{min}[\Omega] \approx 3\times10^{5}\rho(T)[\Omega\text{m}] \tag{337}.$$

Specifically for pure aluminum windings (using Eq. (254)), we have

$$R_{Al}^{toroid}(T)[\Omega] = \left(1.43\times10^{-9}T[K] - 8.7\times10^{-8}\right)\frac{r_{toroid}[\text{m}]\, n_{rf}\left[\text{m}^{-1}\right]\left(a_{rf} + l_{rf}\right)[\text{m}]}{t_{rf}[\text{m}]\, h_{rf}[\text{m}]} \tag{338}$$

and for this specific geometry case we have

$$R_{toroid}^{min}\{\text{Al}\}(T)[\Omega] \approx 3.44\times10^{-5}T(\text{K}) - 2.08\times10^{-3} \tag{339}.$$

If the r.f. coil could be maintained at about 300K, $\rho_{Al} \approx 2.73\times10^{-8}$ Ωm, then the resistance of the winding is approximately R_{toroid}^{min}\{Al\}(T = 300 K, r_{toroid} = 0.3 m, $t_{rf} = 4\times10^{-4}$ m, n_{rf} =16 m^{-1}) ≈ 8 mΩ. The inductive reactance of the r.f. coil is given by

$$X_L[\Omega] = \omega_{rf}\left[\text{s}^{-1}\right]L[\text{H}] \tag{340}.$$

At B_0 = 0.04 T, when the coil is on resonance, from Eq. (9) we have $\omega_{rf} \approx 7.3\times10^6$ rad s^{-1} (ν_{rf} = 1.17 MHz). For n_{rf} = 16 m^{-1}, r_{toroid} = 0.3 m, and choosing $A_{rf} = 2.5\times10^{-3}$ m^2, we have from Eq. (331) $L \approx 1.5$ μH, from which we have $X_l \approx$ 11 Ω. Therefore, $X_l \gg R_{toroid}$ at the highest frequencies (in this example more than three orders of magnitude).

9.1.2.3 Current and power dissipated in r.f. coil

In order to reach a maximum required r.f. field magnitude of about 2.7 mT (see Sec. 7.3.4.3), with a winding density $n_{rf} = n_{rf}(r_{toroid} = 0.3 \text{ m}) = 16$ m^{-1}, from Eq. (233), we require a peak current of $I_{pk} \approx 2.7\times10^{-3}/(1.26\times10^{-6}\times 16)$ = 134 A! Therefore, having eliminated the high voltage problem we appear to run into problems with peak current. *This may ultimately impose restrictions on the minimum wavelength*. Nonetheless, because the load is almost entirely inductive at high frequencies (see Sec. 9.1.2.2), the high frequency current in the coil lags the voltage by approximately 90°. The heat dissipated in the r.f. coil is only that due to the resistance. In the example given in Sec. 9.1.2.2 for room temperature aluminum windings of cross-sectional area 0.25 cm^2, $R_{toroid} \approx 8$ mΩ, therefore the maximum r.m.s. power dissipated in the r.f. coil is approximately $P_{RMS}^{rf}\{\text{Al}\}(T = 300 \text{ K}, r_{toroid} = 0.3 \text{ m}, n_{rf} = 16 \text{ m}^{-1}, A_w^{rf} = 2.5\times10^{-5} \text{ m}^2) \approx (134/\sqrt{2})2 \times 8\times10^{-3} \approx 72$ W. This is not excessive.

9.1.3 Requirements for the MIEZE detection system

As shown in Sec. 6.1.6, high-resolution operation requires flight path length uncertainties no greater than several tens of microns and frequencies in the 1 MHz range. Therefore, the active part of the detector is required to be flat and thin whilst capturing neutron events within thicknesses of only tens of microns. The most suitable detector type appears to be a scintillator-photomultiplier combination. The small event capture depth has implications for the efficiency of the detector system and probably requires a ^{6}Li-glass, ^{6}LiF/ZnS:Ag, or ^{6}LiF/ZnS:Cu,Al,Au-type scintillator. Such scintillators also have the advantages of rapid decay times with no afterglow. The response time of the data acquisition system should preferably be in the 1 ns to 10 ns range and must be able to handle up to about 4 MHz gated signals if N = 2 bootstrap coils are used (note the signal is a frequency $4\omega_0$ for N = 2 – see Sec. 9.1.1).

9.2 Permanent magnet options for NRSE

One problem associated with the static field coil is that neutron absorption and scattering in the appreciable number of windings traversed by the beam imposes a strict upper limit on the winding thickness parallel to the

beam. As we saw in Sec. 7.3.3.1, this may lead to high power dissipation in the coil at high fields. One may envisage replacing the static field coils by a ferromagnetic or anti-ferromagnetic material that transmits neutrons. Because the static field magnitude can no longer be varied, a scan of τ_{NRSE} must involve a *symmetrical* scan of the coil separation in both arms of the spectrometer whilst maintaining $\delta(BL) = 0$ (the echo point). This contrasts with changing the static field magnitude at $\delta(BL) = 0$ in the coil case. A schematic of a quasi-elastic NRSE spectrometer using permanent magnets to provide the static field ($N = 1$) is shown in Figure 58.

9.2.1 Comparison of static field coils versus permanent magnets for NRSE

(a) Coil

- τ_{NRSE} scan is performed usually by fixing L_0 and varying B_0.
- Requires anodized aluminum windings.
- High resolution applications require very flat and parallel windings.
- Flat thin (in beam direction) Al windings make production of (0.03 to 0.04) Tesla fields challenging. Heat dissipation is proportional to the coil surface area (can be several kW for several tens of mT with typical Al windings unless cryogenically cooled).
- Coil cooling is hampered within beam area.

(b) Permanent magnet

- τ_{NRSE} scan with fixed B_0, B_1 and varying *both* L_0 and L_1.
- High resolution applications require essentially the same tolerances (but probably easier to achieve).
- Field homogeneity should be very good inside the magnet and field boundaries are abrupt.
- Requires high transmission/ low scattering material.
- Magnet must reside *inside* the r.f. coil - requires an electrically insulating magnetic material.
- Magnet possibly requires an externally-applied saturation field.
- Fixed r.f. frequency - (no r.f. circuit tuning, fixed impedance).
- Resonance width requires similar field magnitudes in each magnet to within a few tens of μT.
- No heat removal problem.

- Compact with no coil circuitry (electrical or cooling).

9.2.2 Definition of the required instrument parameters using permanent magnets

In the following, we develop a set of inequalities defining parameter boundaries required to achieve the requested performance of the spectrometer using permanent magnets. By no means do the parameters referred to here constitute an exhaustive list but they are significant contributing factors that drive the instrument performance.

9.2.2.1 Coil unit geometry

The coil unit would consist of a permanent magnetic material surrounded by the r.f. coil (with a perpendicular field axis) as shown in Figure 59. We will henceforth make reference to the dimensions given in Figure 59.

9.2.2.2 B_0L_0 magnitude criterion for accessing τ_{NRSE} = 30 ns at λ = 8 Å

The goal of accessing τ_{NRSE} = 30 ns at λ = 8 Å is expressed by Eq. (226). If we assume that there is an upper limit on L_0 imposed by spatial constraints (represented by L_0^{max}), then we may define a minimum *required* value of B_0 criterion as:

$$B_0^{max}\left[\mathrm{T}\right] \geq \frac{0.157}{NL_0^{\max}\left[\mathrm{m}\right]} \qquad \text{minimum } B_0 \text{ magnitude to reach } \tau_{NRSE} = 30 \text{ ns at } \lambda = 8 \text{ Å} \qquad (341).$$

9.2.2.3 Minimum wavelength (λ = 2 Å) r.f. voltage criterion

An approximate expression for the r.f. voltage in terms of the r.f. coil parameters and the neutron wavelength is given by Eq. (286), where a_{rf} and l^{rf}_{axial} are given in Figure 59:

$$V_{rf}^{pk}\left[\mathrm{V}\right] \approx 2.5\times10^4 \frac{n_{rf}\left[\mathrm{m}^{-1}\right] l^{rf}_{axial}\left[\mathrm{m}\right] a_{rf}\left[\mathrm{m}\right]}{\left\langle \lambda_i \right\rangle \left[\mathrm{\overset{o}{A}}\right]} B_0\left[\mathrm{T}\right] \qquad (342),$$

where we know that a_{rf} cannot be smaller than the beam height, say $a_{rf}^{min} \approx 0.03$ m. Making this maximum voltage criterion compatible with typical high voltage cable ratings (see Sec. 7.3.4.3), we have

$$V_{rf}^{max} < 1500\mathrm{V} \qquad (343)$$

which, from Eq. (342), equates to

$$\frac{n_{rf}\left[\mathrm{m}^{-1}\right] l_{axial}^{rf}\left[\mathrm{m}\right] a_{rf}\left[\mathrm{m}\right]}{\left\langle \lambda_i \right\rangle \left[\mathrm{\mathring{A}}\right]} B_0^{max}\left[\mathrm{T}\right] \quad \leq \quad 0.06 \qquad (344)$$

as was the case in Sec. 7.4. We take the most demanding minimum operating wavelength, which we assume to be λ = 2 Å, therefore

$$n_{rf}\left[\mathrm{m}^{-1}\right] l_{axial}^{rf}\left[\mathrm{m}\right] a_{rf}\left[\mathrm{m}\right] B_0^{max}\left[\mathrm{T}\right] \quad \leq \quad 0.12 \qquad (345).$$

We remember that B_0 is also subject to the constraint (341), therefore we require

$$L_0^{max}\left[\mathrm{m}\right] \geq 1.3 \frac{n_{rf}\left[\mathrm{m}^{-1}\right] l_{axial}^{rf}\left[\mathrm{m}\right] a_{rf}\left[\mathrm{m}\right]}{N} \quad \text{maximum r.f. voltage at min } \lambda \text{ (= 2 Å) criterion} \qquad (346).$$

9.2.2.4 Required Resolution: Tolerance criteria for B_0, l_{B0}, and beam divergence

In order to ensure an elastic signal magnitude of at least $P_x^{\,0}$ at $\tau_{NRSE}(\lambda = 8\ \text{Å}) = 30$ ns, maximum tolerances on the values of B_0, l_{B0}, and the divergence $\Delta\theta$ are imposed. If the contributions to the depolarization of the beam due to the uncertainties in these parameters are equal, we can use Eqs. (223), (224), and (225), for $\Delta B_0^{\,FWHM}$, $\Delta l_{B0}^{\,FWHM}$, and $\Delta\theta_{max}$ respectively. We assume that the intrinsic field variation in the permanent magnet is a fixed property of the material of magnitude ΔB_{mat} and that the material can be cut to no better than an uncertainty of Δl_{mat} in the beam direction. If we choose a resolution signal $P_x^{\,0}(\tau_{NRSE} = 30\ \text{ns}, \lambda = 8\ \text{Å}) \geq 0.5$ then Eq. (223) can be rewritten in terms of a condition on the variable parameter l_{B0}, i.e.,

$$l_{B_0}\left[\mathrm{m}\right] \leq \frac{2.2\times10^{-6}}{\sqrt{N}\Delta B_{mat}\left[\mathrm{T}\right]} \qquad \text{originating from } \Delta B_0 \text{ criterion} \qquad (347),$$

where we have substituted $\langle\lambda\rangle$ = 8 Å from our reference point. Note that this condition should not be especially demanding for any realistically attainable ΔB_{mat}. Likewise, for the same requirements $P_x^{\,0}(\tau_{NRSE} = 30\ \text{ns}, \lambda = 8\ \text{Å}) \geq 0.5$, the tolerance condition (224), once Δl_{mat} has reached a reasonable minimum value, imposes a condition on the magnitude of B_0, i.e.,

$$B_0\left[\mathrm{T}\right] \leq \frac{2.2\times10^{-6}}{\sqrt{N}\Delta l_{mat}\left[\mathrm{m}\right]} \qquad (348),$$

subject to the minimum required B_0 condition (Eq. (341)), from which we have

$L_0^{max}\left[\mathrm{m}\right] \geq 7.1\times10^4 \dfrac{\Delta l_{mat}\left[\mathrm{m}\right]}{\sqrt{N}}$ originating from Δl_{B0} criterion and minimum required B_0 criterion (349).

Applying the $P_x^0(\tau_{NRSE} = 30\text{ ns}, \lambda = 8\text{ Å}) \geq 0.5$ resolution condition to Eq. (225), we have

$$\left(\Delta\theta_{max}\left[\mathrm{rad}\right]\right)^2\left(\lambda = 8\,\mathrm{\mathring{A}}\right) \leq \frac{4.3\times10^{-6}}{NB_0\left[\mathrm{T}\right]L_0\left[\mathrm{m}\right]} \quad (350),$$

subject to the condition (341) which leads to

$\Delta\theta_{max}\left(\lambda = 8\,\mathrm{\mathring{A}}\right) \leq 5.2\times10^{-3}$ rad maximum divergence criterion for $P_x^0(\tau_{NRSE} = 30\text{ ns}, \lambda = 8\text{ Å})$ (351).

9.2.2.5 Tolerance criterion for B_{rf} - r.f. penetration of the permanent magnet and absorbed r.f. power

Variations of the magnitude of B_{rf} within the static field region lead to reduced flipping efficiencies and consequently reduced signal magnitudes. One source of attenuation of B_{rf} is absorption of the r.f. field by the permanent magnet and the associated heating. In the medium-wave (MW) to short-wave (SW) frequency band that is relevant to the NRSE (i.e., far from molecular vibrations that reside in the > 100 GHz microwave range), the average value of the Poynting vector (which, for a plane wave, is the energy density × the phase velocity) in a material of conductivity, σ, permeability, μ, and permittivity, ε, may be expressed as

$$\begin{aligned} S_{av} &= \frac{H_{rf}^2}{4}\left(\frac{\omega\varepsilon+\sqrt{\omega^2\varepsilon^2+\sigma^2}}{\sqrt{\omega^2\varepsilon^2+\sigma^2}}\right)\left[\frac{2\omega\mu}{\left(\sqrt{\omega^2\varepsilon^2+\sigma^2}+\omega\varepsilon\right)}\right]^{1/2}\exp\left(-\left[2\omega\mu\left(\sqrt{\omega^2\varepsilon^2+\sigma^2}-\omega\varepsilon\right)\right]^{1/2}y\right) \\ &= \frac{H_{rf}^2}{4}\left(\frac{\omega\varepsilon+\sqrt{\omega^2\varepsilon^2+\sigma^2}}{\sqrt{\omega^2\varepsilon^2+\sigma^2}}\right)\left[\frac{2\omega\mu}{\left(\sqrt{\omega^2\varepsilon^2+\sigma^2}+\omega\varepsilon\right)}\right]^{1/2}\exp\left(-2\frac{y}{\delta}\right) \end{aligned} \quad (352),$$

where δ is the attenuation length and ω is the angular frequency of the electromagnetic radiation. There are two obvious limiting cases:

(i) Perfect insulator: $\sigma \to 0$ and $\delta \to \infty$ where no electromagnetic radiation is absorbed.

(ii) Good conductor: $\sigma \gg \omega\varepsilon$ and $\delta \to (2/\mu\sigma\omega)^{1/2}$ (otherwise called the skin depth [see Eq. (294)]).

For the good conductor,

$$S_{av} = H_{rf}^2\left[\frac{\mu\omega}{8\sigma}\right]^{1/2}\exp\left(-2\frac{y}{\delta}\right) \quad (353).$$

For the applied r.f. *H*-field as shown in Figure 60 with a slab thickness $l_{B0} \gg \delta$ in the direction of S_{av}, and slab area *ac*, the Poynting vector may also be interpreted as follows:

$$S_{av} = \frac{energy}{vol}.phase\ velocity = \frac{energy}{ac\ dy}.\frac{dy}{dl_{B_0}} = \frac{power}{ac} \tag{354}$$

i.e., the power per unit slab area, *ac*. We see from Eq. (353) that almost 90 % of the r.f. energy is absorbed in the first layer of the slab of thickness δ, as indicated in Figure 60. In fact, after a thickness l_{B0} of the slab, the power absorbed per unit slab area is

$$\Delta S_{av} = H_{rf}^2 \left[\frac{\mu\omega}{8\sigma}\right]^{1/2} \left[1 - \exp\left(-2\frac{l_{B_0}}{\delta}\right)\right] \approx H_{rf}^2 \left[\frac{\mu\omega}{8\sigma}\right]^{1/2} \quad \text{for } l_{B_0} \gg \delta \tag{355}.$$

Note that the power absorbed per unit area increases as the square root of the frequency.

A criterion for the required electromagnetic properties of the magnetic material is obtained by assuming that the attenuation of the r.f. field corresponds to a value of ΔB_{rf} which produces a precession angle of 180°-β around the direction of B_{rf} (see also Sec. 2.2), in which β must not exceed ± 2.5°. In this respect, the effect of ΔB_{rf} does not significantly compromise the usable bandwidth $\Delta\lambda/\lambda$, (± 2.5° corresponding to a $\Delta\lambda/\lambda$ of about ± 1.4 %, i.e., about 3 % FWHM). Thus, by setting

$$\frac{\Delta B_{rf}}{B_{rf}} = 0.03 \tag{356},$$

we are requiring that the exponential in Eq. (352) over the thickness of the crystal, l_{B0}, is less than 0.03, i.e.,

$$\exp\left(-2\frac{l_{B_0}}{\delta}\right) \le 0.03 \tag{357},$$

which in turn implies

$$\delta \ge 0.57 l_{B_0} \quad = 0.57 l_{\pi} \quad \approx 0.57 l_{rf} \tag{358},$$

where

$$\delta = \left(\frac{2}{\omega_{rf}\mu\left(\sqrt{\omega_{rf}^2\varepsilon^2 + \sigma^2} - \omega_{rf}\varepsilon\right)}\right)^{1/2} \tag{359}.$$

When Eqs. (358) and (359) are combined with the resonance tuning condition for the r.f. frequency given by Eq. (9), we have:

$$l_{B_0}\left[\mathrm{m}\right] \;= l_{\pi}\left[\mathrm{m}\right]$$

$$\leq \frac{1.83\times10^{-4}}{\left[B_0\left[\mathrm{T}\right]\mu\left[\mathrm{NA^{-2}}\right]\left(\sqrt{\left(1.83\times10^{8}\,B_0\left[\mathrm{T}\right]\right)^2\varepsilon\left[\mathrm{Fm^{-1}}\right]^2+\sigma\left[\mathrm{m\Omega^{-1}}\right]^2}-1.83\times10^{8}\,B_0\left[\mathrm{T}\right]\varepsilon\left[\mathrm{Fm^{-1}}\right]\right)\right]^{1/2}} \quad (360),$$

subject to the minimum B_0 criterion (Eq. (341)).

If the criterion in Eq. (360) is satisfied, the r.f. power absorption will be quite uniformly distributed throughout the thickness of the slab and the power absorbed in the slab volume is

$$P_{rf}^{abs} < 0.03\,ac\frac{H_{pk}^2}{4}\left(\frac{\omega\varepsilon+\sqrt{\omega^2\varepsilon^2+\sigma^2}}{\sqrt{\omega^2\varepsilon^2+\sigma^2}}\right)\left[\frac{2\omega\mu}{\left(\sqrt{\omega^2\varepsilon^2+\sigma^2}+\omega\varepsilon\right)}\right]^{\frac{1}{2}} \quad (361).$$

The remaining issues are to verify that (i) the magnetic material can be sufficiently cooled and (ii) that the absorbed power does not alter the magnetic properties of the material.

9.2.2.6 Examples

9.2.2.6.1 Some simplifications

The gross parameter envelope is defined by satisfying Eqs. (341), (346), (347), (349), (351), and (360) simultaneously, whilst ensuring other factors such as the r.f. power absorption (Eq. (361)) and lesser factors remain under control. In these examples, we make the following simplifications:

- We choose $N = 2$ as this is the most likely bootstrap factor to be used in the spectrometer (see Sec. 3.4.2).
- Because there are two conditions involving L_0^{max}, one involving the tolerance on the materials length (Eq. (349)) and the other involving essentially only parameters that affect the r.f. coil inductance (Eq. (346)), we attempt to impose limits on L_0^{max} using Eq. (349), then examine the consequences for the r.f. coil parameters in Eq. (346) - specifically the coil winding density, given certain limitations on the r.f. coil dimensions.
- For now, the choice of permanent magnetic is left open for a material that satisfies Eqs. (360) and (341) simultaneously whilst maintaining r.f. heating (Eq. (361)) at acceptable levels and providing high neutron transmission and low scattering. The problems associated with Eqs. (360) and (361) essentially reduce to

finding a *good electrically insulating* magnetic material. Satisfying Eq. (341) requires the material to have a suitably large saturation field.

- Satisfying Eq. (351) most likely requires special neutron optical elements between the coils that correct relative flight path differences to a level that does not grossly exceed the factor 1-1/cos θ_{max}.

The above simplifications lead to the following set of conditions that must be satisfied simultaneously:

$$l_{B_0}\left[\mathrm{m}\right] \le \frac{1.56\times10^{-6}}{\Delta B_{mat}\left[\mathrm{T}\right]} \qquad \text{(from Eq. (347))} \qquad (362).$$

$$L_0^{max}\left[\mathrm{m}\right] \ge 5.0\times10^{4}\,\Delta l_{mat}\left[\mathrm{m}\right] \quad \text{(from Eq. (349))} \qquad (363).$$

Combining Eqs. (363) and (346), we have

$$n_{rf}\left[\mathrm{m^{-1}}\right] l_{axial}^{rf}\left[\mathrm{m}\right] a_{rf}\left[\mathrm{m}\right] \le 7.7\times10^{4}\,\Delta l_{mat}\left[\mathrm{m}\right] \qquad (364).$$

$$\Delta\theta_{max}\left(\lambda = 8\,\mathrm{\mathring{A}}\right) \le 5.2\times10^{-3}\ \mathrm{rad} \qquad \text{(from Eq. (351))} \qquad (365).$$

$$l_{\pi}\left[\mathrm{m}\right] \le \frac{1.83\times10^{-4}}{\left[B_0\left[\mathrm{T}\right]\mu\left[\mathrm{NA^{-2}}\right]\left(\sqrt{\left(1.83\times10^{8}\,B_0\left[\mathrm{T}\right]\right)^2\varepsilon\left[\mathrm{Fm^{-1}}\right]^2+\sigma\left[\mathrm{m\Omega^{-1}}\right]^2}-1.83\times10^{8}\,B_0\left[\mathrm{T}\right]\varepsilon\left[\mathrm{Fm^{-1}}\right]\right)\right]^{\frac{1}{2}}} \quad \text{(Eq. (360))} \qquad (366),$$

subject to

$$B_0^{max}\left[\mathrm{T}\right] \ge \frac{7.85\times10^{-2}}{L_0^{max}\left[\mathrm{m}\right]} \quad \text{(from Eq. (341))} \qquad (367).$$

9.2.2.6.2 Example with N = 2, 0.01° slab parallelism, a = c = 0.1 m, and ΔB_{mat} = 50 μT

The slab parallelism of 0.01° is based on what is considered to be reasonably achievable. Over a slab length of 0.1 m, this corresponds to $\Delta l_{mat} \approx 20\ \mu$m. Using these values in the equations in Sec. 9.2.2.6.1, we obtain

$$l_{\pi}\left[\mathrm{m}\right] \le \frac{1.56\times10^{-6}}{\Delta B_{mat}\left[\mathrm{T}\right]} \quad \Rightarrow \quad l_{\pi} \le 0.031\,\mathrm{m}$$

$$L_0^{max}\left[\mathrm{m}\right] \ge 5.0\times10^{4}\,\Delta l_{mat}\left[\mathrm{m}\right] \quad \Rightarrow \quad L_0^{max} \ge 1\,\mathrm{m}$$

For this range of L_0^{max} we have from Eq. (367):

$$B_0^{max}\left[\mathrm{T}\right] \geq \frac{7.85\times10^{-2}}{L_0^{max}\left[\mathrm{m}\right]} \quad \Rightarrow \quad \begin{cases} B_0\left(L_0^{max} = 1\,\mathrm{m}\right) \geq 0.0785\,\mathrm{T} \\ B_0\left(L_0^{max} = 2\,\mathrm{m}\right) \geq 0.0393\,\mathrm{T} \end{cases}$$

$$n_{rf}\left[\mathrm{m^{-1}}\right] l_{axial}^{rf}\left[\mathrm{m}\right] a_{rf}\left[\mathrm{m}\right] \leq 1.54$$

Assuming $a_{rf} \approx c = 0.1$ m and $l^{rf}_{axial} \approx a = 0.1$ m (see also Figure 59), this condition is expressed in terms of a maximum winding density of the r.f. coil, i.e.,

$$n_{rf}^{max}\left[\mathrm{m^{-1}}\right] \leq 154\,\mathrm{m^{-1}}$$

Equation (366) using the above value of l_π becomes

$$B_0\left[\mathrm{T}\right]\mu\left[\mathrm{NA^{-2}}\right]\left(\sqrt{\left(1.83\times10^8\,B_0\left[\mathrm{T}\right]\right)^2\varepsilon\left[\mathrm{Fm^{-1}}\right]^2 + \sigma\left[\mathrm{m\Omega^{-1}}\right]^2} - 1.83\times10^8\,B_0\left[\mathrm{T}\right]\varepsilon\left[\mathrm{Fm^{-1}}\right]\right) \leq 3.5\times10^{-5}$$

subject to $B_0^{max}\left[\mathrm{T}\right] \geq \frac{7.85\times10^{-2}}{L_0^{max}\left[\mathrm{m}\right]}$ (Eq. (367)).

All of these parameters appear to be readily achievable.

9.2.3 Potential problems with the multi-angle permanent magnet geometry

One major issue associated with a permanent magnet option in a multi-angle geometry is either one of crowding of the fourth flipper coil units (detectors in MIEZE-II configuration) as τ_{NRSE} (and hence L_0) is reduced or one of mechanical interference of the coil units with the optical elements necessary to achieve high resolution. These problems are illustrated in Figure 61. Both problems can lead to an insufficient Fourier time range. If corrective mirrors are in place, these are optimized for the highest resolution (i.e., for $L_0 = L_0^{max}$), therefore their performance is expected to degrade for shorter Fourier times where $L_0 < L_0^{max}$. Although the resolution requirements are less stringent at shorter Fourier times, the optical performance degradation should not "out-pace" the relaxation in the resolution requirements as L_0 is reduced, if possible.

If the presence of optical elements or the crowding of the coils limits the range of L_0 excessively, an NSE mode of operation could take over from that point. Preferably this should allow for an overlap of the NRSE and NSE mode Fourier time ranges.

Because the permanent magnetic field is fixed in magnitude, one cannot adopt the method described in Sec. 7.3.6.2 to measure short Fourier times in NSE mode. A possible solution is to rotate the magnets to change the field integral (see following section).

9.3 An NSE permanent magnet configuration?

It is interesting to compare the Fourier time range of a NRSE spectrometer using permanent magnets with that of the NSE configuration using permanent magnets. A possible NSE configuration is shown schematically in Figure 62 where Fourier time scans are performed by tilting the magnets as shown. Comparing the relative Fourier time ranges of the NSE and NRSE configurations amounts to comparing the effective field integrals $2NB_0^{NRSE} L_0$ for the NRSE with $B_0^{NSE} l/\cos\varphi_{max}$ for the NSE, where φ_{max} is the maximum tilt angle of the magnet. For an NRSE machine capable of reaching τ_{NRSE} = 30 ns at λ = 8 Å, we have

$$2NB_0^{NRSE} L_0 \approx 0.3\,\mathrm{Tm} \qquad (368).$$

Large field ferromagnetic materials might have B_0 up to about (1 to 2) T. Therefore in order to reach a field integral of 0.3 Tm with the NSE configuration would require

$$\frac{l}{\cos\varphi_{\max}} \simeq \left(0.15 \text{ to } 0.3\right)\mathrm{m} \qquad (369).$$

This is too thick for any magnetic material to achieve good thermal neutron transmission, therefore the NSE permanent magnet configuration is appropriate only for measuring the lowest end of the Fourier time range (just as was the case with the coils – see e.g. Figure 33).

9.4 Spectrometer guide requirements

The limited area over which the static field may be held sufficiently homogeneous and the need to introduce corrective optics into the spectrometer arms dictates a small area, low divergence, cold neutron beam for this instrument. A curved or curved-straight polarizing guide - velocity selector combination with an end-position provides a highly polarized beam over a broad wavelength range with a fixed floor position. A polarizing guide, such as the one illustrated in Figure 63 at FRM-II, provides a guide field not only for polarized neutrons inside the neutron guide but also up to the spectrometer entrance. If the curved-straight guide geometry is adopted, the possibility of eliminating phase-space non-uniformities due to the curved guide exists above a certain wavelength,

λ', by choosing the guide parameters according to the prescription of a "Phase-Space Tailoring" (PST) guide [28, 29]. From Table 7, we see that the tolerances on the incident beam divergence are very stringent. For example, if we seek and elastic polarization $P_x^0 = 0.5$ at $\tau_{NRSE} = 30$ ns and $\lambda = 8$ Å, we require a divergence corresponding to only 28.9 % of a natural Ni-coated neutron guide at $\lambda = 8$ Å for equal contributions from the main contributors to the resolution (see Sec. 6.1.5). Even if the beam divergence was the dominant contribution to the elastic depolarization, then we might still expect to require a divergence no more than about $\sqrt{3} \times 28.9\ \% \approx 50\ \%$ of natural Ni (about the critical angle of the uncoated glass, $m \approx 0.5$). We examine the implications for a PST guide designed to achieve this limit of operation.

To constrain the parameters for illustration purposes we suppose that we will limit the beam size to a ($W \times H$) = 3 cm × 3 cm beam and the total length of the curved-straight guide combination to $L_{tot} = L_c + L_{str} = 50$ m, where L_c is the length of the curved section and L_{str} is the length of the straight section.

There is a compromise to be made between the short neutron wavelength and gamma ray filtering of the guide and the minimum wavelength of the instrument. The short neutron wavelength filtering of the guide may be characterized in terms of the "characteristic wavelength" of the curved section of guide, λ_c. In the small angle approximation λ_c is given by the expression

$$\lambda_c \approx \sqrt{\frac{2W}{\rho}} \frac{1}{\gamma_{Ni} m_{out}} \tag{370}$$

where W is the width of the guide, ρ is the radius of curvature, m_{out} characterizes the factor by which the critical angle of the reflective coating on the outer radius of the curved section of guide exceeds that of natural Ni, and γ_{Ni} characterizes the critical angle of natural Ni per unit neutron wavelength and has the value $\gamma_{Ni} \approx 1.73 \times 10^{-3}$ rad Å^{-1}. λ_c characterizes the points at which:

(i) The transmitted beam in an ideal (perfect reflectivity and circular curvature) long (no line-of-sight) curved guide (ILCG) consists only of trajectories that have had no contact with the internal radius.

(ii) The 2-D transmission of the ILCG with respect to an equivalent (coatings characterized by the same m_{out}) 2-D ideal long (divergence limited by critical angle) straight guide (EILSG) is exactly 2/3.

(iii) The wavelength below which the transmitted 2-D phase space area decreases $\propto \lambda^3$ (transmission with respect to the 2-D EILSG $\propto \lambda^2$).

A reasonable compromise for useful intensity at a minimum operational wavelength of λ_{min} = 2 Å and good filtration of epithermal neutrons is to set $\lambda_c \approx 4$ Å.

If the required conditions for PST operation are met, it can be shown [29] that λ' is given by the expression

$$\lambda' = \frac{m_{out}}{\sqrt{\left(m_{out}^2 - m_{in}^2\right)}} \lambda_c \qquad (371)$$

where m_{in} characterizes the critical angle of the coating on the inner radius of the curved guide section. Note that λ' exists within the range from λ_c (when $m_{out} \gg m_{in}$) up to ∞ (when $m_{in} \geq m_{out}$). Thus PST operation cannot occur for $\lambda < \lambda_c$, which is logical since it relies on neutrons transmitted having undergone reflections from the inner radius of the curved section.

For the curved guide to be termed "long" (no line of sight [LOS]), its length, L_c, must satisfy (in the small angle approximation):

$$L_c \geq L_{LOS} \approx \sqrt{8W\rho} \qquad (372).$$

A particularly favorable (and luxurious) situation for gamma-ray filtering occurs when $L_c \geq 2\ L_{LOS}$, whereby neither direct, nor once-scattered (reflection geometry) gamma rays are viewable. Thus we will set a further constraint $L_c = 2\ L_{LOS}$, i.e., $L_c = 4\sqrt{(2W\rho)}$ in the following examples.

The displacement of the end of the curved-straight guide combination with respect to the original guide axis at the entrance (which may be an important parameter in instrument placement) is given by

$$d_{tot} = d_c + d_{str} \quad = \rho\left(1 - \cos\left(\frac{L_c}{\rho}\right)\right) + L_{str} \sin\left(\frac{L_c}{\rho}\right) \qquad (373).$$

Parameters for several guides that satisfy the PST guide conditions with the above constraints are summarized in Table 11.

Table 11. Parameters for guides satisfying the idealized PST guide conditions above a wavelength λ', given the constraints λ_c = 4 Å, L_{tot} = 50 m, W = 3 cm, $L_c = 2L_{LOS}$ with $m_{in} \geq 0.5$, m_{str} =0.5, for several radii of curvature. The last two entries illustrate the effect on the guide parameters of coating first only the inner radius of the curved section with natural Ni (m = 1) [no change], then also coating the straight section with m = 1 (e.g. an interchangeable straight section), for better performance when operating at lower static fields.

ρ (m)	L_{LOS} (m)	L_c (constr. = $2L_{LOS}$) (m)	L_{str} (constr. $L_{str} = L_{tot} - L_c$ with L_{tot} =50m)	L_{str}(min) [minimum required L_{str} for ideal PST ($\lambda > \lambda'$)]	m_{out} (constr. to obtain λ_c (ILCG) = 4 Å)	m_{in} (for ideal PST operation $m_{in} \geq m_{str}$)	Assumed maximum m_{str} (to achive required NRSE elastic polarization)	λ' (deal PST guide operation for $\lambda > \lambda'$) (Å)	Displacement of guide end with respect to origin guide axis, d_{tot} (m)
100	4.90	9.80	40.20	8.58	3.54	0.5	0.5	4.041	4.41
150	6.00	12.00	38.00	8.54	2.89	0.5	0.5	4.061	3.52
200	6.93	13.86	36.14	8.50	2.50	0.5	0.5	4.082	2.98
300	8.49	16.97	33.03	8.41	2.04	0.5	0.5	4.125	2.35
500	10.95	21.91	28.09	8.23	1.58	0.5	0.5	4.216	1.71
500	10.95	21.91	28.09	8.23	1.58	1.0	0.5	4.216	1.71
500	10.95	21.91	28.09	3.31	1.58	1.0	1.0	5.160	1.71

Table 11 gives examples of the type of guide parameters required to achieve the reasonable elastic signal at the highest fields, for which the only coated surface of the glass guide would be the outer radius of the curved sections! To improve the guide performance when such stringent constraints on the beam collimation do not exist, either a guide with large *m* coatings could be used with interchangeable collimators, or conceivably one could have a curved section with, for example, natural Ni ($m = 1$) on the inner radius and top/bottom surfaces with interchangeable straight sections, one having all Ni coatings and the other being simply of super-polished glass ($m \approx 0.5$). Take, for example, the $\rho = 500$ m guide in Table 11: Substituting $m = 1$ instead of $m = 0.5$ only for the curved section (keeping $m_{str} = 0.5$) does not change any of the listed parameters or the functioning of the PST guide. If in addition $m_{str} = 1$ (an interchangeable straight guide of identical dimensions but with $m = 1$ is brought in), all that changes is that the minimum required length of the straight section for PST operation reduces and the wavelength above which ideally perfect PST operation is achieved increases a little. Note that below λ_c, although ideal PST operation is impossible, the existence of the straight section of guide after the curve does tend to rectify phase space asymmetries [30] in the transmitted beam and for wavelengths between λ_c and λ', this latter effect occurs in addition to partial PST operation.

The guide systems described in Table 11 are illustrated schematically in Figure 64 and their simulated performance is shown in Figure 65, assuming that they originate from an in-pile beam port equivalent to NG-1 at the NCNR with the Unit 2 liquid hydrogen cold source. These guides are modeled with no velocity selector and no polarizer. For comparison, the intensity of the existing NG-5 guide at the beam exit preceding the first NSE solenoid is also shown under the same conditions of no velocity selector and no polarizing cavity for a fair comparison. Figure 66 shows the horizontal angular distributions for $\lambda = 8$ Å for the guides listed in Table 11 and for the NG-5 guide which has ^{58}Ni coatings ($m \approx 1.18$). Note that $\lambda = 8$ Å is above λ' for all the curved-straight guides in Table 11. The figure illustrates the uniform horizontal angular distributions within the limits imposed by the critical angles of the straight sections (indicated by the vertical bold black lines – dashed for $m = 0.5$ and solid for $m = 1$ natural Ni]) which is indicative of the near-ideal PST operation of the curved-straight guides. Figure 67 shows the estimated integral fluxes at the guide exits as a function of the primary selected wavelength assuming (i) a velocity selector with a triangular transmission function with respect to wavelength of peak transmission 0.83, operating with 10 % $\Delta\lambda/\lambda$ (FWHM) and (ii) a polarizing cavity having a wavelength-independent transmission of 0.45. We note that the

predicted flux of the m_{str} = 1 guide is comparable to that of the NG-5 at the NSE instrument under similar conditions but with a reduced beam divergence (see Figure 66).

10 Appendix A: Summary of useful NRSE formulas

(L_0 = length between coil centers, l=total coil length, l_{B0} = length of one π-flipper coil assuming the static field region encloses the r.f. field region, l_π=length of combined r.f. and static field region (usually=l_{rf} for π flipper coils), N=number of π flipper coils in Bootstrap, M=total number of π-coils traversed by the beam in the instrument).

Larmor angular frequency (=ω_{rf} at resonance)

$$\omega_0 = \gamma_n B_0 \qquad \text{Eq. (5)}$$

with $\gamma_n = \dfrac{2|\mu_n|}{\hbar} = 1.832472\times10^{8}\ \text{rad s}^{-1}\text{T}^{-1}$ Eq. (6).

Larmor frequency (=r.f. frequency at resonance)

$$\nu_0\,[\text{MHz}] = \nu_{rf}^{reson}\,[\text{MHz}] = \frac{\gamma_n B_0}{2\pi} = 29.1647\,B_0\,[\text{T}] \quad \text{Eq. (8).}$$

Larmor period=r.f. period at resonance

$$\tau_0\,[\mu\text{s}] = \frac{1}{\nu_0\,[\text{MHz}]} = \frac{0.03429}{B_0\,[\text{T}]} \qquad \text{from Eq. (8).}$$

"Effective 4-coil NRSE precession frequency"

$$\nu_{eff}\,[\text{MHz}] = 2N\nu_0\,[\text{MHz}] = 58.3294\,NB_0\,[\text{T}].$$

Actual number of precessions in one π flipper coil length l_π

$$N_{prec}^{\pi} = \frac{\nu_0 l_{B_0}}{v_n} = \frac{\varphi_\pi}{2\pi} = \frac{\gamma_n}{2\pi}\frac{m_n}{h} B_0 l_{B_0}\lambda = 7.3722\times10^{3} B_0\,[\text{T}]\, l_{B_0}\,[\text{m}]\,\lambda\left[\text{Å}^{\circ}\right].$$

Approximate full width at half maximum of resonance curve (i.e. 50% drop in polarizing efficiency) for a general value of l_π is very well fitted by

$$\Delta\nu_{FWHM}\left[\mathrm{Hz}\right]=\frac{3.16\times10^{3}}{l_\pi\left[\mathrm{m}\right]\lambda_n\left[\mathrm{\mathring{A}}\right]} \quad \text{Eq. (59).}$$

Frequency shift for 1% drop in the polarizing efficiency is well fitted by

$$\Delta\nu_{99\%}\left[\mathrm{Hz}\right]=\frac{198}{l_\pi\left[\mathrm{m}\right]\lambda_n\left[\mathrm{\mathring{A}}\right]} \quad \text{Eq. (60).}$$

Tolerance on B_0 field in each π-flipper in a machine with a total of M π-flippers (e.g. M=8) (Gaussian -equal contributions)

$$\Delta B_0^{FWHM}=\frac{h}{m_n\gamma_n}\frac{2\sqrt{\ln 2\ln\left(\frac{1}{P_x^0}\right)}}{\sqrt{3N}l_{B_0}\lambda_i} \approx \frac{2.08\times10^{-5}\sqrt{\ln\left(\frac{1}{P_x^0}\right)}}{\sqrt{N}l_{B_0}\left[\mathrm{m}\right]\lambda_i\left[\mathrm{\mathring{A}}\right]}\ \mathrm{Tesla} \quad \text{Eq. (223).}$$

Tolerance on coil flatness in each π-flipper in a machine with a total of M π-flippers (e.g. M=8) (Gaussian - equal contributions)

$$\Delta l_\pi^{FWHM}=\frac{2h}{m_n\gamma_n}\frac{\sqrt{\ln 2\ \ln\left(\frac{1}{P_x^0}\right)}}{\sqrt{3N}B_0\lambda_i} \approx \frac{2.08\times10^{-5}\sqrt{\ln\left(\frac{1}{P_x^0}\right)}}{\sqrt{N}B_0\left[\mathrm{T}\right]\lambda_i\left[\mathrm{\mathring{A}}\right]}\ \mathrm{meters} \quad \text{Eq. (224).}$$

Tolerance on beam divergence in each arm of a machine with a total of M π-flippers (e.g. M=8) (uniform incident and scattered polar angles up to $\Delta\theta_{\max}$ - equal contributions)

$$\Delta\theta_{\max} \approx \sqrt{\frac{h\sqrt{45\ln\left(\frac{1}{P_x^0}\right)}}{6Nm_n\gamma_n B_0 L_0 \lambda_i}} \simeq 4.91\times10^{-3}\sqrt{\frac{\sqrt{\ln\left(\frac{1}{P_x^0}\right)}}{NB_0[\mathrm{T}]L_0[\mathrm{m}]\lambda_i\left[\mathring{\mathrm{A}}\right]}}[\mathrm{rad}] \qquad \text{Eq. (225).}$$

, for $\left|\Delta\theta_{\max}\right| <\sim \frac{6.7\times10^{-3}}{\sqrt{NB_0[\mathrm{T}]L_0[\mathrm{m}]\lambda_i\left[\mathring{\mathrm{A}}\right]}}[\mathrm{rad}]$

Net phase change in 4 equal coils, midpoints of coils in first arm separated by L_0, midpoints of coils in second arm separated by L_1

$$\varphi_{NRSE} \quad = \quad 2N\gamma_n\left[\frac{B_0L_0}{v_i}-\frac{B_1L_1}{v_f}\right] \quad = \quad \frac{2Nm_n\gamma_n}{h}\left[B_0L_0\lambda_i - B_1L_1\lambda_f\right] \qquad \text{Eq. (80),}$$

When tuned for QENS with $B_0L_0=B_1L_1$

$$\varphi_{NRSE}[\mathrm{rads}] = 92641.8N\left[B_0[\mathrm{T}]L_0[\mathrm{m}]\lambda_i\left[\mathring{\mathrm{A}}\right] - B_1[\mathrm{T}]L_1[\mathrm{m}]\lambda_f\left[\mathring{\mathrm{A}}\right]\right].$$

NRSE Fourier time ($v_f=v_i+\delta v$, $\delta v \ll v_i$ approximation)

$$\tau_{NRSE} = \frac{2N\hbar\gamma_n B_0 L_0}{m_n v_i^3} \quad = \quad \frac{N\gamma_n}{\pi}\left(\frac{m_n}{h}\right)^2 B_0L_0\lambda_i^3 \quad = \quad 2N\nu_0 L_0\left(\frac{m_n}{h}\right)^2\lambda_i^3 \qquad \text{Eq. (152).}$$

where

$$\tau_{NRSE}[\mathrm{ns}] = 0.37271\,N\,B_0[\mathrm{T}]L_0[\mathrm{m}]\left(\lambda_i\left[\mathring{\mathrm{A}}\right]\right)^3$$
$$= 1.27794\times10^{-2}\,N\,\nu_0[\mathrm{MHz}]L_0[\mathrm{m}]\left(\lambda_i\left[\mathring{\mathrm{A}}\right]\right)^3 \qquad \text{Eq. (153).}$$

Effects of Dispersion: Flipping efficiencies

Flipping efficiency for a wavelength λ_i for single flipper tuned for resonance and for exact π flips for the mean neutron wavelength $\langle\lambda_i\rangle$.

$$\frac{P_{disp}}{P_{ideal}} = \sin^2\left(\frac{\pi}{2}\frac{\lambda_i}{\langle\lambda_i\rangle}\right) \qquad \text{Eq. (31).}$$

Averaged over various incident wavelength distributions:

1. *Rectangular*

$$\left\langle\frac{P_{disp}}{P_{ideal}}\right\rangle_{1\,coil}(\text{rectangular}) = \left[\frac{1}{2} + \frac{1}{\alpha_{FW}\pi}\sin\left(\frac{\pi}{2}\alpha_{FW}\right)\right] \quad \text{Eq. (35)} \quad \text{with } \alpha_{FW} = \frac{\Delta\lambda_{FW}}{\langle\lambda_i\rangle} \text{ Eq. (34).}$$

2. *Triangular*

$$\left\langle\frac{P_{disp}}{P_{ideal}}\right\rangle_{1\,coil}(\text{triangular}) = \frac{1}{2} + \frac{1}{\pi^2\alpha_{FWHM}^2}\left(1-\cos\left(\pi\alpha_{FWHM}\right)\right) \text{ Eq. (39) with } \alpha_{FWHM} = \frac{\Delta\lambda_{FWHM}}{\langle\lambda_i\rangle} \text{ Eq. (38).}$$

3. *Gaussian*

$$\left\langle\frac{P_{disp}}{P_{ideal}}\right\rangle_{1\,coil}(\text{Gaussian}) = \frac{1}{2}\left(1+\exp\left[-\left(\frac{\pi}{4}\right)^2\frac{\alpha_{FWHM}^2}{\ln 2}\right]\right) \text{ Eq. (42) with } \alpha_{FWHM} = \frac{\Delta\lambda_{FWHM}}{\langle\lambda_i\rangle} \text{ Eq. (38).}$$

Approximate maximum achievable static field for *n* turns cm^{-1} (long solenoid approximation)

$$B_0[\text{T}] \approx 4\pi\times10^{-7}\, n\left[\text{m}^{-1}\right] I[\text{A}] \simeq 1.26\times10^{-6}\, n\left[\text{m}^{-1}\right] I[\text{A}] \qquad \text{Eq. (233).}$$

Required current in static field coil to produce a static field B_0

$$I[\text{A}] = \frac{2.5\times10^6}{\pi}\frac{B_0[\text{T}]}{n\left[\text{m}^{-1}\right]} \approx 8\times10^5\frac{B_0[\text{T}]}{n\left[\text{m}^{-1}\right]} \qquad \text{Eq. (234).}$$

Magnetic pressure acting outwards on B_0 coil windings

$$P_{mag}\left[\mathrm{Nm^{-2}}\right] = \frac{\left(B[\mathrm{T}]\right)^2}{8\pi\times10^{-7}} \approx 4\times10^5\left(B[\mathrm{T}]\right)^2 \qquad \text{Eq. (261).}$$

Approximate deflection of unconstrained winding length l_u due to magnetic pressure

$$y_{\max}[\mathrm{m}] \approx 1.25\times10^4 \frac{\left(B[\mathrm{T}]\right)^2 l_u[\mathrm{m}]^4}{E\left[\mathrm{Nm^{-2}}\right]t[\mathrm{m}]^3} \qquad \text{Eq. (266).}$$

Resistance of static field coil of external surface area A_{surf} with tightly-wound, rectangular cross-section windings of thickness t

$$R[\Omega] = \frac{\rho(T)[\Omega\mathrm{m}]\left(n\left[\mathrm{m^{-1}}\right]\right)^2 A_{surf}\left[\mathrm{m^2}\right]}{t[\mathrm{m}]} \qquad \text{Eq. (242).}$$

Required voltage across static field coil of external surface area A_{surf} with tightly-wound, rectangular cross-section windings of thickness t

$$V[\mathrm{V}] = I[\mathrm{A}]R[\Omega] = \frac{2.5\times10^6}{\pi}\frac{\rho(T)[\Omega\mathrm{m}]n\left[\mathrm{m^{-1}}\right]A_{surf}\left[\mathrm{m^2}\right]}{t[\mathrm{m}]}B_0[\mathrm{T}] \qquad \text{Eq. (247).}$$

Power dissipated in static field coil of external surface area A_{surf} with tightly-wound, rectangular cross-section windings of thickness t

$$P[\mathrm{W}] = I[\mathrm{A}]V[\mathrm{V}] = \left(I[\mathrm{A}]\right)^2 R[\Omega]$$
$$\approx \frac{6.25\times10^{12}}{\pi^2}\frac{\rho(T)[\Omega\mathrm{m}]A_{surf}\left[\mathrm{m^2}\right]}{t[\mathrm{m}]}\left(B_0[\mathrm{T}]\right)^2 \qquad \text{Eq. (251).}$$

Specifically for Al windings down to $T \sim 80$ K

$$P_{Al}[\mathrm{W}] \approx \left(B_0[\mathrm{T}]\right)^2 \frac{A_{surf}\left[\mathrm{m^2}\right]}{t[\mathrm{m}]}\left(72.2T(\mathrm{K}) - 4.37\times10^3\right) \qquad \text{Eq. (255).}$$

B_{rf} required for π flip (amplitude of r.f. field=$2B_{rf}$).

$$B_{rf}\left[\mathrm{T}\right] \simeq \frac{6.782232\times10^{-5}}{l_{rf}\left[\mathrm{m}\right]\lambda_n\left[\mathrm{\overset{o}{A}}\right]} = \frac{6.782232\times10^{-5}}{l_{\pi}\left[\mathrm{m}\right]\lambda_n\left[\mathrm{\overset{o}{A}}\right]} \qquad \text{Eq. (14).}$$

Required peak amplitude of r.f. field

$$B_{rf}^{pk}\left[\mathrm{T}\right] = 2B_{rf}\left[\mathrm{T}\right] \simeq \frac{1.35645\times10^{-4}}{l_{rf}\left[\mathrm{m}\right]\lambda_n\left[\mathrm{\overset{o}{A}}\right]} = \frac{1.35645\times10^{-4}}{l_{\pi}\left[\mathrm{m}\right]\lambda_n\left[\mathrm{\overset{o}{A}}\right]} \qquad \text{Eq. (15).}$$

Approximate skin-depth in aluminum

$$\delta_{Al}\left[\mathrm{mm}\right] \simeq \frac{83}{\sqrt{\nu\left[\mathrm{Hz}\right]}} \qquad \text{Eq. (295).}$$

Approximate ratio of resistance at frequency ν to D.C. resistance for band windings with $h \gg t$

$$\frac{R(\nu)}{R_0} \approx \frac{\int_0^{t/2} dx}{\int_0^{t/2} \exp\left(-\frac{x}{\delta}\right) dx} = \frac{t}{2\delta\left[1-\exp\left(-\frac{t}{2\delta}\right)\right]} \qquad \text{Eq. (296).}$$

Approximate required peak current in r.f. coil

$$I_{rf}^{pk}\left[\mathrm{A}\right] \simeq \frac{B_{rf}^{pk}\left[\mathrm{T}\right]}{\mu\left[\mathrm{NA^{-2}}\right]n_{rf}\left[\mathrm{m^{-1}}\right]} \simeq \frac{1.356\times10^{-4}}{\mu\left[\mathrm{NA^{-2}}\right]n_{rf}\left[\mathrm{m^{-1}}\right]l_{rf}\left[\mathrm{m}\right]\left\langle\lambda_i\right\rangle\left[\mathrm{\overset{o}{A}}\right]}$$

$$\simeq \frac{108}{n_{rf}\left[\mathrm{m^{-1}}\right]l_{rf}\left[\mathrm{m}\right]\left\langle\lambda_i\right\rangle\left[\mathrm{\overset{o}{A}}\right]} \quad (\text{in air}) \qquad \text{Eq. (280).}$$

r.f circuit values at exact impedance matching condition

r.m.s. current in r.f. coil at exact impedance matching (Z_0 usually 50Ω)

$$I_{rf}^{rms}\left[\mathrm{A}\right] = \frac{I_{rf}^{pk}\left[\mathrm{A}\right]}{\sqrt{2}} \simeq \frac{9.592\times10^{-5}}{\mu\left[\mathrm{NA^{-2}}\right] n_{rf}\left[\mathrm{m^{-1}}\right] l_{rf}\left[\mathrm{m}\right]\left\langle\lambda_i\right\rangle\left[\mathrm{\mathring{A}}\right]} \simeq \frac{76.3}{n_{rf}\left[\mathrm{m^{-1}}\right] l_{rf}\left[\mathrm{m}\right]\left\langle\lambda_i\right\rangle\left[\mathrm{\mathring{A}}\right]}$$ Eq. (281).

Approximate maximum voltage in r.f. coil (long solenoid approx, length l^{rf}_{axial}, thickness in beam direction l_{rf}, width perpendicular to l^{rf}_{axial} and $l_{rf} = a_{rf}$)

$$V_{rf}^{pk}\left[\mathrm{V}\right] \approx 2.5\times10^{4} \frac{n_{rf}\left[\mathrm{m^{-1}}\right] l_{axial}^{rf}\left[\mathrm{m}\right] a_{rf}\left[\mathrm{m}\right]}{\left\langle\lambda_i\right\rangle\left[\mathrm{\mathring{A}}\right]} B_0\left[\mathrm{T}\right]$$ Eq. (286).

using $L \approx \mu_0 n_{rf}^2 l_{axial} A_{rf}$ (Eq. (284)) which can be restated as:

Approximate self-inductance of long solenoid

$$L\left[\mathrm{H}\right] \approx 4\pi\times10^{-7}\left(n_{rf}\left[\mathrm{m^{-1}}\right]\right)^2 l_{axial}^{rf}\left[\mathrm{m}\right] A_{rf}\left[\mathrm{m^2}\right]$$
$$\approx 1.26\times10^{-6}\left(n_{rf}\left[\mathrm{m^{-1}}\right]\right)^2 l_{axial}^{rf}\left[\mathrm{m}\right] A_{rf}\left[\mathrm{m^2}\right]$$ Eq. (285).

Required r.m.s. power supply voltage at exact impedance matching (assuming Z_0=50Ω) (typically much smaller than HV across coil itself)

$$V_{rms}^{PS}\left[\mathrm{V}\right] \simeq \frac{152.7\sqrt{Z_0\left[\Omega\right] R\left[\Omega\right]}}{n_{rf}\left[\mathrm{m^{-1}}\right] l_{rf}\left[\mathrm{m}\right]\left\langle\lambda_i\right\rangle\left[\mathrm{\mathring{A}}\right]} = \frac{1079.4\sqrt{R\left[\Omega\right]}}{n_{rf}\left[\mathrm{m^{-1}}\right] l_{rf}\left[\mathrm{m}\right]\left\langle\lambda_i\right\rangle\left[\mathrm{\mathring{A}}\right]}$$ Eq. (289).

the heat dissipated in the whole circuit is

$$P_{rf\ circuit} = 2\left(I_{rms}^{PS}\right)^2 Z_0 = \frac{\left(V_{rms}^{PS}\right)^2}{2Z_0}$$ Eq. (290).

Power dissipated as heat in the r.f. coil (occurs only due to its resistance) at exact impedance matching is

$$P_{coil} = \left|\frac{V_{rms}^{PS}}{2}\left(\frac{1}{Z_0} + j\omega C_2\right)\right|^2 R = \frac{\left(V_{rms}^{PS}\right)^2}{4Z_0} = \left(I_{rf}^{rms}\right)^2 R$$ Eq. (293).

Approximate maximum rate of change of current in r.f. coil

$$\left(dI/dt\right)_{\max}\left[\mathrm{As}^{-1}\right] = I_{rf}^{pk}\left[\mathrm{A}\right]\omega_{rf}\left[\mathrm{s}^{-1}\right] \approx 1.832\times10^{8}\, I_{rf}^{pk}\left[\mathrm{A}\right]B_0\left[\mathrm{T}\right] \qquad \text{Eq. (283).}$$

Approximate tolerances on r.f. coil

Using the criteria $\alpha_{FWHM}^{eff} \approx \sqrt{\left(\frac{\Delta\left(B_{rf}l_{rf}\right)}{B_{rf}l_{rf}}\right)^2+\left(\frac{\Delta\lambda_{FWHM}}{\langle\lambda_i\rangle}\right)^2} \le 1.05\frac{\Delta\lambda_{FWHM}}{\langle\lambda_i\rangle}$ and $\frac{\Delta\lambda_{FWHM}}{\langle\lambda_i\rangle}\le 10\%$, we have

$$\frac{\Delta\left(B_{rf}l_{rf}\right)}{B_{rf}l_{rf}} = \frac{\sqrt{2}\Delta B_{rf}}{B_{rf}} = \frac{\sqrt{2}\Delta l_{rf}}{l_{rf}} <\sim 0.03$$

for equal contributions to resolution function (Eq. (302)), with

$$\Delta B_{rf}^{pk}\left[\mathrm{T}\right] \simeq \frac{2.9\times10^{-6}}{l_{rf}\left[\mathrm{m}\right]\langle\lambda_i\rangle\left[\overset{\circ}{\mathrm{A}}\right]} \qquad \text{Eq. (303)}$$

and $\frac{\Delta l_{rf}}{l_{rf}} <\sim 0.02$ (see Eq. (302), i.e., for l_{rf} ~ 0.025 m, Δl_{rf} < ~ 0.6 mm).

Length of toroidal r.f. coil winding, toroid radius r, cross-section $a_{rf}\times b_{rf}$

$$l_w^{rf} \approx 4\pi r_{toroid}\, n_{rf}\left(a_{rf}+l_{rf}\right) \qquad \text{Eq. (334).}$$

Self-inductance of toroidal solenoid of mean radius r and cross-sectional area A_{rf}

$$L_{toroid}\left[\mathrm{H}\right] = 2\pi r_{toroid}\mu_0 n_{rf}^2 A_{rf} = 8\pi^2\times10^{-7}\left(n_{rf}\left[\mathrm{m}^{-1}\right]\right)^2 r_{toroid}\left[\mathrm{m}\right]A_{rf}\left[\mathrm{m}^2\right] = 7.9\times10^{-6}\left(n_{rf}\left[\mathrm{m}^{-1}\right]\right)^2 r_{toroid}\left[\mathrm{m}\right]A_{rf}\left[\mathrm{m}^2\right] \qquad \text{Eq. (331).}$$

Resistance of toroidal solenoid of mean radius r

$$R_{toroid} = \rho(T)\frac{4\pi r_{toroid}\, n_{rf}\left(a_{rf}+l_{rf}\right)}{t_{rf}h_{rf}} \qquad \text{Eq. (336).}$$

Specifically for Al rectangular windings $t_{rf} \times h_{rf}$:

$$R_{Al}^{toroid}(T)[\Omega] = \left(1.43\times10^{-9} T[K] - 8.7\times10^{-8}\right) \frac{r_{toroid}[\mathrm{m}]\, n_{rf}\left[\mathrm{m}^{-1}\right]\left(a_{rf} + l_{rf}\right)[\mathrm{m}]}{t_{rf}[\mathrm{m}]\, h_{rf}[\mathrm{m}]} \quad \text{Eq. (338).}$$

Stray fields

For stray field for total precession in arm of length L, with <10° precession angle:

$$B_{stray}[\mathrm{T}]\, L[\mathrm{m}] \le \frac{3.8\times10^{-6}}{\langle\lambda_i\rangle\left[\overset{\circ}{\mathrm{A}}\right]} \quad \text{Eq. (305).}$$

Unshielded "Zero field path" precession due to Earth's magnetic field

$$\left\langle \Delta\varphi_{stray} \right\rangle [\mathrm{rad}] \approx \frac{\gamma_n m_n}{h} B_{stray} L \langle\lambda_i\rangle = 4.63\times10^4\, B_{stray}[\mathrm{T}]\, L[\mathrm{m}] \langle\lambda_i\rangle \left[\overset{\circ}{\mathrm{A}}\right] \quad \text{Eq. (304).}$$

Example: Earth's magnetic field (zip code 21737 Oct 8 2008) = 5.25×10^{-5} T, horizontal component=2.06×10^{-5} T, vertical component 4.83×10^{-5} T, L = 2 m, $\langle\lambda_i\rangle$ = 8 Å, $\langle\Delta\varphi_{stray}\rangle$ = 35.8 rads = 2050.1° = 5.7 turns.

Acknowledgements

We are grateful to our colleagues in Europe for their generous sharing of knowledge and experience in the construction and operation of NRSE machines. In particular we thank Roland Gähler (ILL, Grenoble, France), Bob Golub (HMI, Berlin, Germany) and Thomas Keller (FRM-II, Munich, Germany). We also thank Klauss Thillosen (ILL), Serguei Klimko (ILL), Klaus Habicht (HMI), Mike Snow (University of Indiana), and also our colleagues at the NIST, in particular Chuck Majkrzak, Ivan Schroder, Nick Rosov (who is sadly missed), and Dan Neumann.

Figure Captions

Figure 1. (a) Coordinate system showing initial neutron polarization direction. (b) Larmor precession with angular velocity ω_0. of the neutron magnetic moment in the *xy* plane due to the static field B_0 along *z* (viewed in the lab frame); (c) Larmor precession of μ about B_{rf} viewed in a frame which is rotating (at angular velocity ω_0) synchronous with the resonant component of the r.f. field (magnitude B_{rf}).

Figure 2. A sinusoidal oscillating field of angular frequency ω_0, amplitude $2B_{rf}$ decomposed into two counter-rotating components each of magnitude B_{rf} rotating at ω_0.

Figure 3. Classical precession of the neutron magnetic moment around the resonant component of the r.f. field in the rotating frame of the r.f. field component.

Figure 4. Coil flipping efficiencies calculated using Eq. (58) for l_π= 3 cm for a π-flipper whose r.f. field magnitude B_{rf} is tuned optimally to produce exact π-flips for monochromatic, well collimated beams of single wavelength λ_n (zero dispersion approximation). These curves are plotted as a function of the difference in the Larmor frequency ν_0 and the r.f. frequency ν_{rf} in kHz. These curves can be used equivalently either if we assume (i) perfect static field homogeneity (fixed ν_0) with varying ν_{rf} or for (ii) departures of ν_0 from the nominal value $\langle \nu_0 \rangle$ due to static field inhomogeneity for the case $\nu_{rf}=\langle \nu_0 \rangle$ as well as general cases in between.

Figure 5. A 4-single π coil NRSE instrument.

Figure 6. Some possible π-flipper spin echo arrangements.

Figure 7. On entering the static field region, the degeneracy of the spin up and spin down states of a neutron, of initial energy $\hbar\omega_1$ with its spin vector lying in the *xy* plane, is lost due to the magnetic potential gradient at the entrance to the coil. Inside the field, the spin-parallel state is increased in kinetic energy by $\mu_n B_0$ and the antiparallel

state is reduced in kinetic energy by $-\mu_n B_0$. The total (kinetic+potential) energy remains fixed at $\hbar\omega_i$ throughout the process. The total splitting is $\hbar\omega_0$, where ω_0 is the classical Larmor angular frequency. Usually $\hbar\omega_0 \ll \hbar\omega_i$. On exiting the coil, the splitting disappears, but the relative phase of the matter waves associated with the spin up and spin down states has been shifted by $\omega_0 l_{B0}/v_i$, corresponding to classical Larmor precession of the spin around the field direction during its time in the field.

Figure 8. An r.f. flipper tuned for perfect spin flips for a non-dispersive flipper (or a monochromatic beam). The r.f. region is deliberately shown shorter than the static field region (as is the case for an r.f. coil placed inside a static field coil). The flipper is tuned for exact π-flips within the r.f. field region so that $\gamma_n B_{rf} l_{rf}/v_i = \pi$. In this case, by the time the neutrons are exiting the r.f. field region a complete inversion of the spin states occurs via exchange of photons with the r.f. field (of angular frequency $\omega_{rf}=\omega_0$). The absorption and emission of r.f. photons means that, in contrast to the case shown in Figure 7, the total energy of individual spin states is not conserved, as shown. The splitting of the total energy reaches a maximum of $2\hbar\omega_0$ at the exit boundary of the r.f. field, whilst the additional splitting in kinetic energy experienced due to the spin inversion does not manifest itself until the neutron crosses the static field boundary on the exit side of the coil. Because the kinetic energies of the two states differ by $2\hbar\omega_0$ at the exit of the coil, the relative phase of the spin up and down states go in and out of phase corresponding to a Larmor precession angular frequency in the subsequent *zero* field region of $2\omega_0$. This precession in the zero field has been referred to as anomalous or "wrong" Larmor precession by Mezei [10].

Figure 9. The oscillating r.f. field by itself does not change the average energy of the neutrons. In the field overlap region (length $l_\pi = l_{B0}$), the spin inversion occurs where all the change in the total energy of the two spin states occurs and where the effective Larmor precession angular frequency is ω_0. The additional splitting of the kinetic energy brought about by the spin inversion is felt at the exit of the static field region, after which the effective Larmor precession frequency is $2\omega_0$.

Figure 10. This is similar to the situation shown in Figure 8, but with a reduction in flipping efficiency due to dispersion (see Sec. 2.2) or a departure from the exact resonance condition (see Sec. 2.3). A fraction of the neutrons that are not flipped return to their original kinetic energy state on leaving the static field region (light gray dashed lines) and these neutrons have no splitting of their total energy. The flipped neutron fraction is represented by the dark gray dashed lines.

Figure 11. Some examples of Monte Carlo-simulated NRSE echo signals in the vicinity of the echo point demonstrating the effects of varying different parameters in isolation. Columns 1 to 3 are for elastic non spin-flip scattering (or no neutron energy change through the spectrometer). Column 4 is for quasielastic non spin-flip scattering. For each of these simulations there are no sample size effects, coil dispersion is switched off, and $\Delta B_0 = \Delta l_{B0}$ (zero field inhomogeneity and perfect dimensions of the flipper coils). Additionally for columns 1 and 4 zero beam divergence is assumed. The effects of dispersion on the spin echo signal are studied in Sec. 8.2.

Figure 12. Simulated and analytical predictions of the effect of ΔB_0 on the elastic polarization $P_x^{\,0}$ for $\tau_{NRSE} = 15$ ns at 8 Å, $N = 1$, with other spectrometer parameters given in the plot title.

Figure 13. Simulated and analytical predictions of the effect of ΔB_0 on the elastic polarization $P_x^{\,0}$ for $\tau_{NRSE} = 30$ ns at 8 Å, $N = 2$, with other spectrometer parameters given in the plot title.

Figure 14. Simulated and analytical predictions of the effect of Gaussian fluctuations of the π-flipper length resulting from independent Gaussian fluctuations of the flatness of the windings on the entrance and exit sides of the coil. In this example, $N = 1$, $\tau_{NRSE} = 15$ ns and the other spectrometer parameters are given in the plot title.

Figure 15. Simulated and analytical predictions of the effect of Gaussian fluctuations of the π-flipper length resulting from independent Gaussian fluctuations of the flatness of the windings on the entrance and exit sides of the coil. In this example $N = 2$, $\tau_{NRSE} = 30$ ns and the other spectrometer parameters are given in the plot title.

Figure 16. Essentials of the "simplified" divergence model.

Figure 17. Monte Carlo simulated (black circles) and analytical predictions for the relationship between maximum divergence $\Delta\theta_{\max}$ ($\Delta\theta$ uniformly distributed up to $\Delta\theta_{\max}$) and P_x^0 for the case $N = 1$, $\tau_{NRSE} = 15$ ns. The other spectrometer parameters are given in the plot title. The analytical approximation (as expressed by Eq. (213) [Eq. (216) for the particular case of $|\Delta\theta_i^{max}| = |\Delta\theta_f^{max}| = |\Delta\theta_{max}|$] describes the simulation very well and is represented by the red curve. The approximation (Eq. (222)) that should be valid for $|\Delta\theta_{max}| <\sim 8.4\times10^{-3}$ rad to within 1% is shown by the blue dashed curve.

Figure 18. Monte Carlo simulated (black circles) and analytical predictions for the relationship between maximum divergence $\Delta\theta_{\max}$ ($\Delta\theta$ uniformly distributed up to $\Delta\theta_{\max}$) and P_x^0 for the case $N = 2$, $\tau_{NRSE} = 30$ ns. The other spectrometer parameters are given in the plot title. The analytical approximation (as expressed by Eq. (213) [Eq. (216) for the particular case of $|\Delta\theta_i^{max}| = |\Delta\theta_f^{max}| = |\Delta\theta_{max}|$] describes the simulation very well and is represented by the red curve. The approximation (Eq. (222)) that should be valid for $|\Delta\theta_{max}| <\sim 6.0\times10^{-3}$ rad to within 1% is shown by the blue dashed curve.

Figure 19. Parameter tolerances (see legend for units) required to achieve a specified minimum elastic (resolution) polarization P_x^0 for $\tau_{NRSE} = 30$ ns at 8 Å with the above spectrometer dimensions (B_0=0.0393 T) with approximately equal contributions to the depolarization coming from ΔB_0, Δl_{B0}, and $\Delta\theta_{max}$.

Figure 20. A N=2 bootstrap coil on the RESEDA spectrometer at FRM-II. The zero field flight paths are magnetically shielded by a double-skinned μ-metal enclosure (removed). The μ-metal screen on the face of the coil, the r.f. coil air cooling connections (blue) and the static field coil water cooling connections (black) are visible (photo kindly allowed by T. Keller, FRM-II).

Figure 21. Estimated neutron transmission of the combined 32 layers of windings for a 4 $N = 2$ coil NRSE assuming that the static field and r.f. coil windings each have equal thickness t. These curves are based on the total cross-section of pure aluminum at 300 K.

Figure 22. A static field coil developed for the Zeta spectrometer at the ILL, Grenoble using circular section Al wire. This type of coil is used for lower resolution applications. (Photos kindly allowed by R. Gähler, ILL).

Figure 23. Dimension parameters of the static field coil using tightly-wound rectangular cross-section windings.

Figure 24. A short circular solenoid.

Figure 25. Variation of axial magnetic field along the axis of idealized solenoids of differing diameter:axial length ratio, η.

Figure 26. Two r.f. coils developed at the ILL. Left (smaller) uses anodized pure Al tape for the windings in the beam area. The larger model (right) uses circular section anodized pure Al wire. (Photos kindly allowed by R. Gähler, ILL, Grenoble).

Figure 27. r.f. filter with lossless cables. R includes the resistance (likely mainly from the r.f. coil).

Figure 28. r.f. filter with losses in cables (cable resistance, represented by R_{cable}, and conductance of dielectric, represented by G_{cable}).

Figure 29. Part of the high voltage r.f. circuit used to energize the r.f. coils at FRM-II, Munich (photo kindly allowed by T. Keller, FRM-II).

Figure 30. r.f. coil dimensions assuming rectangular cross-section windings.

Figure 31. Using a 4-N = 1 coil NRSE spectrometer in NSE mode for measuring small Fourier times. The r.f. field is turned off in the coils. (a) using the static field of two coils for the precession fields (b) using the static field of all four coils to access higher τ.

Figure 32. Using a 4-N = 2 coil NRSE spectrometer in NSE mode for measuring small Fourier times. The r.f. field is turned off in all coils: (a) all static fields on, using π flippers (b) (if feasible) switching off all wrong field directions (no π flipper) (c) switching off all but two of the fields.

Figure 33. Fourier time (τ_{NRSE}) ranges resulting from evenly-spaced values of B_0 in the range from about 1.7 mT (the minimum for NRSE operation in this example) to 0.04 T for both NSE mode (red circles) and NRSE mode (blue squares). This example is for λ_i = 8 Å, N = 2, L_0 = 2 m, and l_{B0} = 0.03 m. The curve happens to correspond to a 40 neV quasi-elastic scatterer in a highly-idealized spectrometer with quasi-perfect resolution (perfectly ideal construction, field uniformity etc.) and zero coil dispersion. Identical values of B_0 were used for each mode. Note that the NSE mode is highly compressed in τ_{NRSE} with respect to the NRSE mode for equivalent static fields.

Figure 34. A coupling coil at the exit of a μ-metal housing on the NRSE-TAS spectrometer at the FRM-II, Garching, Germany (photo kindly allowed by T. Keller). The windings are bent outwards at the exit to avoid attenuation of the beam and to ensure an adiabatic transfer from the polarizer/analyzer field to the CC guide field.

Figure 35. The effective magnetic field in a coordinate frame fixed to the rotating field. Two situations are shown tending towards the extreme adiabatic and non-adiabatic cases.

Figure 36. Simulated spectrometer resolution function using the field inhomogeneity, coil length uncertainty and beam divergence calculated according to Eqs. (223), (224), and (225) (simplified incident-scattered divergence model) to give an estimated $P_x^{\,0}$ (λ = 8 Å , τ_{NRSE} = 30 ns) = 0.7, 0.5, and 0.3 with flipper dispersion switched off.

Figure 37. Simulated spectrometer resolution function using the field inhomogeneity, coil length uncertainty and beam divergence calculated according to Eqs. (223), (224), and (225) (simplified incident-scattered divergence model) to give an estimated $P_x^{\,0}$(λ = 8 Å, τ_{NRSE} = 30 ns) = 0.5, but with λ_0 = 12 Å. Coil dispersion switched off. The uncertainty values used are given in the legend.

Figure 38. This example shows the effect of incident and scattered beam divergence in isolation with random polar angles up to $\theta_c^{\text{Nat Ni}}$ (λ = 8 Å) (simplified divergence model) with no other spectrometer imperfections and no dispersion.

Figure 39. A simulated quasielastic experiment for Γ(HWHM) = 0.025 μeV. Black curve- simulated "measured data"; red curve - simulated resolution function; blue curve - simulated measured data divided by simulated resolution function; green curve - theoretical intermediate scattering function for Γ(HWHM) = 0.025 μeV.

Figure 40. Simulated elastic (resolution) spin echo signal (asymmetric scan) at τ_{NRSE} = 30 ns (no coil dispersion) . Note that the peak polarization at zero asymmetry should match the value of the resolution curve at τ_{NRSE} = 30 ns in Figure 39 within statistics.

Figure 41. Simulated quasi-elastic spin echo signal (asymmetric scan) at τ_{NRSE} = 30 ns (no coil dispersion). Note that the peak polarization at zero asymmetry should match the value of the simulated raw quasielastic data curve at τ_{NRSE} = 30 ns in Figure 39 within statistics.

Figure 42. A simulated quasielastic experiment for Γ(HWHM) = 0.05 μeV. Black curve- simulated "measured data"; red curve - simulated resolution function; blue curve - simulated measured data divided by simulated resolution function; green curve - theoretical intermediate scattering function for Γ(HWHM) = 0.05 μeV.

Figure 43. Simulated effects of flipper coil dispersion for rectangular incident wavelength spectra compared with analytical approximations (see Sec. 2.2.2) for various values of $\alpha_{FW} = \Delta\lambda_i^{FW}/\langle\lambda_i\rangle$, for a “perfect” instrument ($\Delta B_0 = 0$, $\Delta l_{B0} = 0$, $\Delta\theta_{max,i} = \Delta\theta_{max,f} = 0$) and for elastic scattering (resolution function).

Figure 44. Simulated effects of flipper coil dispersion for triangular incident wavelength spectra compared with analytical approximations (see Sec. 2.2.2) for various values of $\alpha_{FWHM} = \Delta\lambda_i^{FWHM}/\langle\lambda_i\rangle$, for a “perfect” instrument ($\Delta B_0 = 0$, $\Delta l_{B0} = 0$, $\Delta\theta_{max,i} = \Delta\theta_{max,f} = 0$) and for elastic scattering (resolution function).

Figure 45. Simulated effects of flipper coil dispersion for Gaussian incident wavelength spectra compared with analytical approximations (see Sec. 2.2.2) for various values of $\alpha_{FWHM} = \Delta\lambda_i^{FWHM}/\langle\lambda_i\rangle$, for a "perfect" instrument ($\Delta B_0 = 0$, $\Delta l_{B0} = 0$, $\Delta\theta_{max,i} = \Delta\theta_{max,f} = 0$) and for elastic scattering (resolution function).

Figure 46. Comparison of resolution functions with (black curve) and without (blue curve) dispersion switched on ($\Delta\lambda_i^{FWHM}/\langle\lambda_i\rangle$ = 10 %, triangular) using spectrometer uncertainties expected to give $P_x^0(\lambda = 8$ Å, $\tau_{NRSE} = 30$ ns) = 0.5 in the *absence* of dispersion. The dispersive resolution in the absence of all other spectrometer uncertainties is shown by the red curve. The similarity of the ratio of the black to the red curve (green curve) to the simulated non-dispersive signal (blue curve – also the red curve in Figure 39 and Figure 42) demonstrates that the effects of dispersion are approximately decoupled from uncertainties which lead to depolarization in the perpendicular plane for $\Delta\lambda/\lambda$ = 10 %.

Figure 47. Comparison of resolution functions with (black curve) and without (blue curve) dispersion switched on ($\Delta\lambda_i^{FWHM}/\langle\lambda_i\rangle$ = 30 %, triangular) using spectrometer uncertainties expected to give $P_x^0(\lambda = 8$ Å, $\tau_{NRSE} = 30$ ns) = 0.5 in the *absence* of dispersion. The dispersive resolution in the absence of all other spectrometer uncertainties is shown by the red curve. The similarity of the ratio of the black to the red curve (green curve) to the simulated non-dispersive signal (blue curve – also the red curve in Figure 39 and Figure 42) demonstrates that the effects of dispersion are approximately decoupled from uncertainties which lead to depolarization in the perpendicular plane for $\Delta\lambda/\lambda$ = 30 %.

Figure 48. A simulated quasielastic experiment with Γ(H WHM) = 0.025 μeV with dispersion switched ON for a very broad incident wavelength range ($\Delta\lambda_i^{FWHM}/\langle\lambda_i\rangle$ = 30 %, triangular). Black curve- simulated "measured data"; red curve - simulated dispersive resolution function; blue curve - simulated measured data divided by simulated resolution function; green curve - theoretical intermediate scattering function for Γ(HWHM) = 0.025 μeV.

Figure 49. Simulated elastic (resolution) spin echo signal (asymmetric scan) at τ_{NRSE} = 30ns - dispersive case with $\Delta\lambda_i^{FWHM}/\langle\lambda_i\rangle$ = 30 %, triangular. Note that the peak polarization at zero asymmetry should match the value of the resolution curve at τ_{NRSE} = 30 ns in Figure 48 within statistics.

Figure 50. Simulated quasi-elastic spin echo signal (asymmetric scan) at τ_{NRSE} = 30ns - dispersive case with $\Delta\lambda_i^{FWHM}/\langle\lambda_i\rangle$ = 30 %, triangular. Note that the peak polarization at zero asymmetry should match the value of the simulated raw quasielastic data curve at τ_{NRSE} = 30 ns in Figure 48 within statistics.

Figure 51. A more realistic situation for determining path length differences in the NRSE spectrometer.

Figure 52. Calculation of probability density for polar angle θ from an ideal guide characterized by uniform horizontal and vertical divergence angles in the range $0 \rightarrow \theta_c^x$ and $0 \rightarrow \theta_c^z$ respectively.

Figure 53. Probability density for polar angle θ from an ideal guide characterized by equal uniform horizontal and vertical divergence angles in the range $0 \rightarrow \theta_c$.

Figure 54. Resolution functions (λ = 8 Å) for the coil window and sample sizes given in the legend. For ease of comparison with previous results, the values of $\Delta B_0/B_0$ and Δl_π, L_0 and l_{B0} are exactly those that give $P_x^0(\lambda$ = 8 Å, τ_{NRSE} = 30 ns) = 0.5 in the simplified model case. The difference here is in the incoming and scattered beam divergence acceptance.

Figure 55. Simulated $P(\theta)$ of incident and scattered neutron trajectories that exit the final coil for the λ = 8 Å cases shown in Figure 54. It is expected that the divergence is largely limited by the coil window sizes on both sides of the sample.

Figure 56. Simulated $P(\theta)$ of incident and scattered neutron trajectories that exit the final coil for λ = 1 Å with W_{win} = H_{win} = 3 cm. It is expected that the divergence on the *incident* side is largely determined by the characteristic $P(\theta)$

of the guide, whereas the *scattered* beam divergence is driven by the coil window size. The inset shows $P(\theta_i)$ on a scale that is more easily compared with Figure 53.

Figure 57. Schematic of a possible MIEZE-II NRSE instrument configuration (as proposed by Gähler).

Figure 58. Schematic of a quasi-elastic NRSE instrument using permanent magnets to provide the static field.

Figure 59. Schematic of flipper coil unit using a permanent magnetic material.

Figure 60. With the r.f. *H*-field oriented as shown in a slab of good conductor, most of the r.f. power is absorbed perpendicular to the plane containing *E* and *H* (in the direction of the Poynting vector) within the skin depth, δ, if $l_{B0} > \delta$.

Figure 61. Possible mechanical interferences when using permanent magnets with a multi-angle geometry.

Figure 62. A possible NSE configuration using permanent magnets.

Figure 63. A section of the polarizing guide feeding the 3-axis NRSE at the FRM-II. The vertical bars are the permanent magnets (photo kindly allowed by T. Keller, FRM-II).

Figure 64. Approximately modeled curved straight guide geometries for simulation of the guide systems described in Table 11.

Figure 65. Simulated differential flux spectra ($d\varphi/d\lambda$) for the guide systems described in Table 11 and for NCNR guide NG-5 at the beam exit upstream of the first solenoid assuming no velocity selector and no polarizer.

Figure 66. Horizontal angular distributions for λ = 8 Å for the guides listed in Table 11. Note that λ = 8 Å is above λ' for all the guides. The figure illustrates the very uniform horizontal angular distributions within the limits

imposed by the critical angles of the straight sections (indicated by the vertical bold black lines for m = 0.5 and m =1 natural Ni]) which is indicative of the near-ideal PST operation of these guides. The guide – curve color correspondence is the same as shown in Figure 65.

Figure 67. Estimated integral fluxes at the guide exits as a function of primary selected wavelength assuming a velocity selector with a triangular transmission function with respect to wavelength, operating with 10% $\Delta\lambda/\lambda$ (FWHM) and with a typical peak transmission of 0.83 and a polarizing cavity having a wavelength-independent transmission of 0.45.

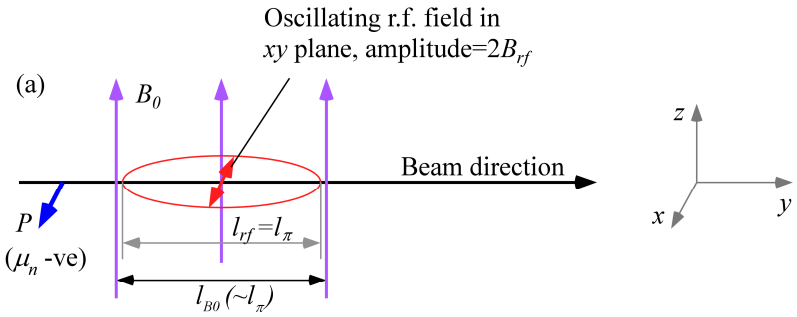

(b) Larmor precession of μ_n due to static field B_0

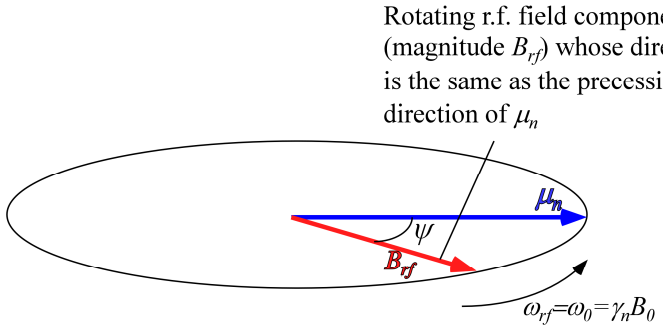

(c) Precession of μ_n angular frequency $\omega_p=\gamma_n B_{rf}$ about B_{rf} (rotation angle $\beta=\pi\nu_n/[\gamma_n l_{rf}]$) in rotating frame

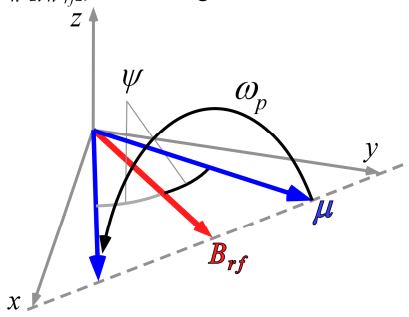

Figure 1. Jeremy C. Cook.

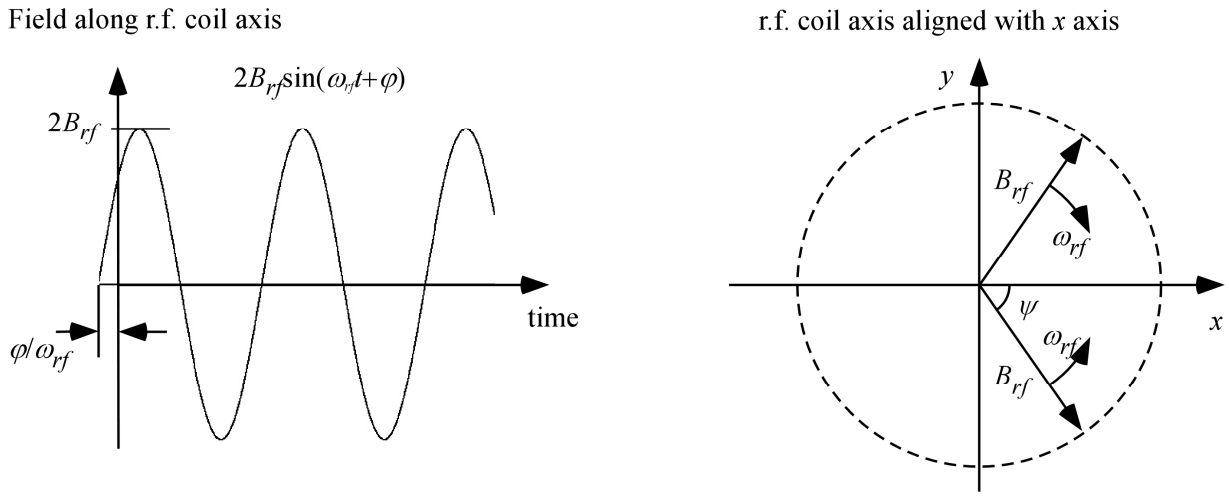

Figure 2. Jeremy C. Cook.

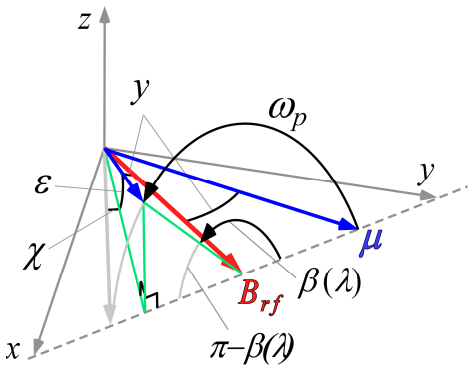

Figure 3. Jeremy C. Cook.

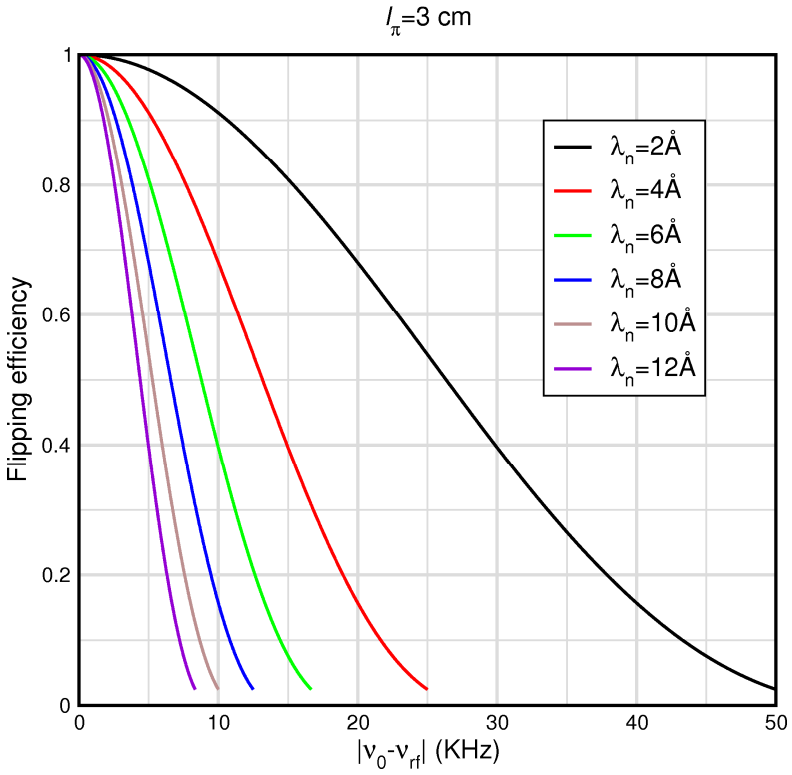

Figure 4. Jeremy C. Cook.

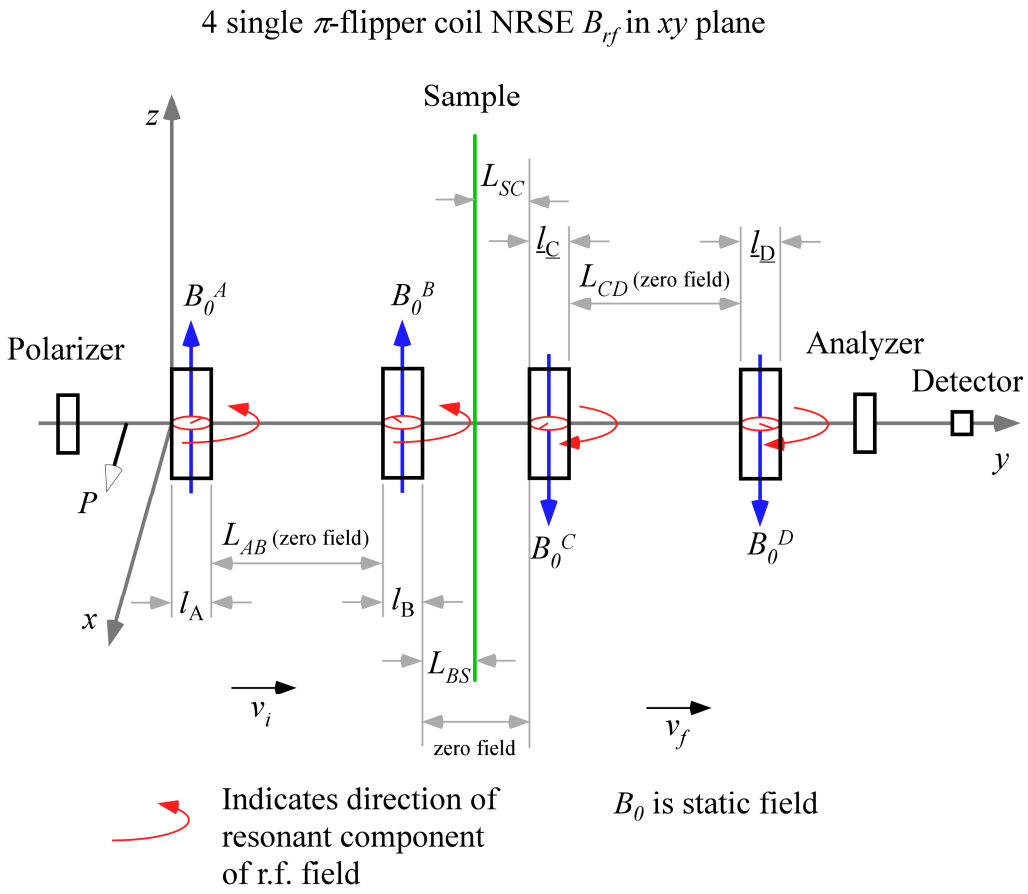

Figure 5. Jeremy C. Cook.

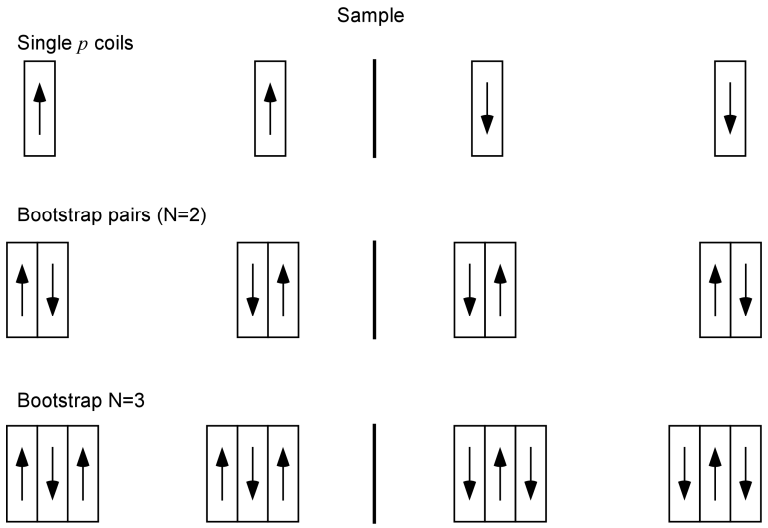

Figure 6. Jeremy C. Cook.

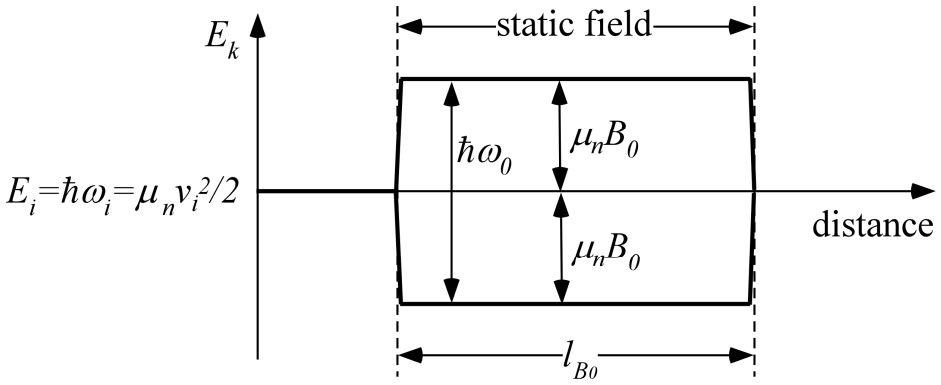

Figure 7. Jeremy C. Cook.

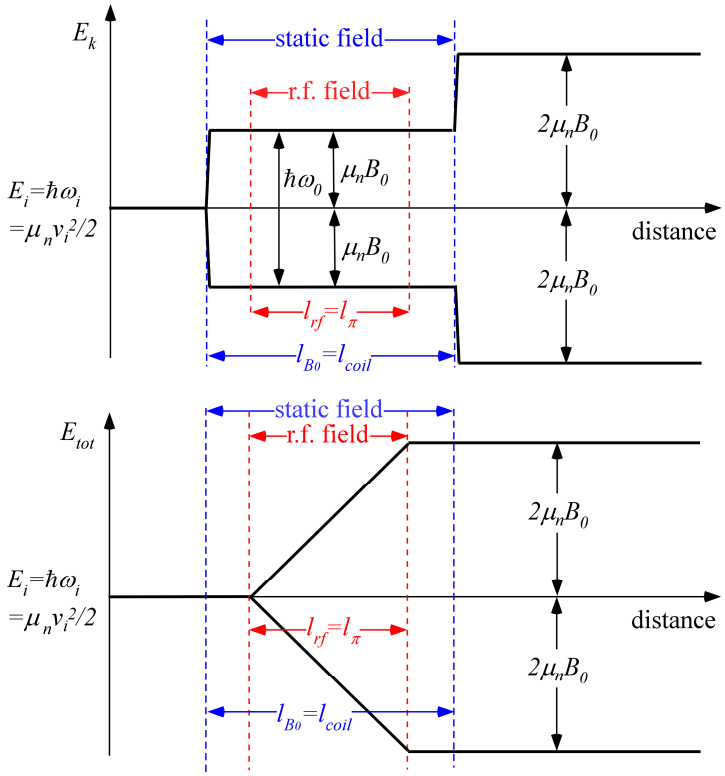

Figure 8. Jeremy C. Cook.

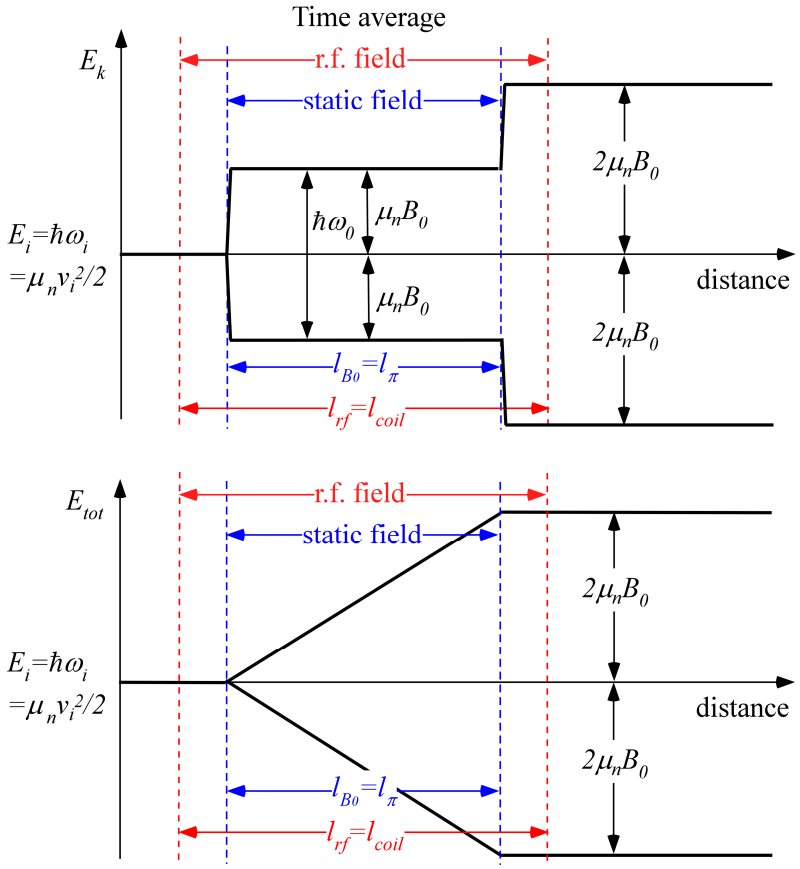

Figure 9. Jeremy C. Cook.

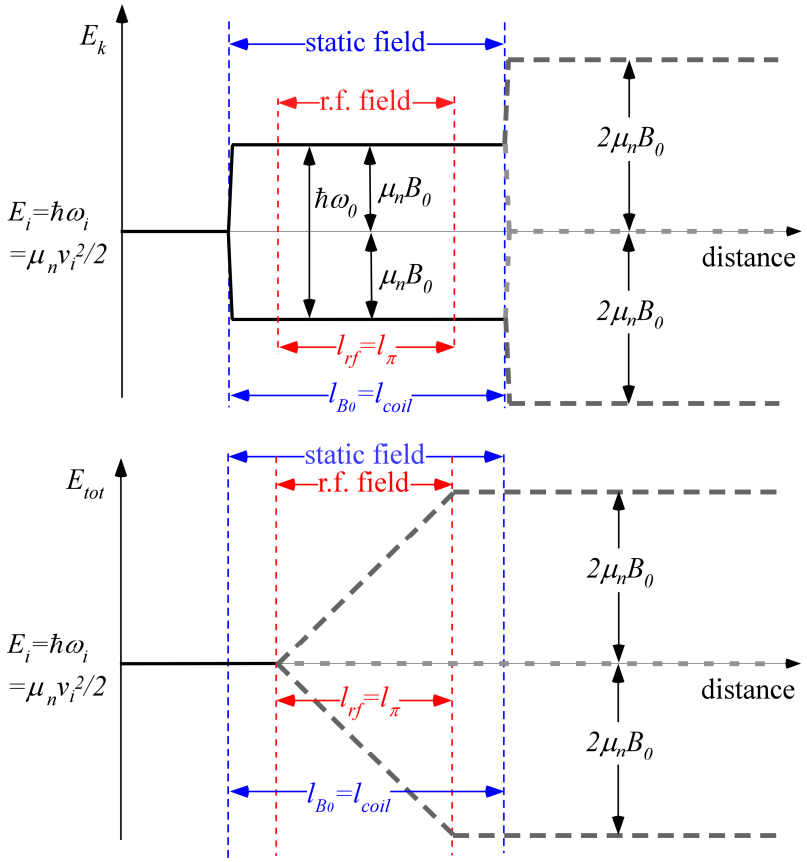

Figure 10. Jeremy C. Cook.

Elastic non-spin flip scattering (zero divergence)	**Elastic non-spin flip scattering ($\Delta\lambda_i/\langle\lambda_i\rangle$=0)**	**Elastic non-spin flip scattering ($\Delta\lambda_i/\langle\lambda_i\rangle$=10%)**	**Quasielastic non-spin flip scattering ($\Delta\lambda_i/\langle\lambda_i\rangle$=0, zero divergence)**
1. $\Delta\lambda_i/\langle\lambda_i\rangle$=0	1. $div_{i,f}=5\times10^{-4}$ rad/Å	1. $div_{i,f}=5\times10^{-4}$ rad/Å	1. Γ=0.025 μeV
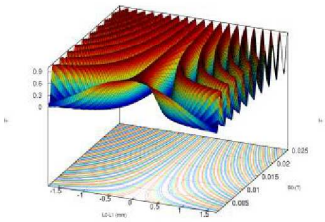	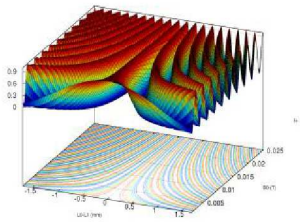	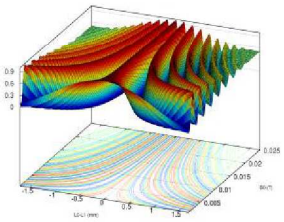	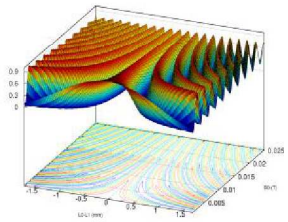
2. $\Delta\lambda_i/\langle\lambda_i\rangle$=10% (triangular)	2. $div_{i,f}=1\times10^{-3}$ rad/Å	2. $div_{i,f}=1\times10^{-3}$ rad/Å	2. Γ=0.05 μeV
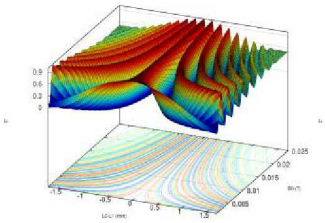	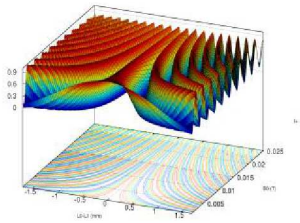	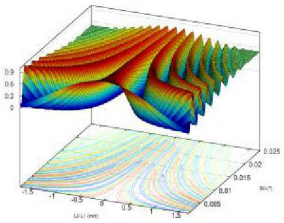	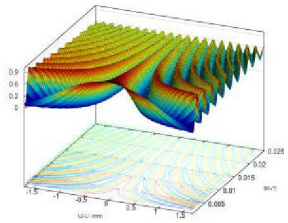
3. $\Delta\lambda_i/\langle\lambda_i\rangle$=20% (triangular)	3. $div_{i,f}=2\times10^{-3}$ rad/Å	3. $div_{i,f}=2\times10^{-3}$ rad/Å	3. Γ= 0.2 μeV
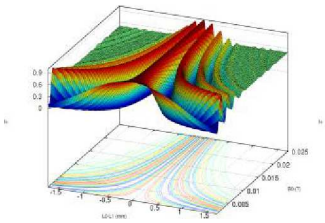	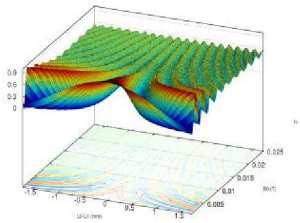	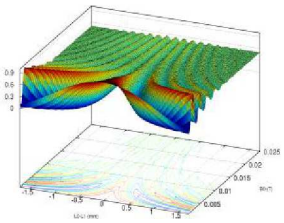	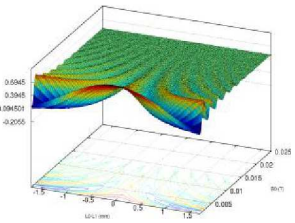

Figure 11. Jeremy C. Cook.

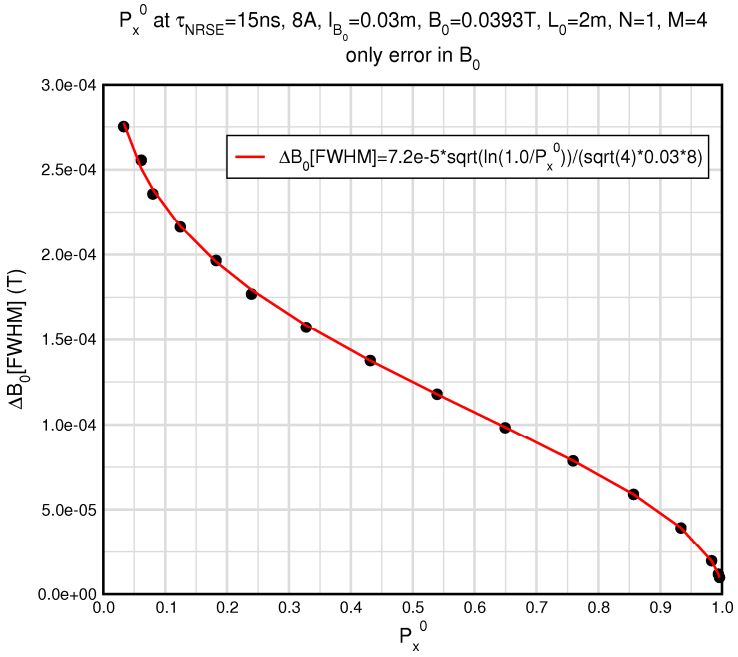

Figure 79. Jeremy C. Cook.

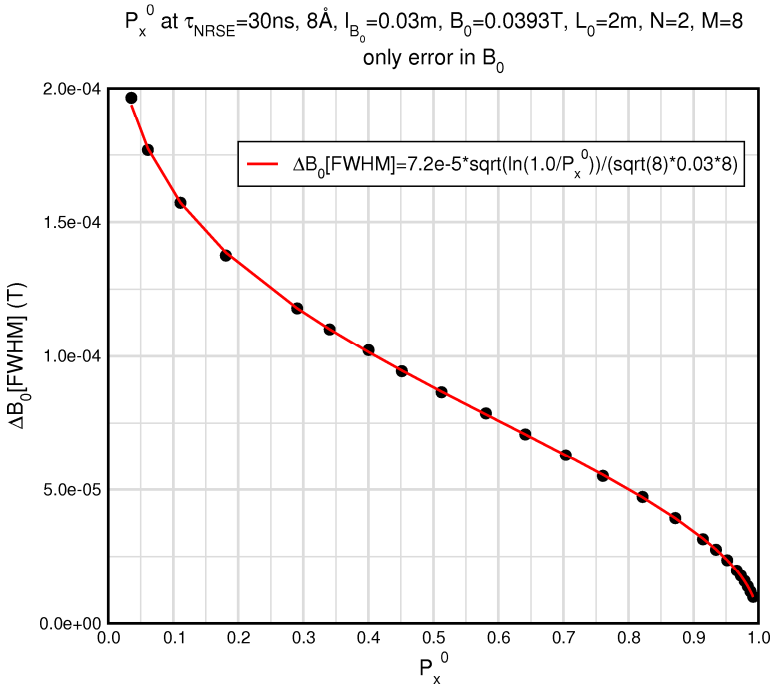

Figure 80. Jeremy C. Cook.

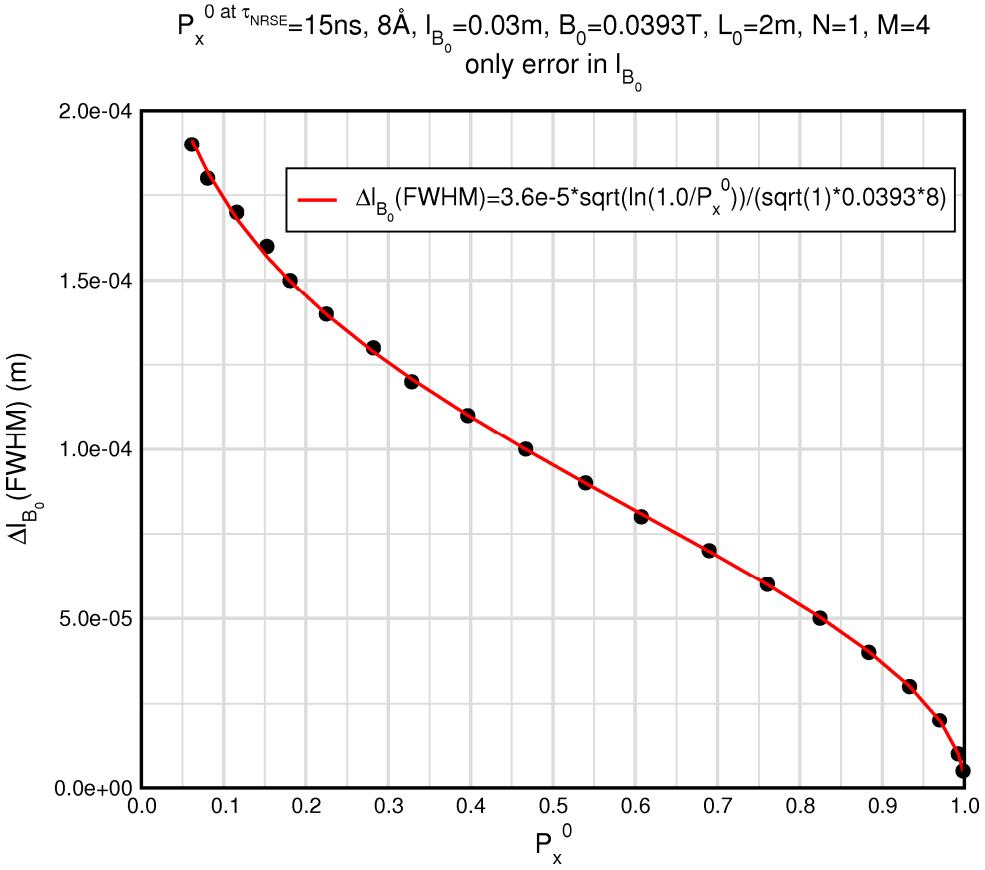

Figure 81. Jeremy C. Cook.

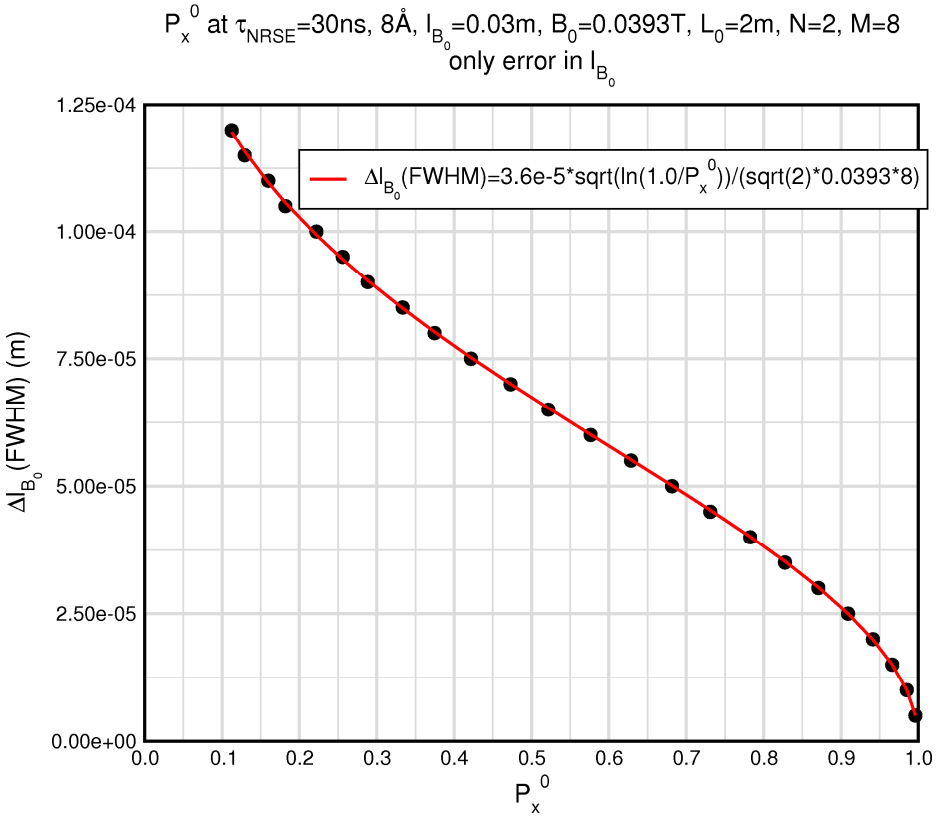

Figure 82. Jeremy C. Cook.

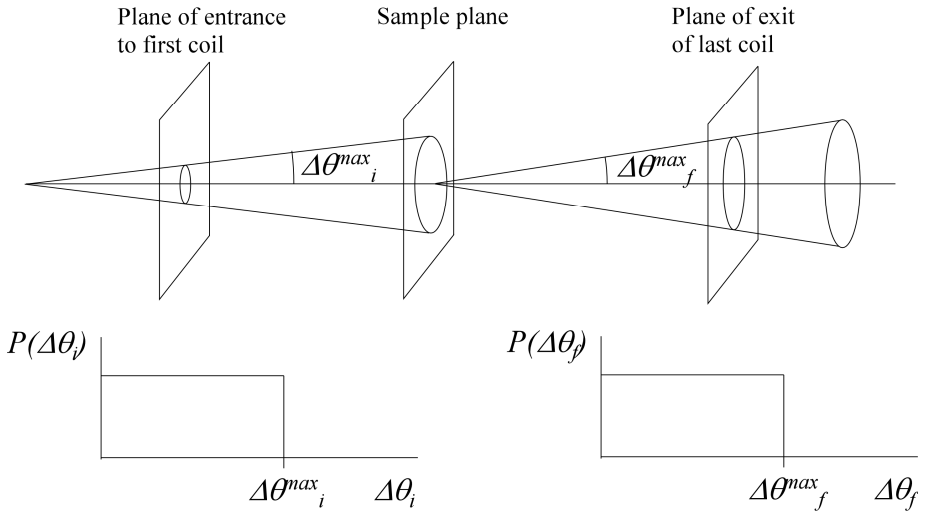

Figure 83. Jeremy C. Cook.

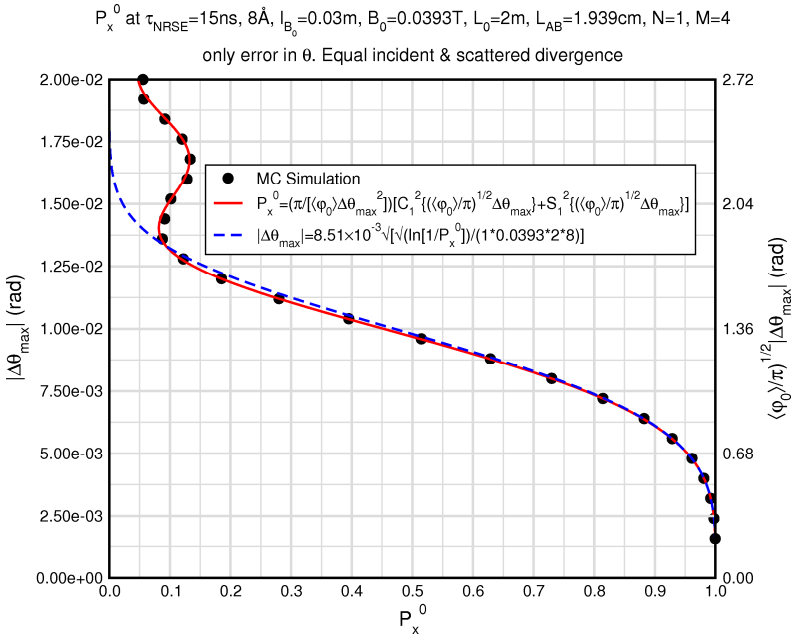

Figure 84. Jeremy C. Cook.

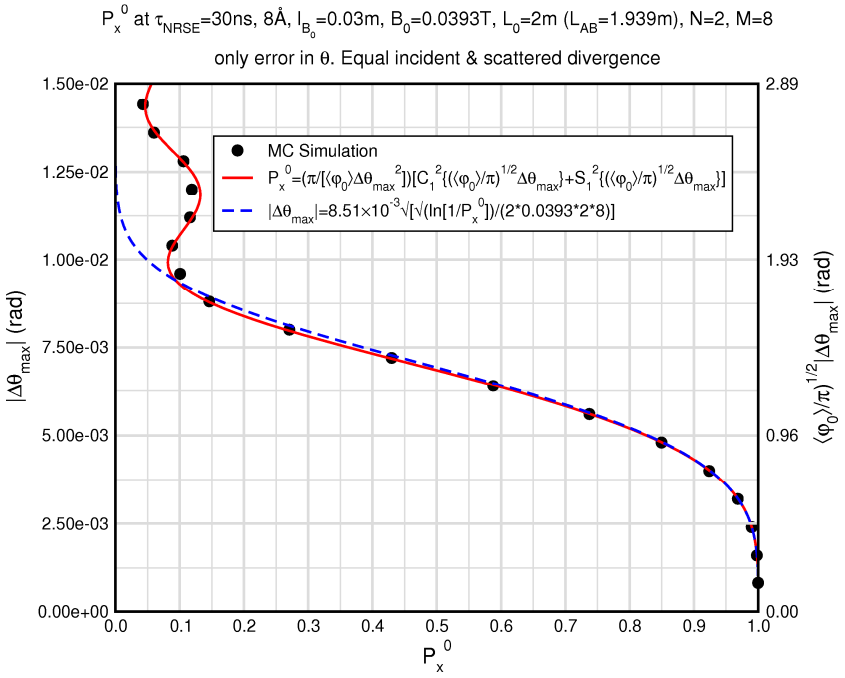

Figure 85. Jeremy C. Cook.

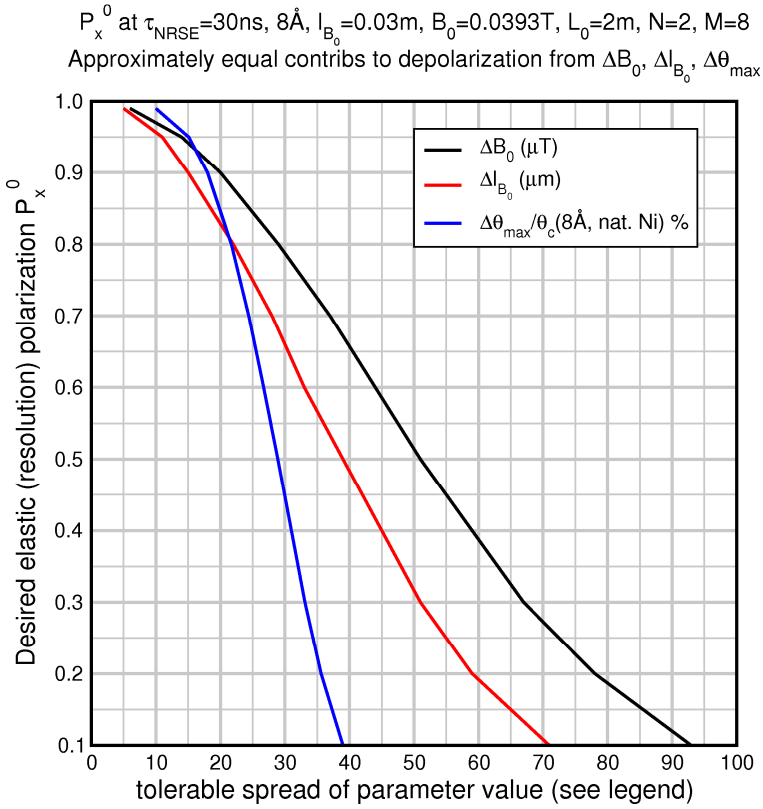

Figure 86. Jeremy C. Cook.

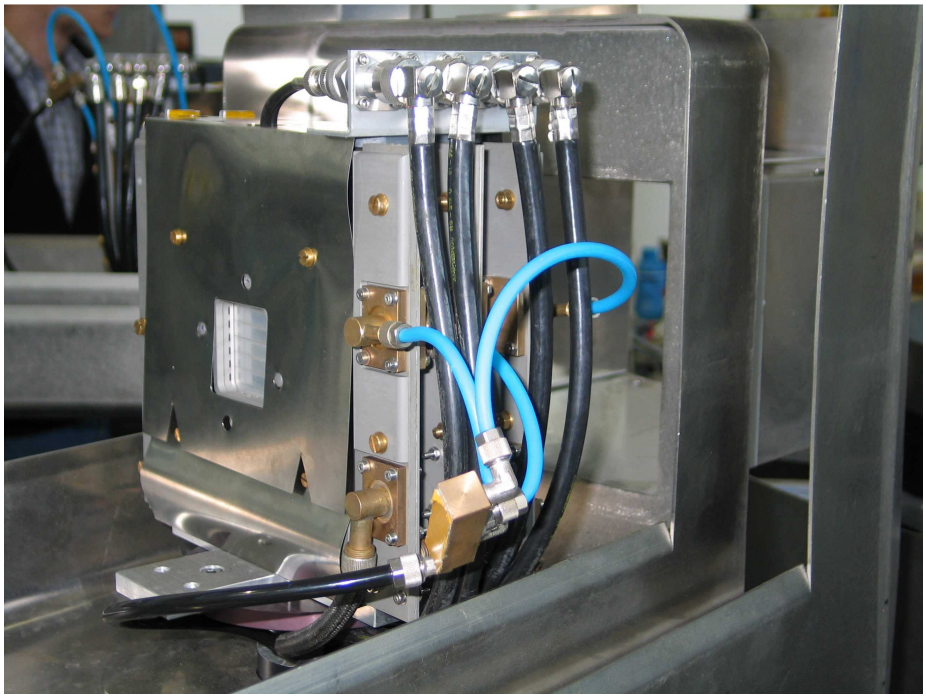

Figure 87. Jeremy C. Cook.

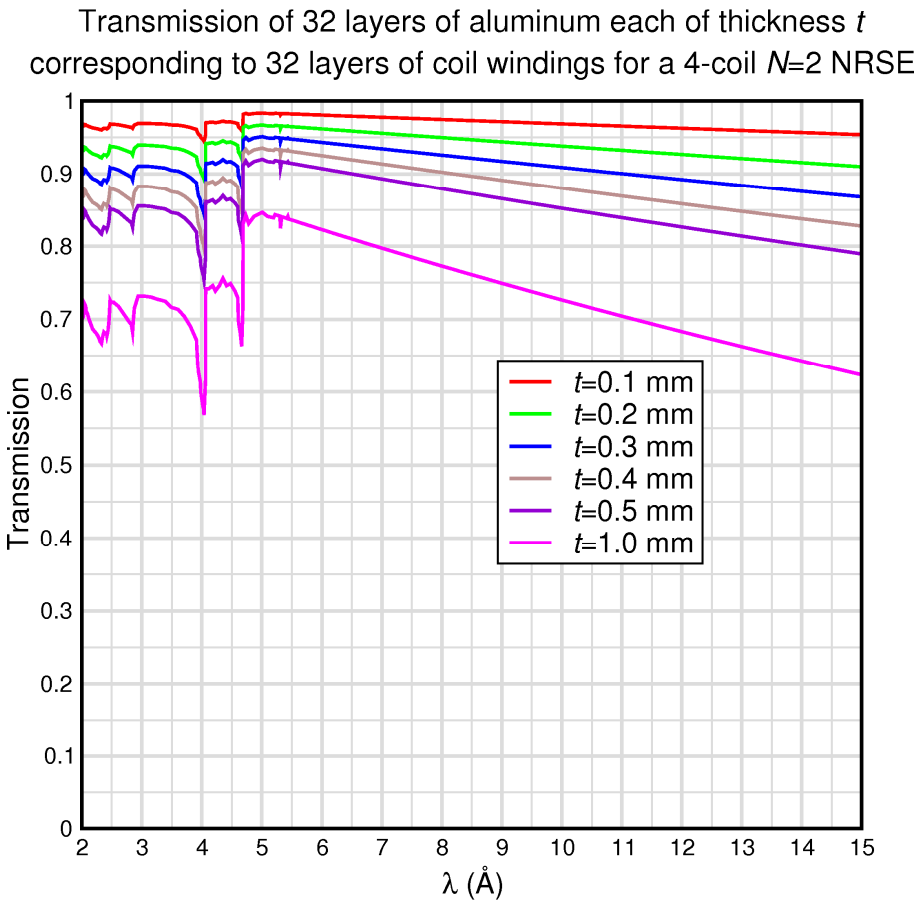

Figure 88. Jeremy C. Cook.

Figure 89. Jeremy C. Cook.

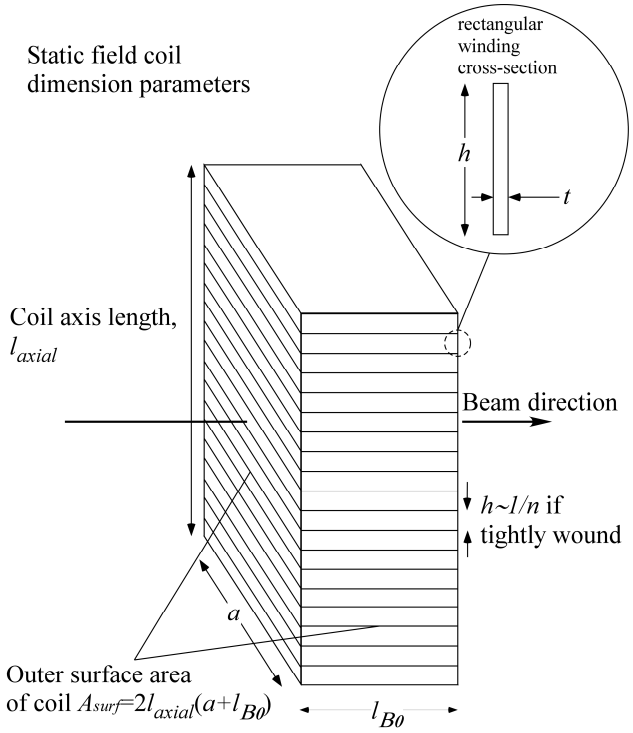

Figure 90. Jeremy C. Cook.

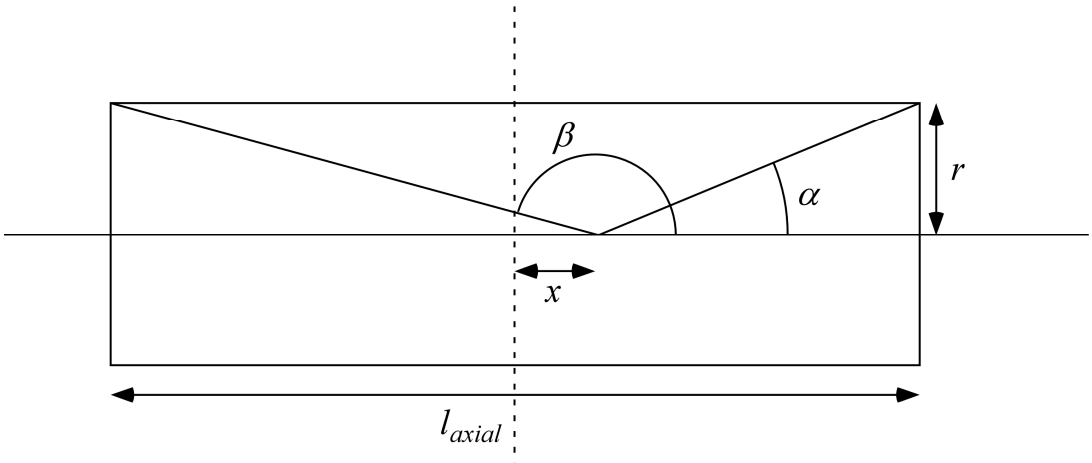

Figure 91. Jeremy C. Cook.

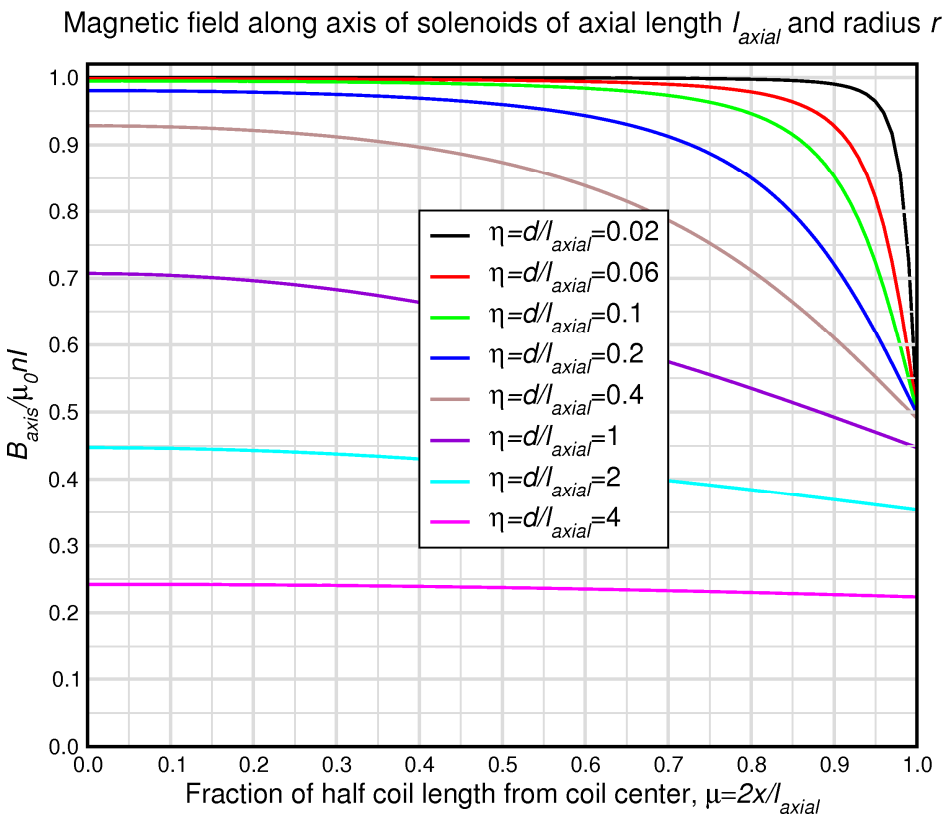

Figure 92. Jeremy C. Cook.

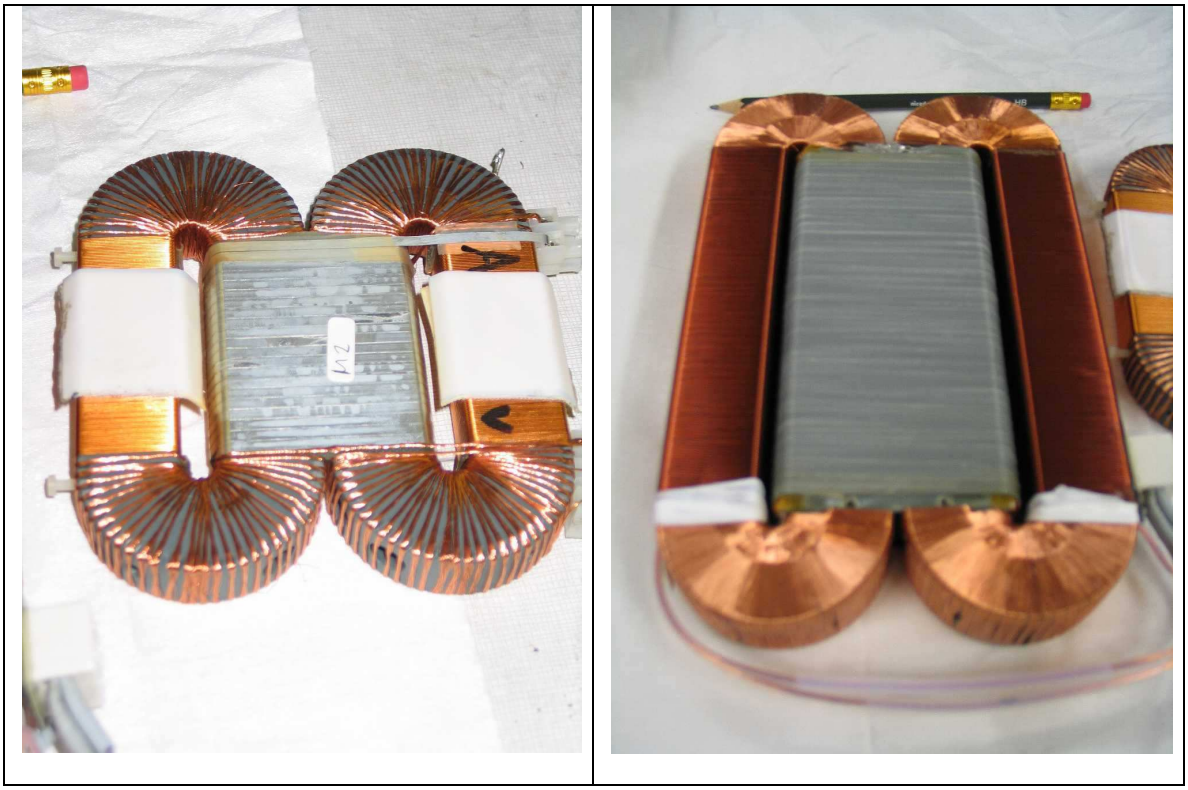

Figure 93. Jeremy C. Cook.

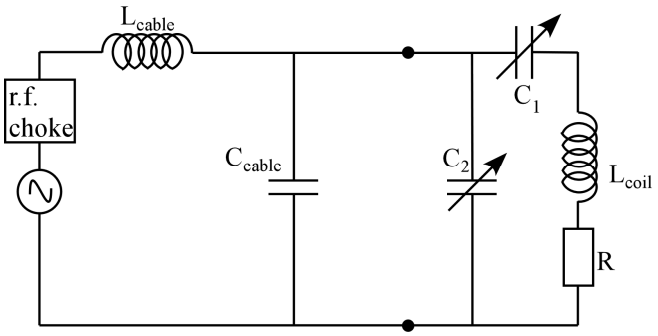

Figure 94. Jeremy C. Cook.

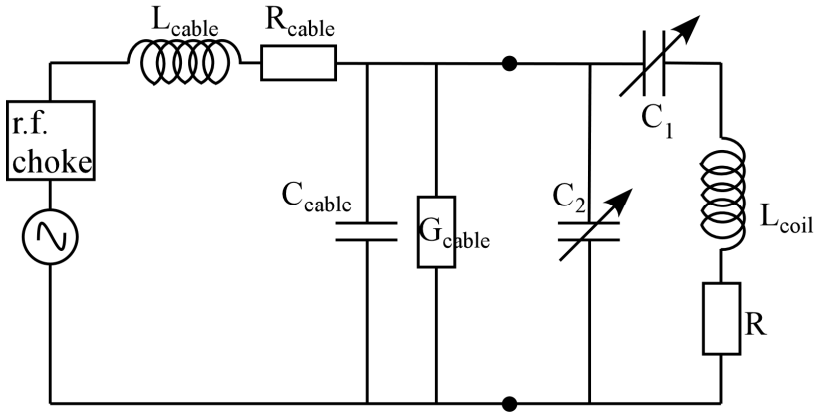

Figure 95. Jeremy C. Cook.

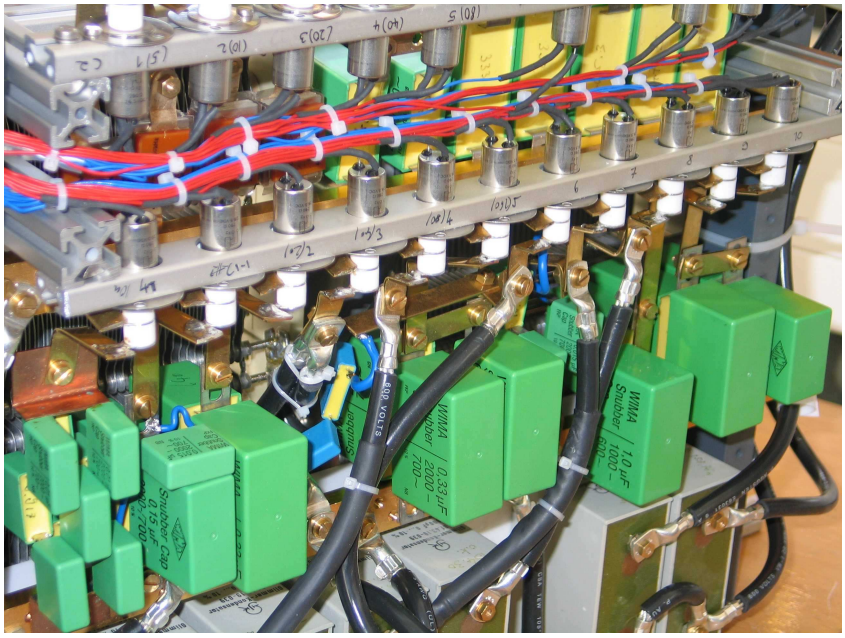

Figure 96. Jeremy C. Cook.

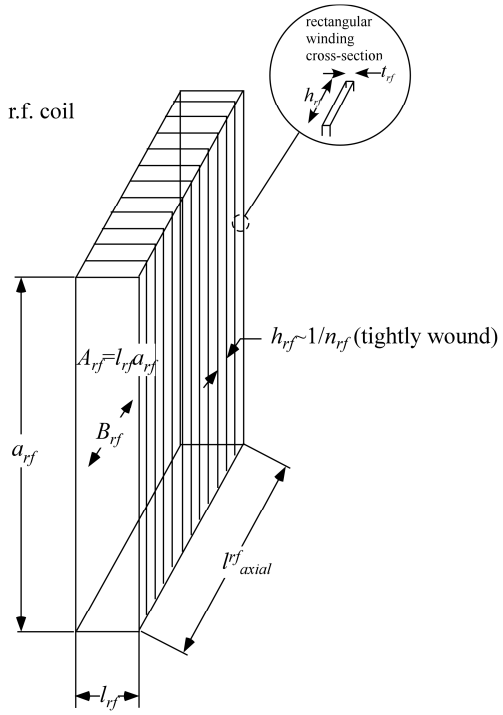

Figure 97. Jeremy C. Cook.

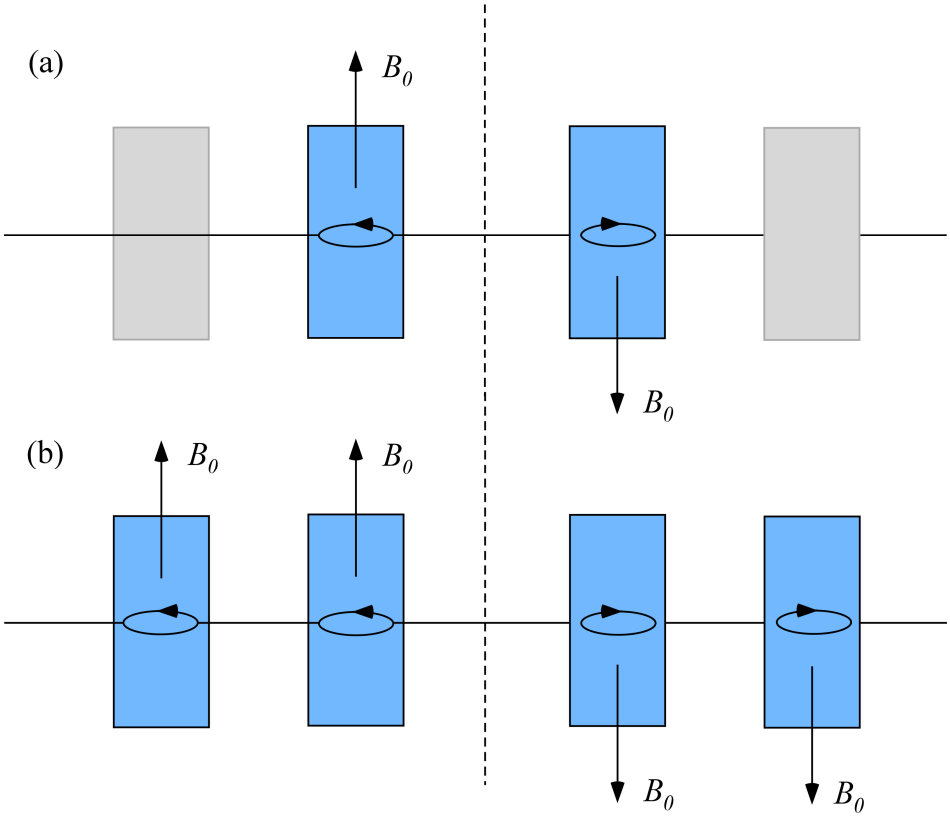

Figure 98. Jeremy C. Cook.

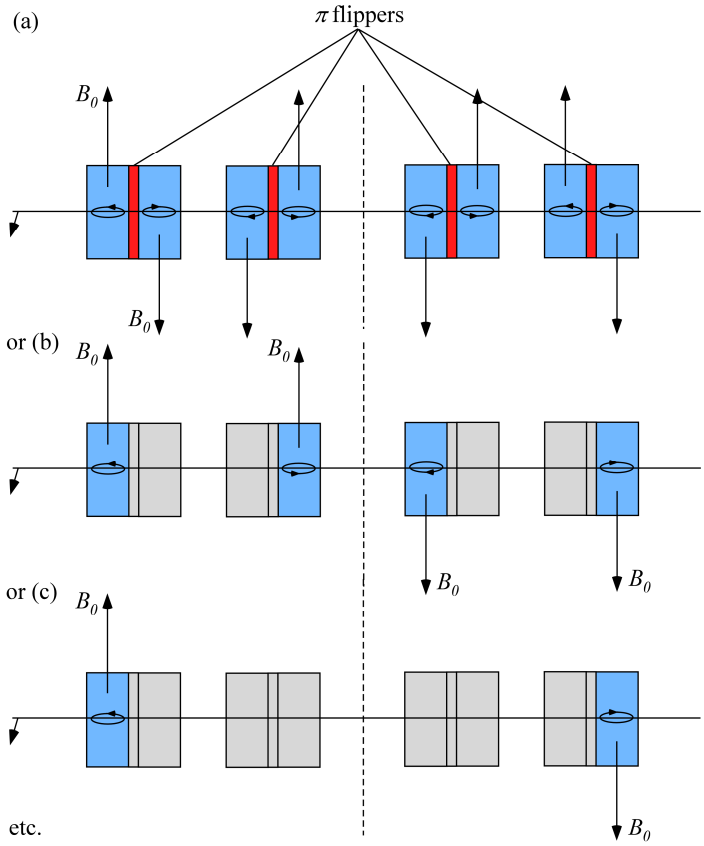

Figure 99. Jeremy C. Cook.

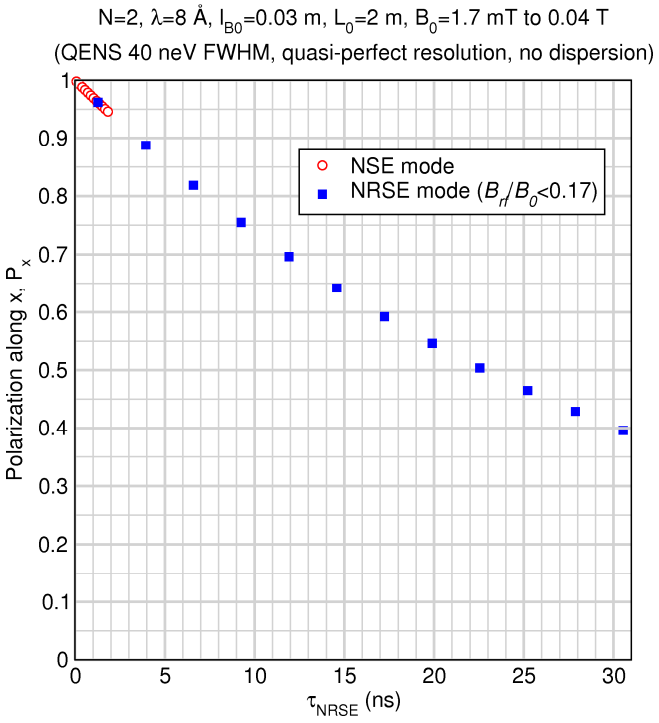

Figure 100. Jeremy C. Cook.

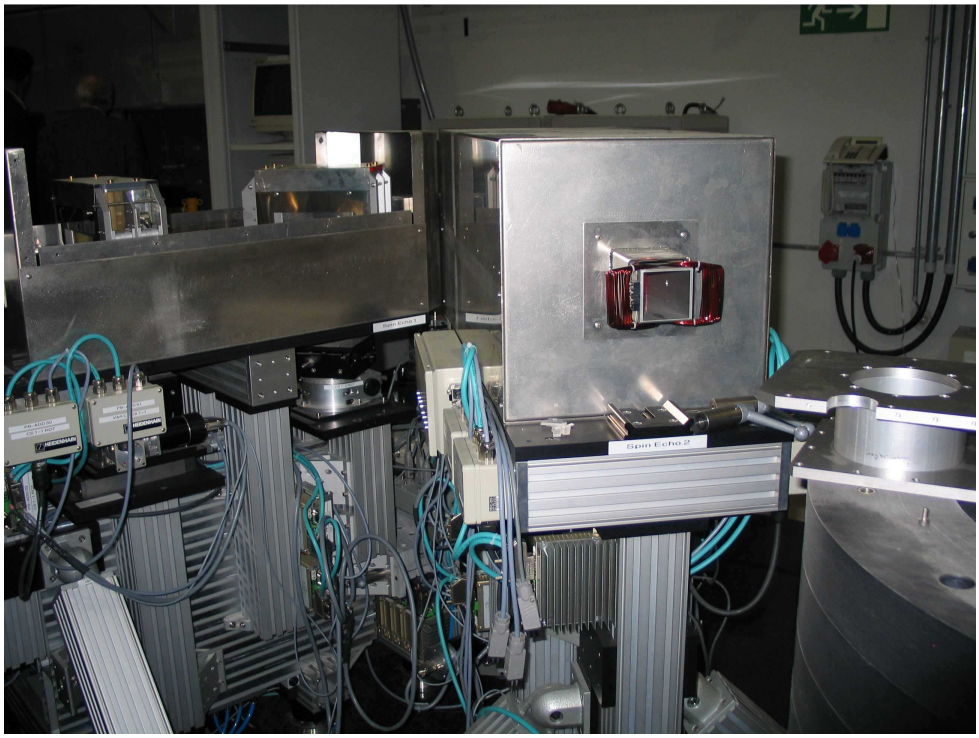

Figure 101. Jeremy C. Cook.

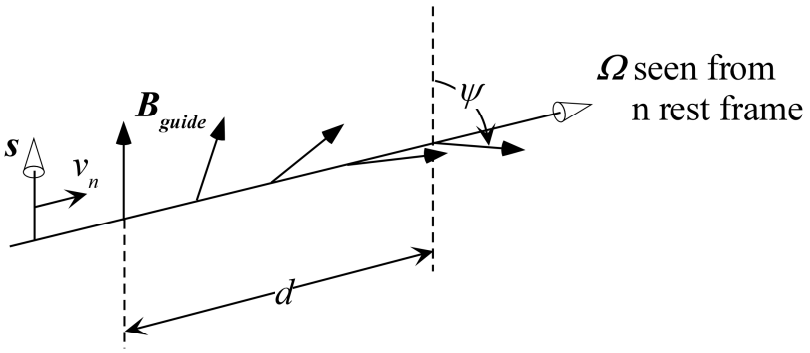

Approaching adiabatic approximation: Apparent field turn frequency $\Omega \ll$ Larmor frequency due to $\boldsymbol{B}_{guide}$

Approaching non-adiabatic approximation: Apparent field turn frequency $\Omega \gg$ Larmor frequency due to $\boldsymbol{B}_{guide}$

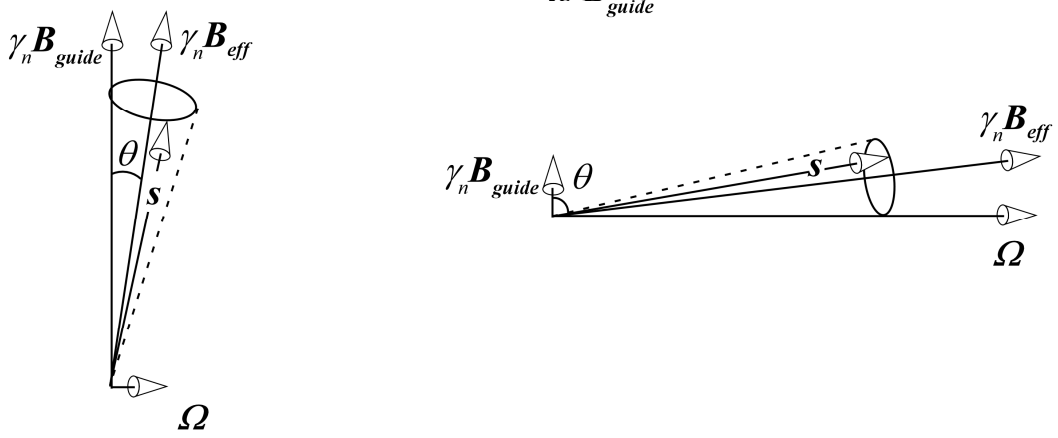

Figure 102. Jeremy C. Cook.

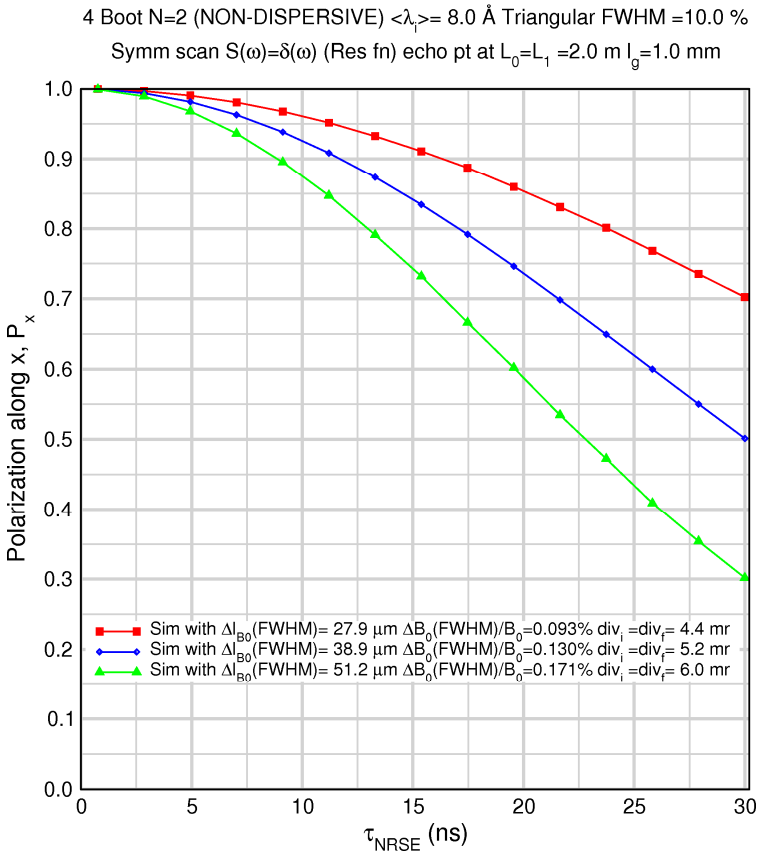

Figure 103. Jeremy C. Cook.

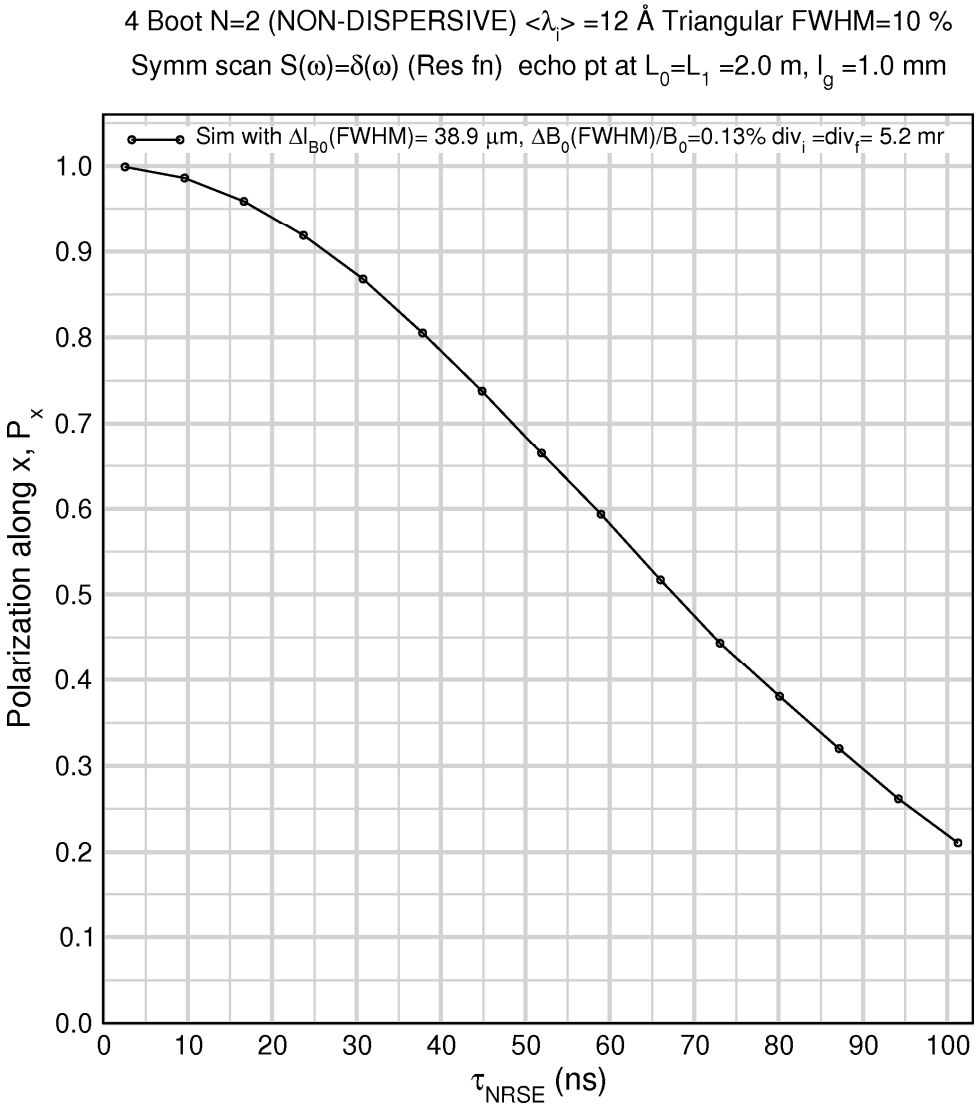

Figure 104. Jeremy C. Cook.

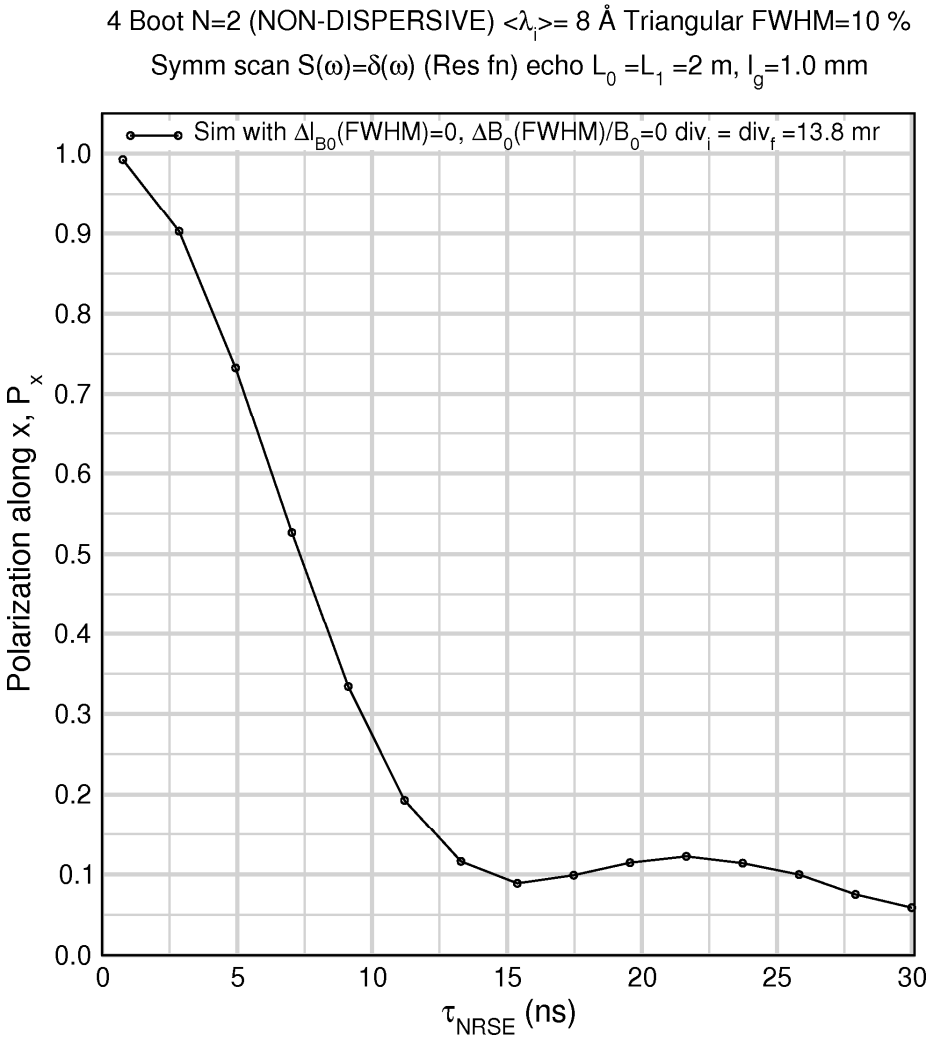

Figure 105. Jeremy C. Cook.

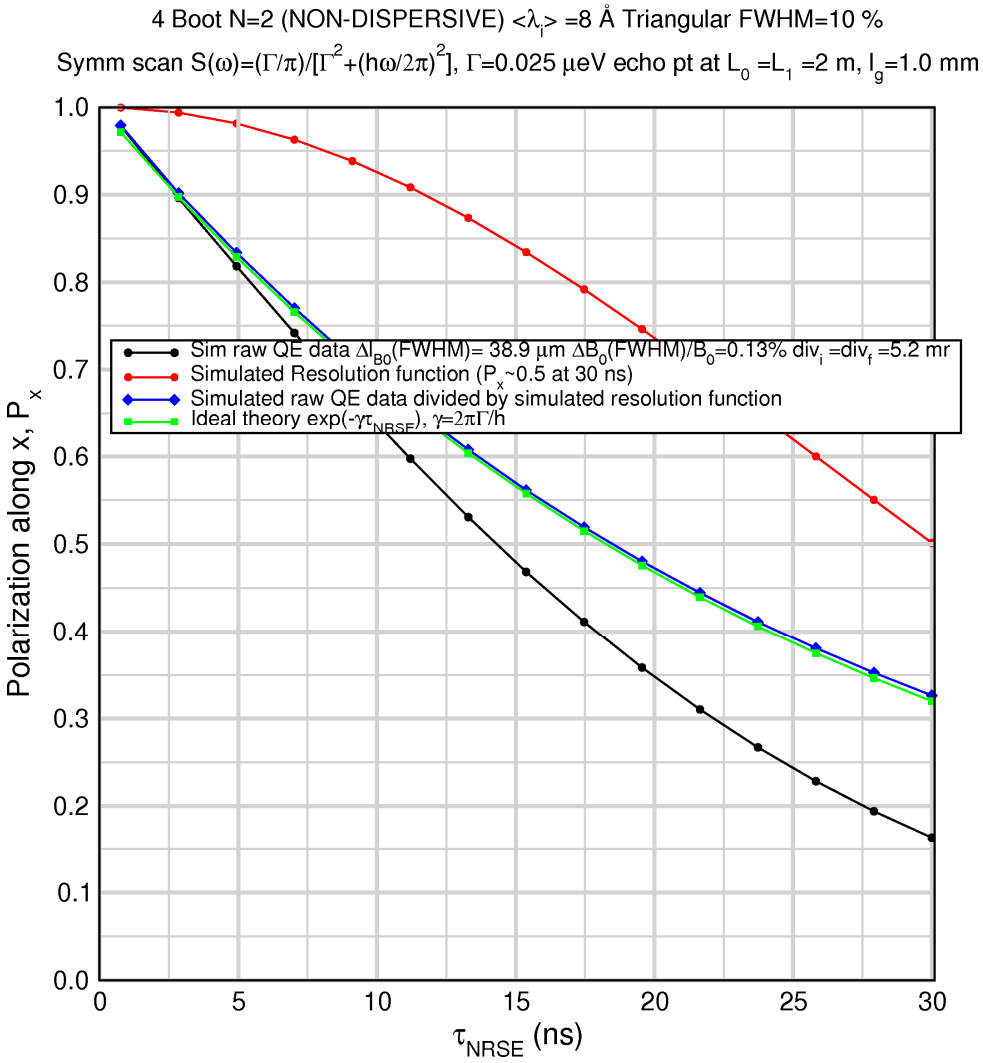

Figure 106. Jeremy C. Cook.

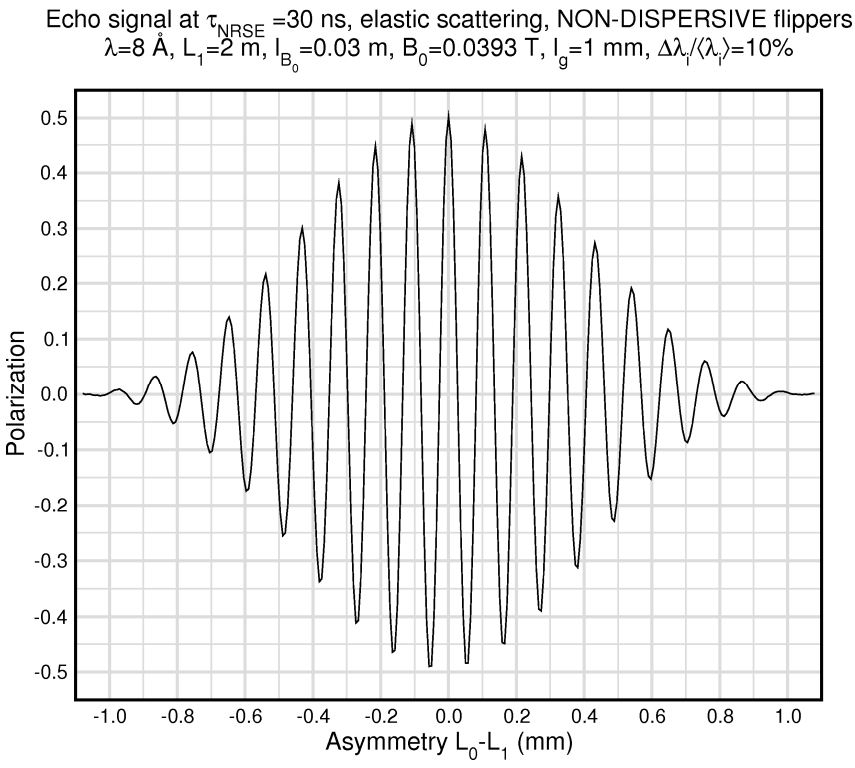

Figure 107. Jeremy C. Cook.

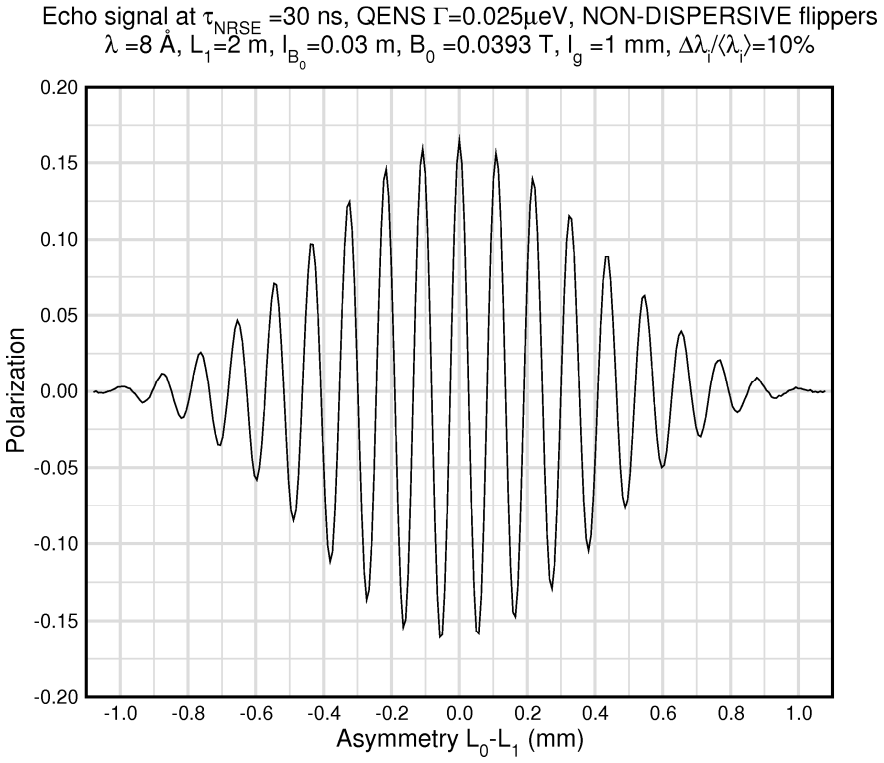

Figure 108. Jeremy C. Cook.

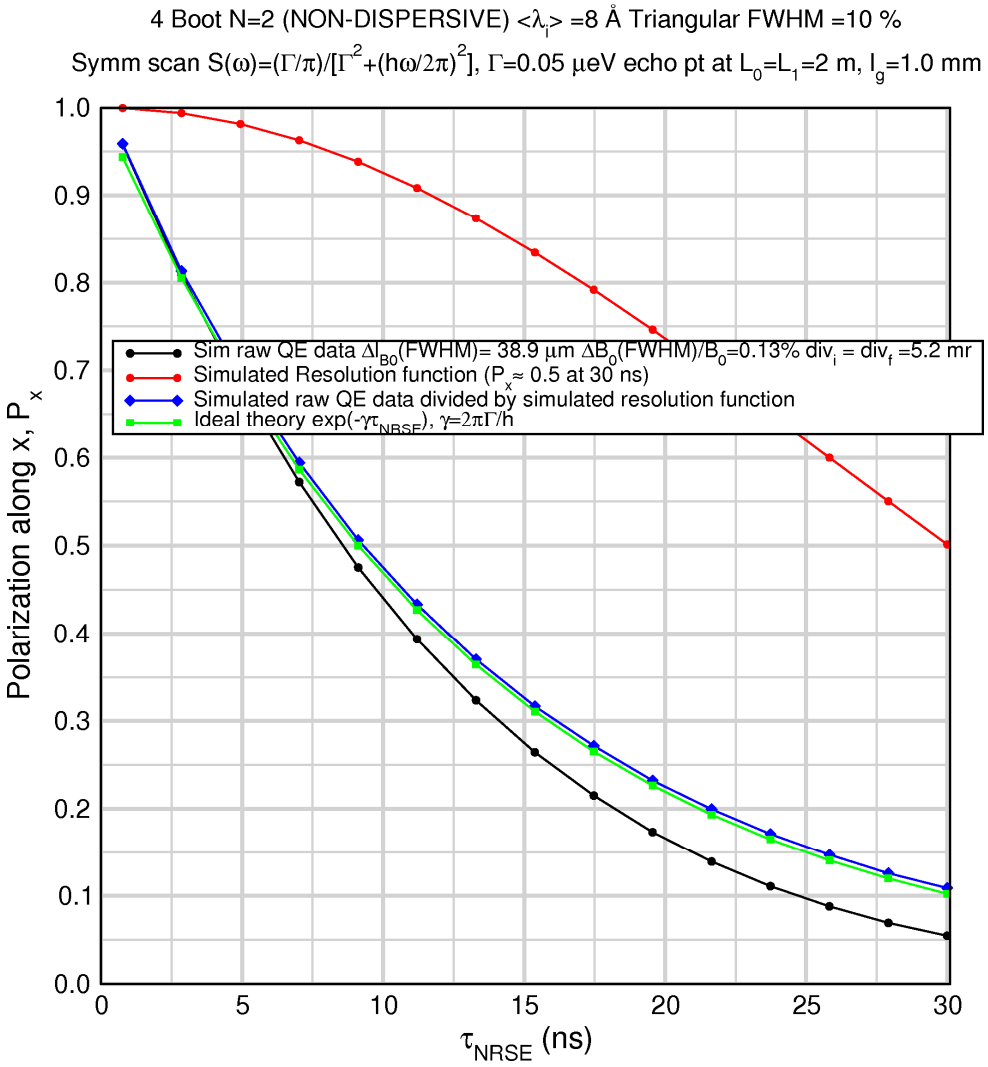

Figure 109. Jeremy C. Cook.

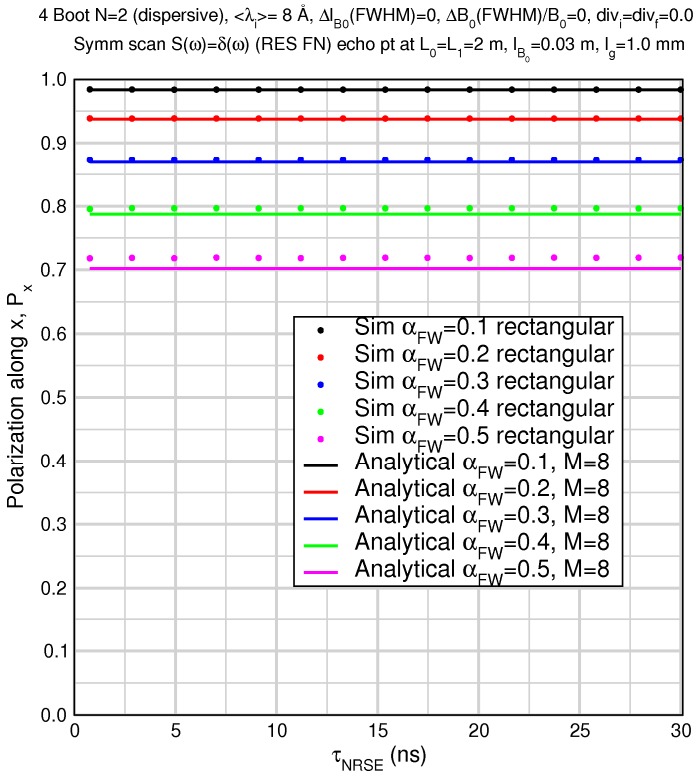

Figure 110. Jeremy C. Cook.

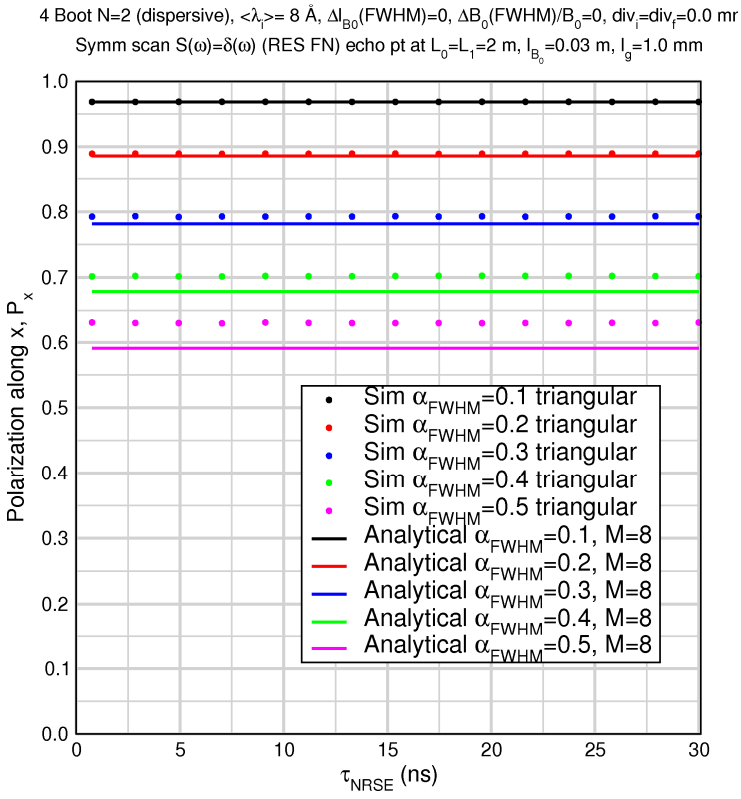

Figure 111. Jeremy C. Cook.

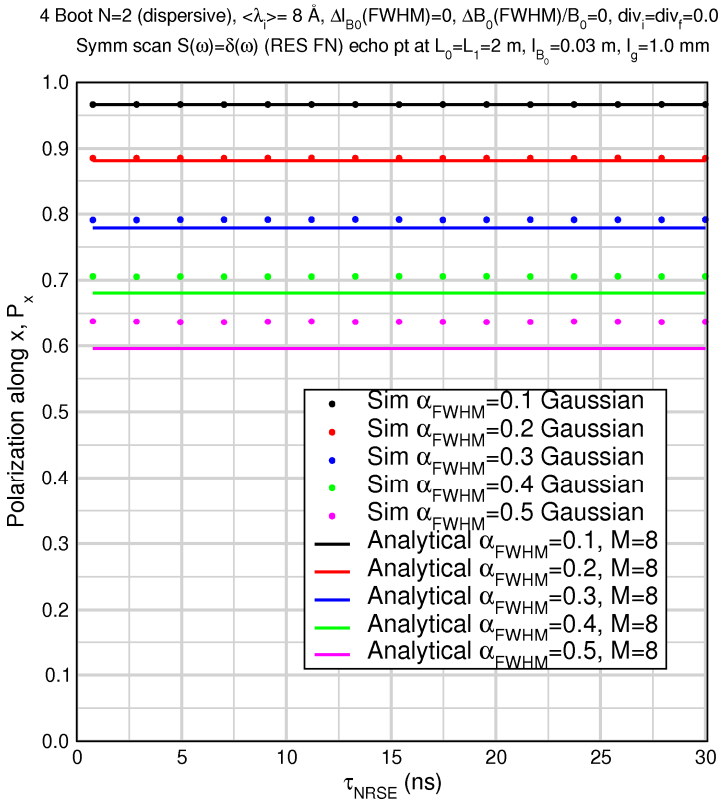

Figure 112. Jeremy C. Cook.

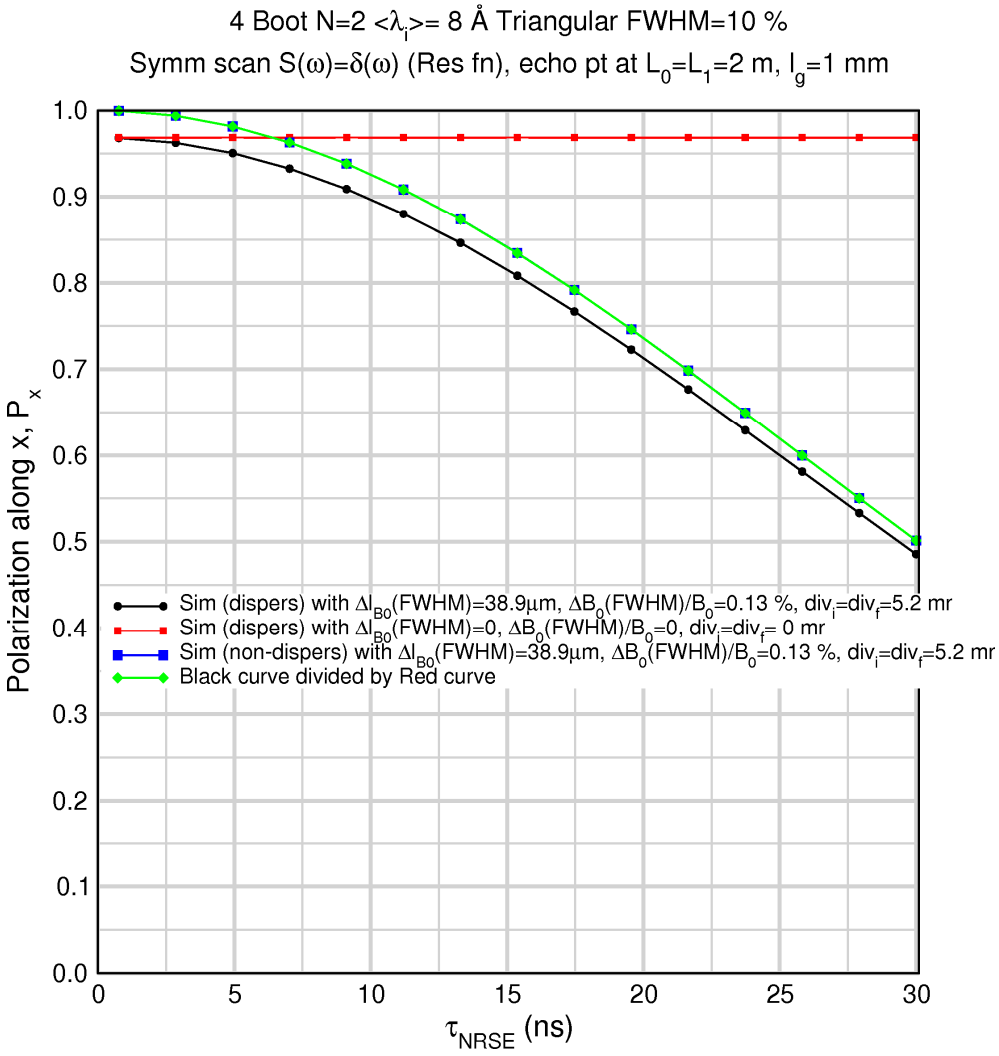

Figure 113. Jeremy C. Cook.

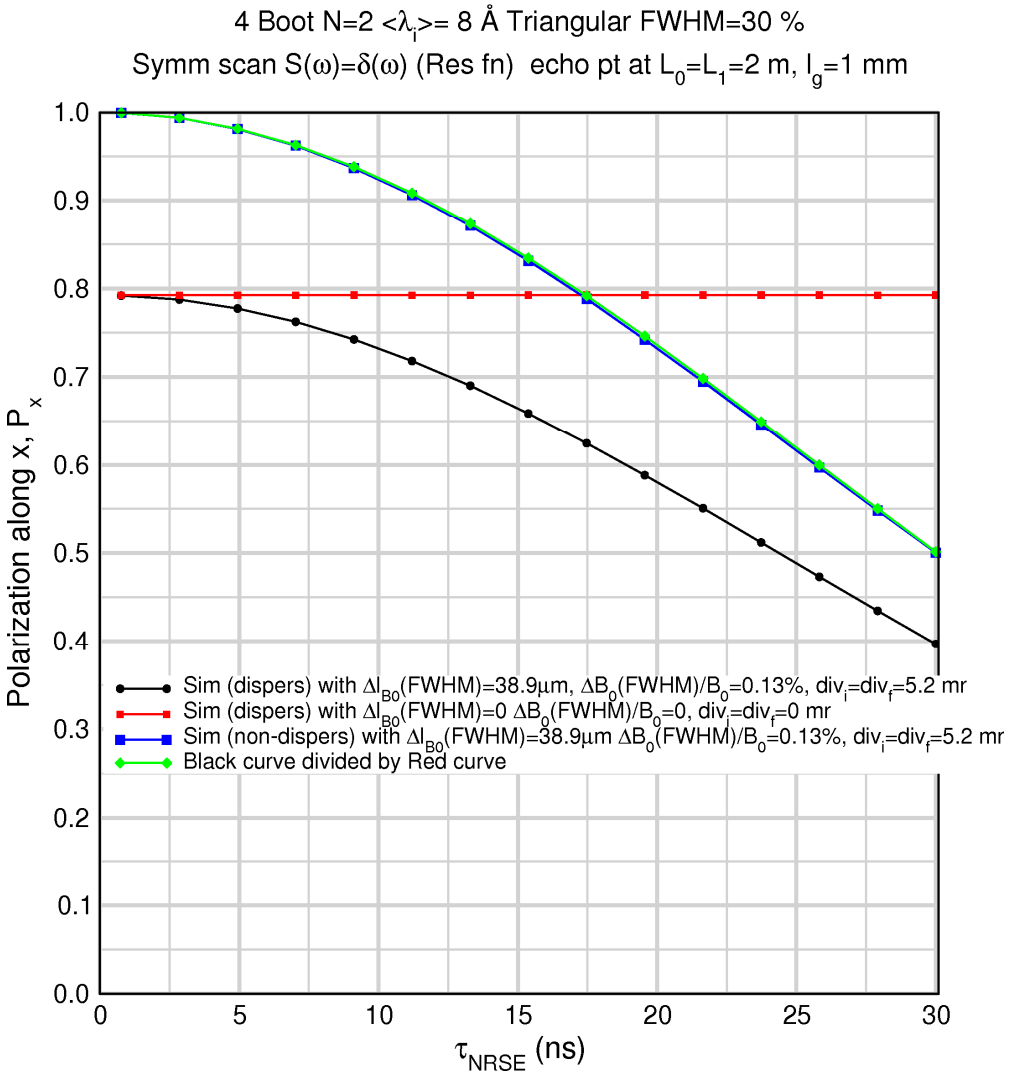

Figure 114. Jeremy C. Cook.

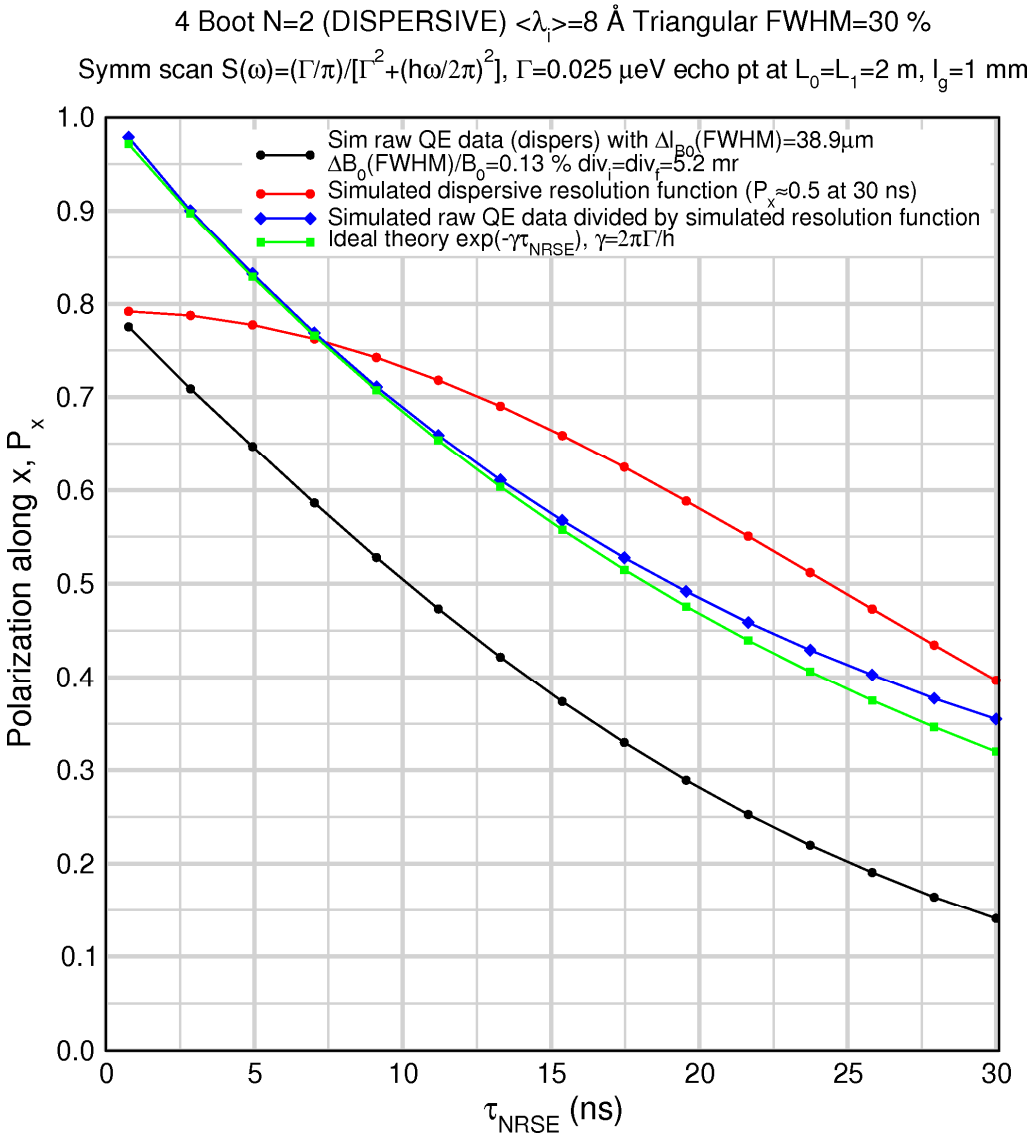

Figure 115. Jeremy C. Cook.

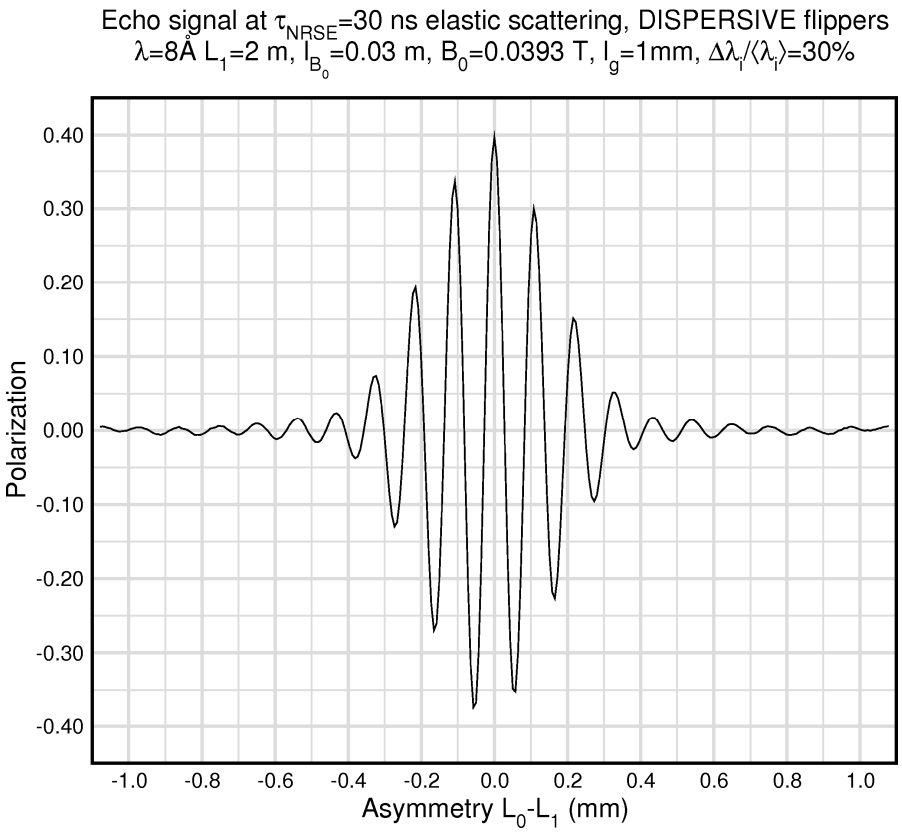

Figure 116. Jeremy C. Cook.

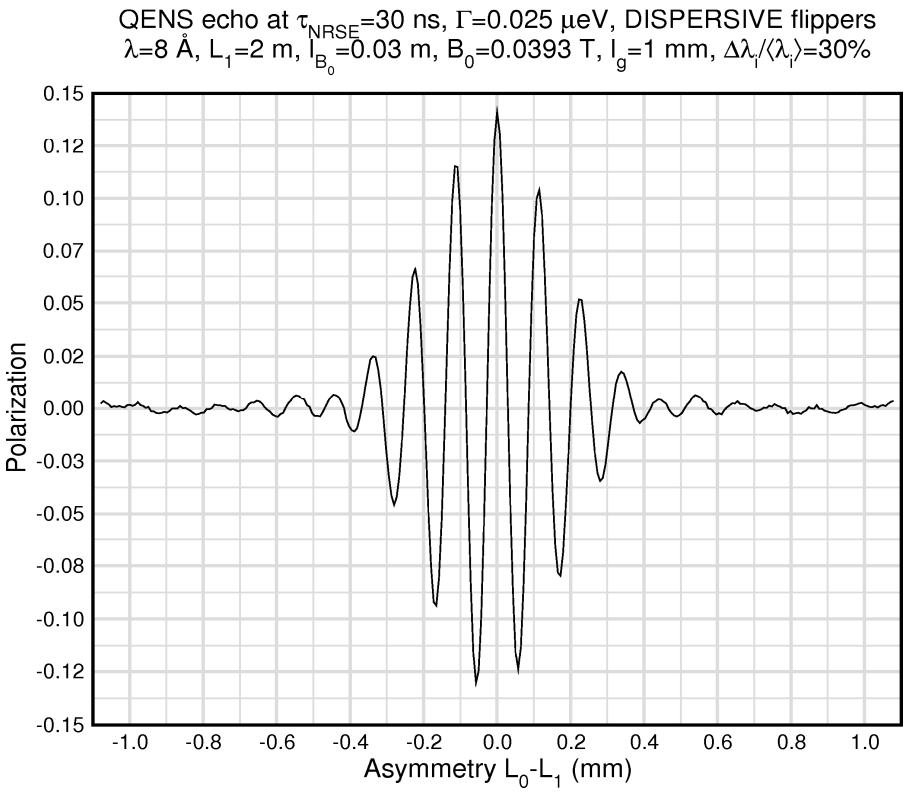

Figure 117. Jeremy C. Cook.

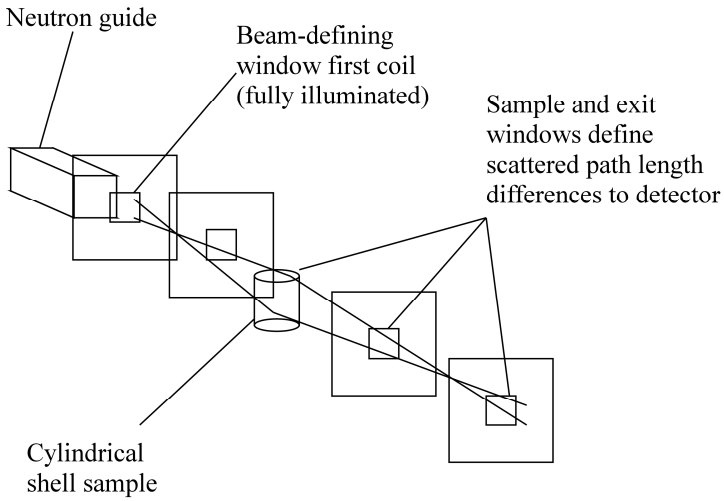

Figure 118. Jeremy C. Cook.

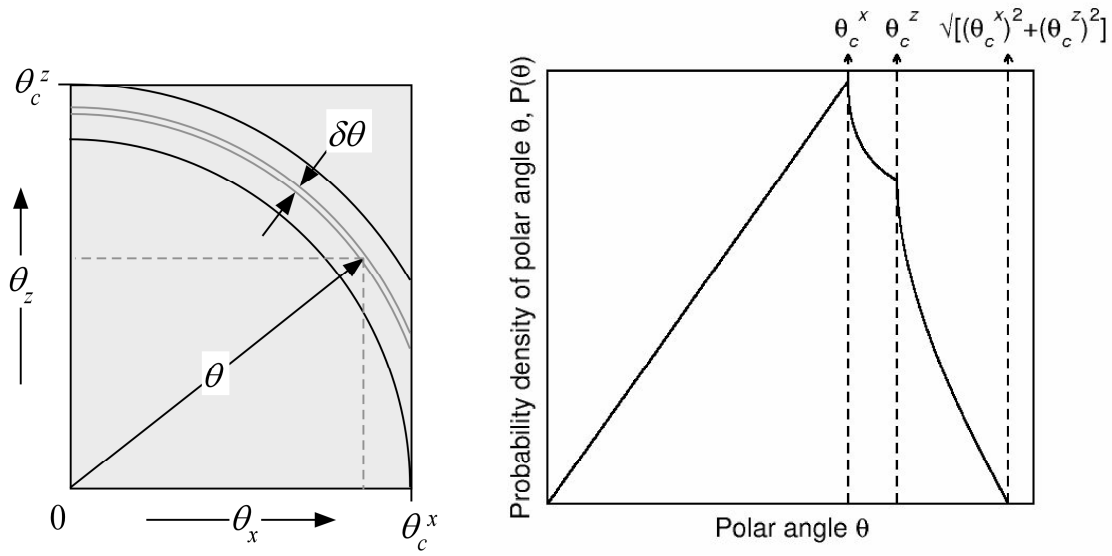

Figure 119. Jeremy C. Cook.

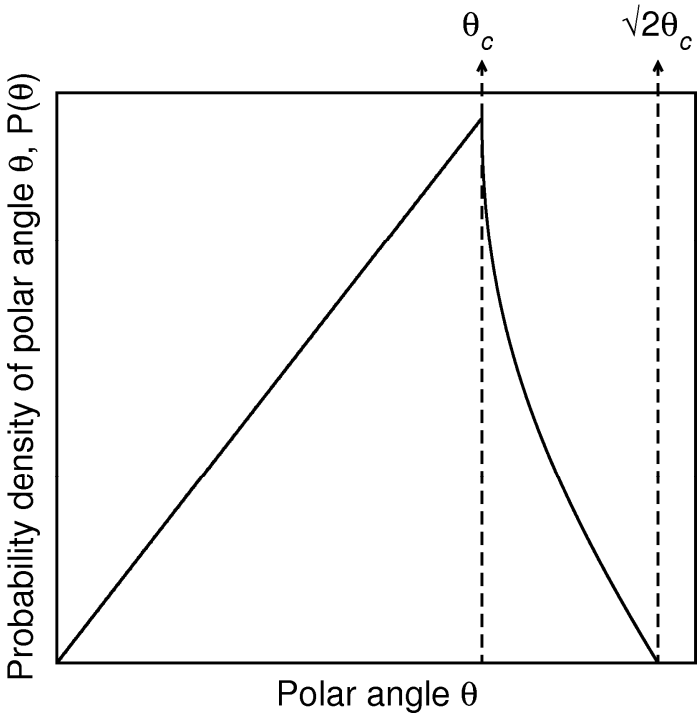

Figure 120. Jeremy C. Cook.

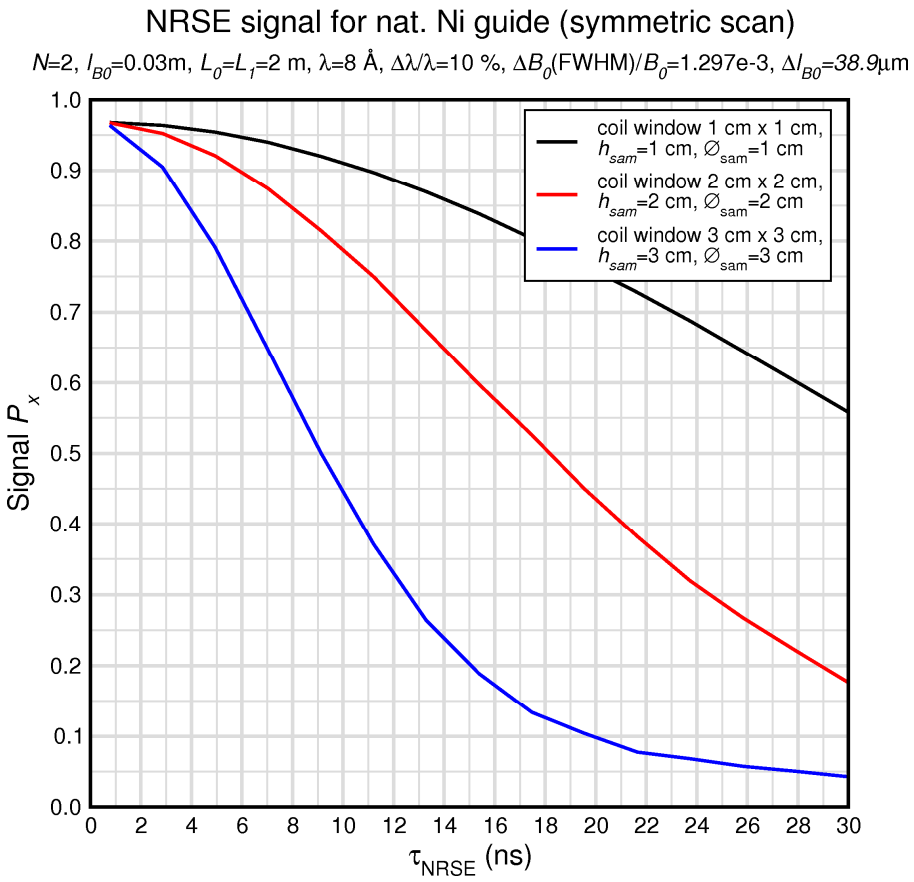

Figure 121. Jeremy C. Cook.

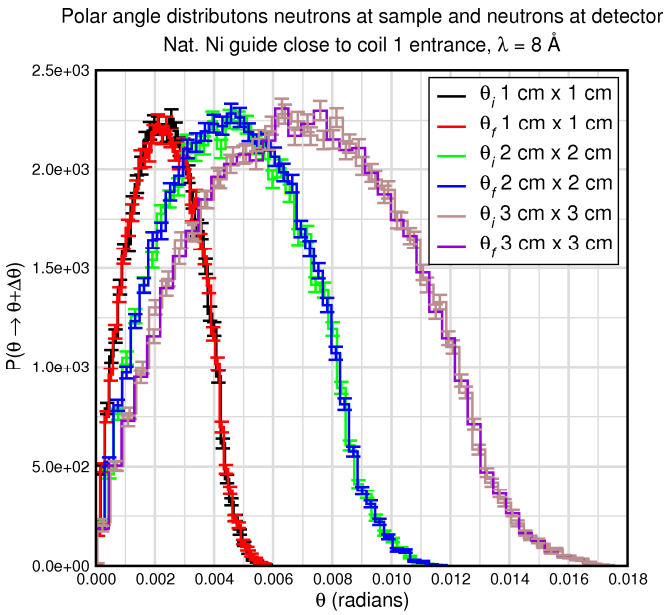

Figure 122. Jeremy C. Cook.

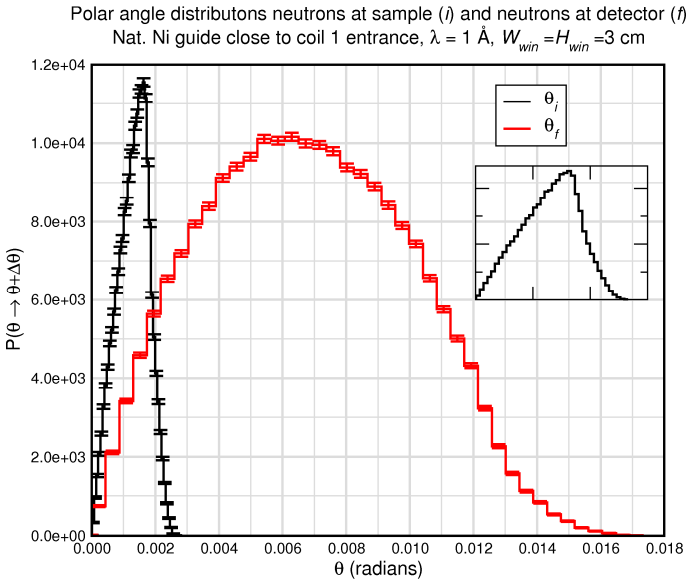

Figure 123. Jeremy C. Cook.

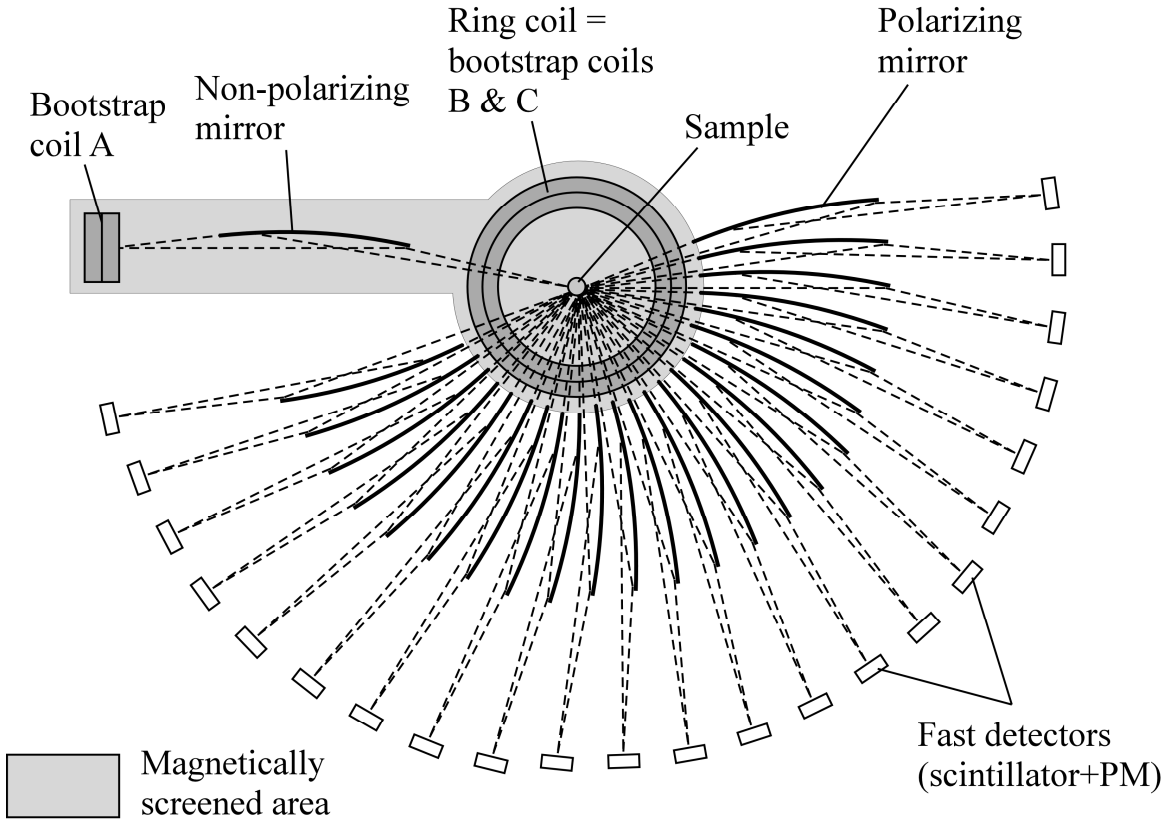

Figure 124. Jeremy C. Cook.

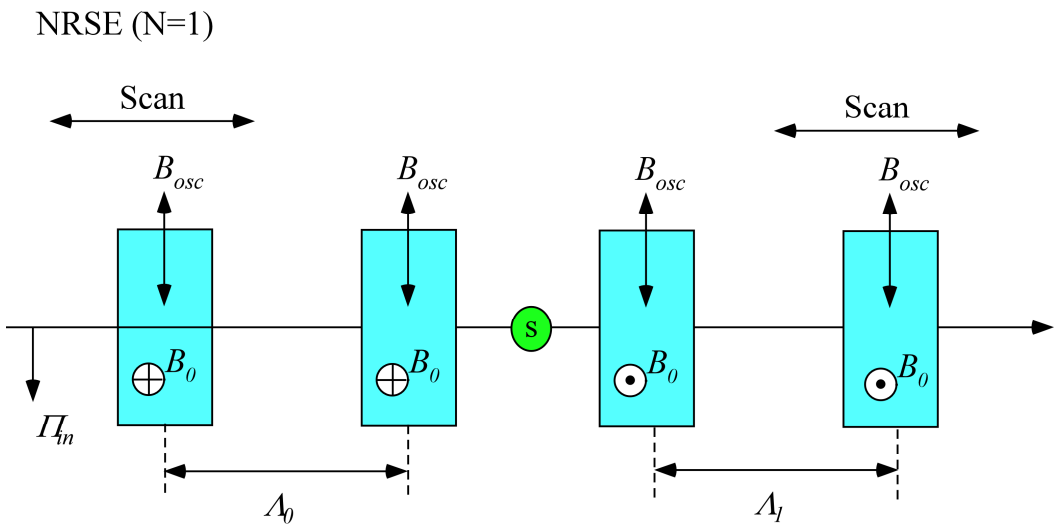

Figure 125. Jeremy C. Cook.

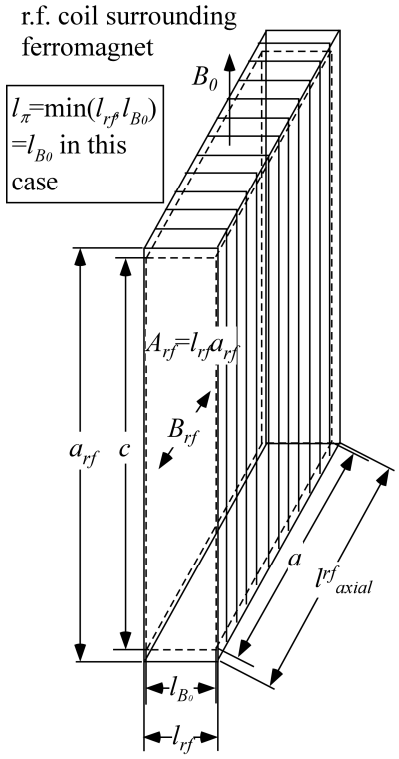

Figure 126. Jeremy C. Cook.

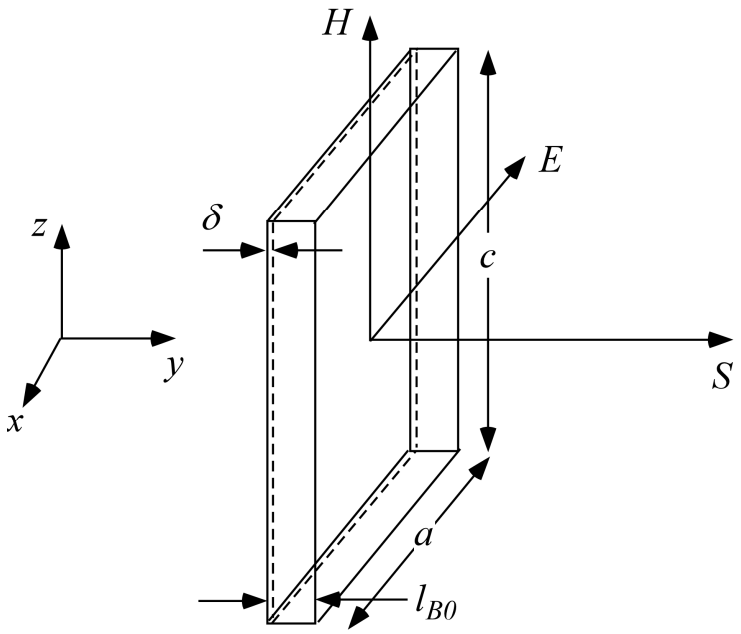

Figure 127. Jeremy C. Cook.

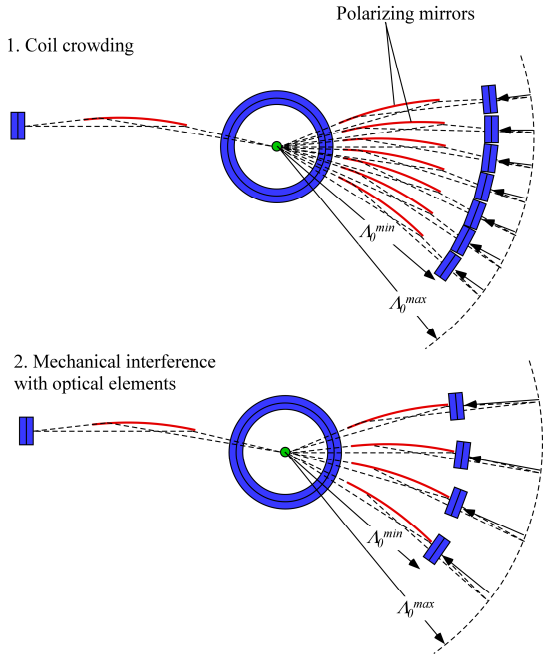

Figure 128. Jeremy C. Cook.

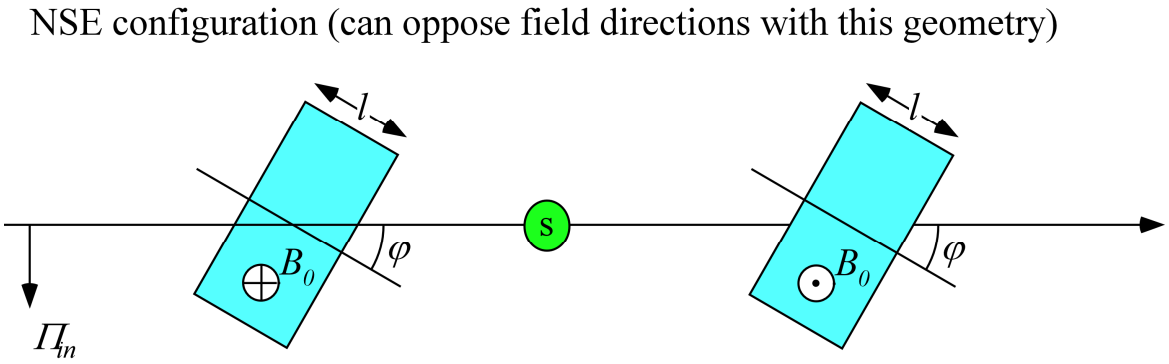

Figure 129. Jeremy C. Cook.

Figure 130. Jeremy C. Cook.

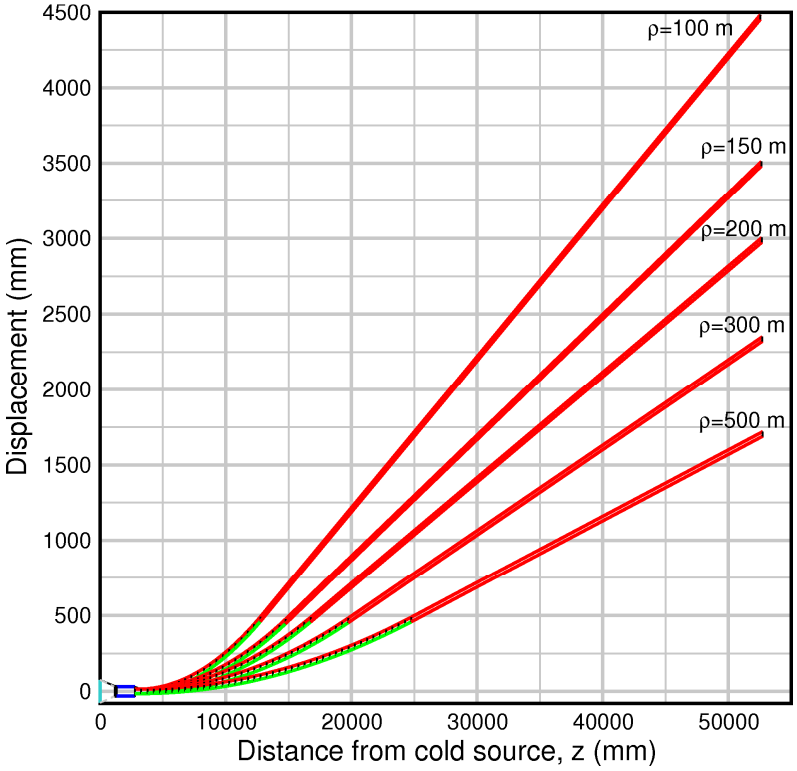

Figure 131. Jeremy C. Cook.

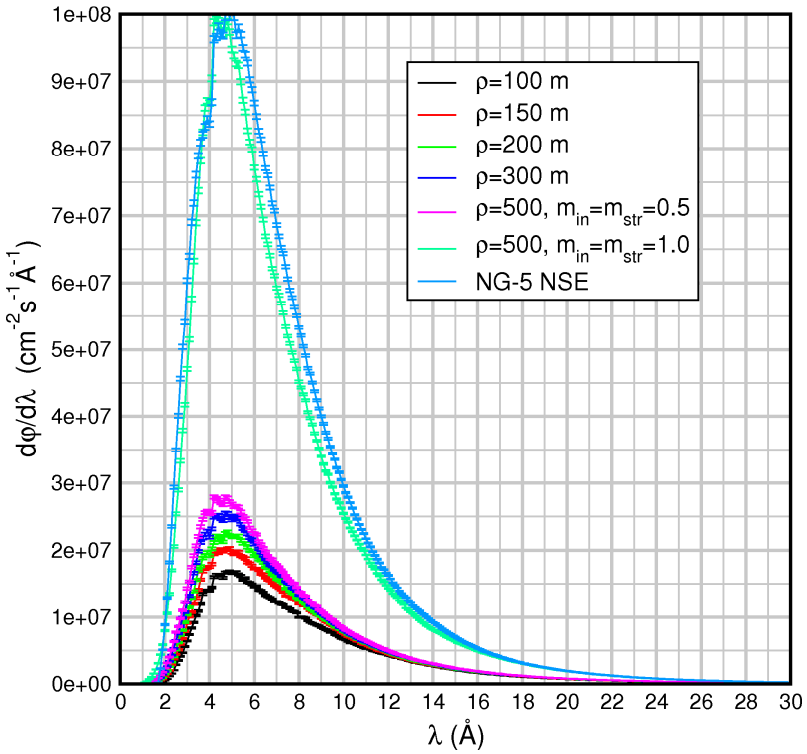

Figure 132. Jeremy C. Cook.

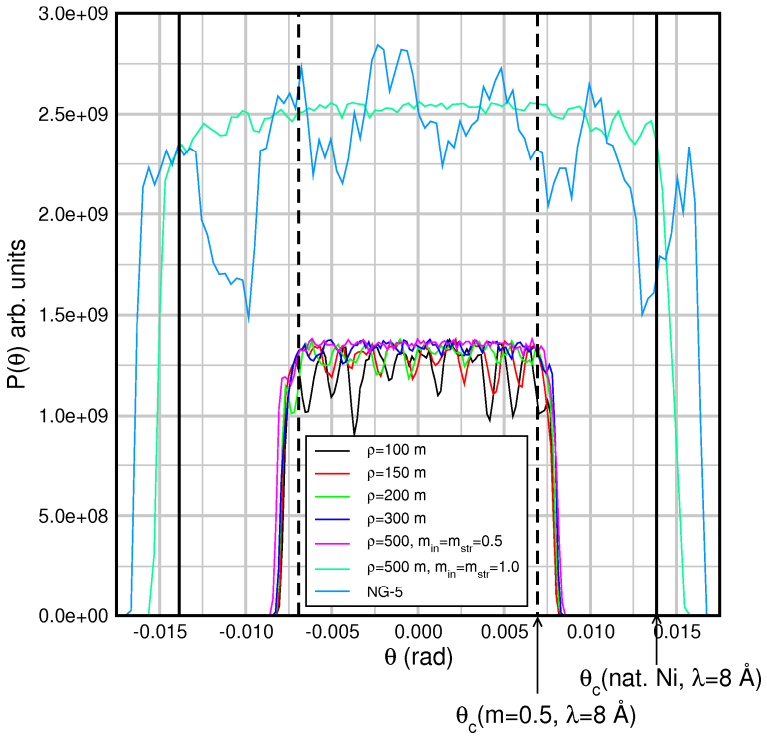

Figure 133. Jeremy C. Cook.

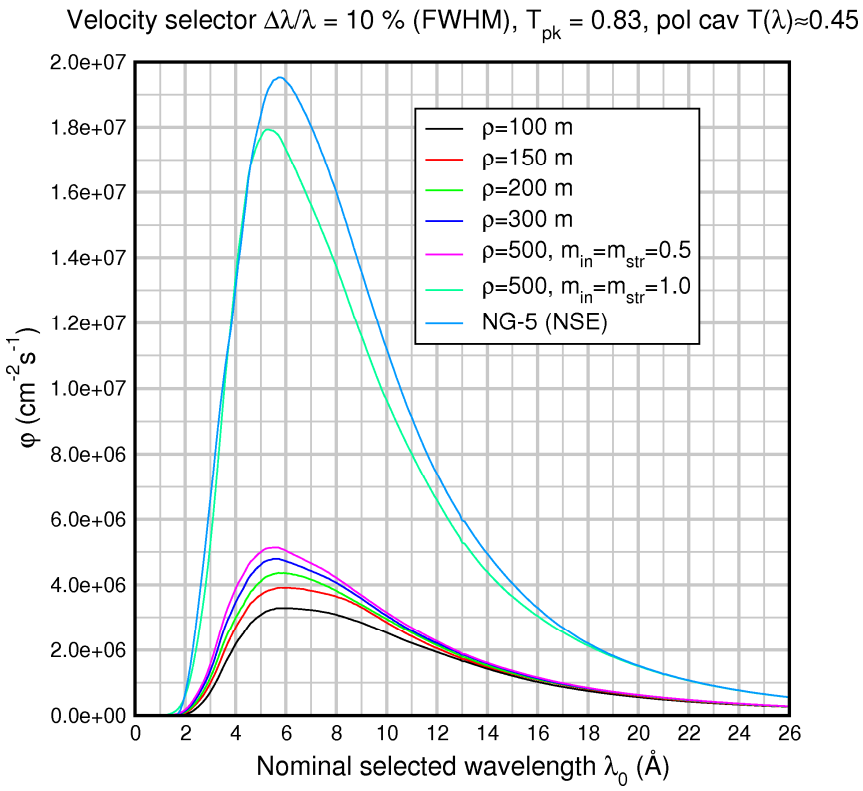

Figure 134. Jeremy C. Cook.

References

[1] R. Golub and R. Gähler, *Phys.Lett.A.* **123** (1987) 43.

[2] R. Gähler and R. Golub, *J.Phys.France* **49** (1988) 1195.

[3] F. Mezei, *Lecture notes in physics* **128**, 3. Springer-Verlag, Berlin (1980).

[4] I. I. Rabi, S. Millman, P.Kusch, and J. R. Zacharias, *Phys.Rev* **55** (1939) 526.

[5] F. Bloch and A. Siegert, *Phys.Rev.* **57** (1940) 522.

[6] L. W. Alvarez and F. Bloch, *Phys.Rev.* **57** (1940) 111.

[7] T. Keller, P. Zimmermann, R. Golub, and R. Gähler, *Physica B* **162** (1990) 327.

[8] R. Gähler, R. Golub, and T. Keller, *Physica B* **156 & 157** (1989) 653.

[9] F. Mezei, *Physica B* **137** (1986) 295-308.

[10] F. Mezei, *Physica B* **151** (1988) 74.

[11] M. Köppe, P. Hank, J. Wuttke, W. Petry, R. Gähler, and R. Kahn, *J.Neutron.Research*, **4** (1996) 261.

[12] M. Köppe, M. Bleuel, R. Gähler, R. Golub, P. Hank, T. Keller, S. Longeville, U. Rauch, and J. Wuttke, *Physica B* **266** (1999) 75.

[13] R. Golub, R. Gähler, and T. Keller, *Am.J.Phys.* **62** (1994) 779.

[14] E. Krüger, *Nukleonika* **25** (1980) 889.

[15] J. B. Hayter, *Z.Physik.B* **31** (1978) 117.

[16] K. D. Mielenz, *J.Res.NIST*, **102** (1997) 363-365.

[17] M. A. Heald, *Math.Comp*. **44** (1985) 459-461.

[18] Neutron Cross-Sections, Brookhaven National Laboratory report B.N.L. 325, D. J. Hughes and R. L. Schwartz, (1958).

[19] D. Dubbers, P. El-Muzeini, M. Kessler, and J. Last, *Nucl.Inst.Methods.A.* **275** (1989) 294.

[20] J. E. Shigley and L. D. Mitchell, "Mechanical Engineering Design" 4th Edition, McGraw-Hill 1983.

[21] A. P. Wills, *Phys.Rev.* **9** (1899) 193.

[22] T. Keller, Ph.D. Thesis, Technischen Univerität München (1993).

[23] N. F. Ramsey, "Molecular Beams" (Oxford University Press, 1956).

[24] A. W. Rücker, *Phil.Mag*. **37** (1894) 95.

[25] Du Bois, *Wied.Ann*. **63** (1897) 348.

[26] D. Dubbers, *Nucl.Inst.Methods.A.* **243** (1986) 511.

[27] T. Keller, R. Golub, and R. Gähler in "Neutron Spin Echo - A technique for high resolution neutron scattering" Ed. E. R. Pike, P. C. Sabatier, Academic Press (2001).

[28] D. F. R. Mildner and J. C. Cook, Nucl.Instrum.&.Meth A **592** (2008) 414-419.

[29] J. C. Cook, "Design and estimated performance of a new neutron guide system for the NCNR Expansion Project", *Rev.Sci.Instrum.,* **80** (2009) 023101.

[30] J. R. D. Copley and D. F. R. Mildner, Nucl.Sci.&.Eng. **110** (1992) 1-9.